



HAL
open science

Le déplacement asymétrique des parois de domaine magnétiques : ses causes et ses effets

Mohamed Ali Nsibi

► **To cite this version:**

Mohamed Ali Nsibi. Le déplacement asymétrique des parois de domaine magnétiques : ses causes et ses effets. Mesoscopic Systems and Quantum Hall Effect [cond-mat.mes-hall]. Université Grenoble Alpes, 2019. English. NNT : 2019GREAY047 . tel-02512896

HAL Id: tel-02512896

<https://theses.hal.science/tel-02512896>

Submitted on 20 Mar 2020

HAL is a multi-disciplinary open access archive for the deposit and dissemination of scientific research documents, whether they are published or not. The documents may come from teaching and research institutions in France or abroad, or from public or private research centers.

L'archive ouverte pluridisciplinaire **HAL**, est destinée au dépôt et à la diffusion de documents scientifiques de niveau recherche, publiés ou non, émanant des établissements d'enseignement et de recherche français ou étrangers, des laboratoires publics ou privés.

THÈSE

Pour obtenir le grade de

DOCTEUR DE LA COMMUNAUTE UNIVERSITE GRENOBLE ALPES

Spécialité : **Physique de la matière condensée**

Arrêté ministériel : 25 mai 2016

Présentée par

Mohamed Ali NSIBI

Thèse dirigée par **Gilles GAUDIN**
et co-encadrée par **Ioan Mihai MIRON**

préparée au sein du **Laboratoire SPINTEC**
et de l'**École Doctorale de physique de Grenoble**

Asymmetric magnetic domain walls motion in a two-dimensional geometry: causes and effects

Thèse soutenue publiquement le **16 octobre 2019**,
devant le jury composé de :

M. Jan VOGEL

Directeur de Recherche, Institut Néel, Président

M. Jean-Marie GEORGE

Directeur de Recherche, Unité Mixte de Physique CNRS/Thales, Rapporteur

M. Joo-Von KIM

Directeur de Recherche, Centre de Nanosciences et de Nanotechnologies,
Rapporteur

M. Pietro GAMBARDELLA

Professeur, ETH Zürich, Examineur

M. Reinoud LAVRIJSEN

Professeur assistant, Eindhoven University of Technology, Examineur

M. Ioan Mihai MIRON

Chargé de Recherche, SPINTEC, Co-encadrant de thèse

M. Gilles GAUDIN

Directeur de Recherche, SPINTEC, Directeur de thèse



List of Abbreviations

BLS – Brillouin light scattering technique
BW – Bloch domain wall
CD – The Chiral Damping mechanism
CIDWM – Current-induced domain wall motion
DMI – Dzyaloshinskii-Moriya interaction
DRAM – Dynamic random-access memory
DW – Magnetic domain wall
DW_{U-D} – Up/down domain wall
DW_{D-U} – Down/up domain wall
FIDWM – Field-induced domain wall motion
FM – Ferromagnetic layer
GMR – Giant Magnetoresistance
HDD – Hard disk drive
HM – Heavy metal layer
LLG – Landau-Lifshitz-Gilbert equation
MOKE – Magneto-optical Kerr effect microscopy
MRAM – Magnetic random-access memory
MTJ – Magnetic tunnel junction
NW – Néel domain wall
PMA – Perpendicular magnetic anisotropy
SHE – Spin Hall effect
SIA – Structural inversion asymmetry
SkHA – Skyrmion Hall angle
SkHE – Skyrmion Hall effect
SOC – Spin-orbit coupling
SOT – Spin-orbit torques
SPLEEM – Spin-polarized low energy microscopy
SP-STM – Spin-polarized scanning tunneling microscopy
SRAM – Static random-access memory
STT – Spin-transfer torques
TMR – Tunneling magnetoresistance
XMCD-PEEM – X-ray magnetic circular dichroism photoemission electron microscopy

List of symbols

- A_{ex} – Exchange interaction stiffness
- D – The DMI constant
- d – Diameter of a circular magnetic domain / magnetic bubble
- H_K – Magnetostatic ‘shape’ anisotropy effective field of a Bloch wall
- H_{DL} – The effective “damping-like” magnetic field
- H_{DMI} – The local effective DMI field
- H_{dip} – Dipolar magnetic field
- H_{FL} – The effective “field-like” magnetic field
- H_{th} – The thermal magnetic field
- H_x – The applied in-plane magnetic field
- H_z – The applied out-of-plane magnetic field
- H_z^{mb} – The external out-of-plane field stabilizing magnetic bubbles
- J – The charge current density vector
- K – Magnetostatic ‘shape’ anisotropy of a Bloch wall
- K_{dip} – Dipolar energy constant
- K_{eff} – Effective uniaxial anisotropy constant
- M – The local magnetization
- M_s – Saturation magnetization
- m – The unit magnetization vector
- m_{DW} – The DW core magnetization unit vector
- n – Topological charge of a skyrmion
- n_{DW} – the DW normal vector
- T_{DL} – The damping-like torque from SOT
- T_{dip} – The dipolar torque
- T_{FL} – The field-like torque from SOT
- T_α – The damping torque
- t_{FM} – Thickness of the ferromagnetic layer
- v_{DW} – The DW velocity
- v_{DU} – Velocity of the down/up DW
- v_{sk} – Velocity of the magnetic skyrmion bubble
- v_{UD} – Velocity of the up/down DW
- α, α_0 – The isotropic Gilbert damping parameter
- α_c – The chiral component of the damping parameter
- Δ – DW width parameter
- σ_0 – Energy density of a Bloch wall

σ_{DW} – Energy density of a DW

θ_{SH} – Spin Hall angle of a metal

θ_{skH} – The skyrmion Hall angle

ϕ_d – The drift angle of the magnetic bubble

ϕ_J – The angle between \mathbf{J} and \mathbf{n}_{DW}

ϕ_J^{max} – The angle of largest displacement of the DW

μ_0 – Magnetic permeability of vacuum

Contents

List of Abbreviations.....	ii
List of symbols	iii
Contents.....	v
Introduction	1
I. State of the art	6
I.1. Energies in a ferromagnetic system.....	6
I.1.1. The Zeeman energy.....	7
I.1.2. The exchange energy.....	7
I.1.3. The magnetic dipolar energy	7
I.1.4. The magnetic anisotropy energy.....	9
I.2. Domain walls in perpendicular magnetic anisotropy films.....	9
I.2.1. Perpendicular magnetic anisotropy (PMA) thin films.....	9
I.2.2. Domain walls in PMA materials	10
I.2.3. DW motion in PMA materials	11
I.3. Field-induced DW motion (FIDWM).....	12
I.3.1. LLG equation	12
I.3.2. Displacement of a DW by a magnetic field	14
I.3.3. Flow regime of motion	15
I.3.4. Creep regime of motion	16
I.4. Current-induced DW motion (CIDWM)	17
I.4.1. Spin-transfer torques (STTs)	17
I.4.1.1. Adiabatic STT	18
I.4.1.2. Non-adiabatic STT	18
I.4.1.3. Displacement of a DW by STT.....	19
I.4.2. Spin-orbit torques (SOTs)	20
I.4.2.1. Rashba Effect and Spin Hall effect (SHE) in SIA materials	21
I.4.2.2. The field-like term of SOT	22
I.4.2.3. The damping-like term of SOT	24
I.4.2.4. Displacement of DWs by SOTs	26
I.5. Chiral DWs motion in SIA materials	28
I.5.1. Dzyaloshinskii-Moriya Interaction (DMI).....	28
I.5.2. Chiral Néel DWs induced by DMI.....	29
I.5.3. Direct evidence of Chiral Néel walls in SIA materials.....	30
I.5.4. DW motion in the presence of DMI.....	32
I.5.4.1. The effect of DMI on FIDWM	32

I.5.4.2. The DMI + SOT mechanism for CIDWM	33
I.5.5. Techniques to quantify DMI	36
I.5.5.1. Techniques not based on DW motion.....	36
I.5.5.2. Techniques based on DW motion	37
I.6. Chiral Damping in DWs	43
I.6.1. The experimental evidence of Chiral Damping.....	43
I.6.1.1. The failure of the DMI-induced asymmetry mechanism.....	43
I.6.1.2. The proposal of chiral dissipation in FIDWM	44
I.6.1.3. A possible description of the Chiral Damping.....	45
I.6.2. Phenomenology and origin of the Chiral Damping	47
I.6.3. The coexistence of different chirality-induced asymmetries	48
Conclusions	51
II. Experimental techniques.....	54
II.1. Samples fabrication.....	54
II.1.1. Thin films deposition	54
II.1.2. Fabrication of wires for DW motion.....	54
II.2. DWs under Magneto-optic Kerr effect (MOKE) microscopy	55
II.3. DW motion by the injection of an electric current	57
II.3.1. Current-induced DW Motion set-up.....	57
II.3.2. DW motion in the presence of external magnetic fields	58
II.3.3. Measurements of DW motion.....	58
III. The asymmetric non-collinear current-induced DW motion in SIA materials.....	61
III.1. The non-collinear DW motion	61
III.2. Asymmetric distortion of magnetic circular domains	65
III.3. Non-collinear DW motion in Pt/Co/AlO _x	66
III.3.1. The DMI + SOT mechanism in the flow regime	67
III.3.2. The DW motion in the presence of an in-plane magnetic field	69
III.3.2.1. Effects of the in-plane magnetic field	69
III.3.2.2. Measurement of the angle ϕ/J_{max}	73
III.3.3. Asymmetric DW motion in the creep regime	75
III.4. Non-collinear DW motion in Pt/Co/Pt	76
III.4.1. The presence of the DMI in Pt/Co/Pt	76
III.4.2. Asymmetric non-collinear DW motion	78
III.4.3. The numerical collective coordinate model	79
III.4.4. The role of the thermal fluctuations.....	81
III.4.4.1. The DW motion in the absence of the thermal fluctuations.....	81
III.4.4.2. The DW motion in the presence of the thermal fluctuations	82
III.4.5. The interplay between the DMI and the Chiral Damping	84

III.4.5.1. Effects of the in-plane magnetic field	84
III.4.5.2. The role of the Chiral Damping in CIDWM	88
Conclusions	93
IV. The DW tilt in SIA materials	95
IV.1. The formation of a DMI-induced DW tilt	95
IV.2. The DW tilt and the non-collinear DW motion	96
IV.3. The DW tilt in Pt/Co/AIOx	97
IV.4. The DW tilt in Pt/Co/Pt	98
Conclusions	99
V. The extrinsic mechanism of the Skyrmion Hall Effect.....	101
V.1. The intrinsic SkHE	102
V.1.1. Magnetic skyrmions.....	102
V.1.2. Current-induced motion and the SkHE.....	103
V.1.2.1. The emergent electromagnetism.....	103
V.1.2.2. The Thiele Equation of motion	105
V.1.2.3. The Skyrmion Hall angle (SkHA)	107
V.1.2.4. Experimental observations of the intrinsic SkHE.....	107
V.1.3. The intrinsic SkHE and the asymmetric DW motion in the non-collinear configuration .	109
V.2. Chiral magnetic bubbles in Pt/Co/Pt and Pt/Co/AIOx	110
V.2.1. Formation of chiral magnetic bubbles	110
V.2.2. Stabilization of chiral magnetic bubbles with an out-of-plane field.....	111
V.2.3. Vanishing intrinsic SkHE in Pt/Co/Pt and Pt/Co/AIOx	112
V.3. The emergence of the extrinsic SkHE	113
V.3.1. The effects of the asymmetric non-collinear DW motion on the skyrmion bubbles.....	113
V.3.1.1. The distortion of the skyrmion bubbles into ellipses in Pt/Co/Pt	114
V.3.1.2. The “apparent” SkHE in Pt/Co/Pt under low current densities	115
V.3.1.3. Hopping-like motion in Pt/Co/Pt under large current densities.....	118
V.3.2. Evidence of “extrinsic” SkHE in Pt/Co/AIOx	119
V.3.2.1. The skyrmion bubbles motion under low current densities.....	119
V.3.2.2. The skyrmion bubble motion under large current densities	120
V.3.3. The mechanism of the extrinsic SkHE.....	123
V.3.4. The extrinsic SkHE and magnetic skyrmion dynamics	124
Conclusions	126
General conclusions.....	128
Appendix	132
References	156
Résumé	172
Abstract	173

Introduction

In magnetism, research covers rich and different topics. Among these, we have the investigation of the microscopic origin of the magnetization (strongly correlated electron systems, frustrated magnetism, etc.) and nanomagnetism which focuses on the collective behaviors of the magnetization (magnetization dynamics, magnonics, etc.). In nanomagnetism, the dynamics of domain walls (DWs), skyrmions or vortex is attractive. These magnetic objects are interesting from both fundamental and technological points of view. They exhibit many exotic properties that are very promising for novel spintronics devices and applications. Spintronics, where magnetism and electronics are combined, offers the opportunity to control the local magnetization of a material by the spin of a free conduction electron or vice versa. Spintronics has emerged as a research field after the discovery of three major effects. The first effect is the Giant Magnetoresistance effect (GMR), reported in 1988 and rewarded by a Nobel Prize in 2007 that was jointly attributed to A. Fert and P. Grünberg. Subsequently, two complementary phenomena of GMR were evidenced; the Spin-transfer torque (STT) followed by the Tunneling Magnetoresistance effect (TMR). GMR is the change in the electrical resistance of a multilayered device upon the modification of its magnetic state. The multilayered device consists of two ferromagnetic layers that are separated by a conducting non-magnetic spacer. The relative orientation between magnetizations of the two ferromagnetic layers defines the device magnetic state, i.e. whether they are parallel or anti-parallel. STT allows changing the magnetic state by the transfer of angular momentum that is mediated via a spin-polarized electric current flowing from one ferromagnetic layer to another. When the non-magnetic spacer is an insulating oxide layer, we speak instead of a TMR and the device is called a Magnetic Tunnel Junction (MTJ). In MTJs, the difference in resistance can reach high ratios up to several hundred percent. The implementation of these effects in Hard Disk Drives (HDD) has led to a significant enhancement of the storage density capacity, reaching nowadays more than 1 Tbit/inch². This is one example of the huge impacts that spintronics has been bringing to the technology and the industry of electronic devices.

Many ideas and proposals have then emerged to make use of spintronics potential in higher levels of the memory hierarchy where the devices are based on CMOS technology. For years, the development of CMOS devices has been following the Moore's law that predicts a density increase (number of components per integrated circuit) by a factor of two each year. However, it is not possible to extrapolate such a trend to the indefinite future. Major challenges and physical limits like thermal stability, power leakage and power consumption impede the scaling of CMOS devices. In order to overcome these hurdles, an alternative approach relies on spintronics, as non-volatility, high data retention and reduced power consumption in the static mode of magnetic memories are desirable. Nevertheless, CMOS memory devices are still advantageous since they have fast bit access/write time rates like in Static random-access memory (SRAM) typically found in the central processor unit cache of a computer. In return, SRAM has a low density and high operational power consumption. Dynamic random-access memory (DRAM) located in an intermediate level in the memory hierarchy is slower but has a higher density than SRAM. In any case, SRAM and DRAM are volatile. Therefore, development of non-volatile scalable magnetic states manipulated at faster rates (high-speed data transfer), at low power and with low bit failure rate is required in order to have spintronics devices embedded in or even replacing SRAM and/or DRAM.

Such a spintronics device is the Magnetic random-access memory (MRAM) that unlike HDD has a much faster bit access time. MRAMs are composed essentially of nano-pillar-patterned MTJs whose magnetic state defines the encoded binary data (either "0" or "1"). The STT-MRAM is attractive because it is non-volatile and scalable. To write bits, electric current flows vertically through the MTJ and controls the magnetic state by STT mechanism. The read out is ensured by the TMR effect. In this technology, writing and reading schemes share the same electric current path accelerating the aging of the tunnel barrier. This is disadvantageous when aiming for a fast switching

rate as it requires large current densities. STT devices suffer as well from an incubation delay that is enhanced by thermal fluctuations. Consequently, the switching time distribution can be several nanosecond wide. Unintentional bit write event can then occur during the reading operation for example.

In order to optimize the STT-MRAM, a great effort has been devoted for the development of ultrathin ferromagnetic films with perpendicular magnetic anisotropy (PMA) that can be implemented in MTJs. PMA materials are interesting thanks to their high thermal stability, which provides a high data retention. The Pt/Co/AlOx stack is a PMA structure that was initially developed to be a lower electrode for MTJs. In this structure, PMA originates from the strong spin-orbit coupling (SOC) at interfaces that is induced by the structural inversion asymmetry (SIA). Research studies carried out in this stack have put in evidence a new efficient mechanism for the current-induced magnetic switching through SOC. The charge to spin conversion from the spin Hall Effect (SHE) and/or the Rashba effect when an electric current flows in the plan of the stack promotes Spin-orbit torques (SOT) that act on the local magnetization of the ferromagnetic layer. A new concept of SOT-MRAM has then emerged. Henceforth, the writing operation is based on an electric current injected in-plane whereas the current flowing perpendicularly to MTJ is used only for the reading operation. Although this three terminal geometry is more demanding in terms of size, it has the advantage to decouple writing and reading schemes solving some issues of the STT-MRAM. Consequently, the junction experiences less stress from the electric current and the two processes can be optimized independently. The MTJ exhibits then a better endurance as there are reports of a robust SOT-switching up to over 10^{12} repeated cycles at current densities up to $4 \cdot 10^{12}$ A.m⁻². The SOT-based magnetic switching has also faster time rates. The spin accumulation at the interface that leads to SOT is orthogonal to the quiescent state of the magnetization of the ferromagnetic layer. It reduces thereby the incubation delay compared to STT. Actually, reliable and reproducible magnetic switching were obtained with current pulses as short as 200 ps in Pt/Co/AlOx and Ta/CoFeB/MgO stacks. By offering as many functionalities as the STT-MRAM, these characteristics make the SOT-MRAM very competitive and a potential candidate to replace DRAM and SRAM in the memory hierarchy.

In SOT-MRAM, the magnetic switching in PMA films takes place through nucleation of DWs and their subsequent propagation. DWs are very thin (~ 5 nm), much thinner than the size of a typical device. A large DW velocity is mandatory to have a fast switching time. Further on, the critical switching current is mostly dependent on the DW mobility rather than on the initial nucleation barrier. The control of the DW motion would allow then partial and reliable switching that could be implemented to develop memristor devices for neuromorphic computing applications. Besides this idea, S. S. Parkin, in 2004 at IBM, proposed another type of devices that is also based on the DW motion. It is called the racetrack memory where series of magnetic domains, corresponding to encoded bits, are shifted towards a read/write head by the injection of a spin-polarized electric current. Magnetic domains are separated by DWs that can be displaced through STT in the direction of the moving electrons. Moreover, tracks can stand vertically giving access to three-dimensionality thus improving the storage capacity of the device. This concept is then promising for large density and fast random-access memories. Its feasibility relies on fast and reproducible DW motion at low critical current densities.

During several years, intensive efforts from many research groups did not succeed in obtaining such desirable features of the DW motion with the STT mechanism. The observation of a fast motion, up to 400 m.s⁻¹ against the electron flow, in the Pt/Co/AlOx stack by I. M. Miron *et al.* in 2011 was a breakthrough. This efficient DW motion could not be explained by STT and was attributed to the combined action of SOT and the interfacial Dzyaloshinskii-Moriya interaction (DMI). DMI is a consequence of SIA in this kind of materials. It ensures that DWs are driven by SOT in a unidirectional motion, i.e. either in or against the electron direction. DMI has also enabled the observation of other magnetic textures such as skyrmions. An intensive effort is currently in progress to optimize DMI for the stabilization of magnetic skyrmions with a sub-10 nm size. It was predicted that magnetic skyrmions require low current densities, compared to DWs, to be manipulated and are

less disturbed by the presence of disorder in materials. They hold then the promise for more energy efficient spintronic devices for either logic or ultra-high-density data storage applications. It is therefore crucial to investigate in depth the roles of SOT and DMI in the dynamics of these magnetic textures, e.g. DWs and magnetic skyrmions.

Concerning SOT, they act on the finite average magnetization of the DW (the DW core magnetization). Consequently, SOT depend on the relative angle between the electric current direction and the DW core magnetization. Thus, an oblique injection of the electric current with respect to the DW allows modifying the action of SOT. It is called the DW motion in a “non-collinear configuration”. C. K. Safeer *et al.* evidenced in 2015 an asymmetric DW motion in such a geometry by studying DWs in Co/AlO_x nanowires patterned on top of a Pt layer. On the one hand, by taking advantage of the asymmetric DW motion, C. K. Safeer *et al.* designed a shape-controlled magnetic switching that helped to demonstrate the field-free SOT magnetic switching. On the other hand, the asymmetric DW motion in the non-collinear geometry cannot be explained by the SOT + DMI mechanism, which calls for a more complete and complex model. Therefore, it is essential to pursue the study of the non-collinear DW motion. It is also important to perform this study in various SIA materials. This will allow understanding the asymmetric DW motion that is paramount to develop efficient and flexible magnetic switching schemes.

As for DMI, it defines the DW equilibrium configuration in SIA materials. For instance, the orientation of the DW core magnetization depends on the magnitude of the DMI. It is then possible to identify the DMI by modulating the DW core magnetization. Such a modulation can be achieved using an external magnetic field oriented in the plane of the structures. In order to understand the role of DMI, we investigate the DW motion in the presence of an in-plane magnetic field. By studying DWs driven by magnetic fields in the Pt/Co/Pt stack, E. Jué *et al.*, identified, in 2015, a new mechanism induced by SIA. It is the Chiral Damping mechanism. It consists in a magnetic damping that depends on the DW chirality, i.e. the direction of rotation of the magnetization within the DW. This new mechanism enriches the understanding of magnetization dynamics and implies the reconsideration of reports of the DW motion. A first step will be to explore the role of Chiral Damping in the current-induced DW motion.

In this context, the main objective of this thesis was to provide a more complete picture of magnetization dynamics. I have studied then the motion of different magnetization textures (DWs and magnetic bubbles). To push forward the understanding of SOT, DMI and the Chiral Damping, I have chosen to study the DW motion in a non-collinear geometry relative to the injected current and in the presence of an external in-plane magnetic field. I have carried out this study in two different Pt/Co-based heterostructures with PMA. The investigated structures are Pt/Co/AlO_x and Pt/Co/Pt. The former structure has a large SIA whereas the latter is a low SIA material. The question is then how characteristics of the DW motion change with the variation of SIA. By comparing results in these two structures, this thesis unveils the dependence of the DW motion on the extent of SIA. My results confirm the failure of the DMI + SOT mechanism and are in part explained by including the Chiral Damping along with the DMI and SOT. I have evidenced then the interplay between chiral energy and chiral dissipation in SIA materials. The DW motion in the non-collinear geometry has been found to exhibit the similar features in Pt/Co/AlO_x and Pt/Co/Pt. I have then tried to find out what consequences such a motion can induce. Following this, I have discovered that the non-collinear DW motion can have a significant effect on current-induced skyrmion bubbles motion. The results of this thesis give new insights on dynamics of DWs and skyrmion bubbles in SIA materials. These efforts will help to understand magnetic textures interactions with electric current allowing the design of desirable future spintronics devices with well-defined functionalities.

This manuscript is divided into five chapters.

In the first chapter, I present the state of the art of the DW motion in PMA multilayers. This introduction is necessary to interpret our experimental results described in chapters three, four and

five. We review the spin-orbit coupling induced mechanisms in SIA ultrathin layers. A special attention is given to the following mechanisms: SOT, DMI and Chiral Damping.

In the second chapter, I describe the used experimental techniques in this thesis. I describe the fabrication process of samples and introduce the magneto-optical Kerr effect employed to image the motion of the magnetic textures. In the end, I present the experimental set-up to inject the electric current and the methods to measure displacements and velocities of DWs.

The third, fourth and fifth chapters are dedicated to the experimental results and their interpretation. In the third chapter, I present the experimental observations of the DW motion in the non-collinear geometry relative to the electric current. This motion is asymmetric in both structures. It is even maintained upon the variation of the DW internal structure by an external in-plane magnetic field. The interpretation of these findings using a numerical model reveals the significant role of the Chiral Damping along with the DMI and SOT in the current-induced motion of DWs. However, these three combined phenomena remain insufficient to account for all observations of DWs dynamics in both the large and the low SIA materials.

In the last two chapters, I present the two important consequences of the non-collinear DW motion. First, I have investigated the possible relation between the non-collinear DW motion and the formation of the DW tilt in wires in the fourth chapter. I have experimentally evidenced that the former mechanism is responsible for the emergence of the latter effect in the Pt/Co/AlO_x structure.

Second, the asymmetric DW motion in the non-collinear geometry shows striking similarities with the so-called skyrmion Hall effect (SkHE). These similarities have led us to extend the scope of this thesis towards the investigation of current-induced motion of skyrmion bubbles. In the fifth chapter, I describe the unexpected experimental results of this study in both Pt/Co/Pt and Pt/Co/AlO_x stacks. These results have demonstrated a new mechanism of skyrmion bubbles deflection; an extrinsic Skyrmion Hall effect. The asymmetric non-collinear DW motion generates such a contribution to the SkHE. This new concept enriches the scope of magnetic skyrmions dynamics.

Finally, I close the manuscript by giving general conclusions and the perspectives.

I. State of the art

In this chapter, I will introduce some concepts of solid-state magnetism that are essential to address the experimental work presented in the following chapters. During the thesis, the focus was on magnetic domain wall (DW) motion in ultrathin layers with perpendicular magnetic anisotropy (PMA) and structural inversion asymmetry (SIA). I first present magnetic interactions that govern the ferromagnetic state, lead to the formation of DWs and give rise to PMA. Next, I describe field-induced DW motion (FIDWM) and current-induced DW motion (CIDWM) in materials with PMA. Further, I discuss the emergent phenomena from SIA and their impact on DW motion: spin-orbit torques (SOT), the Dzyaloshinskii-Moriya interaction (DMI) and the novel Chiral Damping concept.

I.1. Energies in a ferromagnetic system

In solid materials, magnetism arises from the arrangement within an atom, according to the Hund's rule, of quantized magnetic dipole moments associated to spins of electrons. A spin is an intrinsic angular momentum carried by an electron, depicted as a particle that spins or precess around its own axis. This picture is misleading as the spin has a quantum nature with only two states: a spin up or a spin down. If the arrangement of spins leads to a partially filled shell, the atom gets a net magnetic moment. In materials called paramagnetic materials, these magnetic moments point in random directions giving a total zero magnetization. They yield a net magnetization when they align parallel to an external magnetic field. Other materials involve magnetic moments that align spontaneously in the same direction without an external magnetic field. They are the anti-ferromagnetic, ferrimagnetic or ferromagnetic materials characterized by a spontaneous (or a remanent) magnetization M_s . It is the net magnetic moment per unit volume (or mass). Depending on their mutual interaction, the magnetic moments of neighboring atoms align anti-parallel in anti-ferromagnetic and ferrimagnetic materials or parallel in ferromagnetic materials. Since in this work we deal with ferromagnetic thin layers, we will consider only magnetic moments that align spontaneously parallel to each other.

In a ferromagnet, thermal fluctuations perturb the mutual orientation of neighboring magnetic moments. Above a certain temperature called the Curie temperature T_C , they end up destroying the magnetic order and the material is henceforth paramagnetic ($M_s = 0$). Since we are interested in ferromagnetic materials that can be used in everyday life from domestic refrigerator magnets to sensors and data storage devices, we will restrict ourselves to materials with T_C above the room temperature of 300 K. This is satisfied for example by 3d transition metals (Fe, Co, and Ni) and a wide variety of their alloys [Levy, Fanter and Wolf, 1972].

All atomic magnetic moments of a macroscopic ferromagnet are not necessarily aligned in the same direction. The magnetic structure can be composed of microscopic regions, called magnetic domains, within which all magnetic moments are aligned. The boundary separating adjacent regions is called the DW. The stabilization of such complex structures and patterns results from the minimization of the total energy in the ferromagnetic system. For instance, the total energy is essentially the sum of several contributions commonly; the Zeeman interaction ϵ_z , the exchange interaction ϵ_{ex} , the dipolar interaction ϵ_{dip} and the magnetic anisotropy interaction ϵ_{anis} [O'Handley, 2000; Buschow and de Boer, 2003].

I.1.1. The Zeeman energy

The Zeeman energy term corresponds to the interaction between the local magnetization¹ \mathbf{M} and a magnetic field. This interaction tends to align \mathbf{M} parallel to the applied magnetic field. It writes as follow:

$$\epsilon_z = -\mu_0 \mathbf{M} \cdot \mathbf{H}_{app} \quad (\text{I.1})$$

where μ_0 is the magnetic permeability of vacuum and \mathbf{H}_{app} the external applied magnetic field.

I.1.2. The exchange energy

The exchange interaction ϵ_{ex} is a short-range interaction characterized by the exchange constant J_{ij} that couples neighboring magnetic moments \mathbf{S}_i and \mathbf{S}_j . It arises from quantum mechanical phenomena that promotes magnetic moments to align in the same direction ($J_{ij} > 0$) or in opposite directions ($J_{ij} < 0$). ϵ_{ex} writes as follow:

$$\epsilon_{ex} = -\sum_{i,j} J_{ij} S_i S_j \cos \phi_{i,j} \quad (\text{I.2})$$

where $\phi_{i,j}$ is the angle between \mathbf{S}_i and \mathbf{S}_j . There is an energy cost when magnetic moments are misaligned. This interaction does not specify any particular orientation for the moments. For micromagnetic considerations, the discrete system of magnetic moments is modeled by a continuously varying magnetization. The exchange interaction writes then as an integral over the volume of the ferromagnet.

$$\epsilon_{ex} = \int A_{ex} \left[(\nabla M_x)^2 + (\nabla M_y)^2 + (\nabla M_z)^2 \right] dV \quad (\text{I.3})$$

The misalignment is accounted for by the gradients of the components of the local magnetization \mathbf{M} . A_{ex} is the exchange interaction stiffness that incorporates the exchange constant J_{ij} and the structure of the material. If only the exchange interaction existed, a ferromagnetic material would be a single macro-domain with uniform magnetization.

This short-range interaction has a characteristic length; the exchange length $l_{ex} = \sqrt{2A_{ex}/(\mu_0 M_s^2)}$. The exchange interaction is considered negligible between two moments separated by a distance much larger than l_{ex} and all moments located within this length can be modeled as a unique acting macro-spin. By taking values of A_{ex} and M_s available in literature for comparable structures to ours [Metaxas et al., 2007; Miron et al., 2010], l_{ex} is estimated to be more than 4 nm whereas the thicknesses of the ferromagnetic layers considered in this thesis are less than 1 nm. In consequence, we assume that the magnetization \mathbf{M} does not depend on the position along the normal to the film (the z-axis) and that the magnetic structure is two-dimensional.

I.1.3. The magnetic dipolar energy

A magnetic moment, by analogy the local magnetization \mathbf{M} , is a magnetic dipole whose magnetic stray field \mathbf{H}_{dip} lines are curling around to fulfill the magnetic flux closure, as there can be

¹ The local magnetization \mathbf{M} (or simply “magnetization”) corresponds to the density of all magnetic moments in a ferromagnet. Inside the magnetic material, \mathbf{M} is a function of the position vector \mathbf{r} with $\mathbf{M}(\mathbf{r}) = \frac{d\mathbf{m}}{dr^3}$ and $\mathbf{m} = \iiint \mathbf{M}(\mathbf{r}) dr^3$ (\mathbf{m} the net magnetic moment of the material, $d\mathbf{m}$ the elementary magnetic moment and dr^3 the volume element).

no free magnetic monopoles according to the Gauss's law for magnetism, $\nabla \cdot \mu_0(\mathbf{H} + \mathbf{M}) = 0$. In a ferromagnetic material, \mathbf{H}_{dip} is then antiparallel to a neighboring \mathbf{M} destabilizing the single domain configuration favored by the exchange interaction. We refer to this gain in the ferromagnetic energy as the magnetic dipolar interaction. Locally, this interaction is small compared to the exchange interaction but it is a long-range interaction that can influence the spatial distribution of the magnetization. Since a dipole can be viewed as an association of positive and negative charges, the dipolar interaction can be modeled by the interaction between \mathbf{M} and \mathbf{H}_{dip} produced by those charges. For ultrathin magnetic layers (**Figure I.1**), the strength of \mathbf{H}_{dip} depends strongly on the orientation of \mathbf{M} with respect to the thin film plane. For a magnetization \mathbf{M} uniformly oriented along an axis in the film plane (**Figure I.1.a**), the uncompensated positive and negative charges are far away from each other. The resulting \mathbf{H}_{dip} is small. In the contrary, when \mathbf{M} is aligned along the film thickness (**Figure I.1.b**), the magnetic charges are closer to each other creating a large \mathbf{H}_{dip} . In order to minimize charges at the surfaces and thus to reduce the dipolar interaction, the ferromagnet breaks into multiple smaller domains at the expense of the exchange interaction (**Figure I.1.c**).

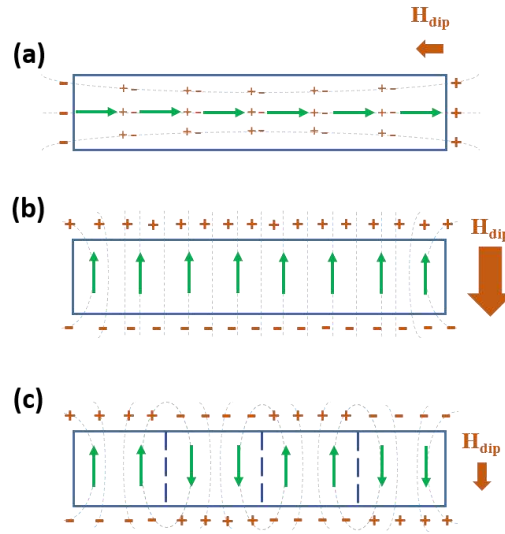


Figure I.1 Distributions of magnetostatic charges in a thin magnetic film. Magnetization are (a) in-plane and (b)-(c) out-of-plane. The green arrows indicate the local orientation of the magnetization \mathbf{M} inside the magnetic film. The magnetostatic charges are represented in orange. The uncompensated charges emerge at the surface of the film and they create a dipolar field \mathbf{H}_{dip} (orange arrow) inside the material. In order to reduce \mathbf{H}_{dip} , the magnetic film breaks into domains (c).

The energy due to the dipolar field \mathbf{H}_{dip} , also called the shape anisotropy or the magnetostatic energy is expressed as [Hubert & Schäfer 2009]:

$$\epsilon_{dip} = -\frac{1}{2} \mu_0 \int \mathbf{M} \cdot \mathbf{H}_{dip} d\tau^3 \quad (\text{I.4})$$

Here, \mathbf{H}_{dip} is related to the magnetization \mathbf{M} through (for a uniform magnetization)

$$\mathbf{H}_{dip} = -\mathbf{N} \cdot \mathbf{M} \quad (\text{I.5})$$

where \mathbf{N} is the demagnetizing tensor ($H_{dip}^i = -\sum_j N_{ij} M_j$) with $i, j = x, y$ or z . It is very difficult to calculate \mathbf{N} and to have \mathbf{H}_{dip} for an arbitrary shaped magnetic material. Nevertheless, it can be analytically calculated for some common geometries in literature [Aharoni 1998]. Qualitatively, as we can infer from **Figure I.1**, it is energetically favorable for the magnetization to orient in-plane along the largest dimension of the film so to have less magnetic charges. This is valid unless we take into consideration an additional energetic anisotropic term.

I.1.4. The magnetic anisotropy energy

A ferromagnetic material can be anisotropic. In other words, it has a preferential direction, for example an “easy axis” (along which the magnetization prefers to point) and a “hard axis”. The magnetization does not orient along the hard axis unless a large external magnetic field is applied. The crystal structure of the material is often the source of such anisotropy. An easy axis corresponds usually to a particular crystallographic axis. That is why the magnetic anisotropy is referred to as the “magnetocrystalline anisotropy”. The relationship between the crystal structure and the magnetization fundamentally arises from spin-orbit coupling (SOC). The spin-orbit interaction couples the spin of an electron to its orbital momentum. The crystal field from the lattice breaks the symmetry of the orbital momentum setting thus a preferential orientation for magnetic moments. In the simplest case of an uniaxial anisotropy, the magnetic anisotropy energy can be written as:

$$\epsilon_{anis} = K_u \sin^2 \theta \quad (\text{I.6})$$

where K_u is the uniaxial anisotropy constant and θ the deviation angle of the magnetic moment from the easy axis (the polar angle). The magnetocrystalline anisotropy can originate from both the bulk and the interface. The engineering of the interface contribution can thus induce an out-of-plane easy axis in ultrathin ferromagnetic films. Such stacks with perpendicular magnetic anisotropy have been attracting a considerable attention for more than a decade. One reason behind this interest is the study of DWs whose dynamics hold the promise to be fast, efficient and reproducible.

I.2. Domain walls in perpendicular magnetic anisotropy films

I.2.1. Perpendicular magnetic anisotropy (PMA) thin films

The investigated magnetic layers have thicknesses less than 1 nm. The shape anisotropy through the dipolar field, in consequence, is large and tries to keep the magnetization in the plane. In the meantime, by properly engineering the “interfacial anisotropy”, it is possible to bring the easy axis out-of-plane providing thus these layers with PMA.

The interfacial anisotropy in thin films is well established and was evidenced in various multilayers with heavy-metal/ferromagnet (HM/FM) and ferromagnet/oxide (FM/Ox) interfaces [Dieny & Chshiev 2017]. To name a few, we have as HM/FM interfaces Pt/Co, Ta/CoFeB, W/CoFeB, Ta/CoFe, Hf/CoFeB, Pd/FePd etc. [Bandiera et al. 2011; T. Liu et al. 2012; Ahn & Beach 2013; Lee et al. 2014]. As for FM/Ox interfaces, we cite Co/AlOx and CoFeB/MgO [Lacour et al. 2007; Rodmacq et al. 2009; A Manchon et al. 2008; A. Manchon et al. 2008].

For the HM/FM interface, the large spin-orbit interaction plays the key role in promoting the PMA as HMs have a strong SOC. The efficiency of such coupling depends strongly on the state of the interface. Varying the thickness of the HM or the FM has an impact on the perpendicular magnetic anisotropy (PMA) confirming its interfacial origin [Sokalski et al. 2012]. On the contrary, the spin-orbit interaction is weaker in FM/Ox interfaces [Monso et al. 2002]. However, the degree of its oxidation tunes the magnetic anisotropy. An optimal oxidation of this interface allows having a strong PMA whereas an over- or under-oxidation reduces it drastically [Rodmacq et al. 2003]. The thermal annealing, as it helps oxygen atoms to migrate towards the interface thus optimizes its oxidation, gives also a large PMA [Rodmacq et al. 2009]. The PMA originates from an overlap between the Oxygen $2p_z$ and the transition metal $3-d$ orbitals confirmed by *ab-initio* calculations [Yang et al. 2011].

In the present work, the investigated systems are Pt/Co/Pt and Pt/Co/AlO_x. In these systems, both interfaces of the FM layer contribute to the magnetic anisotropy as described above. They exhibit a stable PMA at room temperature.

I.2.2. Domain walls in PMA materials

As we have already seen in section I.1.3, in order to reduce its dipolar field, a ferromagnetic material tends to demagnetize at equilibrium in such a way that the net total magnetization is small or zero. For instance, it gets divided into magnetic domains within which magnetization is uniform (**Figure I.1**). The separation between adjacent magnetic domains is the domain wall (DW). A DW is the region in which the magnetization \mathbf{M} rotates gradually between the orientations of the two domains (between up and down in PMA materials). Forming a DW costs energy; an exchange energy term, as magnetic moments within the DW are not parallel with respect to each other and an anisotropy energy term because magnetic moments deviate from the easy axis. The formation of DWs is then the outcome of the competition between the dipolar, exchange and magnetic anisotropy interactions. This competition dictates the DW width parameter Δ that writes as [O'Handley, 2000]:

$$\Delta = \sqrt{A_{ex}/K_{eff}} \quad (\text{I.7})$$

A large PMA tends to make the DW thinner as it reduces the number of the magnetic moments not aligned along the easy axis. If the DW is very thin, the angle between the neighboring magnetic moments is important so the cost in exchange energy is considerable. The exchange interaction favors then a large DW. In ultrathin films with an out-of-plane anisotropy, DWs are usually narrow ($\lesssim 10$ nm) and adopt either a Bloch or a Néel configuration (**Figure I.2**). When the magnetization rotates in the plane of the wall (around the x -axis in **Figure I.2**), the DW is of the Bloch-type. It is a Néel wall when it rather rotates in the plane normal to the wall (defined by the z - and x -axis in **Figure I.2**).

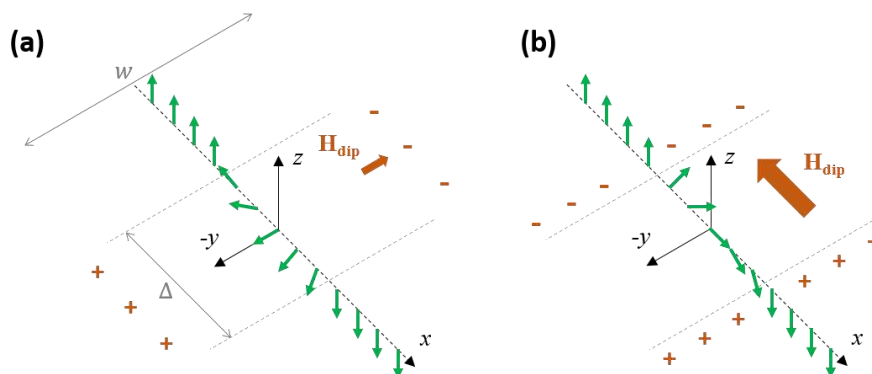


Figure I.2 Schematic diagrams of magnetic DWs in thin films with PMA. (a) Bloch wall: \mathbf{M} rotates inside the DW plane. (b) Néel wall: \mathbf{M} rotates perpendicular to the DW plane. Here, the stripe width w is much larger than the DW width Δ ($w \gg \Delta$). The dipolar energy dictates the stable configuration of a DW. The magnetostatic charges are depicted in orange and the arrow corresponding to the dipolar field \mathbf{H}_{dip} scales with its magnitude.

Having one of this two DW configurations relies on the dipolar energy in the DW that depends on the DW width and on the dimensions of the system. For an unpatterned magnetic film, DWs adopt a Bloch configuration as free magnetostatic surface charges are repelled towards infinity (cf. **Figure I.2.a**). Instead, a Néel wall would yield a sizeable dipolar field inside the DW. In the case of a stripe, when the DW width Δ is smaller than the stripe width w , a Bloch wall would cost similarly less dipolar energy than a Néel wall. On the contrary, a Néel wall is favored when the stripe becomes narrow ($w < \Delta$). In the case where w and Δ are comparable, the DW adopts an intermediate configuration between Bloch and Néel configurations. An experimental study by [T Koyama et al. 2011] shows a transition between Bloch and Néel walls at $w \approx 60$ nm in strips made of Co/Ni

multilayers. The competition between exchange, dipolar and anisotropy energy does not lead to any preferential sense of rotation of \mathbf{M} inside the wall. Therefore, there is an equal probability for the magnetization to rotate clockwise or anti-clockwise from up to down. However, we will see later in section I.5.2, that Néel walls can be stabilized in wide wires if a certain interaction called the Dzyaloshinskii-Moriya interaction is present in the FM.

The energy density per unit area of a Bloch wall σ_0 can be written as [Heide, Bihlmayer and Blügel, 2008; Rohart and Thiaville, 2013; Bernard-Mantel et al., 2017]:

$$\sigma_0 = 4\sqrt{A_{ex}K_{eff}} \quad (\text{I.8})$$

In Eqs. I.7 and I.8, K_{eff} is the effective uniaxial anisotropy constant. Since the thickness of the ferromagnetic film t_{FM} is much thinner than the DW width or the exchange length, the effective uniaxial anisotropy is written $K_{eff} = K_u - K_{dip}$. K_{dip} is the dipolar energy density seen in section I.1.3 and is expressed as [Thiaville et al., 2012]:

$$K_{dip} = \mu_0 M_s^2 / 2 \quad (\text{I.9})$$

The DW has also a magnetostatic ‘shape’ anisotropy term K that favors the Bloch configuration in PMA thin films [Thiaville et al., 2012].

$$K = N_x \mu_0 M_s^2 / 2 \quad (\text{I.10})$$

where N_x is the demagnetizing coefficient of the wall defined as $N_x = t_{FM} \ln(2) / (\pi \Delta)$ [Tarasenko et al. 1998]. We associate with the magnetostatic ‘shape’ anisotropy an effective field H_K within the Bloch wall whose magnitude writes [Thiaville et al., 2012]:

$$H_K = \frac{2K}{\mu_0 M_s} \quad (\text{I.11})$$

We note that DWs sit perpendicularly to the wire in PMA materials in order to minimize their length and hence their energy.

The structures with PMA are interesting thanks to their thermal stability that helps having more stable data storage devices with higher density and retention. In the meantime, DWs are rigid objects whether they are of the Bloch or the Néel type. With the appropriate driving mechanism, they are able to move without their configuration being distorted. Their narrow width is important in order to ensure a larger storage density in new concepts of mass storage devices such as the race-track memory [Parkin, Hayashi and Thomas, 2008] based on PMA materials. Similarly, in the SOT-MRAM, for moderate magnetic dot sizes, the magnetization switching is achieved through nucleation and subsequent DW propagation. In both cases, the spin-orbit interaction induces a high current-induced DW velocity (cf. section I.1.4.2.4). Therefore, there is a need to optimize the DW motion in PMA materials as that could be beneficial for future spintronic devices. For this purpose, it is important to fully characterize and understand magnetic field- and current-induced DWs dynamics. In the rest of this manuscript, we will adopt the following convention to refer to the different DWs in PMA materials. Unless it is mentioned differently, our frame of reference would always correspond to the one adopted in **Figure I.2**. We call an up/down DW and we designate it by DW_{U-D} a DW within which the magnetization \mathbf{M} rotates from the up to the down domain when going from the left to the right (along $+\mathbf{u}_x$). The other DW is the down/up DW designated by DW_{D-U} .

I.2.3. DW motion in PMA materials

Moving magnetic DWs is possible by the application of an external magnetic field or the injection of an electric current in the plane of the film. It is also possible to induce dynamics of DWs by polarized laser pulses as recently reported [Lambert et al., 2014; Quessab et al., 2018]. However,

the scope of this thesis is limited to field-induced DW motion (FIDWM) and current-induced DW motion (CIDWM). On the one hand, the DW motion under a magnetic field is straightforward to imagine. To minimize the Zeeman energy, a magnetic domain expands if its magnetization \mathbf{M} is in the same direction as an external field. The adjacent domains, magnetized in the opposite direction, shrink. In a stripe, two neighboring DWs move then opposite to each other (**Figure I.3**). On the other hand, the electric current induces DW motion thanks to another type of interaction: the transfer of spin angular momentum that creates torques acting on the magnetization, the spin torques. These torques induce a unidirectional DW motion either against or along the current flow depending on the exact dominant mechanism and on the materials involved. From the memory application point of view, the CIDWM is the preferred method the FIDWM, DWs are all moving in the same direction allowing information to be conserved and transferred. This mechanism led the race-track memory concept [Parkin et al. 2008; Hayashi et al. 2008]. Since they are important to interpret our experimental results, we describe in the following these different mechanisms of DW motion.

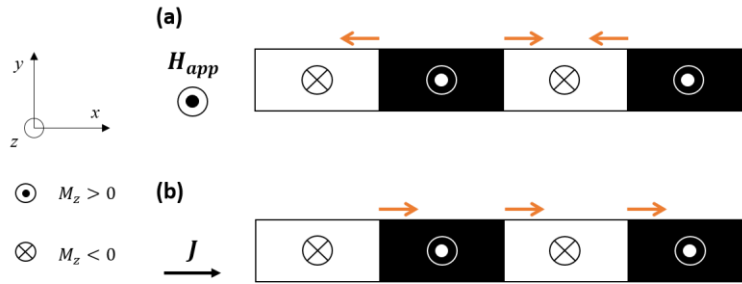


Figure I.3 Schematic diagram of DW motion in thin magnetic films with PMA. The DWs driven by (a) an out-of-plane magnetic field \mathbf{H}_{app} and by (b) a charge current \mathbf{J} . An up (down) magnetic domain corresponds to positive (negative) M_z and is represented by a black (bright) contrast. The orange arrows give the direction of motion of DWs. Successive DWs move in opposite directions under \mathbf{H}_{app} and along the same direction under the current \mathbf{J} . The conventions represented here for the orientation of magnetization \mathbf{M} and magnetic field \mathbf{H} are adopted in the rest of this manuscript

I.3. Field-induced DW motion (FIDWM)

It is easy to derive the direction of motion of a DW under a magnetic field. However, the actual dynamics of DWs is much more complex. If one considers a single magnetic moment, a magnetic field will induce a torque leading to an endless precession of the moment around this field. An additional damping term allows the magnetization to eventually align along the magnetic field. The case of a DW is more complicated as the applied magnetic field distorts its internal structure during the motion generating other torques whose combination leads to FIDWM.

I.3.1. LLG equation

The low-energy dynamics of the magnetization \mathbf{M} is well described by the Landau-Lifshitz-Gilbert equation (LLG). This equation considers an effective magnetic field \mathbf{H}_{eff} that includes all possible energy contributions ϵ_{eff} from exchange interaction, magnetic anisotropy, dipolar interaction, external applied field etc. The time evolution of the magnetization is then described by an energy term including these different torque contributions and a phenomenological dissipation term [Gilbert 2004]:

$$\frac{\partial \mathbf{m}}{\partial t} = -\gamma(\mathbf{m} \times \mu_0 \mathbf{H}_{eff}) + \alpha \mathbf{m} \times \frac{\partial \mathbf{m}}{\partial t} \quad (\text{I.12})$$

$$\mu_0 \mathbf{H}_{eff} = -\frac{1}{M_s} \frac{\partial \epsilon_{eff}}{\partial \mathbf{m}} \quad (\text{I.13})$$

Here \mathbf{m} is the normalized magnetization vector $\mathbf{m} = \mathbf{M}/M_s$, γ the gyromagnetic ratio $\gamma = ge/2m_e$ (g the electron's g -factor ~ 2 , $e > 0$ the electron charge and m_e the electron mass) and α the phenomenological dimensionless damping constant ($\alpha > 0$). When considering the LLG equation, the amplitude of each magnetic moment per unit volume is assumed to be equal to M_s . The LLG equation is only valid for temperatures sufficiently below T_C , such that the amplitude of the magnetization is conserved. Otherwise, we require another model that is the Landau-Lifshitz-Bloch equation

[Garanin 1997]. The LLG equation can be rewritten as follows:

$$\frac{1+\alpha^2}{\gamma\mu_0} \frac{\partial \mathbf{m}}{\partial t} = -(\mathbf{m} \times \mu_0 \mathbf{H}_{eff}) - \alpha \mathbf{m} \times (\mathbf{m} \times \mathbf{H}_{eff}) \quad (\text{I.14})$$

where the renormalization of the precession frequency resembles the form originally proposed by [L. LANDAU, 1935].

The first term in the LLG equation is a torque that causes the magnetization to precess around \mathbf{H}_{eff} . The second term is the torque that brings back the magnetization towards the direction of \mathbf{H}_{eff} . It is the damping torque \mathbf{T}_α . Its strength is quantified by α and is proportional to the time derivative of \mathbf{m} . The damping torque \mathbf{T}_α is perpendicular to the magnetization and to its trajectory. The damping mechanism is associated with the relaxation of the magnetization due to the change in the electronic levels of the lattice through SOC.

Magnetic damping from Spin-Orbit Coupling (SOC)

SOC mediates the variation of the energy of the delocalized electrons at the Fermi level in a metallic ferromagnetic system when the magnetization rotates with respect to the crystal axis or the magnetic easy axis. This variation leads to a dissipative effect: the magnetic damping. [Gilmire et al. 2008] derived a model for a SOC-induced effective field that acts on the magnetization and it has the following expression:

$$\mathcal{H}_{eff} = -\frac{1}{\mu_0 M_s} \sum_{nk} \left[\rho_{nk} \frac{\partial \varepsilon_{nk}}{\partial \mathbf{M}} + \varepsilon_{nk} \frac{\partial \rho_{nk}}{\partial \mathbf{M}} \right] \quad (\text{I.15})$$

When the magnetization \mathbf{M} rotates, the total energy of electrons varies by changing the energy of the electronic states ($\partial \varepsilon_{nk}/\partial \mathbf{M}$) and/or by changing their occupancy ($\partial \rho_{nk}/\partial \mathbf{M}$). Within the perturbation limit, the occupancy ρ_{nk} of a given energy of an electronic state with a given energy can be expressed as $\rho_{nk} = f_{nk} - \tau(df_{nk}/dt)$ with f_{nk} the equilibrium distribution function and τ the relaxation time towards this equilibrium. The first term of the Eq. I.15 can then be written as a sum of two effective magnetic fields:

$$\mathcal{H}_{eff} = \mathcal{H}_{anis} + \mathcal{H}_\alpha \quad (\text{I.16})$$

$$\mathcal{H}_{anis} = -\frac{1}{\mu_0 M_s} \sum_{nk} f_{nk} \frac{\partial \varepsilon_{nk}}{\partial \mathbf{M}} \quad (\text{I.17})$$

$$\mathcal{H}_\alpha = -\frac{\tau}{\mu_0 M_s} \sum_{nk} \left(-\frac{df_{nk}}{d\varepsilon_{nk}} \right) \left(\frac{d\varepsilon_{nk}}{d\mathbf{M}} \right)^2 \frac{\partial \mathbf{M}}{\partial t} \quad (\text{I.18})$$

The effective anisotropy field \mathcal{H}_{anis} does not depend on the rate of the precession of the magnetization and it arises from anisotropy of the energy levels when $(\partial \varepsilon_{nk}/\partial \mathbf{M}) \neq 0$. The second field is an effective damping field \mathcal{H}_α that vanishes for quasistatic variations of the magnetization $(\partial \mathbf{M}/\partial t) \approx 0$. In this case, the only field acting on the magnetization is \mathcal{H}_{anis} . However, when the magnetization varies rapidly, the second effective field becomes relevant, as the electronic states does not have time to relax to the new equilibrium.

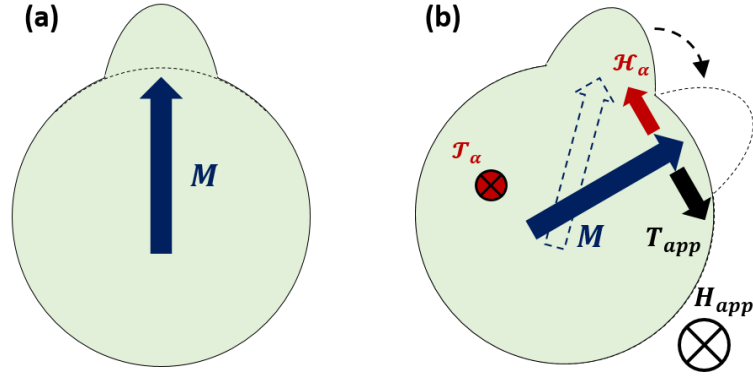


Figure I.4 Magnetic damping from spin-orbit coupling in metallic ferromagnets. (a) Schematic of the influence of the magnetization \mathbf{M} on the Fermi sphere. The Fermi sphere is deformed by SOC. (b) The emergence of the damping mechanism from SOC. An applied \mathbf{H}_{app} rotates \mathbf{M} but the electrons do not follow adiabatically. The dashed arrow shows the magnetization vector at equilibrium with the electronic distribution whereas the dashed line indicates the Fermi sphere at equilibrium with the rotating \mathbf{M} . The damping field \mathcal{H}_α arises to restore \mathbf{M} at equilibrium with the actual electronic distribution. It induces a damping torque \mathcal{J}_α that brings \mathbf{M} parallel to \mathbf{H}_{app} . A figure adapted from [Miron 2009].

A simplistic picture, as depicted in **Figure I.4**, represents the SO interaction coupling the magnetization and electron states. At equilibrium, the magnetization leads to a deformation of the Fermi sphere. An applied external field \mathbf{H}_{app} rotates the magnetization. The electronic distribution falls behind with the characteristic time τ and does not follow adiabatically the magnetization. The increase in the spin-orbit energy leads to the emergence of an effective damping field \mathcal{H}_α . As we can see in **Figure I.4**, the torque associated with this effective damping field cant the magnetization out of the plane to align it with the applied magnetic field. The second term of the Eq. **I.15** gives a second mechanism of damping. The occupancy ρ_{nk} changes with the magnetization. The magnetization is then relaxed (damping) through the SOC by electronic interband transitions.

I.3.2. Displacement of a DW by a magnetic field

To describe how a magnetic field propagates a DW in PMA materials, we use a simplified one-dimensional representation of the LLG equation. The DW is reduced to a single normalized magnetization sitting at its center; the DW core magnetization \mathbf{m}_{DW} . The displacement of the DW is the outcome of the action of the torques on \mathbf{m}_{DW} . A torque that lies in the plane distorts the internal structure of the DW by canting away \mathbf{m}_{DW} from its initial equilibrium configuration. An out-of-plane torque lifts up (or brings down) \mathbf{m}_{DW} inducing the displacement of the DW. As a consequence, the velocity of the motion is proportional to the out-of-plane torque.

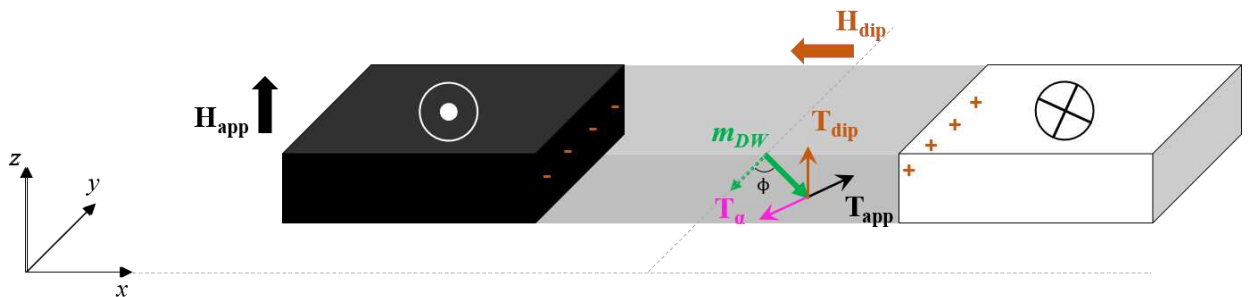


Figure I.5 Mechanism of the FIDWM. Schematic diagram of the different torques acting on the DW core magnetization upon the application of an external magnetic easy axis field \mathbf{H}_{app} . The dashed green arrow corresponds to the initial configuration of a Bloch DW. \mathbf{H}_{app} is associated with a torque \mathbf{T}_{app} that rotates \mathbf{m}_{DW} in the plane creating a dipolar field \mathbf{H}_{dip} (emphasized by the magnetostatic charges at the DW boundaries). The damping torque \mathbf{T}_α compensates \mathbf{T}_{app} ensuring the stability of \mathbf{m}_{DW} in the steady-state regime of motion. Finally, the dipolar torque \mathbf{T}_{dip} pulls \mathbf{m}_{DW} out of the plane resulting in the DW motion.

The torque \mathbf{T}_{app} ($\mathbf{T}_{app} = -\gamma(\mathbf{m}_{DW} \times \mu_0 \mathbf{H}_{app})$) from the external field \mathbf{H}_{app} , applied along the $+z$ -axis, distorts the DW from its Bloch initial configuration by rotating \mathbf{m}_{DW} in the (x, y) plane (the film plane). The induced x -component (m_x) of \mathbf{m}_{DW} builds new magnetostatic charges at the planes of the DW yielding a dipolar field \mathbf{H}_{dip} . This field through the dipolar torque \mathbf{T}_{dip} ($\mathbf{T}_{dip} = -\gamma(\mathbf{m}_{DW} \times \mu_0 \mathbf{H}_{dip})$) drives the DW forward along the $+x$ -axis. The damping torque \mathbf{T}_α ($\mathbf{T}_\alpha = \alpha(\mathbf{m}_{DW} \times \frac{\partial \mathbf{m}_{DW}}{\partial t})$) associated with the second term in the right side of the LLG equation opposes the in-plane rotation of \mathbf{m}_{DW} . When the in-plane component of \mathbf{T}_α fully compensates \mathbf{T}_{app} , the DW is no more distorted and acquires an equilibrium deformation angle ϕ_{eq} . It is henceforth subjected only to \mathbf{T}_{dip} and to the out-of-plane component of \mathbf{T}_α . Finally, it is the distortion by \mathbf{H}_{app} that drags DWs through the creation of the dipolar field.

I.3.3. Flow regime of motion

In an ideal environment, the structure of the magnetic material does not have any imperfections that could pin the DW. In addition, no thermal fluctuations are considered and the DW moves solely from the combined action of torques described above. This is the flow regime of motion of DWs. [Schryer & Walker 1974] were among the first to describe the displacement of a DW under a magnetic field in the flow regime. According to their model, the FIDWM is divided into two velocity regimes: a steady-state regime and an oscillatory regime (**Figure I.6**).

For low applied magnetic fields, the DW undergoes a motion in the steady-state regime. As described above, the damping torque fully compensates the distortion of the local magnetic moments. Therefore, the displacement of the DW is equivalent to a simple translation along the x -axis. The velocity is proportional to the applied field and depends on the DW width Δ and the damping parameter α . In the steady-state regime, the DW velocity v_{DW} is proportional to the driving force, the applied magnetic field \mathbf{H}_{app} , through the mobility μ_1 . v_{DW} is written as:

$$v_{DW} = \mu_1 H_{app} = \frac{\gamma \Delta}{\alpha} H_{app} \quad (\text{I.19})$$

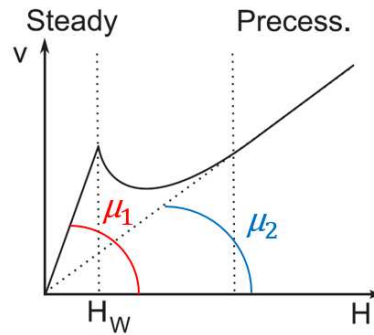


Figure I.6 The variation of the DW velocity as a function of an easy axis magnetic field \mathbf{H} in the flow regime. The DW is driven in an ideal film. The Walker breakdown at \mathbf{H}_W separates the steady and the precessional regimes. The mobility of the DW drops from μ_1 (steady-state) to μ_2 (precessional).

Above a certain magnetic field, called the Walker field H_W ($H_W = \alpha M_s/2$), the velocity of the DW drops drastically and then begins to increase linearly again. We refer to the decrease of the velocity as the Walker breakdown. The motion that follows is called the precessional or oscillatory regime of motion during which the DW core magnetization \mathbf{m}_{DW} rotates continuously. The Walker breakdown takes place when the damping torque \mathbf{T}_α does not compensate anymore the torque \mathbf{T}_{app} from the applied field. The dipolar torque \mathbf{T}_{dip} is proportional to the magnitude of the dipolar field and the y -component of \mathbf{m}_{DW} (**Figure I.5**). This torque \mathbf{T}_{dip} is maximum when the DW core magnetization has a deformation angle $\phi = \pi/4$ with respect to the y -axis. When \mathbf{H}_{app} cants \mathbf{m}_{DW}

beyond this angle, the in-plane component of \mathbf{T}_α (proportional to \mathbf{T}_{dip}) cannot compensate anymore \mathbf{T}_{app} . The DW does not henceforth maintain its structure during the propagation. \mathbf{m}_{DW} keeps precessing around the z -axis, resulting in a periodic transformation between Bloch and Néel configurations and the dipolar torque changing periodically its sign. Then, in the high field case, only the damping torque drives the DW forward giving a reduced average velocity compared to the steady-state regime [Mougin et al. 2007]. In the oscillatory regime of motion, the DW velocity is given by:

$$v_{DW} = \mu_2 H_{app} = \frac{\alpha\gamma\Delta}{1+\alpha^2} H_{app} \quad (\text{I.20})$$

I.3.4. Creep regime of motion

The model used in the previous section describes the DW motion in a flow regime for an ideal structure. Only few studies for PMA structures identified the flow regime and the Walker breakdown in experiments [Tarasenko et al. 1998]. However, realistic ferromagnetic layers have imperfections and defects such as impurities, intermixing with the adjacent layer, disorder, grain boundaries in the crystallographic structure, etc. Locally at these imperfections, the magnetization \mathbf{M} encounters abrupt changes in magnetic interactions. Consequently, some defects act like nucleation sites where it is easier to reverse the orientation of \mathbf{M} and others act like pinning sites. At low magnetic driving fields, due to their narrow width, DWs in PMA materials are trapped by these defects and imperfections in the structure. At zero temperature and below a magnetic field threshold, the DW does not move. However, at a finite temperature, thermal activation helps to depin the DW. The motion of DWs is therefore governed by the pinning landscape and the thermal activation at the low field regime. The regime where the force acting on a DW is negligible as compared to the depinning force but where the DW is still moving, even if at a very low velocity, is called the creep regime. Consequently, the steady-state regime and the Walker breakdown are typically obscured by this regime in PMA materials. Most of the experimental investigations of the flow regime of motion have demonstrated indeed the oscillatory regime of motion [Metaxas et al. 2007; Yamada et al. 2011; Burrowes et al. 2013]. The FIDWM can be divided into three regimes: the creep regime, the depinning regime and the flow regime (Figure I.7).

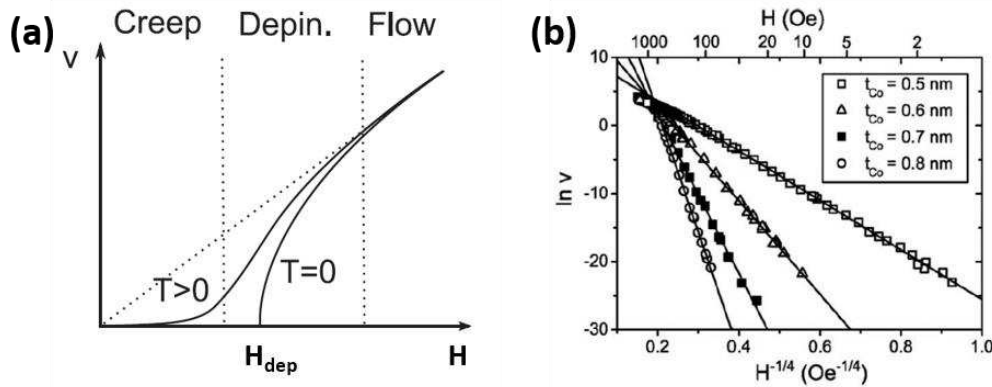


Figure I.7 The variation of the DW velocity as a function of an easy axis magnetic field \mathbf{H} in the creep regime. (a) Theoretical variation of the DW velocity v in a disordered film at zero and finite temperature. The three different regimes: creep, depinning and flow are labeled. H_{dep} is the critical magnetic field to move a pinned DW at zero temperature. The thermal activation helps propagating the DW at lower magnetic fields than H_{dep} . The Walker breakdown can either be hidden by the creep and depinning regimes or occur at larger \mathbf{H} . (b) Logarithm of the DW velocity v as a function of the applied field. The linear variation of $\ln(v_{DW})$ vs $H_z^{-1/4}$ is a hallmark of the creep regime of motion as expected from Eq. I.24. Figures extracted and adapted from [Metaxas et al. 2007].

In the creep regime, the motion of a DW in PMA materials can be modeled by the dynamics of an elastic interface driven by a force in a weak disordered medium [Lemerle et al. 1998].

The variation of the DW velocity v_{DW} with respect to an applied magnetic field along the normal to film \mathbf{H}_z follows the creep scaling law that writes [Gorchon et al. 2014]:

$$v_{DW} = v_0 \exp \left[-\frac{U_c H_p^{1/4}}{k_B T} H_z^{-1/4} \right] \quad (\text{I.21})$$

where U_c is the height of the pinning barrier, H_p is the pinning field and k_B the Boltzmann constant. The prefactor v_0 can be expressed as:

$$v_0 = d_0 f_0 \exp \left[C \frac{U_c}{k_B T} \right] \quad (\text{I.22})$$

with $C \approx 1$ an empirical constant, d_0 the average distance between two pinning centers and f_0 the attempt depinning frequency. The equation (I.21) is then rewritten as:

$$v_{DW} = d_0 f_0 \exp \left[-\frac{E}{k_B T} (H_z^{-1/4} - H_c^{-1/4}) \right] \quad (\text{I.23})$$

The term $E = U_c H_p^{1/4}$ includes all the energy contributions and $H_c = H_p / C^4$ gives the critical field that determines the limit of the creep regime. The DW velocity can be expressed using the following logarithmic equation:

$$\ln(v_{DW}) = \ln(d_0 f_0) - \frac{E}{k_B T} (H_z^{-1/4} - H_c^{-1/4}) \quad (\text{I.24})$$

The linear dependence of $\ln(v_{DW})$ on $H_z^{-1/4}$ is the signature of the creep regime of motion as depicted in **Figure I.7.b** [Metaxas et al. 2007; D. Y. Kim et al. 2018]. The linear variation is clear in the small driving force limit ($H_z \ll H_c$). By increasing the magnetic field up to $H_z \approx H_c$, we reach the limit of the creep regime and the equation (I.24) is not valid anymore. The curve of $\ln(v_{DW})$ bends in the vicinity of H_c and we have $v_{DW} \sim d_0 f_0$.

Above the critical field, the DW velocity increases and enters the depinning regime of motion. As the magnetic field is further increased, the motion of DW is not anymore perturbed by pinning sites and the velocity becomes linear as predicted theoretically in the flow regime.

As mentioned earlier, injecting a current is preferred to have a unidirectional motion of DWs in contrast with the FIDWM where different DWs move opposite to each other. The action of a current has been usually described as that of effective magnetic fields exerted on the internal structure of the DW. Consequently, as seen in the FIDWM, the motion under current comes via the distortion of the DW and undergoes different regimes of motion namely; creep, depinning and flow regime.

I.4. Current-induced DW motion (CIDWM)

An electric current may induce a DW motion along or against the electron flow. In PMA structures, the spin-transfer torque mechanism was the first to be proposed and evidenced to induce a DW motion along the electron flow. Later, a new type of torques has emerged; the spin-orbit torques, and is associated with the possibility of having a DW motion against the electron flow (along the charge current direction). In this section, I introduce the main aspects of both mechanisms.

I.4.1. Spin-transfer torques (STTs)

In a normal nonmagnetic metal, the spins of conduction electrons do not orient in any particular direction. In contrast, the spins of conduction electrons flowing in a ferromagnetic metal

are “spin-polarized”. In other words, the spins of these electrons are polarized along the direction of the local magnetization. The parameter P gives the extent or the degree to which these spins are aligned with a given direction ($0 \leq |P| \leq 1$). Through an s - d interaction between $3d$ localized electrons carrying ‘magnetism’ in transition metals (Co, Fe and Ni) and $4s$ conduction electrons, conduction electrons experience a spin-dependent scattering. Conduction electrons with a spin parallel to the local magnetization are less scattered than conduction electrons with a spin oriented in the opposite direction. This spin-dependent scattering generates the spin-polarization of conduction electrons in ferromagnets. Typically, in $3d$ transition metal ferromagnet, the spin polarization is positive ($P > 0$). The mechanism of the spin-transfer torque STT arises from a transfer of angular momentum between the spin-polarized electrons and the magnetization inside a DW as the total angular momentum is conserved. [Berger, 1978] was among the first to propose this mechanism to drag DWs in macroscopic film. Starting in the 2000s, the DW motion in STT became a hot topic promoted among other reasons by advancements in the submicron lithography of nanowires and motivated by the promise of sustainable DW motion with low current densities in PMA materials for scalable and high-performance spintronic devices.

I.4.1.1. Adiabatic STT

Incoming spin-polarized electrons encounter a varying magnetization when they cross a DW. Due to the magnetization gradient, their spin direction rotates to align locally with \mathbf{M} . Thus, their spin angular momentum varies. Because the overall angular momentum in the system must be conserved, there has to be a change in the angular momentum of the local magnetization in the DW. The magnetic moments in the DW rotates inducing a DW motion along the flow of the conduction electrons. This is the mechanism induced by the so-called adiabatic torque that can be written as [Thiaville et al., 2004, 2005; Xiao, Zangwill and Stiles, 2006]:

$$\mathbf{T}_A = -(\mathbf{u} \cdot \nabla) \mathbf{m} = \frac{g\mu_B P}{2eM_s} (\mathbf{J} \cdot \nabla) \mathbf{m} \quad (\text{I.25})$$

where μ_B is the Bohr magneton and \mathbf{J} the current density vector. We refer to \mathbf{u} as the spin drift velocity. According to this expression, if the current flows in the x -direction (the long axis of a wire), the adiabatic torque \mathbf{T}_A scales with the gradient of the magnetization ($-\partial \mathbf{m} / \partial x$). In PMA thin films, as the z -component m_z of the magnetization varies along the wire x -axis, the torque \mathbf{T}_A is normal to the film plane. It distorts the DW by canting its internal magnetization \mathbf{m}_{DW} out of the plane. According to the LLG equation, the damping torque \mathbf{T}_α ($\mathbf{T}_\alpha = \alpha \mathbf{m}_{DW} \times \mathbf{T}_A$) has then an x -component canting \mathbf{m}_{DW} in the (x, y) plane. By analogy with the distortion in the FIDWM (Figure I.5), a dipolar field \mathbf{H}_{dip} , normal to the DW, is created. Consequently, \mathbf{H}_{dip} induces a torque \mathbf{T}_{dip} ($\mathbf{T}_{dip} = -\gamma(\mathbf{m}_{DW} \times \mu_0 \mathbf{H}_{dip})$) that is out of the plane and opposes \mathbf{T}_A . If the current is not large enough, the canted DW internal structure \mathbf{m}_{DW} reaches a canting equilibrium angle ϕ_{eq} at which \mathbf{T}_{dip} fully compensates \mathbf{T}_A . The STT needs then to overcome the maximum limit of \mathbf{T}_{dip} to be able to propel the DW. This corresponds to a threshold current density J_{th} in adiabatic STT-driven DW motion that is intrinsic and exists even in a perfect wire. However, the prediction of such a threshold current density considering only the adiabatic STT fails to explain experimental observations of less important threshold densities in DW motion [Yamaguchi et al. 2004; Kläui et al. 2005]. A second term in STT was then introduced [Zhang & Li 2004; Thiaville et al. 2004].

I.4.1.2. Non-adiabatic STT

This second torque is often called the non-adiabatic torque \mathbf{T}_{NA} and writes can be written as:

$$\mathbf{T}_{NA} = -\beta \mathbf{m} \times [-(\mathbf{u} \cdot \nabla) \mathbf{m}] \quad (\text{I.26})$$

The non-adiabatic torque is parameterized by a dimensionless coefficient β ($\beta = T_{NA}/T_A, \beta > 0$) and it is perpendicular to the adiabatic STT. In PMA materials, this torque acts on a DW identical to the torque from an applied field oriented along the easy z -axis, the normal to the film plane. This similarity with the FIDWM mechanism renders the J_{th} extrinsic like the depinning field in FIDWM, which depends on pinning landscape and thermal activation. The non-adiabatic term accompanies then the adiabatic STT in moving DWs.

There have been several approaches and theoretical proposals for the microscopic origin of the non-adiabatic term in STT. One approach is to consider that the electrons do not fully follow adiabatically the gradient of the magnetization \mathbf{M} while flowing through the DW. They can be reflected from the DW instead of crossing it. For this to be significant, the DW width should be very close or smaller than the Fermi wavelength (of the order of nm in 3d transition metals). In this case, the gradient of the magnetization is too important for the spin-polarized electrons to be able to track it [Tatara and Kohno, 2004; Barnes and Maekawa, 2005]. Another approach considers the effect of scattering or spin-flip from SOC for the spins of conduction electrons [Zhang and Li, 2004]. When conduction electrons cross the DW, an out-of-equilibrium spin density $\delta \mathbf{s}$ emerges. It comes from the component of the spins that is not aligned with local magnetic moments. This spin density $\delta \mathbf{s}$ precesses around the magnetization thanks to the s - d exchange interaction with a time constant τ_{sd} and scatters also due to the spin-flip with a time constant τ_{sf} . The theoretical description of such interactions yields an approximation of β as follows:

$$\beta = \frac{\tau_{sd}\tau_{sf}}{(\tau_{sd}^2 + \tau_{sf}^2)} \approx \frac{\tau_{sd}}{\tau_{sf}} \quad (\text{I.27})$$

This approximation comes from the difference in the order of magnitude between the two time constants (in a FM, $\tau_{sd} \sim 10^{-14}$ s and $\tau_{sf} \sim 10^{-12}$ s). One can think that a material with large SOC will present large spin scattering that would enhance the non-adiabatic STT. The utility and validity of this reasoning is limited as a strong SOC decreases the spin-polarization P of the current. The non-adiabatic STT cannot be enhanced in that case.

I.4.1.3. Displacement of a DW by STT

The LLG equation that includes both terms of STT is given by:

$$\frac{\partial \mathbf{m}}{\partial t} = -\gamma (\mathbf{m} \times \mu_0 \mathbf{H}_{eff}) + \alpha \mathbf{m} \times \frac{\partial \mathbf{m}}{\partial t} - (\mathbf{u} \cdot \nabla) \mathbf{m} - \beta \mathbf{m} \times [-(\mathbf{u} \cdot \nabla) \mathbf{m}] \quad (\text{I.28})$$

Let us consider the action of an electric current flowing along the x -axis on the core magnetization \mathbf{m}_{DW} of a DW_{U-D} (Figure I.8). The direction of the effective magnetic field associated with the adiabatic torque \mathbf{T}_A is normal to the DW, lying in the plane of the film while the one associated with the non-adiabatic torque \mathbf{T}_{NA} is along the magnetic easy-axis. \mathbf{T}_{NA} rotates \mathbf{m}_{DW} in the film plane yielding a dipolar field \mathbf{H}_{dip} . The dipolar torque \mathbf{T}_{dip} adds then to \mathbf{T}_A and both combined cant \mathbf{m}_{DW} out of the plane, hence moving the DW towards the $-x$ values for a charge current flowing towards the $+x$ values. At small current, the rigid translation of the DW or the steady-state regime of motion takes place as long as the damping torque \mathbf{T}_α cancels out the action of the non-adiabatic torque \mathbf{T}_{NA} . According to the one-dimensional (1D) model [Thiaville et al., 2005], the DW velocity is:

$$v_{DW} = \frac{\beta}{\alpha} \mathbf{u} = \frac{\beta}{\alpha} \cdot \frac{g\mu_B P}{2eM_s} \cdot J \quad (\text{I.29})$$

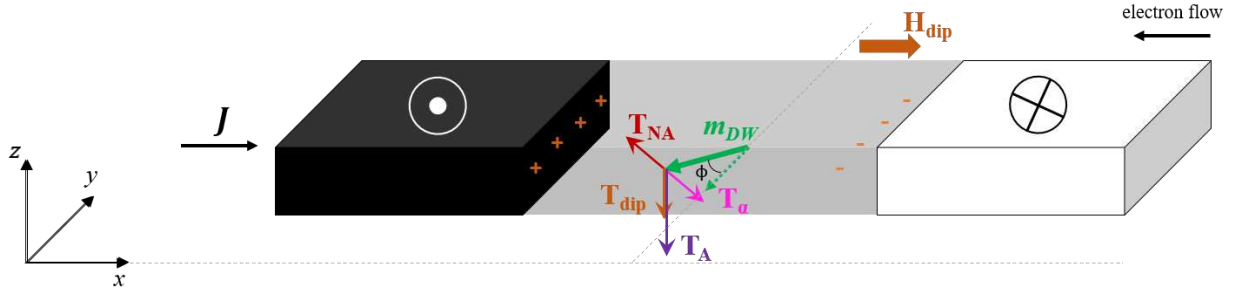


Figure I.8 Mechanism of the CIDWM based on STT. Schematic diagram of the different torques acting on the DW core magnetization from the STT mechanism. The dashed green arrow corresponds to the initial configuration of a Bloch DW. The rotation in the plane of \mathbf{m}_{DW} , by \mathbf{T}_{NA} , gives rise to magnetostatic charges at the DW boundaries inducing a dipolar field \mathbf{H}_{dip} . \mathbf{H}_{dip} acts on \mathbf{m}_{DW} through the torque \mathbf{T}_{dip} adding up to \mathbf{T}_A . This pulls \mathbf{m}_{DW} to the down state resulting in a DW motion along the electron flow.

Like in the FIDWM, above a critical current density, the damping torque \mathbf{T}_α is no longer sufficient to compensate \mathbf{T}_{NA} for $\phi > \pi/4$. The DW undergoes a Walker breakdown and starts to precess continuously under the action of the current and the speed of the DW approaches the spin drift velocity $v_{DW} \rightarrow u$.

It turns out that the current, in very thin films, can experience considerable interfacial scattering that reduces drastically the spin polarization P . This is much enhanced in FM layers interfaced with a nonmagnetic HM (Pt, Ta, W, etc.). The study of [Tanigawa et al. 2013] showed that $P \approx 0.7$ in perpendicularly magnetized Co/Ni layers adjacent to Pt layers with ferromagnetic thickness > 4 nm and no spin polarization could be evidenced at thicknesses < 1 nm. In addition, evidence of STT mechanism was only reported in thick ferromagnet layers [Yamanouchi et al. 2006; Adam et al. 2009; Ueda et al. 2014; Ueda et al. 2015; Ryu et al. 2016]. Moreover, in PMA materials, the thickness of the FM layer needs to be very small ($t_{FM} < 1$ nm) to make sure that the interfacial perpendicular anisotropy contribution (it is inversely proportional to t_{FM}) prevails over the dipolar energy. The STT mechanism is expected therefore to be negligible in these kinds of materials. In such structures based on Pt/Co/Pt layers, there is a wide disparity of reports concerning DW motion. In some studies, no effects from currents are evidenced except a Joule heating effect [Moore et al. 2008; Cormier et al. 2010]. In contrast, others report a current-induced DW motion along the current flow opposite to STT mechanism [Kim et al. 2010; Lee et al. 2011; Lavrijsen et al. 2012]. This huge disparity in DWs motion studies in Pt/Co based multilayers suggest another current-induced mechanism rather than the conventional STT.

I.4.2. Spin-orbit torques (SOTs)

In order to account for these anomalies, another mechanism of spin angular momentum transfer from the electric current to the magnetization \mathbf{M} of the FM has been proposed. It is the crystal lattice via the spin-orbit interaction in the multilayered structure that allows this type of transfer thus the denominations of spin-orbit torques (SOTs). These torques do not depend neither on the gradient of the magnetization nor on the spin polarization of the conduction electrons. Their actions on DWs are then profoundly different from STT and they are dependent on the structure of the layers. The observation of DW motion in Pt/Co/Pt was triggered by the tuning of asymmetries between the bottom and top Pt layers via growth parameters [Lavrijsen et al. 2012]. More remarkable fast DW dynamics against current flow were reported in FM layers sandwiched between HM and an oxide insulator layers [Miron, Moore, et al. 2011; Ryu et al. 2012; Koyama et al. 2013]. In order to induce a strong spin-orbit interaction capable to yield relevant SOTs on the magnetization, structure inversion asymmetry (SIA) is required.

1.4.2.1. Rashba Effect and Spin Hall effect (SHE) in SIA materials

As discussed in section (I.2.1), a large SOC is needed to promote the PMA in ultrathin layers thus the use of HM layers adjacent to the FM layer. This SOC gives also SOTs that act on the ferromagnet. The origin of such torques comes from relativistic considerations of the conduction electrons traveling in the structure. In fact, the Fermi velocity of the moving electrons is close to the relativistic regime. The crystalline electric field \mathbf{E}^{SO} transforms then in their rest frame to an effective magnetic field \mathbf{H}^{SO} [Woodhouse 2003]. This effective relativistic field \mathbf{H}^{SO} is of the form $\sim \mathbf{v} \times \mathbf{E}^{SO}$ where \mathbf{v} is the electron's velocity. It is then orthogonal to both the electric field and the trajectory of the electron. This field induces a net spin polarization transferred to the magnetization via s - d exchange interaction. In other words, the spin polarization created by the current acts as an effective magnetic field on the magnetization (in the form of a torque) [Manchon & Zhang 2008]. Such a mechanism is usually in literature referred to as the Rashba effect in thin films. In general, the Rashba effect describes the spin-polarization of electrons in a non-magnetic materials, that scales with their wavevector \mathbf{k} . The spins "up" ("down") parallel (anti-parallel) to \mathbf{H}^{SO} have their energy reduced (increased). The Fermi surface gets then split. This effect has already been reported at the surface of several metals [LaShell et al. 1996; Krupin et al. 2005; Cercellier et al. 2006]. For a material with an inversion symmetry, this effect vanishes since the electric field from both interfaces is zero by integrating over the electron wavefunction. In order to have a net torque, the inversion symmetry needs to be broken. In PMA thin films, it is possible to break the inversion symmetry and generate a finite electronic potential E_z^{SO} along the out-of-plane direction by having the FM layer sandwiched between two different non-magnetic layers. This is the structural inversion asymmetry (SIA).

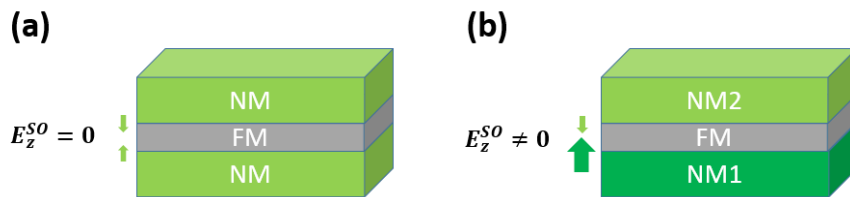


Figure 1.9 SIA multilayered structures. Schematic picture of a multilayered structure with (a) and without (b) inversion symmetry along normal axis parallel to \mathbf{z} . The net crystalline electric field \mathbf{E}^{SO} is fully compensated when FM is sandwiched between identical non-magnetic NM layers. \mathbf{E}^{SO} is non-zero when the top (NM2) and the bottom (NM1) layers are different. NM can be either a HM layer or an oxide layer.

The bulk spin Hall Effect (SHE) is another mechanism originating from the spin-orbit interaction that could lead to spin injection into a ferromagnet. An in-plane electric current flowing through a paramagnetic material (e.g. a HM) produces a spin current. This spin current is orthogonal to the charge current flow. Because of the spin-dependent scattering due to the strong spin-orbit coupling in the HM, one spin orientation scatters in one direction and the other spin orientation in the opposite direction. Polarized spins with a transverse orientation accumulate at the upper and lower surfaces of the layer [Hirsch 1999; Kato 2004] over a thickness related to the diffusion length of spins (in heavy metals \sim nm). In order to have an efficient spin injection, the FM layer is usually grown on top of a HM metal layer (e.g. Pt, Ta, W, etc.) or the way around a HM grown on top of a FM. The strength of the SHE in a material is expressed by the spin Hall angle θ_{SH} that is the ratio between the amplitudes of the transverse spin current J_s and the longitudinal charge current J , $\theta_{SH} = J_s/J$. The injected spin current transforms then into a torque exerted on the local magnetization of the FM layer. The total spin polarization inside a HM has to remain zero. Therefore, the spin accumulation changes sign between its upper and lower surfaces. That is why, if the FM is placed between two identical HM layers with identical interfaces (identical scattering of spins, identical spin mixing conductance, etc.), the net torque vanishes.

To conclude, the structural inversion asymmetry (SIA) in thin films is a general requirement to have net SOTs acting on the magnetization, independently of their precise mechanism. Our structures exhibiting SIA are based on a ferromagnetic thin films sandwiched between a heavy metal

layer and an oxidized metal layer (HM/FM/MOx) or sandwiched between different heavy metal layers (HM1/FM/HM2). Examples of such structures are Pt/Co/AlOx, Ta/CoFeB/MgO, Pt/CoFe/MgO, Pt/Co/Ta and Pt/Co/Pt.

Like the STTs, the SOTs are composed of two components that are perpendicular to each other and to the magnetization \mathbf{M} ; the field-like torque \mathbf{T}_{FL} and the damping-like torque \mathbf{T}_{DL} . In the following, the experimental proof of their existence and their various origins are discussed.

I.4.2.2. The field-like term of SOT

The field-like torque acts as if there were an external transverse magnetic field applied to the structure. It is given by:

$$\mathbf{T}_{FL} = -\gamma \mathbf{m} \times \mathbf{H}_{FL} \quad (\text{I.30})$$

$$\mathbf{H}_{FL} = \tau_{FL} (\mathbf{u}_z \times \mathbf{J}) \quad (\text{I.31})$$

The vector \mathbf{u}_z here is the unit vector normal to the structure defining the axis of the broken inversion symmetry. The parameter τ_{FL} defines the magnitude and the orientation of the field-like torque. This field is oriented in the plane and transverse to the current direction. In the literature, this field is often referred to as the Rashba field despite the fact that its origin may be different from the Rashba interaction.

[Miron et al. 2010] proposed an experimental proof of the field-like torque \mathbf{T}_{FL} in the trilayered structure Pt (3 nm)/Co (0.6 nm)/AlOx (2 nm). The experiment consisted on tailoring the rate of nucleation of reversed magnetic domains in nanowires by short current pulses in the presence of a transverse external magnetic field \mathbf{H}_{ext} . The measurements were carried out in an array of 500 nm-wide wires (**Figure I.10.b**). As seen above, the injection of an electric current is supposed to produce an effective in-plane transverse field \mathbf{H}_{FL} (Eq. I.31) that is similar to a field applied along the y-axis. The energy barrier for perpendicular magnetization reversal becomes then asymmetric with respect to the polar angle θ of the magnetization \mathbf{M} as depicted in **Figure I.10.a**. The strength of the H_{FL}/H_K ratio (with $\mu_0 H_K$ the out-of-plane anisotropy field) lowers the energy barrier in one direction and raises it in the opposite direction of \mathbf{H}_{ext} .

Initially, the nanowires have their magnetization saturated. **Figure I.10.b** and **.c** are images of the nanowires after the injection of the same current pulses for different conditions for \mathbf{H}_{ext} . In the absence of \mathbf{H}_{ext} , the reversal of the magnetization (dark contrast regions) occurs at almost half of the nanowires due to Joule heating. In the presence of \mathbf{H}_{ext} , the rate of the magnetization reversal behaves asymmetrically. It increases for one direction as domain nucleation takes place in every nanowire. For the opposite direction, the domain nucleation disappears. This behavior is in line with the existence of a current-induced \mathbf{H}_{FL} as the Oersted field, with its fixed orientation and small value estimated here to be about 1 mT, cannot account for it. In fact, as depicted in **Figure I.10.a**, if \mathbf{H}_{ext} is parallel to \mathbf{H}_{FL} , the energy barrier is even lowered and we expect more nucleation events. Inversely, when \mathbf{H}_{ext} is opposite to \mathbf{H}_{FL} , it is more difficult to nucleate as the two fields cancel and the energy barrier is higher. While inverting the current direction (**Figure I.10.c**), we get the same behavior by reversing the direction of \mathbf{H}_{ext} . This is a confirmation that this effect is related to the current flow as expected from equation (I.31). The same experiment was performed in the symmetric structure of Pt (3 nm)/Co (0.6 nm)/Pt (3 nm) and it did not show any asymmetric nucleation behavior with respect to \mathbf{H}_{ext} and to the current. This puts on evidence the general requirement of SIA as discussed above to observe the spin-orbit torques. [Miron et al. 2010] estimated the effective transverse field \mathbf{H}_{FL} to be about 1 tesla per $J = 1 \cdot 10^{12} \text{ A}\cdot\text{m}^{-2}$. This value is remarkably large especially in comparison with other reports of field-like torque measurements in similar structures. It was largely overestimated due to the measurement technique and to the role of Joule heating in the nucleation of domains.

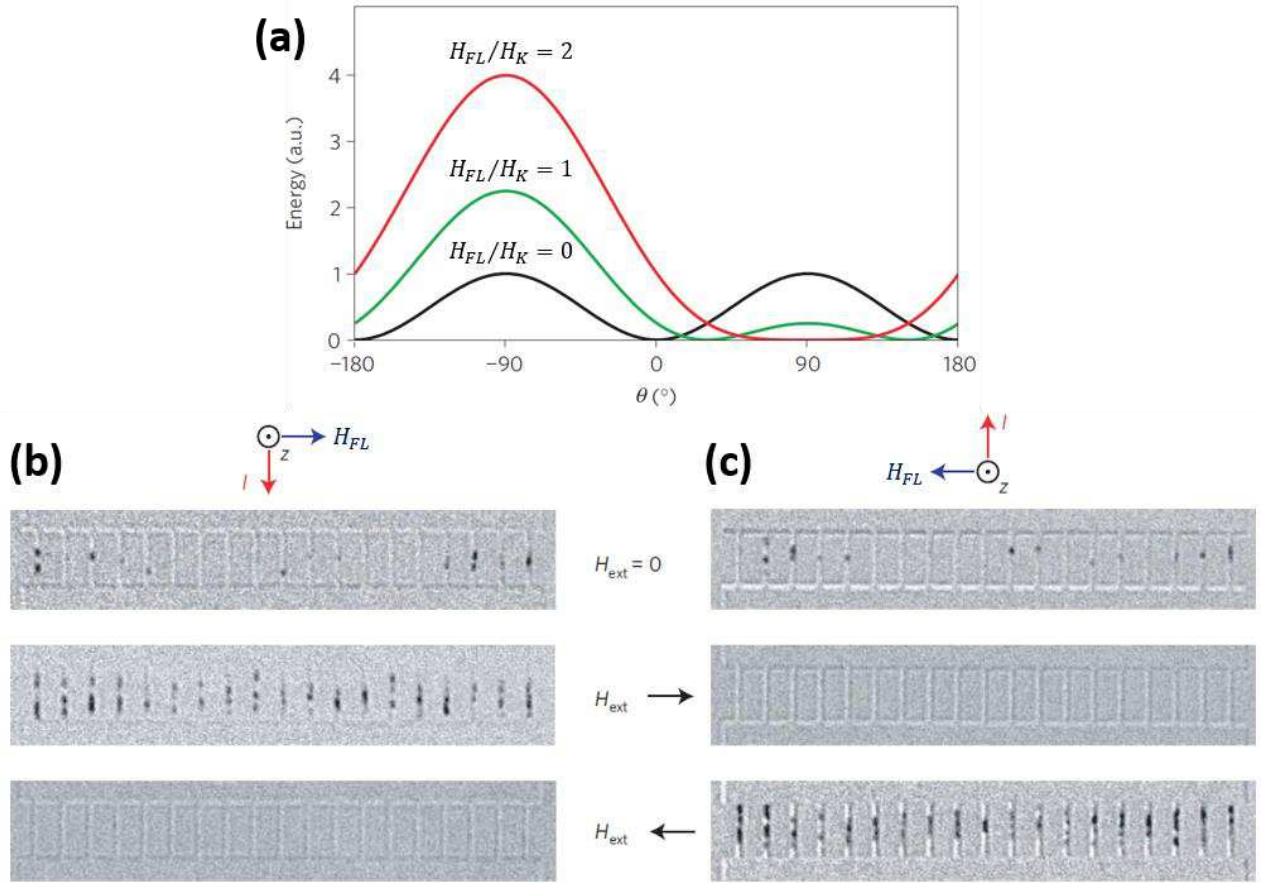


Figure 1.10 Perpendicular magnetization reversal in Pt/Co/AlOx wires in the presence of a current-induced field-like torque and an external applied in-plane transverse magnetic field. (a) Energy barrier for switching of \mathbf{M} in the direction perpendicular to the current flow. The energy is plotted as a function of the polar angle θ (the angle between \mathbf{M} and the anisotropy easy axis parallel to \mathbf{z}) with a current flowing along the wire axis parallel to \mathbf{x} . The current generates an effective magnetic field \mathbf{H}_{FL} that gives an asymmetry in the barrier height. As the ratio H_{FL}/H_K increases, where H_K is the anisotropy field, the energy barrier for nucleating a reversed domain decreases. (b)-(c) Differential Kerr microscopy images in an array of 500-nm-wide patterned wires. The black contrast represents the nucleated domains after current pulse injection. The same positive (b) and negative (c) current with or without an external transverse field \mathbf{H}_{ext} . \mathbf{H}_{ext} increases (suppresses) the nucleation of the reversed domains when it adds to (subtracts from) \mathbf{H}_{FL} . These observations evidence the dependence of \mathbf{H}_{FL} on the sign of the current. A figure extracted and adapted from [Miron et al. 2010].

[Miron et al. 2010] attributed this effect solely to the Rashba interaction from which the effective magnetic field \mathbf{H}_{FL} is referred to as the Rashba effective field \mathbf{H}_R and as proposed in [Manchon & Zhang 2008], it writes:

$$\mathbf{H}_{FL} = \mathbf{H}_R = \frac{\alpha_{RP}}{\mu_0 \mu_B M_S} (\mathbf{u}_z \times \mathbf{J}) \quad (\text{L.32})$$

with α_R the Rashba parameter. α_R is a spin-orbit coupling dependent parameter that can be further enhanced by oxidation [Krupin et al. 2005] or by engineering the suitable alloys [Ast et al. 2007]. Tuning a large Rashba effect emerged then as a possible route to induce an efficient switching of magnetization with a reduced current density thanks to a possible substantial field-like torque combined with STT.

Apart from the Rashba effect, it has been also theoretically predicted that the SHE can be one additional origin of the field-like torque in SIA materials [Haney et al. 2013]. The *ab initio* calculations performed by [Frank Freimuth et al. 2014] suggest that a SHE contribution has to be taken into account to be able to reproduce some of the experimental results concerning the strength of the field-like torque. In fact, some recent experimental investigations reported an increase of the field-like torque with the thickness of the ferromagnet up to the transverse spin diffusion length and a decrease beyond [Lo Conte et al. 2017]. Moreover, [Ou et al. 2016] claim a strong dependence of the field-like torque on the scattering of the spin accumulation generated in the HM on the FM/Oxide interface. Other experimental studies claimed a sizeable field-like component even by inserting a

spacer between the HM and the FM [Fan et al. 2013; Pai et al. 2014]. These are signatures of a bulk effect coming from the SHE in the adjacent HM layer.

Following the work of [Miron et al. 2010], numerous experiments by several groups confirmed the measurement of the field-like term, either in a similar system Pt/Co/AlOx but using a different technique based on the anomalous Hall effect [Pi et al. 2010] or in other structures like the Ta/CoFeB/MgO [Suzuki et al. 2011; Kim et al. 2012]. [Garello et al. 2013] proposed to measure the effective fields from SOTs through the second harmonic analysis of planar and anomalous Hall effects. They corrected then the previous estimate by [Miron et al. 2010] to about 4 mT per $J = 1 \cdot 10^{11}$ A.m⁻² (the ratio is limited to small currents as at higher current densities the scaling is no more linear due to Joule heating). However, other measurements performed for these same structures or similar ones like Pt/Co/GdOx did not yield any significant field-like torque [Emori et al. 2012]. This discrepancy might be partly due to the different measurement methods and to the different preparation procedures of samples.

I.4.2.3. The damping-like term of SOT

In addition to the field-like torque, another component has been proposed in SIA materials and it is given by:

$$\mathbf{T}_{DL} = -\gamma \mathbf{m} \times \mathbf{H}_{DL} \quad (\text{I.33})$$

$$\mathbf{H}_{DL} = -\tau_{DL} \cdot \mathbf{m} \times (\mathbf{u}_z \times \mathbf{J}) \quad (\text{I.34})$$

with τ_{DL} a parameter giving the magnitude and the direction of the effective field \mathbf{H}_{DL} . This spin-orbit torque is often called the ‘‘Slonczewski-like’’ torque in analogy to the spin transfer torque formulated by [Slonczewski 1996] for spin valves magnetic multilayers, or the ‘‘anti-damping’’ torque following the same analogy. Hereafter, we will always refer to \mathbf{T}_{DL} as the damping-like torque.

A year after the proposal of the field-like torque, [Miron, Garello, et al. 2011] proposed the existence of the damping-like torque by studying the current-induced magnetization switching, assisted by an external in-plane field, in a 500x500 nm square-dot of Co/AlOx sitting on a Pt Hall cross (**Figure I.11.a**). The magnetic switching of the dot was evidenced by measuring the anomalous Hall resistance (that represents the M_z component) as a function of the applied current density \mathbf{J} along with the application of a static in-plane field \mathbf{H}_x . The injection of a positive (respect. negative) current results in the switching of the magnetization from up to down (respect. down to up) for a positive \mathbf{H}_x and down to up (respect. up to down) for a negative \mathbf{H}_x . As illustrated in **Figure I.11.b**, by tilting \mathbf{M} slightly along the x -axis, the current induces an effective field \mathbf{H}_{DL} with a negative out-of-plane component that enables the switching of \mathbf{M} to the down state. The sign of the out-of-plane \mathbf{H}_{DL} component depends on the direction of the current and on M_x (defined by the direction of \mathbf{H}_x). It stabilizes then the up state when current and in-plane field are along opposite directions ($J < 0$, $H_x > 0$ in **Figure I.11.c** and $J > 0$, $H_x < 0$ in **Figure I.11.d**). The authors concluded that the current flowing in the plane of the structure induces a torque. This torque enables the switching. It is the damping-like term of SOT. Unlike the field-like torque, its effective field depends on the orientation of the magnetization.

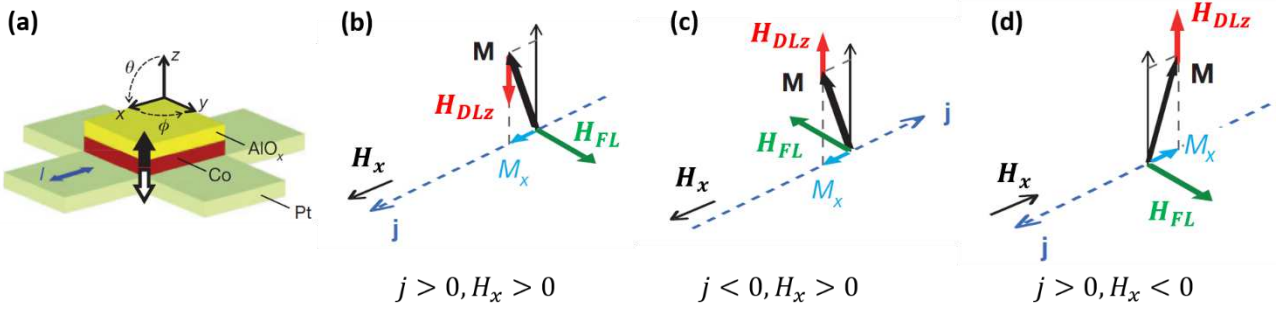


Figure I.11 Description of the magnetization switching by the damping-like torque. (a) Schematic of the Co/AIOx square dot on top of a Pt Hall cross. The black and white arrows indicate the two states of the out-of-plane anisotropy of the magnetization \mathbf{M} , up and down respectively. (b)-(d) dependence of switching on the applied field direction. The bias field \mathbf{H}_x tilts \mathbf{M} yielding a non-zero x -component M_x . The injected current \mathbf{J} generates two effective fields: \mathbf{H}_{FL} and $\mathbf{H}_{DL} \sim \mathbf{H}_{FL} \times \mathbf{M}_x$. The z -component of the effective damping-like field \mathbf{H}_{DLz} acts on the tilted \mathbf{M} as an easy-axis field. For the case (b), $J > 0, H_x > 0$, \mathbf{H}_{DL} switches \mathbf{M} from up to down. For the other two cases, (c) $J < 0, H_x > 0$ and (d) $J > 0, H_x < 0$, \mathbf{H}_{DL} stabilizes \mathbf{M} in the up state. A figure extracted and adapted from [Miron, Garello, et al. 2011].

Initially, [Miron, Garello, et al. 2011] proposed a contribution from the Rashba effect as the origin of the damping-like torque since the SHE alone appeared too small to account for the amplitude of the effective field \mathbf{H}_{DL} . In analogy with reported observations in semi-conductors [Kato et al. 2004], the interplay between the Rashba effective field and the conduction electron spin-dependent mobility at interfaces can lead to an out-of-plane spin orientation at the interface. This out-of-plane spin component can eventually induce the observed torque on \mathbf{M} . [Miron, Garello, et al., 2011] found also that the switching efficiency increases with the oxidation of the upper Al layer suggesting a key role of the Rashba interaction. Right after, theoretical works demonstrated that the Rashba effect alone has two different contributions; field-like and damping-like terms [Wang & Manchon 2012; K.-W. Kim et al. 2012]. Later, in a comparable structure of Pt/Co/AIOx, [L. Liu, Lee, et al. 2012] concluded that the SHE is responsible of the emergence of \mathbf{T}_{DL} rather than the Rashba interaction. They were able to account for the current-induced magnetization switching by considering a large spin Hall angle for Pt ($\theta_{SH} = 0.076$) measured in one of their previous works [Liu et al. 2011]. The same authors report also similar current-induced magnetization switching for other different HM adjacent layers; Ta [L. Liu, Pai, et al. 2012] and W [Pai et al. 2012] in order to confirm the key role of the SHE. Mainly after that, it has been widely accepted that the SHE is the primary origin of the damping-like torque. In this context, the parameter τ_{DL} is often described as:

$$\tau_{DL} = \frac{\hbar\theta_{SH}}{2\mu_0 e M_S t_{FM}} \quad (\text{I.35})$$

We note that Eq I.35 does not take into account the possible effects of spin mixing phenomena at the interface. The strength of the damping-like torque scales with the spin Hall angle of the adjacent HM layers. Consequently, a large number of experimental works has focused on enhancing the damping-like torque through the optimization of θ_{SH} in the stacks for a more efficient manipulation of the magnetization. This can be done for example by modifying the HM layer, either by its thickness, its crystal phase or oxidizing/doping the material [Hao et al. 2015; Demasius et al. 2016; Yu et al. 2016; Ramaswamy et al. 2016]. An alternative way is to sandwich the FM between two different HMs with opposite spin Hall angles [Woo et al. 2014; Yu et al. 2016; Guan et al. 2017; J.-S. Kim, Yune-Seok Nam, Kim, Park, Min-Ho Park & Choe 2018]. Both induced damping-like torques from the bottom and top layers will then add up inside the FM layer.

To conclude, several experimental and theoretical works have established the existence of net torques coming from the SOC in ultrathin multilayers with SIA. A huge debate is still in place concerning their exact physical mechanism due to the large discrepancy and controversy in reported results. Both Rashba effect and SHE through spin orientation and spin accumulation can give the two terms of SOTs. Nevertheless, a wide assumed picture is that the SHE creates $|\mathbf{T}_{DL}| \gg |\mathbf{T}_{FL}|$ whereas the Rashba effect gives the opposite situation [Haney et al. 2013]. The exact separation of these two

contributions by experimental methods is not straightforward. As they share the same SOC origin, changing any material parameter can cause modifications in both effects. Their exact roles are still under debate and there are considerable ongoing efforts in the worldwide community concerning this matter. Instead, the main objective of my thesis is to understand better the action of SOTs in the mechanism of DWs motion in SIA materials with PMA.

I.4.2.4. Displacement of DWs by SOTs

Remarkable experimental observations of DW motion have been reported in SIA materials. The pioneering work of [Moore et al. 2008] showed fast current-induced dynamics with a DW velocity at $\approx 100 \text{ m.s}^{-1}$ opposite to the electron flow in nano-stripes of Pt (3 nm)/Co (0.6 nm)/AlOx (2 nm). A follow-up study in the same system by the same group indicated even higher velocities up to 400 m.s^{-1} and considered for the first time a possible role of SOTs to account for this anomalous DW motion [Miron, Moore, et al. 2011]. This efficient DW motion in SIA materials was also reported later in Co/Ni nanowires based SIA materials [Ryu et al. 2012; Koyama et al. 2013].

Initially, [Miron, Moore, et al. 2011] attributed the large velocities of motion to the stabilization of the DW structure by the action of the field-like torque. For current densities of the order of 10^{12} A.m^{-2} , the DW is expected to propagate in the precessional regime of motion when considering only STT action in the 500 nm wide, $10 \mu\text{m}$ long stripes of Pt/Co/AlOx. This oscillatory regime, even in the limit case of full spin polarization ($P = 1$), cannot yield velocities as high as 400 m.s^{-1} . Therefore, only an STT steady-state regime can explain such fast motion. This suggests a large non-adiabatic efficiency β since the DW velocity is proportional to β/α in this regime. The field-like torque through its effective magnetic field allows to extend the steady-state regime to large current densities thus obtaining a high velocity of motion. Actually, the Rashba field or \mathbf{H}_{FL} is transverse to the stripes (Eq. I.31). It acts then along the magnetization of Bloch wall in the structure. The DW structure is then more stable against precession from the current non-adiabatic torque \mathbf{T}_{NA} . A combination of large \mathbf{H}_{FL} and large β can account for the large velocity in Pt/Co/AlOx.

This proposal should be completed to account for the unexpected direction of motion of DWs. STT predicts a motion along the electron flow, opposite to observations in Pt/Co/AlOx. A negative \mathbf{T}_{NA} is necessary to account for the DW motion against the electron flow. This can arise from two possibilities; either the spin polarization is negative $P < 0$ or the non-adiabatic coefficient $\beta < 0$. However, there is no experimental evidence of $P < 0$ or $\beta < 0$ in Pt/Co/AlOx. A negative spin polarization at the Pt/Co interfaces has already been considered as possible [Sipr et al. 2008; Lee et al. 2010] and a negative β also predicted [Garate et al. 2009]. Recently, an experimental study proposed that $P < 0$ holds in a Pt/Co/Pt structure [Je et al. 2017] where the thickness of the Co layer is very thin ($t_{FM} \leq 0.4 \text{ nm}$).

We have already mentioned that the STT action is vanishing in thin materials. Even the enhanced non-adiabatic torque allegedly attributed to SIA by [Miron et al. 2009] is put into question. In Pt/Co/AlOx, it was estimated that $\beta \sim 1$ whereas $\beta < 0.02$ was extracted in symmetric Pt/Co/Pt structure through DW depinning measurements in a double Hall cross. In such experiment, the DW is subject to a simultaneous action from a current and a magnetic field and its displacement is detected by anomalous Hall measurement. The action of \mathbf{T}_{NA} , as it is equivalent to an easy-axis magnetic field, has been then extracted. However, these measurements were prior to the discovery of the damping-like torque. Therefore, a large β induced by SIA is not anymore conclusive. Moreover, the DW motion was observed along the electron flow in other SIA materials such as Ta/CoFeB/MgO [Fukami et al. 2011; Emori et al. 2013]. In general, the ratio of field-like torque to damping-like torque is smaller than 1 in Pt/FM based multilayers [Pai et al., 2015]. These distinct results suggest reconsidering the proposal of a strong field-like torque with a large \mathbf{T}_{NA} by taking into account the action of the damping-like torque on DWs.

The magnitude of the damping-like term of SOTs depends on the orientation of the DW core magnetization \mathbf{m}_{DW} . The damping-like torque \mathbf{T}_{DL} cannot drive a DW that has a pure Bloch configuration as expected in ultrathin FM layers with PMA. For a Bloch wall, \mathbf{m}_{DW} is orthogonal to both \mathbf{u}_z and \mathbf{J} . Thus, according to Eq. I.34, the resulting \mathbf{T}_{DL} is null (**Figure I.12.a**). To be able to induce a sizeable effect of \mathbf{T}_{DL} , the internal structure of the Bloch wall has to be modified. A longitudinal in-plane field \mathbf{H}_x changes the structure of a Bloch wall to the Néel configuration. In the latter configuration, the magnitude of \mathbf{T}_{DL} is maximum. [Haazen et al., 2013] presented a study of current-induced DW depinning in Pt/Co/Pt stripes in the presence of a bias in-plane magnetic field. An in-plane field indeed forces the DW to adopt the Néel structure. Two adjacent DWs (DW_{U-D} and DW_{D-U}) will have their moments \mathbf{m}_{DW} pointing in the same direction. The effective damping-like field \mathbf{H}_{DL} will point in the same direction on both of the DWs. Consequently, DWs move opposite to each other. The domain expands or shrinks depending on the orientation of \mathbf{H}_x (**Figure I.12.b** and **.c**). We note that both Pt layers in this structure act as a source for SHE. They inject oppositely oriented spin currents in the Co layer. For a symmetric Pt/Co/Pt, no depinning of DWs was reported as spin Hall currents from the two Pt layers cancel each other. For the asymmetric structure by choosing unequal Pt thicknesses, a net injected spin current is possible and DW depinning was obtained. This DW depinning changes directions under the same \mathbf{H}_x while inverting the asymmetry between Pt layers following the symmetry of a net SHE.

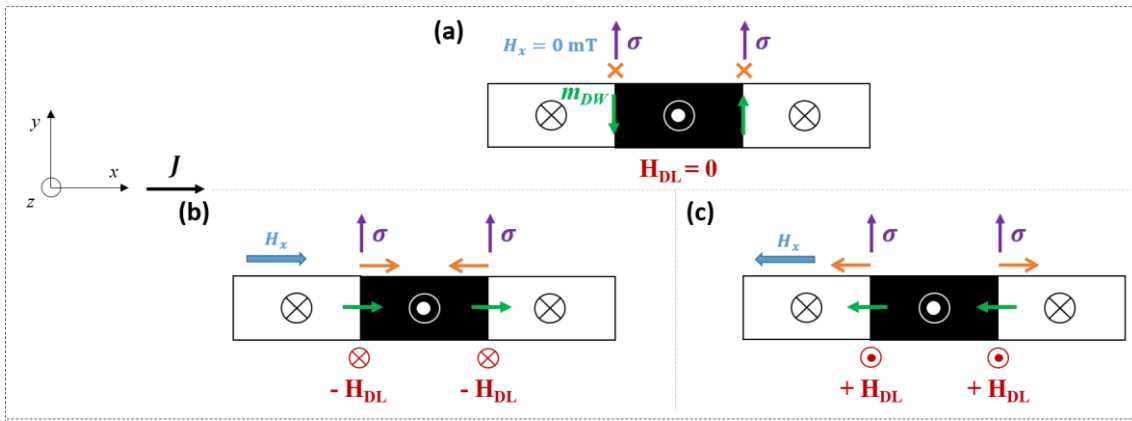


Figure I.12 The action of the damping-like torque \mathbf{T}_{DL} on different DW configurations. Schematics are based on results reported in [Haazen et al. 2013]. The green arrows represent the orientation of \mathbf{m}_{DW} inside each DW. The injected spin current has a polarization vector σ depicted by the purple arrows and it corresponds to a bottom HM layer with $\theta_{SH} > 0$ where the injected current is positive. The orientation of the effective magnetic field \mathbf{H}_{DL} follows $\sigma \times \mathbf{m}_{DW}$. The orange arrows represent the direction of DW motion induced by \mathbf{H}_{DL} . (a) No DW motion for Bloch DWs. The action of \mathbf{T}_{DL} on Néel walls imposed by an external in-plane field \mathbf{H}_x , positive in (b) and negative in (c). The orientation of \mathbf{H}_{DL} is the same for successive DWs yielding opposite directions of motion. The up magnetic domain shrinks (expands) under current in (b) ((c)).

Several other experimental observations of DW depinning and motion are also a clear evidence of the action of \mathbf{T}_{DL} . [Bhowmik et al., 2015; Schulz et al., 2015] reported a current-induced depinning and motion for a DW sitting longitudinal to the current flow in Ta/CoFeB/MgO structures. The application of \mathbf{H}_x , in this case, fixes a Bloch DW structure. \mathbf{m}_{DW} is then either parallel or antiparallel to current. For this particular geometry, the current exerts a zero net STT on the DW. This is because there is no gradient of local spins along the path of the current. Therefore, the observation of the orthogonal motion of DWs with respect to the current flow is solely attributed to the action of \mathbf{H}_{DL} . Reversing the polarity of either the current \mathbf{J} or \mathbf{H}_x reverses the direction of the DW motion. This is consistent with the symmetry of the damping-like torque. The efficiency of the DW depinning depends also on the relative angle of \mathbf{H}_x with respect to \mathbf{J} . The efficiency is maximum when both of them are parallel. Said in other words, the DW has to be in Néel configuration to obtain an efficient current-driven motion in SIA materials. However, experimentally, both DW_{U-D} and DW_{D-U} always move in the same direction without the need of any external longitudinal field in asymmetric magnetic multilayers. The adjacent Néel walls has to alternate direction, i.e. have a uniform chirality in the thin layer. There should be another physical mechanism in the SIA system to stabilize such a non-trivial DW structure. It is the interfacial ‘‘Dzyaloshinskii-Moriya interaction’’.

I.5. Chiral DWs motion in SIA materials

[Thiaville et al. 2012] were the first to propose a new mechanism combining the damping-like torque \mathbf{T}_{DL} and the Dzyaloshinskii-Moriya interaction (DMI). This mechanism accounts for the direction of the DW motion as well as for the large DW velocities. This mechanism stresses the importance of chirality of DWs in their dynamics. We will then explain the mechanism of the combined action of DMI and \mathbf{T}_{DL} on chiral DW motion in the following sections. We will also introduce DW chirality-induced effects that alters the propagation of DWs. Among these effects, we will consider the recently proposed mechanism of Chiral Damping [Jué et al. 2015].

I.5.1. Dzyaloshinskii-Moriya Interaction (DMI)

The DMI arises from the combination of SOC and low symmetry that gives a non-vanishing crystal field as it was proposed historically by [I.E.Dzialoshinskii, 1957]. Typically, the crystal structure of bulk metals lacks this asymmetry. [Moriya, 1960] introduced later a microscopic model to calculate DMI in magnetic systems. When the dimensionality of a system is decreased, it can exhibit a lack of inversion symmetry. [Fert, 1990] extended then DMI to thin films due to a symmetry reduction at interfaces; it is an interfacial DMI.

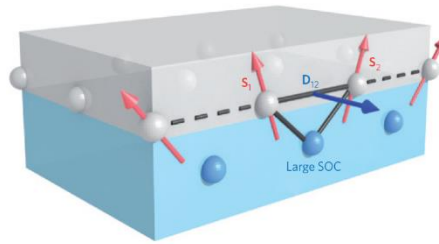


Figure I.13 Dzyaloshinskii-Moriya interaction in thin films. A representation of the DMI at the interface between a ferromagnet (in grey) and a bottom heavy metal layer with a large SOC (in blue). A figure extracted from [Fert et al. 2013].

DMI is an anti-symmetric exchange interaction between neighboring spins at atomic sites i and j of a ferromagnet that is mediated by an adjacent heavy metal atom (**Figure I.13**). It scales with the HM spin-orbit coupling. A simple picture of the action of a non-compensated crystal field at the interface on the itinerant electrons can illustrate the DMI action on adjacent magnetic moments. These electrons ensure the hybridization between adjacent atoms i and j . It can be simply assumed that they keep virtually travelling from one atom to the other with an electron from the atom i always moving opposite to an electron from the atom j . The spin of the former (respect. latter) electron is initially oriented along \mathbf{S}_i (respect. \mathbf{S}_j) the local spin of the atom i (respect. the atom j). This is how simply we can picture the ferromagnetic exchange coupling between adjacent magnetic moments in a ferromagnetic material. However, each electron feels, in its own frame, an effective magnetic field due to the non-compensated electric field provided by the adjacent HM atom. Their spins precess opposite to each other. As with the s - d exchange interaction, the local spins of the atoms tend to align parallel along the electron spins, a finite angle takes place between \mathbf{S}_i and \mathbf{S}_j . The DMI Hamiltonian \mathcal{H}_{DM} between spins \mathbf{S}_i and \mathbf{S}_j can be written as:

$$\mathcal{H}_{DM} = -\mathbf{D}_{ij} \cdot (\mathbf{S}_i \times \mathbf{S}_j) \quad (\text{I.36})$$

with \mathbf{D}_{ij} the DMI vector. For the interfacial DMI, this vector is usually within the film plane and points normal to \mathbf{r}_{ij} , the position vector connecting the atom i to the atom j [Crépieux and Lacroix, 1998]. Thus, unlike the exchange interaction, DMI favors neighboring spins to align orthogonal to each other inducing non-collinear spin texture when there is no preferential

unique orientation for spins (cycloidal spin spiral). This can occur inside a DW since the spin rotates from a one direction to the other [Thiaville et al. 2012]. When DMI is strong enough, some exotic magnetic textures like skyrmions can be stabilized in a uniform state. It can even destroy the uniform state of a FM and induce a helical spin spiral phase [Hervé et al. 2018; Bode et al. 2007; Ferriani et al. 2008].

In thin magnetic films where the nominal thickness is negligible in comparison with the width and the length of the sample, the DMI energy density is given by [Thiaville et al. 2012]:

$$\epsilon_{DMI} = D[m_z \nabla \cdot \mathbf{m} - (\mathbf{m} \cdot \nabla)m_z] \quad (\text{I.37})$$

1.5.2. Chiral Néel DWs induced by DMI

In PMA materials, the DMI can induce chiral DW structure. The definition of the chirality for magnetization textures relies on the adopted rotational direction between adjacent magnetic moments. Depending on the relative sign of the DMI constant D , we get two opposite directions of rotation hence two opposite chiralities. Conventionally, a right-handed (respect. left-handed) chirality corresponds to spins rotating clockwise (respect. anti-clockwise). Based on Eq. I.37, a negative (respect. positive) D fixes a right-handed (respect. left-handed) chirality. Note here that the definition of the DMI constant D sign is ambiguous in literature as several groups employ the opposite convention [Belmeguenai et al., 2015; Gross et al., 2016; Karnad et al., 2018] while others adopt the same convention that we use [Heide, Bihlmayer and Blügel, 2008; Gong Chen et al., 2013; Hrabec et al., 2014; Yang et al., 2015]. The DMI favors then a tilt between two adjacent magnetic moments at the expense of the uniaxial anisotropy and the magnetic exchange. Therefore, unless it is strong, DMI affects mainly the DW where the magnetization \mathbf{M} already deviates from the easy-axis. Inside a DW, the DMI competes with the dipolar interaction. In PMA materials, the favored structure for DWs is the Bloch structure. The magnetostatic ‘shape’ anisotropy effective field \mathbf{H}_K (cf. Eq. I.11 in section I.2.2), oriented along the y -axis (cf. Figure I.2), favors a Bloch structure. Inside a DW, the DMI vector \mathbf{D}_{ij} lies in the plane along the y -axis. According to Eq. I.36, DMI will force then the DW to adopt a Néel structure. This can be modeled by an effective local magnetic field \mathbf{H}_{DMI} normal to the wall (oriented along the x -axis) and defined as [Thiaville et al. 2012]:

$$H_{DMI} = \frac{\pi|D|}{2\mu_0 M_s \Delta} \quad (\text{I.38})$$

with Δ the DW width and M_s the saturation magnetization. In the presence of DMI, the structure of the DW results from the competition between these two local effective fields. Above a critical value $D_c = 4\Delta K/\pi$ [Thiaville et al., 2012], \mathbf{H}_{DMI} stabilizes Néel DWs with a unique direction of rotation in the FM layer. We speak then of homochiral Néel DWs where the DW core magnetizations of adjacent DWs are pointing opposite to each other. When a large enough external in-plane field \mathbf{H}_x is applied, the DW core magnetization can point in the same direction for both DWs. They have then opposite chiralities. This difference in the chirality can reveal asymmetric behaviors between DWs. We refer to them as chiral phenomena in magnetic DWs.

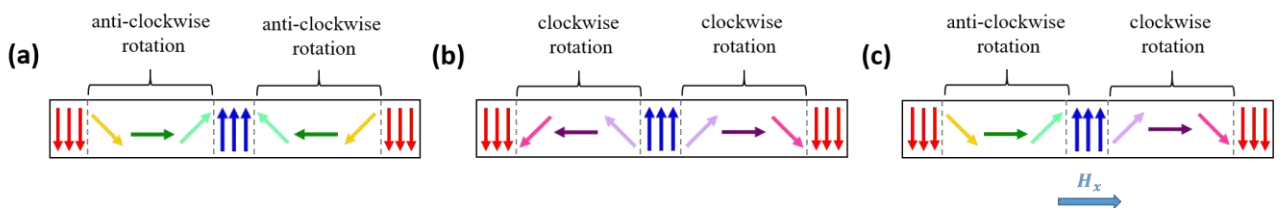


Figure I.14 Schematic diagrams of homochiral Néel walls, (a) left-handed and (b) right-handed, and Néel walls with opposite chiralities in (c). The DMI imposes a unique rotational direction of magnetization inside the two DWs. It is either an anti-clockwise rotation giving the left-handed chirality or a clockwise rotation for a right-handed chirality. (c) The application of an external in-plane field H_x breaks the symmetry and successive DWs have opposite chiralities.

The DMI gives then an additional degree of freedom in spin configurations that is the magnetic chirality. This enriches the possibilities of stable DWs configurations in PMA thin films; achiral Bloch walls, homochiral Néel walls or even mixed walls in between (when $|D| < D_c$). For a stabilized Néel wall, the energy density σ_{DW} decreases in comparison to the energy of a Bloch wall σ_0 and it can be expressed, for large values of D ($|D| > D_c$), as [Heide et al. 2008]:

$$\sigma_{DW} = \sigma_0 - \pi|D| \quad (\text{I.39})$$

The DW energy vanishes then at certain value of D beyond which the uniaxial anisotropy of the system becomes weak against DMI. The magnetization is no longer uniform and the ground state of the system is a cycloid state [Rohart and Thiaville, 2013]. Moreover, a strong DMI can have an effect on the DW width Δ_T according to the Thiele definition [Nakatani et al. 2005]:

$$\frac{2}{\Delta_T} = \frac{1}{t_{FMW}} \int \left(\frac{\partial m}{\partial x} \right)^2 d^3r \quad (\text{I.40})$$

The assumption of $\Delta_T \approx \Delta = \sqrt{A_{ex}/K_{eff}}$ is valid for small values of D . However, at larger values and under certain conditions Δ_T varies a lot. The variation of Δ_T has to be then considered in the DW dynamics. In parallel with the proposal of its existence and its crucial role in DW motion, numerous experimental studies have focused on obtaining direct evidence of interfacial DMI.

I.5.3. Direct evidence of Chiral Néel walls in SIA materials

The first experimental evidence of interfacial DMI was reported in a single atomic layer of Mn grown on top of a single crystal of W(110) [Bode et al., 2007]. Left-handed cycloidal spin spirals were observed at low temperature using Spin-Polarized Scanning Tunneling Microscopy (SP-STM). Concerning DWs, chiral Néel configurations have been reported by several imaging techniques in SIA materials. [Chen et al. 2013] observed Néel walls, at room temperature, in perpendicularly Ni/Fe bilayers grown epitaxially on top of Cu(001) substrate, using Spin-Polarized Low Energy Microscopy (SPLEEM) (Figure I.15.a-e). They evidenced the role of DMI in stabilizing such DWs. While changing the order of film growth, the authors obtained an inversion of chirality; from right-handed in Ni/Fe to left-handed in Fe/Ni. Due to the nature of DMI, flipping interfaces reverses the sign of the DMI and thus the chirality of DWs. In addition, a transition from chiral Néel DWs to achiral Bloch DWs takes place when increasing the thickness of Ni while keeping the Fe layer very thin. Both of these observations confirm the interfacial nature of DMI and its role in forcing homochiral Néel walls in PMA thin films. However, these reports are either at low temperature or for epitaxial ultrathin films.

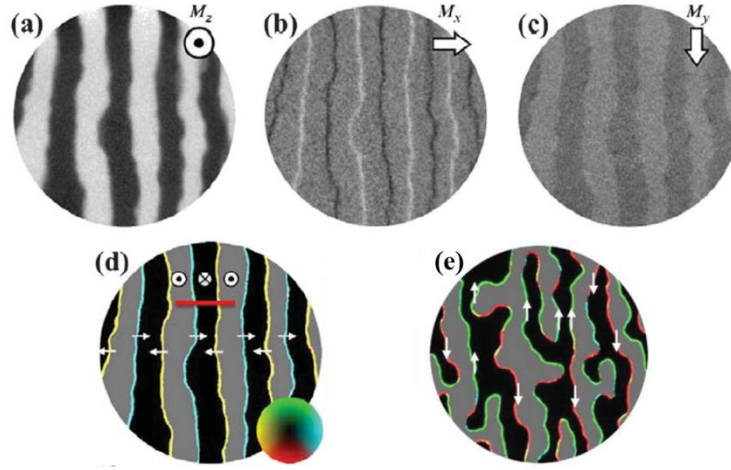


Figure I.15 Experimental evidence of interfacial DMI in thin films. (a)-(c) SPLEEM images of Cu(001)/2 ML Ni/2.5 ML Fe. These images map the magnetization components: (a) M_z , (b) M_x and (c) M_y . The strong contrast in (a) (bright and dark) indicates PMA in the structure. Magnetic contrast is only obtained at DWs in (b) and is very weak in (c). M_y is then vanishingly small in the structure and DWs have therefore a Néel structure. Successive DWs in (b) give different contrast thus DWs are homochiral. (d) and (e) are constructed images from the SPLEEM measurements respectively for Cu(001)/2 ML Ni/2.5 ML Fe and Cu(001)/10 ML Ni/1.3 ML Fe (ML stands for an atomic monolayer). White arrows emphasize the in-plane orientation of the DW core magnetization. (d) highlights the right-handed chiral Néel walls in Cu(001)/2 ML Ni/2.5 ML Fe. In (e), DWs are Bloch walls with no preferential orientation demonstrating the vanishing of DMI when Ni gets thicker. Figures are extracted and adapted from [G. Chen et al. 2013].

For more standard samples that are deposited by sputtering and that are have more compatible with an industrial integration, the debate whether an interfacial DMI is sufficient or not to impose chiral spin textures remained open until some imaging techniques have started to be available. [Tetienne et al., 2014, 2015; Gross et al., 2016] used a scanning magnetometry with nitrogen-vacancy defects in a diamond tip to probe the magnetic structure through a local measurement of the stray field distribution from the sample surface and above a DW. These investigations evidenced left-handed Néel walls in Pt/Co, right-handed Néel walls in W/CoFeB and Bloch walls in Ta/CoFeB based-structures. Later, chiral Néel walls were, as well, observed at room temperature in the Pt (3 nm)/Co (1 nm)/MgO structure grown by DC magnetron sputtering. The used imaging technique is Photoemission Electron Microscopy combined with X-ray Magnetic Circular Dichroism (XMCD-PEEM) [Bouille et al., 2016]. By properly choosing the gazing angle at which the X-ray beam impinges on the sample surface plane, this technique gives a direct imaging of the in-plane orientation of spins. The dichroic contrast becomes sensitive to a possible DW magnetization aligned with the X-ray beam. The peak and dip in the contrast observed while crossing adjacent DWs confirm the stabilization of left-chiral Néel walls thanks to a strong DMI parameter of $|D| = 2.05 \pm 0.3 \text{ mJ.m}^{-2}$ (Figure I.16.a-b).

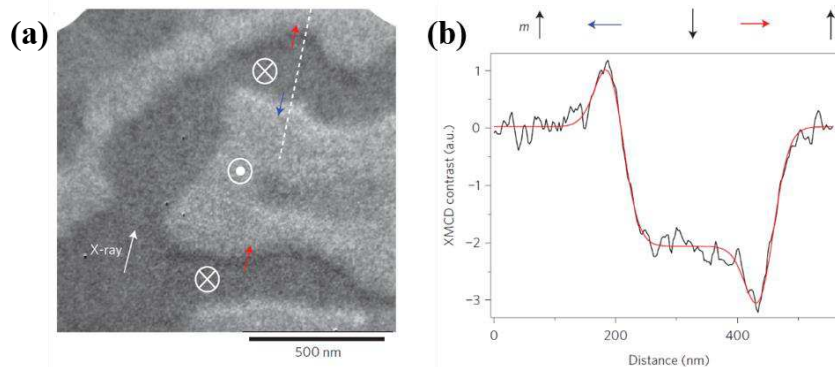


Figure I.16 Evidence of chiral Néel DWs using X-ray Magnetic circular Dichroism (XMCD-PEEM). (a) Image of a multidomain state in a thin film of Pt/Co/MgO. Adjacent DWs perpendicular to the X-ray beam (white dotted line) have thin white and black lines which correspond to a magnetization being parallel and antiparallel to the beam. This is an evidence of a left-handed Néel wall highlighted by the linescan, in (b), of the magnetic contrast along the dotted white line. Figures are extracted from [Bouille et al., 2016].

These findings are in line with a DMI lying at interfaces in SIA materials. Several theoretical approaches tried then to get an understanding of the origin, sign and magnitude of the DMI in thin films. [Kim et al., 2013] have already suggested that DMI and the Rashba effect share a common interfacial origin. [Kashid et al., 2014] proposed that the sign and strength of DMI are determined by the bonding between d orbitals of the magnetic ($3d$ for Fe, Co) and nonmagnetic elements ($5d$ for Pt, Ir and Au), the bandwidth and the energy difference between occupied and unoccupied states of different spin projections. This study relied on tight-binding model and *ab initio* calculations. One year after, [Yang et al., 2015] found, using first-principles calculations for Pt/Co bilayers, that the dominant contribution of DMI comes from Co spins of the interfacial Co layer. The contribution decreases drastically as the Co layer is located further away from the interface and it is mainly associated with the SOC of the adjacent Pt layer at the interface. Moreover, they didn't get a correlation between the DMI and the proximity-induced magnetism in Pt as it was proposed to be a dominating factor of DMI in [Ryu et al., 2014]. Afterwards, [Belabbes et al., 2016] performed a systematic study of $5d$ HM/ $3d$ FM interfaces via relativistic first-principles. The investigated $5d$ HMs were W, Re, Os, Ir, Pt and Au and the $3d$ FMs were V, Cr, Mn, Fe, Co and Ni. They obtained, for most of the considered HMs, that the ratio of DMI energy divided by the square of the spin magnetic moment has a monotonic variation; increasing from V to Mn and decreasing from Mn to Ni. This is similar to the dependence of the magnetic moment per atom with the $3d$ transition metal ferromagnet. The interfacial DMI has then a tendency that follows the Hund's first rule. The authors attribute this tendency to the $3d$ orbital occupations and their spin-flip mixing process with the $5d$ states. Several experimental studies reported as well the decrease of the strength of DMI while increasing the thickness of the FM for various examples of elements and stacks [Cho et al., 2015; Kim et al., 2015; Lo Conte et al., 2017] confirming the interfacial origin of DMI.

All of these efforts help to further understand the mechanism of DMI. This is highly important in order to have guiding principles towards the optimization of DMI strength and sign by properly choosing the materials and the structure. In fact, the DMI is essential to have a unidirectional motion of DWs by SOTs in PMA materials which resulted in the regain of interest on DW motion investigation these recent years.

I.5.4. DW motion in the presence of DMI

I.5.4.1. The effect of DMI on FIDWM

In FIDWM, the DMI effective field H_{DMI} stabilizes the DW against precession pushing the Walker field H_W to a larger amplitude of H_z [Thiaville et al. 2012]. It is then possible to attain larger velocities compared to structures with inversion symmetry where the difference in energy between Bloch and Néel wall configurations is small thus reaching the Walker breakdown at smaller values for H_z . Indeed, for a symmetric-like structure such as Pt (4.5 nm)/Co (0.6 nm)/Pt (3.5 nm), [Metaxas et al., 2007] estimated the Walker breakdown to be about $H_W \approx 12.5$ mT whereas in Pt (4 nm)/Co (0.8 nm)/AlOx (3 nm), with large SIA, [Pham et al., 2016] found experimentally $H_W \approx 120$ mT. Beyond the Walker field, the DW velocity exhibits a saturation plateau (**Figure I.17**). [Yamada & Nakatani 2015] attributed this behavior to the emergence of multiple magnetic objects called vertical Bloch lines across the DW in the presence of strong DMI. Between two of these magnetic objects, the DW magnetic moment has an equilibrium azimuthal angle ϕ and does not precess as expected. Thus, the averaged azimuthal angle for the DW remains constant near the value reached at the Walker field. In addition, vertical Bloch lines nucleate, propagate and annihilate in pairs continuously so the process is always accompanied by an emission of spin waves. The combination of these effects suppresses the Walker breakdown and gives a constant average speed of the DW. This trend is absent in the case of a weak DMI for which we retrieve the drastic reduction in DW velocity after the Walker breakdown [Yoshimura et al. 2016].

In the case of a large DMI ($|D| \gg 0.14\mu_0 M_S^2 t_{FM}$) [Thiaville et al., 2012] approximated H_W and the DW velocity v_W at H_W to:

$$H_W \approx \alpha \frac{\pi |D|}{2 \mu_0 M_S \Delta} \quad (\text{I.41})$$

so that

$$v_W \approx \gamma_0 \frac{\pi |D|}{2 M_S} \quad (\text{I.42})$$

Consequently, the measurement of the saturation velocity in the flow regime of motion for SIA materials with large DMI can be an easy and fast way to estimate the strength $|D|$ of DMI.

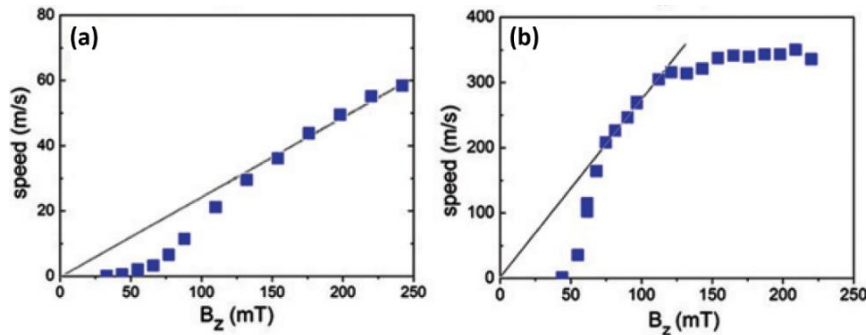


Figure I.17 DW velocity v_{DW} vs out-of-plane field in materials with different DMI. (a) Pt (4)/Co (1)/Pt (4) and (b) Pt (4)/Co (0.8)/AlOx (3) (thicknesses in nm). The thin lines in both plots emphasize the slope of the corresponding linear variation in the flow regime of motion, precessional and steady-state for (a) and (b), respectively. In (a), the exponential variation corresponds to the creep regime that hides the Walker breakdown. Thanks to DMI, the extended steady-state motion allows much larger velocities in Pt/Co/AlOx than in Pt/Co/Pt. The limit of the linear increase in Pt/Co/AlOx is followed by a plateau of a constant velocity. Extracted from [Pham et al. 2016].

I.5.4.2. The DMI + SOT mechanism for CIDWM

Nowadays, there is a consensus in nanomagnetism and spintronic communities that uses the DMI + SOT mechanism to interpret CIDWM in PMA thin films with SIA. The two key components of this mechanism are the interfacial DMI that stabilizes homochiral Néel walls and the damping-like torque, induced by the SHE in the adjacent HM layer, which drives DWs in a unidirectional fashion. Thanks to the uniform chirality, promoted by DMI, two consecutive DWs have their internal magnetic moments opposite to each other. \mathbf{H}_{DL} alternates from a DW to the other so they move in the same direction. The DMI + SOT mechanism defines the direction of motion of DWs depending on the sign of two parameters; the DMI constant D and the spin Hall angle θ_{SH} of the HM layer. Note that we consider here a dominant SHE from a bottom HM layer. The two parameters D and θ_{SH} give four possible combinations for a fixed current direction. Considering a positive current $\mathbf{J} = +|J|\mathbf{u}_x$, $\theta_{SH} > 0$ gives a spin polarization $\boldsymbol{\sigma} = \mathbf{u}_z \times \mathbf{u}_x$ along the +y-direction and according to Eq. I.34 results in \mathbf{H}_{DL} pointing up for a DW_{U-D} and pointing down for a DW_{D-U} if the chirality is left-handed $D > 0$. The DWs move therefore along the current direction. Similarly, the combination of $\theta_{SH} < 0$ and $D < 0$ results in a motion along the direction of the current. In contrast, when these two parameters have opposite signs, the DWs move against the current direction (along the electron flow). All of these combinations are depicted in **Figure I.18**. We see then that the DMI + SOT mechanism solves the puzzling issue raised by DWs moving along the current direction, [Miron, Moore, et al. 2011; Ryu et al. 2013]. It reconciles also with the case of DWs that, in spite of moving along the electron flow, do not follow the characteristics of the STT mechanism of motion as in Ta/CoFe/MgO [Emori et al. 2013].

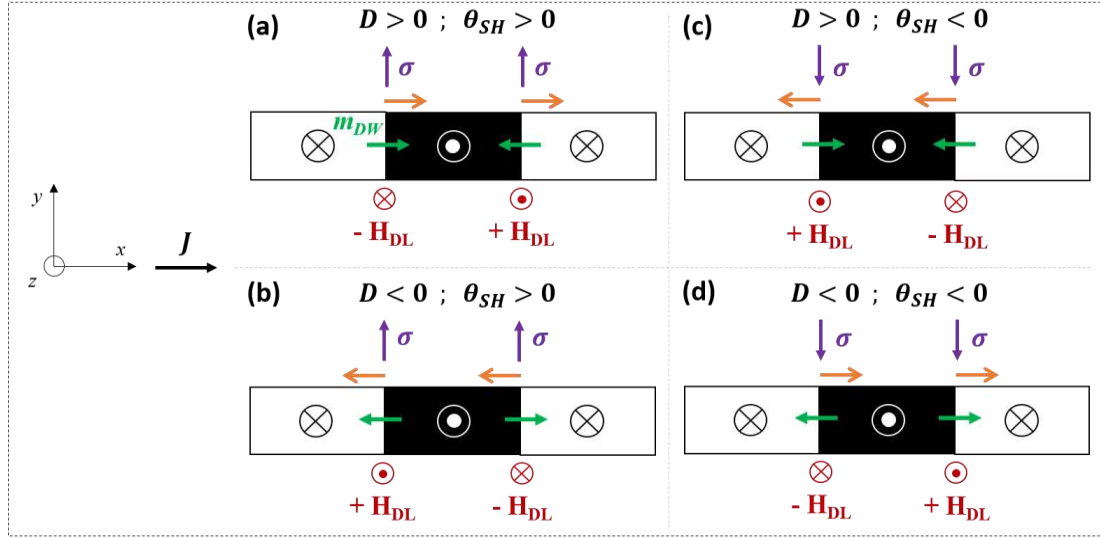


Figure I.18 DW direction of motion based on the DMI and SOT mechanism. The orientation of \mathbf{H}_{DL} defines the direction of the DW motion. We consider a positive current for all for combination. The sign of D fixes the chirality of DWs illustrated by the orientation of \mathbf{m}_{DW} (green arrows). A positive (negative) spin Hall angle θ_{SH} yields a positive (negative) spin polarization vector $\boldsymbol{\sigma}$ (purple arrows) injected from a bottom HM layer. The signs of D and θ_{SH} dictate the motion (orange arrows): it is along the charge current for (a) $D > 0$ $\theta_{SH} > 0$ and (d) $D < 0$ $\theta_{SH} < 0$ and against the current for (b) $D < 0$ $\theta_{SH} > 0$ and (c) $D > 0$ $\theta_{SH} < 0$.

Under injection of a uniform current distribution along the x -axis, the dynamics of the magnetization \mathbf{M} is described by the augmented LLG equation:

$$\frac{\partial \mathbf{m}}{\partial t} = -\gamma \mathbf{m} \times \mathbf{H}_{eff} + \alpha \mathbf{m} \times \frac{\partial \mathbf{m}}{\partial t} - (\mathbf{u} \cdot \nabla) \mathbf{m} - \beta \mathbf{m} \times [-(\mathbf{u} \cdot \nabla) \mathbf{m}] - \gamma \mathbf{m} \times \mathbf{H}_{FL} - \gamma \mathbf{m} \times \mathbf{H}_{DL} \quad (\text{I.43})$$

Here, the effective field \mathbf{H}_{eff} , apart from the standard contributions, includes the local DMI effective field \mathbf{H}_{DMI} . The third and fourth terms on the right side of the LLG equation represent the STT contributions. The fifth term corresponds to the action of the field-like torque. Within the framework of the SOT+DMI mechanism, we restrict ourselves to the damping-like torque action (the sixth term) in concert with the Gilbert damping action (the second term). In fact, the STT and the field-like contributions are negligible compared to the damping-like torque action. In what follows, we describe only a left-handed Néel DW_{U-D} subjected to a \mathbf{T}_{DL} from a bottom HM layer with $\theta_{SH} > 0$. The descriptions of any other type of a Néel DW is straightforward by symmetry arguments. To describe the DMI + SOT mechanism, we use the simplified picture depicted in **Figure I.19** below.

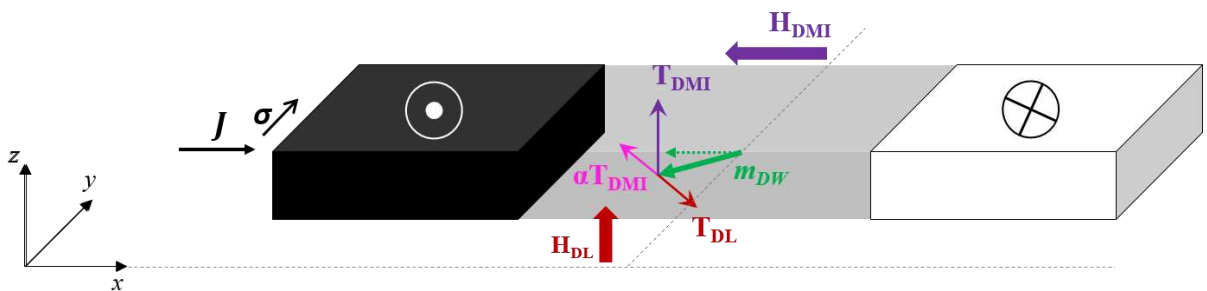


Figure I.19 Mechanism of the CIDWM based on the SOT + DMI mechanism. Schematic diagram of the different torques acting on the DW core magnetization \mathbf{m}_{DW} . The dashed green arrow corresponds to the initial configuration of the left-handed DW_{U-D}. \mathbf{T}_{DL} rotates \mathbf{m}_{DW} in the plane creating the torque from DMI, \mathbf{T}_{DMI} . \mathbf{T}_{DMI} pulls the \mathbf{m}_{DW} out of plane which results in a DW motion along the current direction.

The effective damping-like field \mathbf{H}_{DL} acts on the DW internal magnetic moment \mathbf{m}_{DW} by rotating it in the plane. As this rotation deviates \mathbf{m}_{DW} from its initial equilibrium configuration, the action of the torque $\mathbf{T}_{DMI} = -\gamma \mathbf{m}_{DW} \times \mathbf{H}_{DMI}$ is no longer zero and cants \mathbf{m}_{DW} out of the plane. The in-plane torque associated with the damping, $|\mathbf{T}_\alpha^\parallel| = |\alpha \mathbf{m}_{DW} \times \mathbf{T}_{DMI}| \sim \alpha T_{DMI}$, opposes \mathbf{T}_{DL} whereas its

normal component $\mathbf{T}_\alpha^\perp = \alpha \mathbf{m}_{DW} \times \mathbf{T}_{DL}$ adds up to \mathbf{T}_{DMI} (\mathbf{T}_α^\perp not shown for clarity). This induces the motion of the DW_{U-D} along the charge current flow. In the DMI + SOT mechanism (also referred to as DMI + \mathbf{T}_{DL} in the rest of this manuscript), the velocity of motion is given then by both \mathbf{T}_{DMI} and \mathbf{T}_{DL} .

In the DMI+ \mathbf{T}_{DL} mechanism, there is no Walker breakdown unlike STT-driven DWs. The DW velocity v_{DW} exhibits two regimes (**Figure I.20**). Firstly, at low current, v_{DW} increases linearly with J . In this regime, the DW core magnetization \mathbf{m}_{DW} has in general both x -component m_x (the component along the current direction also referred as $m_{||}$) and y -component m_y (the in-plane component orthogonal to the current flow also referred as m_\perp). Due to the presence of DMI, $|m_x| \gg |m_y|$ and m_x varies little. The variation of \mathbf{H}_{DL} is then promoted largely by the increase of J in this regime. Secondly, at high current, v_{DW} saturates as J keeps increasing. In this regime, the DW deviates from the Néel configuration: m_x decreases notably while m_y increases. Under sufficiently large J , the DW tends towards a quasi-Bloch configuration. As the magnitude of \mathbf{H}_{DL} scales with the product $J|m_x|$, for $J \rightarrow \infty$ and $|m_x| \rightarrow 0$, it is kept constant and v_{DW} saturates in this regime.

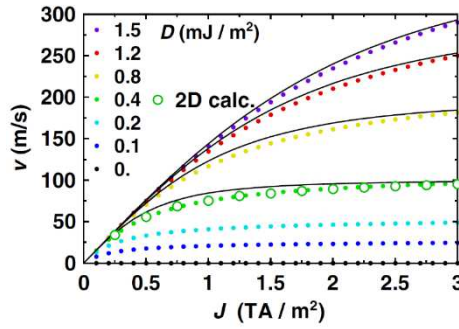


Figure I.20 Calculated DW velocity vs current density for various amplitudes of the DMI. The velocity was estimated while considering only the action of the damping-like torque. The lines depict the results obtained from 1D numerical model and are compared to calculation from the collective coordinate model (filled round symbols). The open symbols, for $D = 0.4 \text{ mJ.m}^{-2}$, correspond to 2D micromagnetic simulations. Figure extracted from [Thiaville et al. 2012].

Some theoretical works, by considering the case where $|H_{DMI}| \gg |H_K|$ (i.e. for homochiral Néel DWs) give an analytical expression for the DW velocity [Thiaville et al. 2012; Martinez et al. 2014]:

$$v_{DW} = \gamma_0 \Delta \frac{\pi}{2} \frac{H_{DMI}}{\sqrt{1 + \left(\frac{\alpha H_{DMI}}{H_{DL}}\right)^2}} \quad (\text{I.44})$$

We can deduce the above two mentioned regime of motion from this expression of DW velocity. At low current, we have $((\alpha H_{DMI}/H_{DL})^2 \gg 1)$ thus v_{DW} is limited by the damping-like torque (linear with J)

$$v_{DW} \approx \frac{\gamma_0 \Delta \pi}{\alpha} H_{DL} \quad (\text{I.45})$$

At large current, we have $((\alpha H_{DMI}/H_{DL})^2 \ll 1)$, v_{DW} becomes DMI-limited and saturates

$$v_{DW} \approx \gamma_0 \Delta \frac{\pi}{2} H_{DMI} \quad (\text{I.46})$$

We see that the stronger the DMI, the larger the current density needed to reach the saturation regime for v_{DW} . Using the DMI + \mathbf{T}_{DL} mechanism, we can then account for the large velocities of motion obtained in structures with large DMI [Miron, Moore, et al. 2011; Ryu et al. 2013] (cf. **Figure III.5.a** in chapter III).

Concerning the field-like term \mathbf{H}_{FL} , it acts equivalently to a transverse magnetic field that is in-plane and orthogonal to the current direction. It cannot induce on its own the displacement of a DW but it tailors its internal structure. Depending on its orientation, it either reduces or increases the in-plane component of \mathbf{m}_{DW} . This leads for the latter case to a decrease in v_{DW} and to an increase for

the former case [Boulle et al. 2013; Boulle et al. 2014; Jué 2013]. For both cases, v_{DW} versus the current density shows similar trend as the one obtained when only considering the action of T_{DL} . In Pt/Co/Pt structures, we have a negligible H_{FL} confirmed by various torque measurements [Drouard, 2014; Trifu, 2017]. In for Pt/Co/AlOx, there is a net H_{FL} but it is still smaller than the damping-like term [Garello et al., 2013] (torque-to-current ratios for T_{FL} and T_{DL} about -4.0 and +6.9 mT per 10^{11} A.m⁻², respectively). For these reasons, we neglect the role of the field-like torque in our Pt/Co based structures.

The interfacial DMI is then of great interest since it stabilizes the chiral Néel type DWs in PMA materials, essential for an efficient CIDWM. These chiral magnetic configurations are very promising candidates for spintronic devices in information processing applications. In particular, looking for systems with strong DMI has become a central focus for several groups thus the need for a precise estimation of DMI. In this context, we have several measurement techniques at our disposal to extract the sign and/or the magnitude of the DMI constant D .

I.5.5. Techniques to quantify DMI

In this section, we briefly introduce a panoply of techniques that allow the estimation of DMI. This will help to understand their strengths and weaknesses compared to methods based on the DW motion (CIDWM or FIDWM). The techniques, described below, are not a complete list of DMI-measurement techniques. A variety of other techniques are available in the literature.

I.5.5.1. Techniques not based on DW motion

I.5.5.1.1. Magnetic imaging techniques

One way to quantify the interfacial DMI is to image cycloidal spin spirals using imaging techniques such as Spin-Polarized Scanning Tunneling Microscopy (SP-STM). This makes it possible to determine with great precision the period of spin spirals and by comparison with the Density Functional Theory, the magnitude of the DMI can be estimated. This experimental technique was carried out on systems consisting of one or two atomic layers of ferromagnetic materials deposited on various heavy metals; W/Mn [Bode et al. 2007; Ferriani et al. 2008] , W(110)/Fe [Meckler et al. 2009] and Ir(111)/Fe [Heinze et al. 2011]. However, this technique requires ultra-high vacuum, low temperatures and grown structures with highly ordered interfaces. This is not suitable from an industrial and application point of view where room temperature applications based on materials grown by sputtering are preferred. This explains the need for more accessible techniques.

An alternative technique employs the scanning transmission X-ray microscopy measurements (STXM) [Woo et al., 2016; Litzius et al., 2017]. This technique allows probing the magnetic multidomain pattern of thin films. The constant D is estimated through the investigation of the stripe domains periodicity variation upon the application of an easy-axis magnetic field. The interplay between magnetic anisotropy, exchange interaction, dipolar interaction and DMI stabilizes the pattern of stripe domains. The periodicity of stripe domains as a function of the field is used to determine the DW energy σ_{DW} . The strength of DMI can then be derived from Eq. I.39. The disadvantage of this technique is that it only applies to systems with large $|D|$ and a relative thick ferromagnetic layers to induce the dendrite phase. It is not therefore a suitable technique to quantify DMI in a wide range of structures.

1.5.5.1.2. BLS measurements technique

The Brillouin light spectroscopy (BLS) technique is based on the inelastic Brillouin light scattering of an electromagnetic wave upon its interaction with spin waves propagating in the ferromagnetic layer following the Stokes process or the Anti-Stokes process [Cortés-Ortuño and Landeros, 2013]. The Stokes process consists in an incident light from a laser beam scattering with a negative shift in the frequency (it loses energy and a spin wave is created) whereas the Anti-Stokes process consists in a positive shift in the frequency (it gains energy and a spin wave is absorbed). With BLS spectra, we determine the difference Δf between the Stokes and Anti-Stokes frequencies. In the presence of DMI, Δf is equal to $\Delta f = D \cdot (2\gamma/\pi M_s) \cdot k$ with k the spin wave vector [Belmeguenai et al., 2015]. The linear regression of the variation of Δf as a function of k allows the estimation of the DMI constant D [Belmeguenai et al., 2015; Nembach et al., 2015]. Usually, the frequency resolution of the BLS technique is 0.1-0.2 GHz [Karnad et al., 2018]. This limits the detection in some structures with weak DMI. For example, [Karnad et al., 2018] reported a weak DMI ($D = +33 \mu\text{J}\cdot\text{m}^{-2}$) in the Ta (5 nm)/CoFeB (0.8 nm)/MgO (2 nm) structure measured by the technique of FIDWM (cf. section 1.5.5.2.2). Indeed, the analysis of BLS spectra yields $\Delta f \approx 0$ in this structure despite the existence of the interfacial DMI. In addition, the accuracy of BLS, in thick ferromagnetic films, is contested because asymmetric magnetic anisotropies at both FM interfaces can lead to similar asymmetry in the dispersion relation [Gladii et al. 2016]. It should be noted however that one of the advantages of the BLS technique is that it does not require to have the exact value of the exchange stiffness A_{ex} to extract D . This eliminates systematic errors resulting from uncertainty in A_{ex} . For instance, the estimation of D from DWs motion requires A_{ex} (cf. section 1.5.5.2).

1.5.5.1.3. Chiral DW depinning measurements

Another approach is to measure the efficiency of SOTs on the depinning mechanism of a DW as used in [Haazen et al., 2013] and later in other works [Je et al., 2017; D. Y. Kim, Min Ho Park, Park, Yu, Joo Sung Kim, Kim, et al., 2018]. This efficiency is defined as $\epsilon_{SOT} = \mu_0 \cdot dH_{depin}/dJ$ with H_{depin} the critical easy-axis magnetic field to depin a DW over the energy barriers. Below H_{depin} , a magnetic field H_z cannot propagate DWs. The action of the damping-like from SOTs is equivalent to an effective out-of-plane field H_{DL} (or H_{SOT}) on DWs. In the presence of a small external out-of-plane magnetic field, and at reasonably low current density J , H_{SOT} does not drive on its own DWs but alters significantly H_{depin} . The method consists in studying ϵ_{SOT} as a function of an external in-plane field H_x oriented normal to the DW. The dependence of H_{depin} on the current density J is sensitive to the internal structure of the DW, i.e. to the m_x component controlled by H_x (Eq I.34). ϵ_{SOT} saturates for a fully oriented DW along H_x and is equal to zero when the DW adopts a Bloch configuration. The in-plane field associated with $\epsilon_{SOT} = 0$ then gives the amplitude of $|H_{DMI}|$ and therefore that of the coefficient $|D|$ (Eq. I.38). Note that the low current density also helps to minimize contributions from Joule heating that would deviate H_{depin} from its linear behavior with respect to J .

1.5.5.2. Techniques based on DW motion

1.5.5.2.1. DMI measurement through asymmetric CIDWM

The investigation of CIDWM in the presence of an external in-plane field H_x was one of the first indirect experimental techniques used to evidence DMI in PMA materials [Ryu et al. 2013;

[Emori et al. 2013]. The dynamics of homochiral Néel walls are tuned by the interplay between \mathbf{H}_{DMI} and \mathbf{H}_x . When \mathbf{H}_x is parallel (antiparallel) to \mathbf{H}_{DMI} , the velocity of a DW increases (decreases). The application of \mathbf{H}_x results in an asymmetric motion between DWs with opposite chiralities, i.e. for up/down (DW_{U-D}) and down/up (DW_{D-U}) with $v_{UD}(J, H_x) = v_{DU}(J, -H_x)$ (with v_{UD} and v_{DU} the velocities of DW_{U-D} and DW_{D-U}, respectively). The observation of such an effect is characteristic of the presence of an interfacial DMI in the structure. The monotonic increase or decrease of v_{DW} relative to the orientation of \mathbf{H}_x indicates the sign of D (the direction of chirality). In addition, the in-plane field modulates the m_x component and transforms the DW into a Bloch wall ($m_x = 0$) for a certain amplitude of \mathbf{H}_x . The action of \mathbf{T}_{DL} is then zero so the current no longer propagates the DW. By further increasing \mathbf{H}_x , m_x changes sign and the DW starts moving in the opposite direction. The field, at which $v_{DW} = 0$, is the field that fully compensates \mathbf{H}_{DMI} within the DW. The value of $|D|$ can then be extracted from the amplitude of \mathbf{H}_x by Eq. I.38.

In the presence of \mathbf{H}_x and at large current, in the steady-state regime of motion, according to Eq. I.46, v_{DW} can be expressed as:

$$v_{DW} \approx \gamma_0 \Delta \frac{\pi}{2} (H_{DMI} + H_x) \quad (\text{I.47})$$

This gives a linear dependence of v_{DW} as a function of \mathbf{H}_x . The estimation of H_{DMI} is then straightforward by taking the intercept of the curve with the horizontal axis (Figure I.21.a). Note that v_{DW} is expected to saturate for large amplitudes of \mathbf{H}_x because \mathbf{m}_{DW} then aligns completely parallel to \mathbf{H}_x .

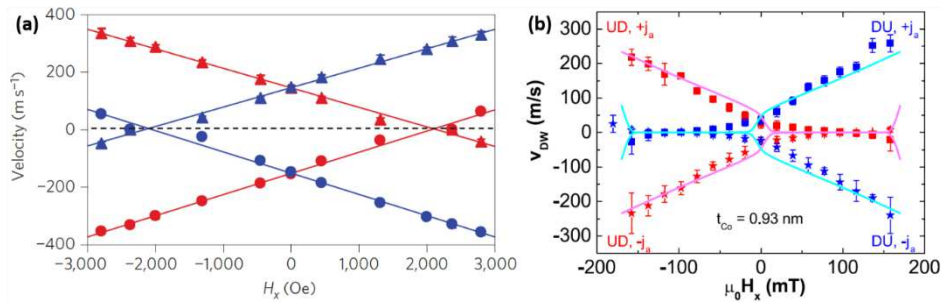


Figure I.21 Current-induced DW velocity v_{DW} as a function of \mathbf{H}_x . Curves correspond to DW_{U-D} (red symbols) and DW_{D-U} (blue symbols). (a) Pt (1.5)/Co (0.3)/Ni (0.7)/Co (0.15)/TaN (5) and (b) Pt (4)/Co (0.93)/AlOx (2). All thicknesses are in nm. The triangular (circular) symbols correspond to a positive (negative) current in (a). The squares (stars) correspond to a positive (negative) current in (b). The current density in (a) is $\sim 1.5 \cdot 10^{12} \text{ A.m}^{-2}$, corresponding to a steady-state motion at large current, whereas it is $\sim 8.7 \cdot 10^{12} \text{ A.m}^{-2}$ characteristic of a creep regime of motion in (b). (a) extracted from [Ryu et al. 2013] and (b) from [Lo Conte et al. 2017].

The change in the DW direction of motion for $\mathbf{H}_x = -\mathbf{H}_{DMI}$ can be hindered by pinning [Vaňatka et al. 2015; Lo Conte et al. 2017]. Prior to changing its direction of motion, the DW remains pinned for a range of \mathbf{H}_x (Figure I.21.b). [Lo Conte et al. 2017] expressed this range as $[-H_{DMI} - \Delta H_x^{dep}, -H_{DMI} + \Delta H_x^{dep}]$. H_{DMI} is then extracted by considering the exact stop field as the center of the observed pinning ranges of \mathbf{H}_x . This estimation method can involve considerable uncertainty. In addition, [Lo Conte et al. 2017] observed that in structures with a significant DW pinning, it is not possible to reverse the DW direction of motion. In this case, the estimation of DMI becomes very difficult from CIDWM measurements.

Furthermore, neglecting other critical parameters such as the DW tilt [Boulle et al. 2013; Martinez et al. 2014], DMI-imposed boundary conditions in wires [Rohart & Thiaville 2013], Joule heating in data analysis may lead to an incorrect estimation of the amplitude of DMI. For these reasons, the straightforward estimation of DMI from CIDWM in the presence of \mathbf{H}_x should be taken with caution. In order to reduce the extent of the above-mentioned complexification, we resort to FIDWM in unpatterned magnetic films; the study of asymmetric expansion of magnetic domains.

1.5.5.2.2. DMI measurement through asymmetric FIDWM

This technique is one of the most widely used to verify the presence and to estimate DMI. One of its main advantages is that we get rid of any current-induced contributions to the dynamics of DWs that could come from SHE and/or Rashba effect. These artifacts make the analysis of the intrinsic role of DMI more complex. Actually, a recent letter [Karnad et al. 2018] evidenced a DMI-component generated by the injection of the electric current. In addition, it is an appropriate technique for films since it avoids lithography processes, which makes it easier and faster to implement.

The asymmetric FIDWM experiment consists of an out-of-plan field \mathbf{H}_z that drives the DWs in the presence of a bias field \mathbf{H}_x applied parallel to the film plane. Each DW experiences a different velocity of propagation along the direction of \mathbf{H}_x , shown in **Figure I.22**. A magnetic domain, initially prepared with a circular shape, becomes oval and elongates in the direction of \mathbf{H}_x . [Kabanov et al. 2010] are among the first to have reported this effect in PMA materials. As in the CIDWM, the asymmetric motion results from the symmetry breaking between chiral DWs by \mathbf{H}_x . Without \mathbf{H}_x , there is a rotational symmetry with respect to the normal of the film plane for the circular domain so that it expands symmetrically under \mathbf{H}_z (**Figure I.22.a**). \mathbf{H}_x breaks the rotational symmetry and the effective total in-plane field varies across the domain and its boundaries due to \mathbf{H}_{DMI} resulting in the anisotropic expansion. For Bloch DWs, the action of \mathbf{H}_x is symmetric between the two DWs lying normal to \mathbf{H}_x so that no anisotropic motion is induced. The presence (respect. the absence) of an asymmetric DW motion in FIDWM would then be an indication of the presence (respect. the absence) of a DMI in the structure.

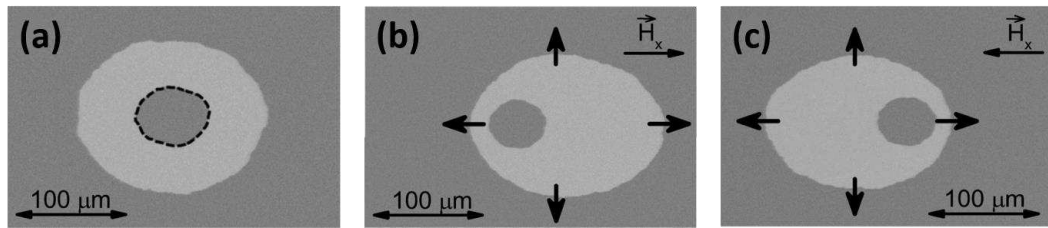


Figure I.22 Asymmetric expansion of a magnetic domain in the presence of an in-plane magnetic field. Differential Magneto-Optical Kerr Effect microscopy images of a magnetic domain expansion driven by \mathbf{H}_z , in the absence of an in-plane field (a), under a positive (b) and a negative \mathbf{H}_x (c). The dashed line in (a) indicates the initial position of the DW corresponding to a down domain. The white contrast represents the area swept by DWs during the expansion of the domain. The black arrows represent the equilibrium orientation of DW internal magnetic moment induced by DMI. This indicates a left-handed chirality. The magnetic domain expansion is symmetric in (a) and asymmetric in (b) and (c). In the presence of \mathbf{H}_x , the DWs on the left and the right move at different velocities. The inversion of the orientation of \mathbf{H}_x reverses the asymmetry of the expansion. Adapted from [Hrabec et al. 2014].

The determination of DMI by FIDWM consists in measuring the DW speed v_{DW} as a function of the applied \mathbf{H}_x . For a circular magnetic domain, v_{DW} is obtained by measuring the displacement at the most right and left locations of the domain where DWs are normal to \mathbf{H}_x . In the flow regime of motion, the mobility of the DW depends on whether we are in the steady-state regime or in the precessional regime. According to Eqs I.19 and I.20, the parameter sensitive to \mathbf{H}_x is the DW width Δ . v_{DW} increases for an increase of Δ and vice versa in the flow regime of motion [Vaňatka et al. 2015]. Δ is the narrowest in PMA materials occurs for a Bloch configuration when \mathbf{H}_x opposes \mathbf{H}_{DMI} . Therefore, the minimum of the v_{DW} vs \mathbf{H}_x curve gives an estimate of the strength of the DMI. However, it is difficult to reach the flow regime of motion as it is often hidden by the creep regime. In addition, the depinning of DWs in sputtered materials usually requires sub-microsecond pulses and/or larger magnetic fields (of the order of 100 mT). It is quite experimentally challenging to generate such magnetic fields in a uniform way in order to investigate the DW motion. Therefore, as proposed in the pioneer work of [Je et al. 2013], the creep regime itself can be used to determine the strength of DMI. In this regime, the dependence of v_{DW} on \mathbf{H}_x under a constant \mathbf{H}_z can be written as follows (according to Eq. I.21):

$$v_{DW}(H_x) = v_0(H_x) \exp[-\epsilon(H_x) \cdot H_z^{-1/4}] \quad (\text{I.48})$$

$\epsilon(H_x)$ denotes the variation of the energetic landscape of a DW upon applying an in-plane field. This term includes several parameters that govern the thermally activated regime of motion and characterize the DW: the thermal fluctuation $k_B T$, ξ the correlation length of the disorder potential, u_c the roughness of the DW segment, Γ the pinning strength, M_S and σ_{DW} the DW energy density per unit area. By assuming that these parameters vary little with \mathbf{H}_x , except σ_{DW} , we write ϵ as:

$$\epsilon(H_x) \propto \sigma_{DW}^{1/4} = \epsilon(0) \cdot \left[\frac{\sigma_{DW}(H_x)}{\sigma_{DW}(0)} \right]^{1/4} \quad (\text{I.49})$$

where $\epsilon(0)$ and $\sigma_{DW}(0)$ denote respectively the values of ϵ and σ_{DW} at $\mathbf{H}_x = 0$. According to the collective coordinates model of a DW [Heide, Bihlmayer and Blügel, 2008; Thiaville et al., 2012], σ_{DW} is given by:

$$\sigma_{DW}(H_x) = \sigma_0 + 2K\Delta \cos^2(\phi) - \pi\Delta M_S(H_x + H_{DMI}) \cos(\phi) \quad (\text{I.50})$$

with σ_0 the DW energy density of a Bloch wall and K the Bloch DW magnetostatic ‘shape’ anisotropy constant. From the minimization condition $\partial\sigma_{DW}/\partial\phi = 0$, considering an equilibrium azimuthal angle ϕ_{eq} during the motion of DW, the DW energy density as a function of \mathbf{H}_x writes:

$$\sigma_{DW}(H_x) = \begin{cases} \sigma_0 - \pi^2\Delta M_S^2 (H_x + H_{DMI})^2/8K & \text{for } |H_x + H_{DMI}| < 4K/\pi M_S \\ \sigma_0 + 2K\Delta - \pi\Delta M_S |H_x + H_{DMI}| & \text{otherwise} \end{cases} \quad (\text{I.51})$$

The top expression in Eq. **I.51** corresponds to the case where the combination of \mathbf{H}_x and \mathbf{H}_{DMI} does not fully transform the DW from a Bloch to a Néel configuration whereas the bottom expression is for a Néel wall whose internal magnetic moment aligns parallel to \mathbf{H}_x .

The open question at this stage is whether the in-plane field modifies most σ_{DW} , the prefactor v_0 or both in the creep regime of motion. By considering equal DW velocities for $(\mathbf{H}_z, \mathbf{H}_x \neq 0)$ and $(\mathbf{H}_z^*, \mathbf{H}_x = 0)$, [Je et al. 2013] assume that v_0 does not depend on \mathbf{H}_x and then obtain:

$$\frac{H_z}{H_z^*} (v_{DW}) = \left[\frac{\epsilon(H_x)}{\epsilon(0)} \right]^{-1/4} = \frac{\sigma_{DW}(H_x)}{\sigma_{DW}(0)} \quad (\text{I.52})$$

To check the validity of this approach, [Je et al. 2013] investigated the anisotropic expansion of magnetic domains in ultrathin Co layers (Pt/Co (0.3 nm)/Pt). The analysis of the two-dimensional contour map $v_{DW}(H_z, H_x)$ for a DW_{U-D} (**Figure I.23.a**) shows an axis of inversion symmetry, at $H_x \approx -26.5$ mT (dashed vertical line), for all equi-velocity contours of v_{DW} (highlighted by black solid lines). This nonzero offset for the axis of symmetry comes from the DMI since the DW experiences a total longitudinal magnetic field equal to $(\mathbf{H}_x + \mathbf{H}_{DMI})$. We then obtain a direct measurement of \mathbf{H}_{DMI} in the structure, $\mathbf{H}_{DMI} = +26.5$ mT (corresponds to right-handed chirality). In **Figure I.23.b**, the equi-velocity contours allow to obtain different curves of $[H_z/H_z^*]$ as a function of \mathbf{H}_x . All the $[H_z/H_z^*]$ plots collapse onto a single curve regardless of the magnitude of v_{DW} suggesting that all values of $[H_z/H_z^*]$ follow a unique function of \mathbf{H}_x . This therefore confirms the assumption that led to the equation **(I.52)**. $\epsilon(H_x)$ can then be obtained experimentally. Its variation as a function of \mathbf{H}_x is shown in **Figure I.23.c**. It allows to verify the creep scaling law in the presence of \mathbf{H}_x by plotting $\ln(v_{DW})$ vs $\epsilon(H_x) \cdot H_z^{-1/4}$ (the inset of **Figure I.23.c**). All the plots of $\ln(v_{DW})$ fall onto a single line with a slope equal to -1 . It is a confirmation that the creep scaling law applies for the FIDWM in the presence of \mathbf{H}_x and that \mathbf{H}_x does not induce an effect on the prefactor v_0 in the studied structure. From all these observations, [Je et al. 2013] conclude that the anisotropic magnetic domain expansion in the presence of \mathbf{H}_x in the creep regime is governed by the asymmetric modification σ_{DW} for the different DWs.

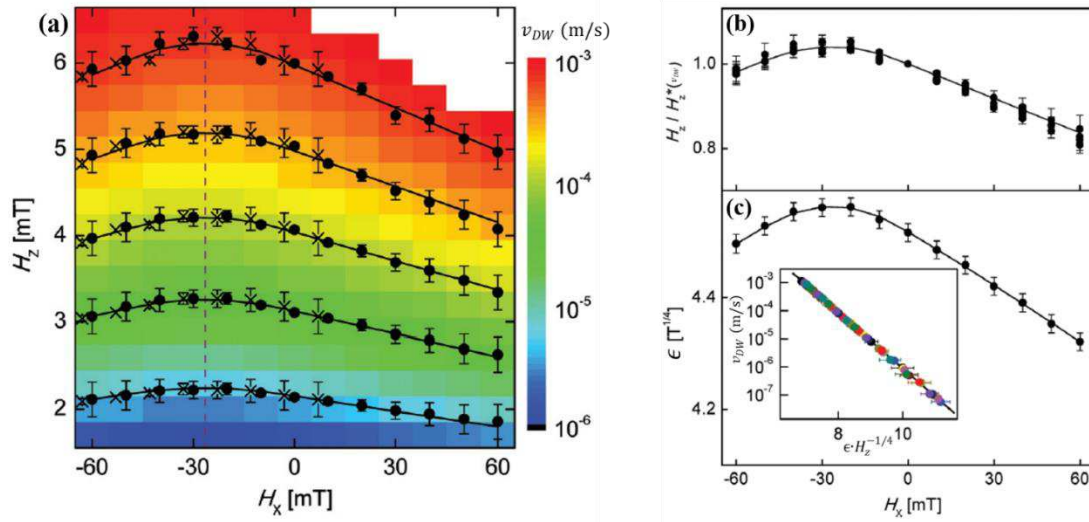


Figure I.23 DW motion in the creep regime under H_z and in the presence of H_x . (a) Two dimensional equi-velocity contour map of v_{DW} as a function of H_x and H_z in Pt (2.5 nm)/Co (0.3 nm)/Pt (1.5 nm). (b) $[H_z/H_z^*](v_{DW})$ and (c) the energetic term ϵ as a function of H_x . Each color of the scale bar to the right of (a) corresponds to a magnitude of v_{DW} . The black solid lines are the best fit for the equi-velocity contours using Eq. 1.48 and the dashed vertical line represents the symmetry axis $H_x = -H_{DMI}$. The best fit (the black solid line in (b)) and the determination of $\epsilon(0)$ (as the slope of $\ln[v_{DW}(0)]$ vs $H_z^{-1/4}$) help extracting $\epsilon(H_x)$ that is plotted in (c). The inset in (c) shows the $\ln(v_{DW})$ vs $\epsilon(H_x) \cdot H_z^{-1/4}$ for various applied H_x (each color corresponds to a value of H_x). Data fall into a single curve confirming that the prefactor v_0 does not change with H_x ($v_0 = 8.4 \pm 0.4 \cdot 10^3$ m.s $^{-1}$). The black solid lines in (b) and (c) were obtained by the best fit using Eq. 1.49 and Eq. 1.51. Extracted and adapted from [Je et al. 2013].

In the model developed by [Je et al. 2013], the expected features of the variation of v_{DW} as a function of the applied in-plane field H_x , at a constant H_z , are depicted in **Figure I.24** below. Several features are considered as fingerprints of a DMI-induced asymmetric DW motion. The v_{DW} curves have a parabolic shape and overlap by an offset shift on the H_x -axis. This offset is equal to $2|H_{DMI}|$. In fact, each curve exhibits a minimum of the velocity when H_x compensates for the local H_{DMI} . This gives the exact amplitude of H_{DMI} allowing the extraction of the sign and the strength of the DMI constant D . This model has been used as a basis for many investigations of DMI via FIDWM in recent years [Hrabec et al. 2014; Petit et al. 2015; Vaňatka et al. 2015; Soucaille et al. 2016; Pham et al. 2016; Khan et al. 2016; Wells et al. 2017; Quinsat et al. 2017; Cao et al. 2017; Shepley et al. 2018; Kuświk et al. 2018; Karnad et al. 2018; Shahbazi et al. 2019].

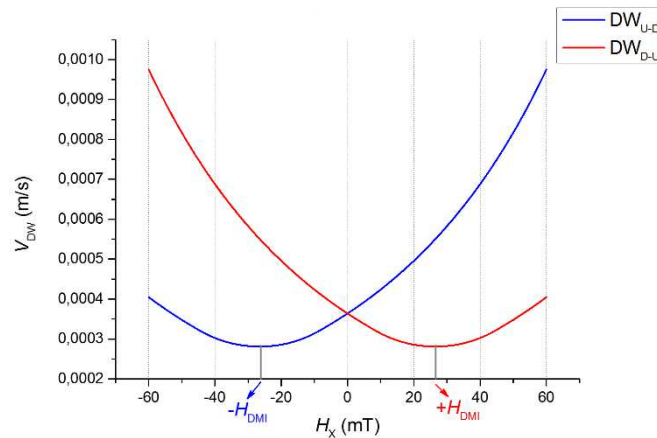


Figure I.24 The curve of the DW velocity v_{DW} as a function of H_x under a constant H_z in the presence of DMI. v_{DW} is calculated for DW_{U-D} (in blue) and DW_{D-U} (in red) in the creep regime motion according to the model developed by [Je et al. 2013]. The values of v_{DW} are calculated at $H_z = +5$ mT according to Eqs. 1.48, 1.49 and 1.51 by taken the magnetic parameters corresponding to the Pt/Co/Pt from [Metaxas et al. 2007; Je et al. 2013]. The curves exhibit a parabolic shape and overlap by shifting them horizontally. These features are fingerprints of DMI-induced asymmetric FIDWM in SIA materials. Numerous studies of DMI are based on the similarity of the v_{DW} vs H_x curves with these features. The minimum of the curve allows to derive the amplitude of DMI.

However, several reports indicate anisotropic magnetic domain expansion in SIA materials that do not follow the model proposed by [Je et al., 2013]. [Lavrijsen et al., 2015] reported that the

v_{DW} vs H_x curves in Pt (4 nm)/Co (0.6 nm)/Pt (4 nm) do not exhibit the exact expected features as shown in **Figure I.24**. Variations in the DW velocity cannot be accounted for by considering only the modification of σ_{DW} by H_x . In addition, [Lavrijsen et al. 2015] use different growth conditions to induce a variation in the interfaces in different stacks of Pt/Co/Pt. This was confirmed by the measurement of a variable uniaxial magnetic anisotropy constant K_u . On the contrary, the estimate of the DMI from the minimum of the curves did give any significant variation as expected since the DMI has an interfacial origin.

Another example was reported by [Vaňatka et al. 2015] for Pt (5 nm)/Co (1 nm)/GdOx samples where the v_{DW} curves show a maximum rather than a minimum making the estimation of DMI difficult in the creep regime. [Vaňatka et al. 2015] have recovered the expected variations of v_{DW} in the limit of the flow regime of motion ($v_{DW} \gg 1 \text{ m.s}^{-1}$). In fact, additional contributions from the in-plane field H_x can play a role in the variation of v_{DW} . [Jué et al. 2016] needed to consider the variation in Thiele DW width Δ_T to account for the behavior of the DW mobility with H_x in the Pt (3 nm)/Co (0.6 nm)/AlOx (2 nm) structure. [Balk et al. 2017], on their side, proposed a modification of the pinning potential of a DW by H_x in order to explain the obtained peak of v_{DW} at $H_x = 0$ in the Pt (35 nm)/Co (0.8 nm)/Pt (1.7 nm) structure. This velocity peak is not expected according to the model of [Je et al. 2013]. An extensive study of the Pt/[Co (0.2 nm)/Ni (0.6 nm)]₂/Co (0.2 nm)/Ta/TaN structure by the group of V. Sokalski also confirmed the limitations of this model, as it cannot account for the inversion of the asymmetry of the magnetic domain growth observed at larger H_x [Lau et al. 2016]. The use of the DW energy elastic band model has allowed some of these limitations to be taken into account [Pellegren et al. 2017]. However, a more recent study in which Iridium was inserted between the bottom Pt layer and the FM layer showed that even the elastic DW energy model does not explain all the trends of v_{DW} [Lau et al. 2018].

All of these reports suggest that the simple model based on σ_{DW} has to be used with extreme caution for the estimation of the DMI amplitude. Actually, [D.-Y. Kim, Park, Park, Kim, Yune-Seok Nam, et al. 2018] suggested that the scheme of [Je et al. 2013] is better applicable in ultrathin FM layers ($t_{FM} \leq 0.4 \text{ nm}$) where the DMI-induced asymmetry in σ_{DW} dominates the anisotropic magnetic domain expansion. Nevertheless, the extreme caution is even more justified as recent reports indicate major contradictions in the determination of DMI within the same structure when using the CIDWM and/or FIDWM measurements [Vaňatka et al. 2015; Karnad et al. 2018]. All these deviations in the DW motion can be attributed to additional chirality-dependent mechanisms. One of these mechanisms, recently proposed, suggests an asymmetric dissipation between different DWs upon the application of H_x . It is called the Chiral Damping mechanism.

I.6. Chiral Damping in DWs

DMI is a well-established phenomenon that originates from SOC and is considered to explain the chiral (or asymmetric) DW dynamics with \mathbf{H}_x in magnetic materials with SIA. So far, no other mechanism has been proposed to contribute to such peculiar motion of DWs until the recent proposal of [Jué et al. 2015]. [Jué et al. 2015] experimentally evidenced, by studying the FIDWM in a series of sputtered Pt (3 nm)/Co (0.6 nm)/Pt (t) structures ($t = 1.56 - 7$ nm), a new mechanism induced by SIA (as DMI). This new mechanism is the Chiral Damping mechanism that also induces an asymmetric DW motion.

I.6.1. The experimental evidence of Chiral Damping

I.6.1.1. The failure of the DMI-induced asymmetry mechanism

Qualitatively, the observation of the growth of a magnetic domain under the combination of \mathbf{H}_z and \mathbf{H}_x is similar to that reported by [Je et al. 2013] for fairly similar Pt/Co/Pt structures (although the Co layer is much thinner, 0.3 nm in [Je et al. 2013]). DWs, moving in the direction of \mathbf{H}_x , have different velocities with a faster DW_{U-D} when $H_x > 0$ suggesting a right-handed chirality induced by DMI. On the contrary, as can be seen from the v_{DW} curves in **Figure I.25**, it is not possible to apply the model developed by [Je et al. 2013] in order to evidence and extract the DMI field \mathbf{H}_{DMI} . The obtained v_{DW} vs H_x curves deviate from the parabolic shape expected in a DMI-based model (**Figure I.24**). \mathbf{H}_{DMI} should act as a bias field that shifts the curves along the horizontal axis. However, it is impossible to overlap the two curves by means of any lateral shifting and this for the entire range of H_z (8 - 20 mT) investigated.

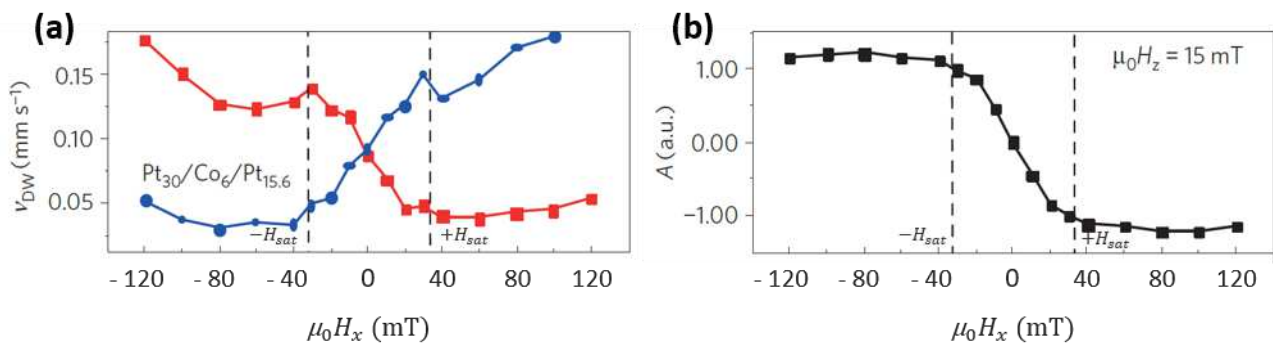


Figure I.25 Chiral Damping induced asymmetric FIDWM in the presence of an in-plane magnetic field. (a) The measured DW velocity as a function of \mathbf{H}_x . The blue (red) symbols correspond to DW_{U-D} (DW_{D-U}). (b) The indicator A of the DW velocity asymmetry as a function of \mathbf{H}_x . The dashed vertical lines indicate the characteristic saturation field H_{sat} ($|H_{sat}| \approx 40$ mT). The asymmetry A varies monotonically and then saturates at $\pm H_{sat}$. A change in the slope of v_{DW} is also observed at H_{sat} for both DWs. The data shown correspond to the measurement made at $H_z = 15$ mT for the Pt (3 nm)/Co (0.6 nm)/Pt (1.56 nm) structure. Extracted and adapted from [Jué et al. 2015].

The raw v_{DW} vs H_x curves are the outcome of symmetric and asymmetric contributions from \mathbf{H}_x . The symmetric contribution is the same for both DWs (for example \mathbf{H}_x modifies the magnetic anisotropy and the pinning landscape). The asymmetric contribution, on the other hand, originates only from SIA and is responsible for the chiral DW motion. It is then necessary to get rid of the symmetric contribution to study the asymmetry of v_{DW} in a straightforward and quantitative manner. This is made possible by the introduction of an indicator A which is the anti-symmetric component of v_{DW} :

$$A = \frac{v_{DU} - v_{UD}}{(v_{UD} + v_{DU})/2} \quad (\text{I.53})$$

with v_{DU} and v_{UD} the velocities of the DW_{D-U} and the DW_{U-D} , respectively. The variation of A is practically the same for any applied H_z . It decreases monotonically between its two symmetric saturation values ($|A_{sat}| \approx 1$ in **Figure I.25.b**) and saturates around $|H_{sat}| \approx 40$ mT. This suggests that the mechanism behind the chiral DW motion saturates at this characteristic magnetic field. In fact, by analyzing thoroughly the raw curves of v_{DW} , it is clear that H_{sat} is relevant for both DWs. They show a change in the slope at $\pm H_{sat}$ for both DWs. According to the DMI-induced asymmetry mechanism, one could expect that only a single DW would exhibit a feature at H_{sat} , due to the local H_{DMI} . The other DW would have already saturated at a smaller amplitude of H_x . Therefore, [Jué et al. 2015] concluded that H_{sat} cannot be identified with H_{DMI} in their samples. In the absence or for a low DMI, H_{sat} could be directly related to the DW demagnetizing field H_K . When $|H_x| > |H_K|$, the DW core magnetization m_{DW} saturates parallel to H_x for both DWs (as depicted in **Figure I.14.c**).

From these observations, the DMI-induced asymmetry mechanism, developed by [Je et al. 2013], fails to explain the anisotropic expansion of magnetic domains. This is an indication that there should be another dominant SIA-induced mechanism, different from DMI, that governs the chiral DW dynamics in Pt (3 nm)/Co (0.6 nm)/Pt (t).

I.6.1.2. The proposal of chiral dissipation in FIDWM

FIDWM can be described by the LLG equation (Eq. I.12) which has two terms to describe the magnetization dynamics. The first term that includes H_{eff} is the energy term or the conservative term. The second term is a dissipation term that depends on the damping rate of the magnetization. Therefore, the asymmetry of the DW motion is either due to a conservative or a dissipative mechanism or both. The conservative mechanism producing the asymmetry is the one described above (cf. section I.5.5.2.2) in which DMI modifies H_{eff} differently for the two DWs, DW_{U-D} and DW_{D-U} . An asymmetry due to a dissipative mechanism means that the difference between DW velocities is due to a difference in the damping of the two DWs, hence the hypothesis of the Chiral Damping mechanism. To examine this hypothesis, the different contributions to the DW motion need to be separated. As the motion takes place in the creep regime (v_{DW} in the range of 10^{-4} m.s $^{-1}$ in **Figure I.25.a**), the scaling law of v_{DW} (Eq. I.24) is well suited for this investigation.

By plotting $\ln(v_{DW})$ vs $H_z^{-1/4}$ (**Figure I.26**), the slope of the linear variation gives the energy term and the intercept $\ln(d_0 f_0)$ contains information on the damping α . As d_0 (the average distance between two pinning centers) is related to the crystallographic order of the structure, a modification of α is most likely reflected in the attempt frequency f_0 . In principle, both energy and damping can contribute to f_0 [Ferré et al. 2013]. However, we will see in the following that the effect, here, comes exclusively from the damping parameter. In fact, there is not an established mechanism linking α to f_0 . [Jué et al. 2015] conducted 2D micromagnetic simulations of the depinning of a DW trapped by a single defect. By calculating the DW depinning time for different damping values and with the same barrier height, they found that f_0 is proportional to the inverse of the damping α ($f_0 \propto 1/\alpha$). Under this perspective, the verification of the origin of the asymmetry relies on the comparison of the $\ln(v_{DW})$ vs $H_z^{-1/4}$ plots, at a constant H_x , between DW_{U-D} and DW_{D-U} . If H_x varies the energy of a DW, it causes a change in the slope as well as a lateral shift (the critical field H_c changes as well). In contrast, if H_x changes f_0 , there is no variation of the slope of the curve but only a vertical shift due to a different intercept.

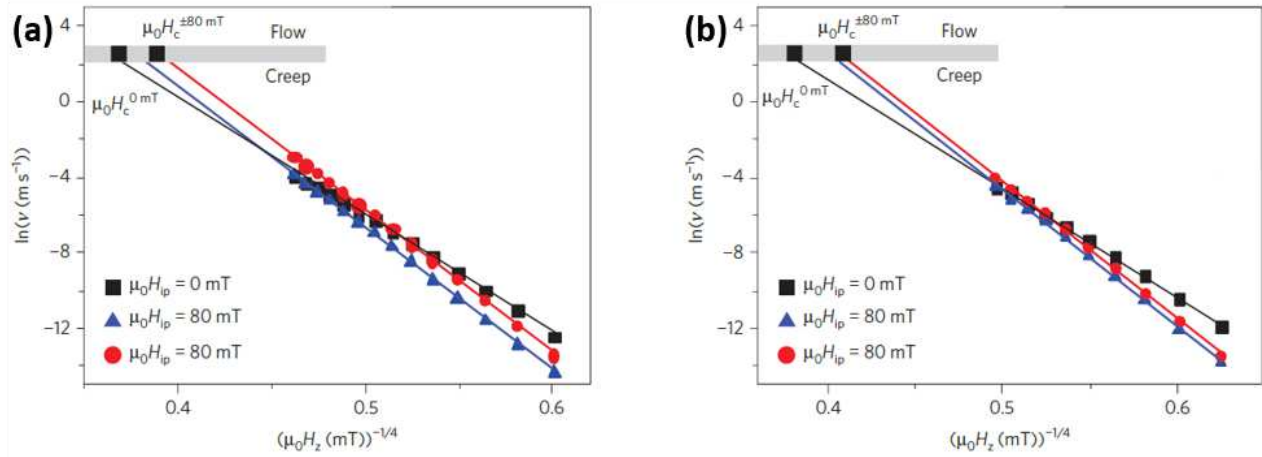


Figure I.26 Effect of Chiral Damping on creep scaling law between different DWs. Plots of creep scaling law for v_{UD} (red symbols) and v_{DU} (blue symbols) for (a) Pt (3)/Co (0.6)/Pt (1.56) and (b) Pt (3)/Co (0.6)/Pt (3). All thicknesses are in nm. Here, \mathbf{H}_{ip} refers to \mathbf{H}_x employed used in the main text to designate the in-plane field normal to the DW. The measurements were performed at $H_{ip} = 80$ mT. The solid lines are linear fits of the data. The grey horizontal line depicts the expected transition from the creep regime to the flow regime of motion at a critical field H_c , which is indicated by the black square. The black symbols are the data in the absence of \mathbf{H}_{ip} in order to highlight the modification in the energy term of the scaling law induced by a non-zero in-plane field. The curves of DW_{U-D} and DW_{D-U} exhibit a change in the slope and a lateral shift due to the change of H_c with respect to the case $\mathbf{H}_{ip} = 0$. The curves of the two DWs are parallel indicating an identical energy term at $\mathbf{H}_{ip} = 80$ mT. The difference between v_{UD} and v_{DU} comes from a vertical shift due to change of the intercept $\ln(d_0 f_0)$. Extracted and adapted from [Jué et al. 2015].

Figure I.25 shows measurements of v_{DW} for different values of H_z at a constant $H_x = +80$ mT for Pt (3 nm)/Co (0.6 nm)/ Pt (1.56 nm) and Pt (3 nm)/Co (0.6 nm)/Pt (3 nm). It is clear that the curves for the two DWs are different by a vertical shift and that they exhibit the same slope. The energies of the two DWs are then similar. Consequently, the difference in the motion results solely from a difference in the attempt frequency f_0 that is accounted for by a difference in the damping α . Moreover, the asymmetric component A is independent of the value of H_z which modifies the velocity v_{DW} confirming that the origin of the asymmetry is not related to the energy of the DW but to the damping (not shown here, cf. [Jué et al., 2015]).

By examining the creep scaling law, [Jué et al. 2015] suggested experimentally that the asymmetric DW motion in FIDWM in Pt/Co/Pt structures is due to a ‘‘Chiral Damping’’ mechanism. A DMI-induced chirality is either absent or weak in these structures compared to this new mechanism when driving DWs by \mathbf{H}_z in a bias field \mathbf{H}_x . This suggests that DWs are mostly of the Bloch configuration (possibly with a small Néel component as DMI cannot be ruled out completely).

I.6.1.3. A possible description of the Chiral Damping

The Chiral Damping mechanism means that the damping of the DW_{U-D} is different from that of the DW_{D-U} . As discussed above, this mechanism saturates for both DWs at the same $H_x = H_{sat}$. This value of H_x is similar to the one required to overcome the demagnetizing field of the DW and change the orientation of \mathbf{m}_{DW} to move from a Bloch configuration to a Néel configuration under the action of an \mathbf{H}_x field. In addition, the damping should increase or decrease depending on the DW chirality, i.e. the direction of rotation of the magnetization when moving from one domain to another. This ensures the asymmetry in the dynamics between the two DWs. In fact, the direction of rotation of a DW is given by the gradient of the out-of-plane component of the magnetization ∇m_z . By definition, this gradient reverses its orientation from the DW_{U-D} to the DW_{D-U} . Following this, a possible chiral component of the damping would depend on the orientation of \mathbf{m}_{DW} with respect to ∇m_z as proposed by [Jué et al. 2015]. The total damping for a DW can then be described mathematically as:

$$\alpha \propto \alpha_0 + \alpha_c \lambda_{ex} (\mathbf{m}_{DW} \cdot \nabla m_z) \quad (\text{I.54})$$

with α_c the coefficient of the chiral component of the damping and λ_{ex} a characteristic length parameter. α_0 includes the intrinsic isotropic damping of the ferromagnetic layer. It offsets the total damping to positive values preventing the unphysical behavior that is a negative dissipation in the system. In principle, α_0 and α_c should depend on the absolute value of the magnetization gradient such that the following condition is always satisfied: $\alpha_0 > \alpha_c \lambda_{ex} |\nabla m_z|$. It is then possible to extract the amount of the Chiral Damping contribution α'_c by adopting Eq. I.54 for the total damping. By expressing the chiral Damping contribution as $\alpha'_c = \alpha_c (\lambda_{ex} |\nabla m_z|)$, the anti-symmetric component A above the saturation can be expressed as:

$$\frac{|A_{sat}|}{2} = \frac{\alpha'_c}{\alpha_0} \quad (\text{I.55})$$

[Jué et al. 2015] found that, approximately, the chiral damping reaches up to between 50% and 60% of the intrinsic damping. For the Pt (3 nm)/Co (0.6 nm)/Pt (1.56 nm) stack, $\alpha_0 = 0.5$ [Miron 2009] which allows to estimate $\alpha_c = 0.3$.

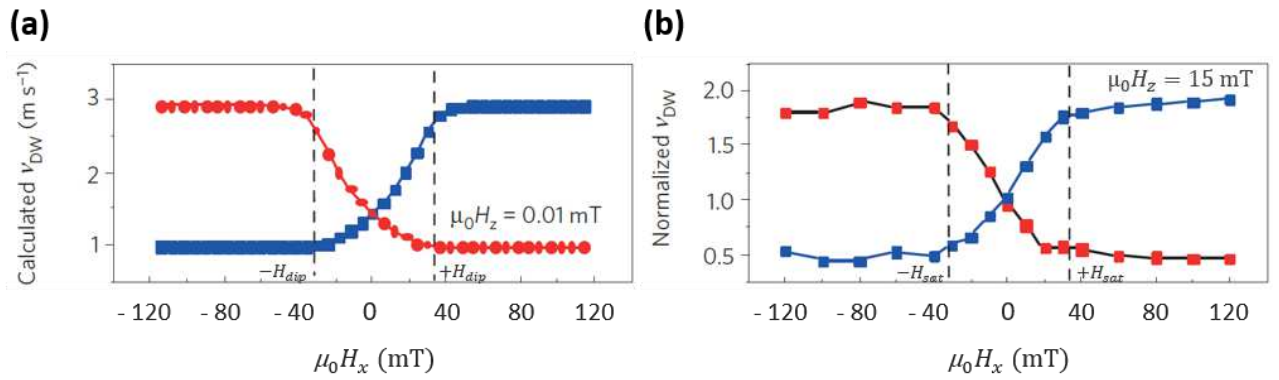


Figure I.27 Calculation of the DW velocity in FIDWM in the presence of \mathbf{H}_x according to the Chiral Damping mechanism. (a) DW velocity calculated by a numerical collective coordinate model at $T = 0$ K and without pinning. The Chiral Damping is defined according to Eq. I.56. The values used in the calculation are: $\alpha_0 = 0.6$, $\alpha_c = 0.3$, $\Delta = 5$ nm, $H_K = 35$ mT and $H_z = 0.01$ mT. (b) The velocities v_{UD} and v_{DU} are normalized to the average velocity at $H_z = 15$ mT in Pt (3 nm)/Co (0.6 nm)/Pt (1.56 nm). These relative velocities have a behavior comparable to that of the anti-symmetric component A and both saturate at \mathbf{H}_{sat} . In (a) and (b), the blue and red curves correspond to DW_{U-D} and DW_{D-U} , respectively. Extracted and adapted from [Jué et al. 2015].

To demonstrate the action of the proposed description of the Chiral Damping, [Jué et al. 2015] studied v_{DW} using a numerical collective coordinate model (at zero temperature and without pinning). This model does not include explicitly $|\nabla m_z|$. It is assumed as a constant, thus $\alpha'_c = \alpha_c$ is constant as well. In principle, $|\nabla m_z|$ is not constant as \mathbf{H}_x changes the DW width. Since the velocities are calculated for DWs moving in the \mathbf{H}_x -direction (DWs normal to the x -axis), the orientation of \mathbf{m}_{DW} with respect to $|\nabla m_z|$ is described by the DW azimuthal angle ϕ (ϕ is defined with respect to the $+x$ -axis). Thus, in the numerical collective coordinate model, the Chiral Damping has a simplified form:

$$\alpha = \alpha_0 + Q\alpha_c \cos \phi \quad (\text{I.56})$$

with $Q = \pm 1$ corresponds to DW_{U-D} ($Q = -1$) and DW_{D-U} ($Q = +1$). The variation of v_{DW} , obtained numerically and depicted in **Figure I.27.a**, is comparable to the variation of the experimental normalized velocity (**Figure I.27.b**). In fact, we normalize the DW velocities by the average velocity in the plane (in the four in-plane directions, $\pm x$ and $\pm y$) so that all symmetric contributions from \mathbf{H}_x are removed. Since the numerical model only includes an asymmetric contribution, the good qualitative agreement with the experimental data, in spite of thermal fluctuations and pinning effects, consolidates the idea of a Chiral Damping mechanism. As expected, the numerical model shows that both DW velocities saturate simultaneously at $|\mathbf{H}_x| = |\mathbf{H}_K|$, which is the field that saturates both DW core magnetizations.

In conclusion, the quantitative study of FIDWM in sputtered structures of Pt/Co/Pt has possibly revealed the existence of a new SIA-induced mechanism. The new mechanism induces asymmetric DW motion that has the same spatial symmetry effects as those expected from the SIA-induced DMI mechanism. However, detailed analysis of the DW velocities curves showed that observations do not reconcile with the DMI-stabilized homochiral Néel walls scenario, suggesting that DWs are of the Bloch-type in Pt/Co/Pt. The investigation of the creep scaling law evidenced a chiral dissipation origin of the asymmetry between DW velocities. This has led to the introduction of new damping term for DWs. Two successive Bloch walls acquire opposite chiralities under an in-plane bias field. They then experience different damping hence the denomination of “Chiral Damping” for this new mechanism. Numerical calculations including the Chiral Damping show results that are compatible with the experimental measurements.

Chiral Damping emerges as a possible physical mechanism likely to exist in structures that exhibit SIA. Unlike the interfacial DMI whose microscopic mechanism has been extensively studied in literature, the origin of the Chiral Damping is not clear. Recently, some theoretical efforts have addressed this issue.

I.6.2. Phenomenology and origin of the Chiral Damping

Dissipation can be expected to become chiral in SIA materials in order to fulfill the Neumann’s principle asserting “any physical properties of a system possesses the symmetry of that system”.

In the hydrodynamic limit of a magnetic system, the dynamics is considered for a continuous magnetic texture and can be described by an extended LLG equation where the damping is written in the form of a non-local second-rank tensor [Akosa et al. 2016]:

$$\frac{\partial \mathbf{m}(\mathbf{r})}{\partial t} = -\gamma \mathbf{m}(\mathbf{r}) \times \mathbf{H}_{eff} + \mathbf{m}(\mathbf{r}) \times \int \boldsymbol{\alpha}(\mathbf{r}, \mathbf{r}') \cdot \frac{\partial \mathbf{m}(\mathbf{r}')}{\partial t} d\mathbf{r}' \quad (\text{I.57})$$

The physical mechanisms associated with the magnetic damping are complex (cf. section I.1.3.1) and involve among others things, magnon scattering and itinerant electron spin relaxation.

Considering the principles of symmetry, [Akosa et al. 2016] have shown that one can construct a chiral damping up to the linear order in magnetization gradient in noncentrosymmetric magnets whether they are three-dimensional bulk systems or thin multilayers systems with SIA. The tensor components of the damping $\boldsymbol{\alpha}$ in the extended LLG equation, written above, are a function of the magnetization direction and of its spatial gradient $\alpha^{ij} = \alpha^{ij}(\mathbf{m}, \nabla \mathbf{m})$. [Hals & Brataas 2014] performed an expansion of α^{ij} up to the first order in the magnetization gradient obtaining:

$$\alpha^{ij} = \alpha_0^{ij} + \sum_{lm} K_{lm}^{ij} m_l m_m + \sum_{klm} L_{klm}^{ij} m_k \partial_l m_m \quad (\text{I.58})$$

with a first term representing the isotropic damping, the second an anisotropic contribution from the crystallographic ordering and the third term yields a chiral damping. Due to the spatial inversion symmetry breaking in the particular case of a two-dimensional system with SIA (from interfaces) along the normal z -axis (the x and y directions are equivalent), the third term of Eq. I.58 can be rewritten in a simpler form:

$$\alpha^{ij} = \alpha_0^{ij} + \alpha_z^{ij} \lambda_{ex} \mathbf{m} \cdot [(\mathbf{u}_z \times \nabla) \times \mathbf{m}] \quad (\text{I.59})$$

For the DW core magnetization \mathbf{m}_{DW} , this equation of damping is equivalent to the Eq. I.54 proposed by [Jué et al. 2015]. This phenomenological approach proves that a Chiral Damping can exist in magnetic materials with SIA. However, it does not give any insights about the physical mechanism responsible for the Chiral Damping.

Chiral Damping is the result of symmetry breaking induced by the structural inversion asymmetry. It can thus be expected that Chiral Damping will be associated with the effects that also result from the spin-orbit interaction in the presence of SIA such as the Rashba effect or multiple contributions of different phenomena (e.g. the damping-like component of SOT). In ferromagnetic systems with such interfacial spin-orbit coupling, it has been shown that the magnetic damping is a tensor linear in both the magnetization gradient and the Rashba strength [K. W. Kim et al. 2012; Kim et al. 2013; Wang et al. 2014; Kim 2015]. Besides this effect, [Akosa et al., 2016] proposed two additional mechanisms that can contribute to the Chiral Damping.

The first one is related to DMI. In transition metal ferromagnets, the itinerant electron spins can also contribute to the DMI with a term that involves exchange between these itinerant spins (s -orbitals) and local spins (d -orbitals); an effective “ s - d ” DMI. Some *ab initio* calculations indicate that this type of interaction can have a significant contribution to the total DMI [Kashid et al. 2014]. Consequently, due to the magnetic texture, the itinerant electron spins experience because an additional effective field, mediated by the strength of the “ s - d ” DMI. According to the model of the damping mediated by itinerant electrons, this induces an additional damping torque on \mathbf{m} which depends on the chirality.

A second mechanism results from the interplay between spin motive force and anomalous Hall effect. The variation of the magnetization texture with time generates local spin currents \mathbf{J}_i^s that depend on the local spatial gradient of \mathbf{m} [Barnes & Maekawa 2007]. In a ferromagnet with a sizeable anomalous Hall effect, these primary spin currents \mathbf{J}_i^s are converted into secondary spin currents \mathbf{J}_j^s that flow along the \mathbf{u}_j direction and are polarized along the $(\mathbf{u}_i \times \mathbf{u}_j)$ direction. These secondary spin currents can be injected in the adjacent spin sink (the HM layer) which exhibits a strong spin relaxation. Similar to the spin pumping mechanism [Tserkovnyak et al. 2002], a damping torque is induced on \mathbf{m} that depends on the spatial magnetization gradient which is similar to the phenomenology of the Chiral Damping component.

Recently, further theoretical efforts considering various models of Rashba and Dresselhaus types of SOC evidenced a chiral renormalization of both the Gilbert damping and the gyromagnetic ratio for a spatially and temporal varying magnetic texture [Freimuth et al. 2017; K.-W. Kim, Lee, Lee, Everschor-Sitte, Olena Gomonay, et al. 2018; Akosa et al. 2018]. [K.-W. Kim, Lee, Lee, Everschor-Sitte, Olena Gomonay, et al. 2018] argue that the chiral gyromagnetic ratio is actually the main mechanism behind the asymmetric DW creep motion in FIDWM and not the Chiral Damping as attributed in [Jué et al. 2015; Akosa et al. 2016]. [Akosa et al. 2018] found, on the contrary, that both chiral damping α_c and chiral gyromagnetism γ_c are intrinsically linked to each other.

The above discussion raised the possibility of the existence of the Chiral Damping in SIA materials. We infer that a plenty many chiral mechanisms induced by the SIA coexist, namely the DMI and the Chiral Damping. However, there is no yet a clear idea of their exact relative strength. We do not know exactly why DMI prevails in some structures [Je et al. 2013] whereas it is negligible compared to the Chiral Damping in others [Jué et al. 2015]. It is also possible to obtain different chiral mechanisms induced by the SIA of a comparable strength.

I.6.3. The coexistence of different chirality-induced asymmetries

In [Jué et al., 2015], it was demonstrated that the Chiral Damping mechanism governs the FIDWM in Pt/Co/Pt stacks. On the contrary, [Je et al., 2013] reported that the energetic chiral term in σ_{DW} accounted for by the DMI effective field was the main mechanism in quite similar Pt/Co/Pt stacks. This apparent contradiction probably stems from the different balance between both phenomena; DMI and Chiral Damping. On the one hand, in [Je et al., 2013], the Co layer is very thin (0.3 nm) which is equivalent to 1.5 monolayer of Co atoms. This, all Co atoms experience the DMI

that comes from adjacent interfaces. On the other hand, the Co layer in [Jué et al., 2015] is much thicker (0.6 nm) so that DMI attenuates further in the ferromagnetic layer. In addition, the deposition conditions are not similar for the two samples studied so the SIA is not equivalent in the two systems. Therefore, the strength of each mechanism differs from one stack to the other. In this section, we report an example of the coexistence of DMI and another chiral mechanism (probably the Chiral Damping) that coexist with comparable strengths in one structure.

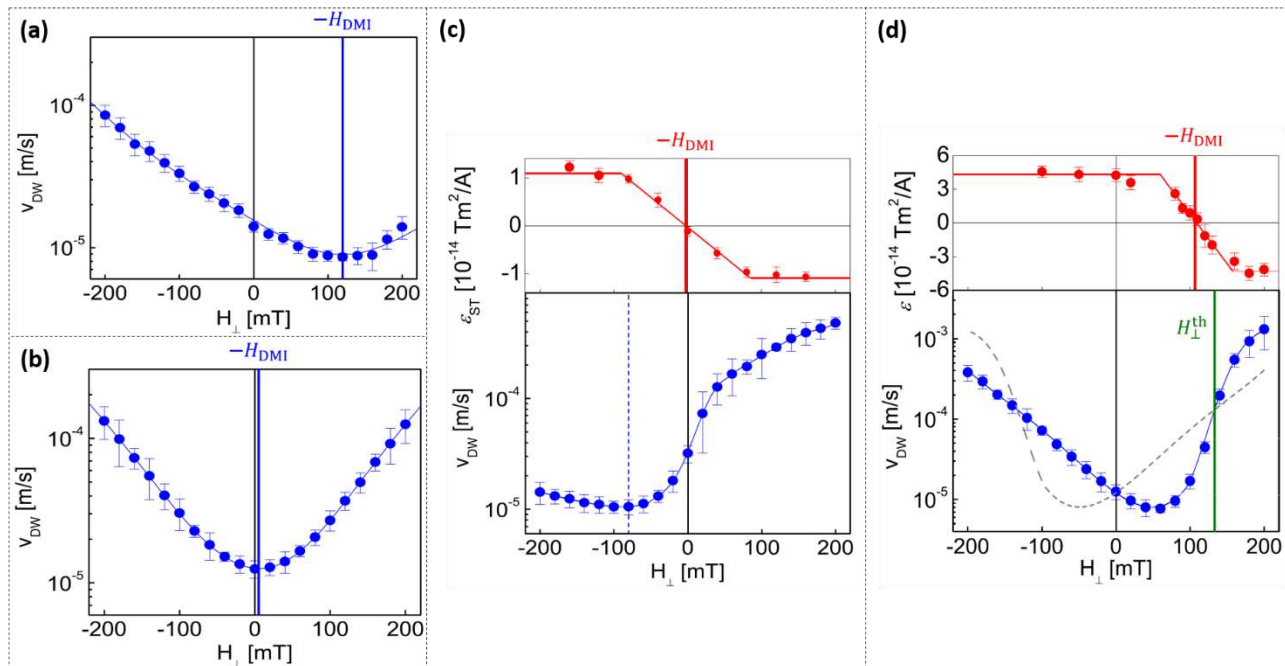


Figure I.28 Coexistence of different chiral mechanisms induced by SIA in thin magnetic layers. v_{DW} as a function of a magnetic in-plane field normal to the DW H_{\perp} (blue curves) when driven by easy-axis magnetic field H_z for various structures: (a) Pt 2.5/Co 0.9/Cu 2.5/Pt 1.5 (sample 1), (b) Pt 4.0/Co 0.3/Pt 1.5 (sample 2), (c) Pt 2.5/Co 0.5/Pt 1.5 (sample 3) and (d) Pt 2.5/Co 0.9/Al 2.5/Pt 1.5 (sample 4). All thicknesses are in nm. In (c) the dotted blue vertical line gives the magnetic field of minimum velocity $H_{min} \cong -80$ mT. In (d) the dashed line gives $v_{DW}(H_{\perp})$ and the green vertical line gives the in-plane field H_{\perp}^{th} at which the asymmetry between DWs reverses. Red curves in (c) and (d) represent the measured spin torque efficiency as a function of H_{\perp} . Extracted and adapted from [Kim, Park, Park, Kim, Yoon-Seok Nam, et al., 2018].

[Kim, Park, Park, Kim, Yoon-Seok Nam, et al., 2018] studied FIDWM in a series of Pt/Co-based multilayers with SIA and reported that the asymmetry in the DW motion cannot be solely attributed to DMI. All samples were deposited using the same DC magnetron sputtering technique. However, due to changes in nominal thicknesses and/or the insertion of an additional layer, they obtained significant differences in the stack properties as well as in the between the asymmetric DW motion (**Figure I.28**). Each of them is representative of a typical behavior.

Sample 1 (Pt (2.5 nm)/ Co (0.9 nm)/ Cu (2.5 nm)/ Pt (1.5 nm)) exhibits a large DMI ($|H_{DMI}| = 120 \pm 5$ mT) evidenced by the DW velocity curve as a function of the in-plane field (**Figure I.28.a**). The parabolic shape and the symmetric variation with respect to a nonzero magnetic field are fingerprints of DMI.

On the contrary, *sample 2* (Pt (4 nm)/ Co (0.3 nm)/ Pt (1.5 nm)) has a negligible DMI confirmed by the symmetric variation of the DW velocity around the zero in-plane magnetic field (**Figure I.28.b**).

The DW velocity variations of *sample 3* (Pt (2.5 nm)/ Co (0.5 nm)/ Pt (1.5 nm)) and *sample 4* (Pt (2.5 nm)/ Co (0.9 nm)/ Al (2.5 nm)/ Pt (1.5 nm)) are asymmetric with a minimum of velocity at a non-zero in-plane field H_{min} (**Figure I.28.c** and **.d**). Here, the DW velocity, in both samples, has no symmetrical parabolic variation with respect to H_{min} . The authors then used another technique to estimate DMI, which is the measurement of the spin torque efficiency ϵ_{ST} as a function of the in-plane field (the top red plots in **Figure I.28.c** and **.d**) [Haazen et al., 2013] (cf. section I.5.5.1.3). The spin torque efficiency is essentially governed by spin-orbit torques, in other terms by

the internal structure of the DW. Therefore, the intercept with the abscissa ($\varepsilon_{ST} = 0$) indicates a Bloch DW where the corresponding magnetic in-plane compensates H_{DMI} . These measurements resulted in a vanishing DMI in *sample 3* and a sizeable DMI in *sample 4* ($|H_{DMI}| = 107 \pm 7$ mT). In *sample 3*, the minimum velocity is shifted to $H_{min} \cong -80$ mT largely away from $H_{\perp} = -H_{DMI} \approx 0$. This large shift is an indication that the mechanism of asymmetry is different from DMI. We refer to this mechanism generically as a chirality-induced asymmetry. The velocity versus in-plane field curve has a shape similar to that used to evidence the Chiral Damping (**Figure I.25.a**). *Sample 4* is a good representative of the situation where DMI and another chirality-induced asymmetry mechanism coexist and are both sizeable (H_{min} is shifted from $-H_{DMI}$). Moreover, the interplay between these two mechanisms depends on the magnitude of the in-plane field. The asymmetry reverses at a threshold magnetic field H_{\perp}^{th} where the DW_{U-D} and DW_{D-U} curves intersect. Several others studies have reported similar asymmetry reversal of the velocity in FIDWM measurements for various different structures. To name a few, we cite [Lau et al. 2016; Quinsat et al. 2017; Cao et al. 2017; Lau et al. 2018].

It should be noted that there is an independent report of the coexistence of Chiral Damping and DMI involving different measurement techniques different from FIDWM. [Zakeri et al. 2012] observed asymmetric damping of spin waves as well as asymmetric dispersion related to DMI in Fe/W bilayers. This consolidates and encourages the consideration of Chiral Damping mechanism in SIA multilayers along with the interfacial DMI.

To summarize, SIA in thin magnetic layers with PMA results in a variety of intriguing SOC phenomena that asymmetrically modify the conservative and dissipative properties of the local magnetization dynamics. One mechanism that influences the conservative (energetic) part is the interfacial DMI. It has attracted a lot of enthusiasm and interest as it gives a major ingredient that helped to understand the large velocities and the unexpected direction of motion of DWs driven by electric current. Since then, DMI has been considered as the main mechanism for interpreting DW motion in PMA thin layers with SIA and a substantial effort has therefore been devoted to the estimating of the amplitude of DMI through FIDWM measurements. Until recently, due to quantitative deviations from the expectations of the DMI-based model, other mechanisms that induce the same spatial symmetry of DW motion were proposed and evidenced, such as the Chiral Damping mechanism. Other possibilities involve asymmetric DW width, magnetic domains tilting etc. These discrepancies indicate that the exact estimation of H_{DMI} through the study of the asymmetric magnetic domain expansion in SIA materials has to be taken with great caution. It is then recommended to do correctly determine the various chirality-induced asymmetry mechanisms in place in the system under consideration as suggested in [D.-Y. Kim, Kim, et al. 2018]. The implications of these new chirality-induced asymmetry mechanisms are fundamental. As they can coexist with DMI, a re-examination of previous investigations of DW motion is required as they did not consider such additional mechanisms. Until now, the Chiral Damping was evidenced and studied only measuring FIDWM. A proper experimental investigation of its role in CIDWM is required along with theoretical work to understand its action. The Chiral Damping could be essential to control magnetic textures for the design of spintronic devices.

Conclusions

These recent years, thin magnetic layers structures with SIA have been extensively studied to understand and control the manipulation of magnetic textures by external magnetic fields and electric currents. The efficient DW motion and the observation of a propagation in the direction of the injected charge current encouraged the abandonment of the standard model of motion based on STTs in favor of new emerging phenomena originating from SOC. The investigation of magnetization dynamics involving DMI and SOT has become a hot topic especially for the topological protected skyrmions, very promising for spintronic and data storage devices. Magnetic DWs are still attractive, at least from a fundamental point of view, as they represent a tool for a faster, easier to implement and more direct investigation of the magnetization dynamics. The study of DW motion can uncover the SIA-induced phenomena not yet fully explored. This is crucial for more efficient manipulation of magnetic textures.

This first chapter then intended to present the main basic concepts essential for apprehending DWs and their dynamics. I started by introducing the relevant magnetic energies and explained how they lead to the formation of magnetic DWs in thin ferromagnetic layers. All possible configurations of DWs were then described for the structures with perpendicular magnetic anisotropy since they represent the scope of this thesis.

In order to discuss the different formalisms behind DW motion, I introduced the LLG equation which describes the temporal evolution of the magnetization. The theory explaining the magnetic field driven DW motion was reviewed subsequently. This is essential because the action of an electric current on a DW is equivalent to that of a set of effective magnetic fields. More precisely, an injected electric current acts on the local magnetization via various mechanisms. The standard action of a spin-polarized current through the STT mechanism was first briefly introduced at first to understand its limitations with respect to recent reports in structures with SIA. Subsequently, a particular importance was given to the SOT mechanism. A thorough understanding of SOT is required to be able to interpret the experimental results of this thesis.

The SOT has emerged as the main mechanism responsible for the efficient DW motion thanks to an additional concept which is DMI. I have detailed the origin of this asymmetric interaction in SIA structures and its important role in inducing homochirality in magnetic thin layers. In this context, various methods to identify the DW chirality and to quantify the amplitude of DMI were described. The asymmetric DW motion in FIDWM is one of these methods. Interestingly, we have seen that it has led to the introduction of an additional SIA-induced mechanism, “Chiral Damping”. The Chiral Damping, the dissipative counterpart of DMI, has emerged as an important mechanism to be considered in magnetic DW dynamics whether driven by magnetic fields or electric currents.

Chiral Damping enriches the spectrum of the phenomena induced by SIA and implies that a re-examination of the well-established SOT + DMI mechanism is needed. The possible co-existence of DMI and Chiral Damping reveals that the DW motion is very rich and ambiguous phenomena. Many questions concerning the DW motion are still open. The main objective of this thesis is then to understand better the DW motion in SIA materials that is crucial from both fundamental and technological points of view. For that end, we have chosen to study the DW motion in a non-collinear geometry or configuration relative to the electric current. In this geometry, we fix the path of the electric current independently from the DW orientation. We dispose then of an additional degree of freedom which allows controlling the spatial and temporal distributions of current-induced torques on the magnetization. Such a non-conventional geometry is attractive because on the one hand it helps to uncover new aspects of SIA. On the other hand, it has recently allowed the demonstration of Field-free SOT magnetic switching by means of shape controlled magnetic switching of Co/AlOx pillars with different flexible geometries on top of a Pt pad [Safer et al., 2015], very promising for future spintronic devices. In addition, we apply an external in-plane magnetic field that modulates the DW core magnetization. By using this method, we intend

to control the action of SOT thus exploring and unveiling any possible interplay between the various chiral mechanisms induced by SIA.

We have carried out these investigations on two representative structures, Pt/Co/AlO_x, a large SIA material and Pt/Co/Pt, a low SIA material. The Pt/Co/AlO_x system is very interesting. Actually, SIA induces robust effects as fast DW motion and efficient magnetization reversal have been already reported in such a material. However, it is difficult to modulate the DW core magnetization in Pt/Co/AlO_x by the in-plane magnetic field due to a large DMI. On the contrary, Pt/Co/Pt offers the opportunity to tune effectively the DW core magnetization. It is then the ideal system to understand the role of DMI and to discover as well the Chiral Damping effects in CIDWM. We were able to demonstrate an asymmetric DW motion in the non-collinear geometry in both structures. These studies show incompatibilities between the widely accepted DMI + SOT mechanism and several features of the DW motion. They also evidence an important interplay between DMI and Chiral Damping in the low SIA structure.

In the following parts of this thesis, we present some consequences of the mechanism of the asymmetric DW motion in the non-collinear geometry. We have thereby studied its potential role in the formation of the DW tilt. Next, we have investigated the possible effects of the asymmetric DW motion on chiral skyrmion bubbles. This last study have led to the proposal of a new mechanism responsible for a well-defined deflection of skyrmion bubbles. We have found that the consequences of the asymmetric DW motion in the non-collinear geometry depends on whether the structure has a low or a large SIA. All of this experimental work will be described in the following chapters.

II. Experimental techniques

In this Chapter, I describe the experimental procedures used in this thesis. I begin with the fabrication protocol of the Pt/Co/Pt and Pt/Co/AlOx samples. Next, I present the wide-field magneto-optic Kerr effect technique employed to probe DWs motion. Finally, I discuss the electric current injection experimental setup and methods to measure DW displacements.

II.1. Samples fabrication

II.1.1. Thin films deposition

Pt/Co/Pt and Pt/Co/AlOx multilayered systems have been extensively studied for many years in SPINTEC. They are interesting materials thanks to the efficient interaction between electric current and local magnetization mediated by the spin-orbit coupling, promising for DW- and skyrmion-based spintronic devices. They are thereby well suited to study and uncover the action of SIA and SOT on magnetic textures. Pt/Co/Pt and Pt/Co/AlOx stacks were deposited on 100 mm-Silicon wafer with either 1 μm or 500 nm-thermally grown SiO₂ using DC (Direct Current) magnetron sputtering technique. The exact structures are Pt (3 nm)/Co (0.6 nm)/Pt (1.5 nm) and Pt (3 nm)/Co (0.6 nm)/AlOx (1.28 nm) referred to as Pt/Co/Pt and Pt/Co/AlOx in this manuscript. The films were grown at room temperature, under 2 10^{-3} mbar of Ar and at a background pressure of 10^{-8} mbar. The deposition rates were 0.0731 nm.s⁻¹ for Pt, 0.0348 nm.s⁻¹ for Co and 0.0954 nm.s⁻¹ for Al. In the Pt/Co/AlOx stacks, the AlOx layer was prepared by oxidizing the top Al layer with a radio-frequency (RF) oxygen plasma at a pressure of 3 10^{-3} mbar and a RF power of 10 Watt for 85 seconds. The multilayers show also a good stability of their magnetic properties over time. No further capping layer is then required to protect the samples.

These two structures exhibit perpendicular magnetic anisotropy (PMA) as grown. These materials constituted the basis of previous works at SPINTEC just as [Miron, 2009; Jué, 2013; Chenattukuzhiyil, 2016] to name a few. The magnetic hysteresis loops, available in [Jué, 2013; Chenattukuzhiyil, 2016] and measured via Extraordinary Hall effect, exhibit square shapes. This indicates the out-of-plane anisotropy with 100% remanence. [Jué et al., 2015] measured an anisotropy field of about $\mu_0 H_{anis} \sim 0.7 - 1$ T in Pt/Co/AlOx and $\mu_0 H_{anis} \sim 0.38 - 0.55$ T in Pt/Co/Pt.

II.1.2. Fabrication of wires for DW motion

To study the CIDWM in Pt/Co/Pt and Pt/Co/AlOx, the required current densities are in the order of 10^{12} A.m⁻². It is then necessary to inject current in confined geometries, i.e. micro or nanowires wires. Wire dimensions are 10 μm wide and 20 μm long (**Figure II.1**). In principle, the width should be reduced in order to inject large current densities. Instead, we privileged a large width in our devices in order to follow DWs motion in a two-dimensional geometry. Actually, we stabilize circular magnetic domains with a diameter that needs to be larger than the resolution limit of our imaging techniques (~ 500 nm). Besides, the wire resistance is proportional to its length. The latter ought to be scaled down to reduce the Joule heating but it needs to be large enough to observe cumulative DW displacements. The choice of 20 μm is a compromise between these two criteria.

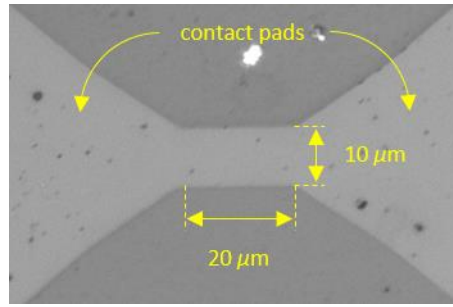


Figure II.1 Optical image of the patterned device.

Devices were patterned by standard photolithography and subsequent ion beam milling (IBE) following the protocol developed at the PTA platform in the CEA Grenoble. The magnetic multilayer is coated by a positive AZ 1512 HS photoresist by spin coating at 2000 rotations/minute for 60 seconds. The resist is then baked at 100°C for 90 seconds. UV exposure and development of the resist define the mask for the IBE. The etching process gives the desired shape for the device. We monitor by SIMS (Secondary Ion Mass Spectroscopy) the atomic species that are being etched which allows us to precisely stop the etching at the bottom Pt layer. This process used for the devices studied in the experiments described in Chapters III, IV and V.

II.2. DWs under Magneto-optic Kerr effect (MOKE) microscopy

In this thesis, we investigate the CIDWM using the wide field magneto-optic Kerr effect microscopy (MOKE) imaging technique. We use a commercial MOKE from “Evico Magnetics”. This technique is well suited as long as magnetic domains and DW displacements are on the micrometer scale.

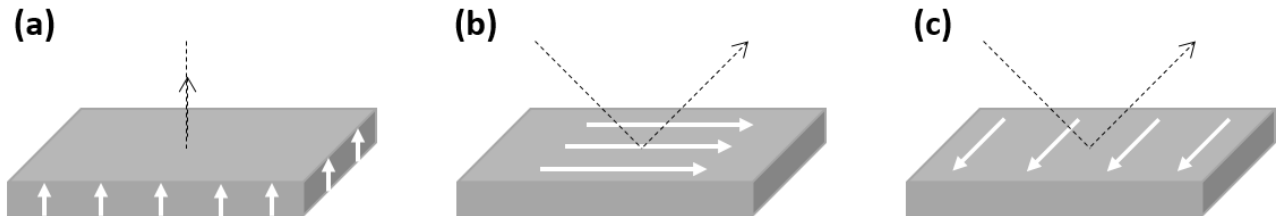


Figure II.2 Different Kerr effect geometries. (a) Polar Kerr effect. (b) Longitudinal Kerr effect. (c) Transverse Kerr effect. White arrows indicate the orientation of the local magnetization.

The Kerr effect results from a magneto-optical interaction between a linearly polarized light and a magnetic material. The penetration depth of the incident light depends on the material and is in the order of 10 nm. The study of magnetism via the Kerr effect is then limited to ultrathin layers or surfaces of bulk systems. The polarization of the optical wave rotates upon reflection at the surface of the magnetic material by an angle whose value depends on the magnetization of the ferromagnetic layer. This angle changes sign upon reversal of the local magnetization. The state of the magnetization can thus be determined by measuring the rotation of the polarization of the reflected light. More particularly in our case, the analysis of this polarization by means of an optical polarizer make it possible to image the different magnetic domains. Depending on the direction of the magnetization with respect to the incidence plane of the light and to the sample surface, we have three different geometries of the Kerr effect: polar, longitudinal and transverse Kerr effects (**Figure II.2**). For the studied PMA materials in this thesis, we employ the polar Kerr effect where the magnetization is perpendicular to the reflection surface and parallel to the incidence plane. In this geometry, the Kerr signal is maximum when the incident light is normal to the surface of the material. For the longitudinal Kerr effect, the magnetization is parallel to both the incidence plane and the reflection surface. As for

the transverse Kerr effect, the magnetization is perpendicular to the incidence plane and parallel to the reflection surface.

In our polar MOKE microscope, the light beam, from a red LED source, passes through a polarizer. The linearly polarized light is then projected normal to the sample through the objective. The same objective collects the reflected light that subsequently passes through the analyzer to detect the rotation of the light polarization. Finally, it reaches the CCD camera where a magnetic image of the sample is constructed and recorded. Magnetic domains are imaged with different magnetic signals or contrasts (dark or bright). Actually, the signal intensity depends on magnetization, the surface reflectivity, incident light intensity, wavelength, relative alignment between the polarizer and the analyzer, etc. To better visualize the effect of a controlled excitation on the ferromagnet, we use the differential imaging mode of the microscope (**Figure II.3**). An image taken before the excitation (i.e. an electric current pulse or a magnetic field pulse) is subtracted from an image taken afterwards. Only regions where the magnetization has been reversed give a magnetic contrast: it corresponds either to a nucleation of a magnetic domain or to a DW displacement. The differential mode has the advantage of enhancing the magnetic contrast and limiting any contribution from the topography of the material surface. In the case of a DW displacement, the magnetic contrast, either dark or bright, depends on the type of the DW, either a DW_{U-D} or a DW_{D-U} , and on its direction of motion. In this manuscript, a dark (bright) contrast corresponds to a magnetization that has been reversed from down (up) state to up (down) state. Consequently, we determine the direction and the amplitude of a DW displacement. By using MOKE, we only get the static state of the magnetization. The exact timescale of the dynamics remains unknown and requires other advanced imaging techniques.

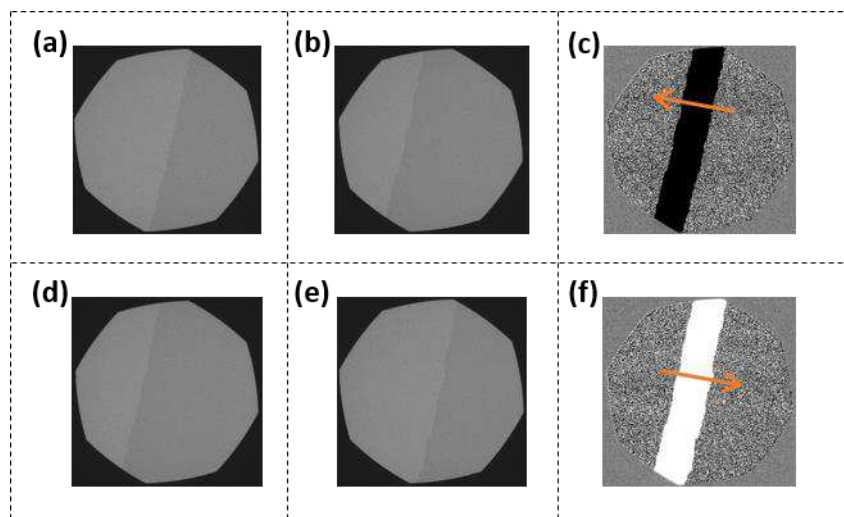


Figure II.3 The differential mode of MOKE. (a), (b), (d), (e) are MOKE images with bright and dark contrasts corresponding to down and up magnetic domains, respectively. The DW is the boundary that separates the two areas of different contrasts. (c) and (f) are MOKE differential images. (c) ((f)) is the subtraction of (a) ((d)) from (b) ((e)) taken after applying an external magnetic field. The orange arrow indicates the direction of motion of the DW_{D-U} in (c) and (f).

Wide-field MOKE microscopy is well suited to monitor the spatial and temporal evolutions of magnetic domains over relatively large time scales and micrometer displacements. Indeed, the diffraction of the light limits the resolution of the MOKE to around 500 nm. It can be improved to about 300 nm using for example a different light source and an oil immersion technique. MOKE technique cannot resolve the internal structure of a DW (its width $\Delta \cong 5$ nm in our structures) but it allows the study of its dynamics under an external driving force (magnetic field, electric current, etc.). Moreover, no special treatment for the multilayer surface is required to perform MOKE microscopy.

For further details concerning the magneto-optic Kerr effect and Kerr microscopy, we refer to the following review [[Schäfer, 2007](#)].

II.3. DW motion by the injection of an electric current

II.3.1. Current-induced DW Motion set-up

The experimental set-up used for the injection of electric current pulses into the samples is shown in **Figure II.4**. The sample is fixed on a sample holder that has two copper contact pads. These copper contact pads are connected to the sample using micro bonding. The input is connected to an ultrafast voltage pulse generator and the output grounded. Two parameters can be set on the generator: the pulse duration and the voltage amplitude. Effects induced by current pulses variable duration (0.3 ns - 20 ns) and voltage amplitude (1 V – 90V) are then investigated under MOKE. The pulse duration is chosen according to the pulse amplitude. The application of a pulse for a relatively long period of time causes over-heating which can cause nucleation events or even damage the sample. Another pulse generator triggers the ultrafast voltage pulse generator and sets the total number of pulses and their frequency. Samples have a resistance in the range of 600 - 900 Ohms. To reduce the impedance mismatch with the generator and have a better transmission of the electrical pulses, we connect a 50 Ohms resistance in parallel. The pulses up to 90 V did not cause substantial damages to the contacts or devices which allowed the DW motion to be probed with the maximum available current density for each structure.

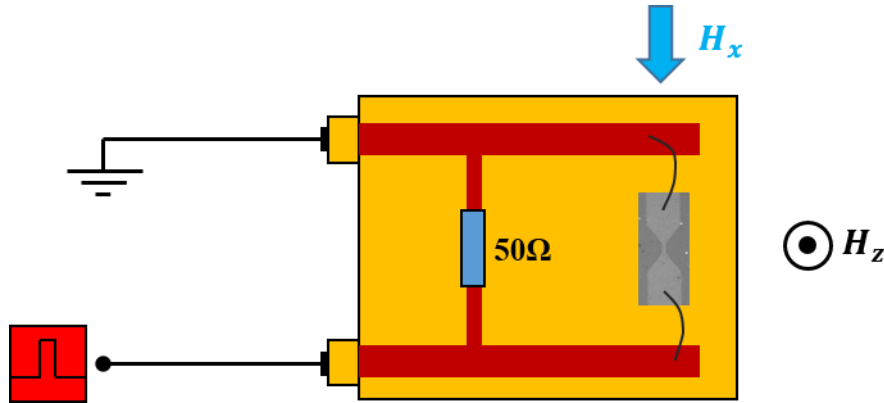


Figure II.4 Schematic representation of the experimental setup used for current injection. The pulse generator is shown in red. By micro bonding, we connect the device to the copper pads. The 50 Ohms resistance is connected in parallel to reduce the impedance mismatch between the device and the generator. The sample holder is grounded to close the circuit. External magnetic fields can also be applied.

Current densities are calculated by dividing the injected current by the wire width and the total effective thickness of the conductive layers, assuming uniform conduction in the metallic layers. Actually, the values of the bulk resistivity of the ferromagnet and the heavy metal are $\rho_{Co} = 62.4 \cdot 10^{-9} \Omega\text{m}$ and $\rho_{Pt} = 105 \cdot 10^{-9} \Omega\text{m}$, respectively. Due to the higher resistivity of Pt, one would expect the current to flow mainly through the Co layer thus a non-negligible STT effect on DWs. Taking into account the thickness dependence of the resistivity, the roles are inverted between Co and Pt. For $t_{Co} = 0.6 \text{ nm}$ and $t_{Pt} = 3 \text{ nm}$, $\rho_{Co} = 9.6 \cdot 10^{-7} \Omega\text{m}$ and $\rho_{Pt} = 2.7 \cdot 10^{-7} \Omega\text{m}$ [Lacy, 2011; Alejos et al., 2017]. The current then flows mainly through the Pt layer (cf. [Cormier et al., 2010] for further discussion), which justifies a dominant SOT mechanism on DWs in our samples as discussed in section I.4. Our estimation is not accurate but still gives a good approximation of the current density flowing in the sample.

II.3.2. DW motion in the presence of external magnetic fields

In Chapter III, we will present the effect of a longitudinal magnetic field H_x on CIDWM. The in-plane magnetic field H_x is applied using an electromagnet placed on a support plate with the sample holder placed between its poles. In this arrangement, any tilt of the electromagnet support plate generates an out-of-plane field component for H_x which can contribute to the DW motion. Based on the symmetry of our system, these errors are removed by adjusting the tilt of the support plate. For this purpose, we examine the displacements of a DW_{U-D} under a positive current in the presence of a positive in-plane field and of a DW_{D-U} under a negative current in the presence of a negative in-plane field. In the presence of a tilt, the opposite in-plane fields are not equivalent resulting in different displacement amplitudes between the two DWs. By progressively changing the orientation of the support plate, we consider the tilt as negligible when both displacements are equal thus respecting the 180° rotation symmetry operation around the z -axis.

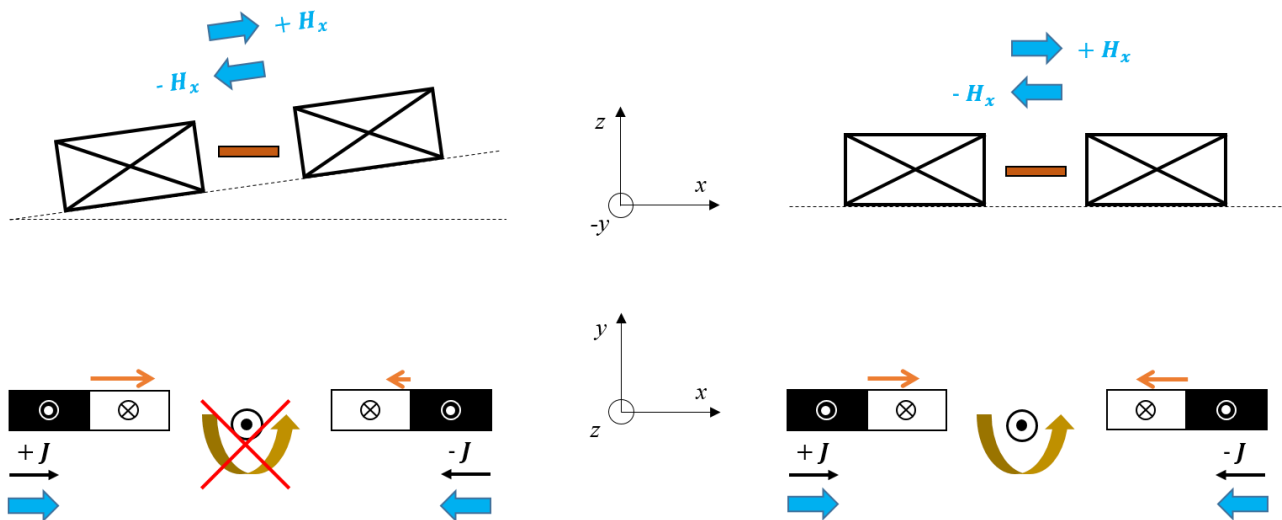


Figure II.5 The arrangement of the electromagnet with respect to the sample. With a tilt, H_x gives an out-of-plane field component (along the z -axis) that breaks the symmetry between DW displacements. When H_x is perfectly in plane, DWs displacements are equivalent by a 180° rotation around the z -axis.

In addition, a Helmholtz coil, made of copper wire, was mounted between the poles of the electromagnet. It generates an external out-of-plane field H_z that helps nucleating DWs and stabilizing magnetic bubbles for our experiment described in Chapter IV. The device is placed in the center of the Helmholtz coil so that H_z is nearly uniform. The amplitudes of H_z and H_x are controlled by bipolar power supplies. The voltage range of the power supplies limits the maximum applied fields. H_x for example was limited to ± 150 mT. The rise and fall times of the H_x -pulses were approximately 200 ms. Therefore, we used a home-built Labview program to ensure that the application of H_z and the injection of the desired current pulses take place during the plateau of H_x . From this point of view, the action of H_x is similar to that of a continuous magnetic field.

II.3.3. Measurements of DW motion

We extract the DW velocity from series of Kerr images. We determine the DW displacement by averaging measurements from at least 10 images taken under the same conditions of pulse duration and amplitude. To obtain DW displacements on the micrometer scale, the pulses were repeated between 3 and 60000 times, depending on the current density J . The elapsed time between the end of one pulse and the beginning of the next can be varied from 10 μ s to 1 second. The variation of the elapsed time between pulses did not influence the overall DW displacement. The elapsed time is then

always long enough for the heat produced during a single pulse to be evacuated. Therefore, when increasing the number of pulses under a given current density, the DW motion is cumulative and the displacement induced by a single pulse is estimated by dividing the total displacement by the number of the pulses. Following this exact procedure, we determine DW displacements for a single pulse with at least three different durations. During the rise and fall times of a pulse, the amplitude of the current density is not well defined. In order to determine the intrinsic DW velocity corresponding to the desired current density, we have to remove contributions to the DW displacement during the rise and fall times. We take then advantage from the fact that rise and fall times are identical for any pulse duration. We determine then the DW velocity of the DW with the slope of the linear fit of the displacement variation as a function of the pulse length (examples are shown in **Figure II.6**). This procedure eliminates errors due to the influence of the rise and fall times. The standard deviation of the slope is used as error bars for the velocity measurement. I have followed this procedure to measure the DW velocity under an electric current in the Pt/Co/Pt structure, depicted in **Figure III.1.c**. For the current-induced magnetic bubbles motion (Chapter IV), I used another procedure to estimate the velocity of these bubbles: the injection of series of fixed-duration pulses. The velocity is then the slope of the linear fit of the total displacement versus the integrated duration of the current injection (single pulse duration x number of pulses) (**Figure V.18**). As discussed, this method is a source of errors that lead to an underestimation of the intrinsic velocities. Nevertheless, it still gives an approximation of the order of magnitude of the velocities.

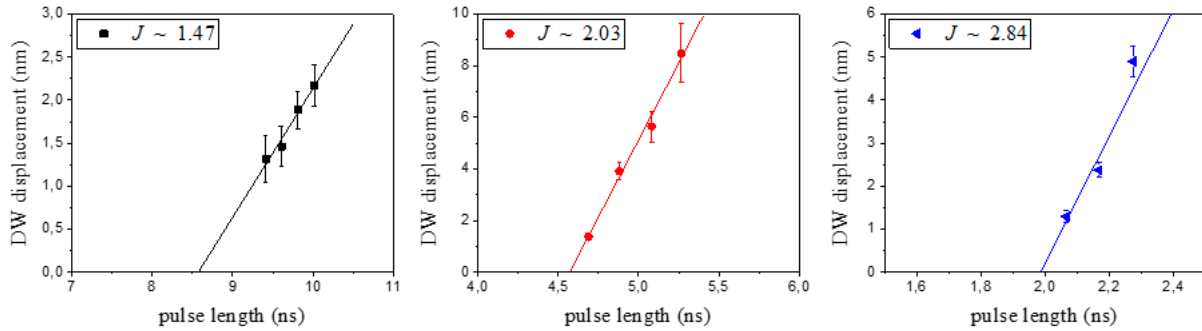


Figure II.6 DW displacement as a function of the pulse duration at three different current densities for Pt/Co/Pt. The slope of the fit gives the DW velocity. The fit does not extrapolate to the origin as the DW is static during most of the pulse rise and fall times. Current densities are in units of 10^{12} A.m^{-2} .

III. The asymmetric non-collinear current-induced DW motion in SIA materials

III.1. The non-collinear DW motion

In MRAMs, research efforts are still focusing on improving the write operation efficiency of the magnetic bits. The writing process relies on torques that are induced by the electric current injection in the MTJ (Magnetic Tunnel Junction). Thereby, it is important to generate efficient current-induced torques in order to reduce both the power consumption and the time rate of the write task. In the case of SOT-MRAMs, the electric current paths of the read and the writing tasks are separated (**Figure III.1.a**). For the read operation, the current travels perpendicular to the Magnetic Tunnel Junction (MTJ) through the tunnel oxide barrier whereas it flows in the plane of the HM layer for the write operation. The tunnel barrier is then less subject to stress which grants the SOT-MRAMs with a better endurance than the STT-MRAMs where the current shares the same path for both operations.

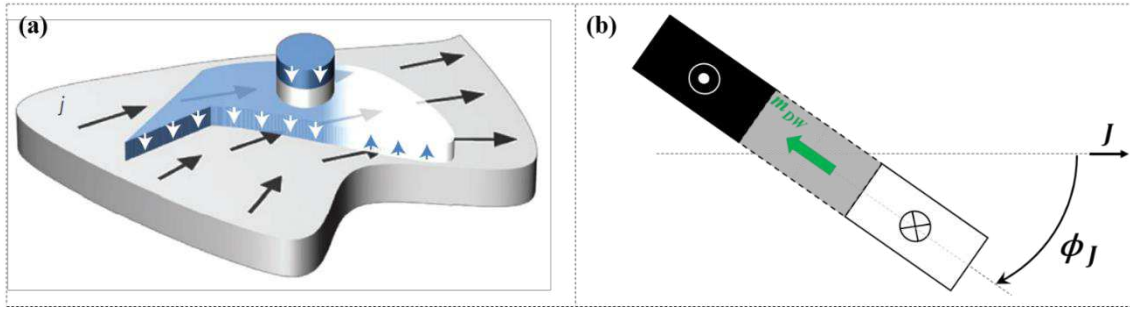


Figure III.1 The spatial distribution of SOT and the non-collinear DW motion. (a) The complex magnetization switching specific to SOT. Based on the in-plane injection of the current, the lower electrode (HM layer) and the magnetic free layer can be shaped independently. By designing the contour of the HM, SOT exhibits a spatial distribution in the plane while the geometry of the free layer dictates the magnetization reversal scheme. A Magnetic Tunnel Junction can be placed on top of the free layer. (b) Schematic diagram of the non-collinear current-induced DW motion. In the case of SOT, the current direction is no more restricted to the direction normal to the DW. The DW can then freely be placed at a finite angle ϕ_J with respect to the current direction. This non-collinear geometry allows studying the action of a spatial dependent SOT. (a) extracted from [Safeer et al., 2015].

In addition, the generation of SOT does not require the current to pass through the ferromagnetic layer. It is then possible to apply the current in any in-plane direction in the HM layer. Consequently, we can shape independently the ferromagnetic layer (**Figure III.1.a**). This additional degree of freedom can bring novel approaches to control the temporal evolution of the magnetization ($\mathbf{M}(x, y, t)$) by a spatial dependent current-induced torques (SOT((x, y))). Actually, the size of the magnetic bits in the SOT-MRAMs is larger than the DW width parameter Δ . The magnetic bits are of few tens of nanometer whereas Δ is less than 10 nanometers in PMA materials. The magnetic switching takes then place through nucleation of the DWs and their subsequent propagation. Therefore, the understanding of the influence of the spatial distribution of SOT on the DW motion can help optimizing the magnetization reversal. As discussed in section I.4.2.4, SOT drive the DWs essentially through the action of the damping-like component \mathbf{T}_{DL} . According to Eqs. I.33 and I.34, the action of \mathbf{T}_{DL} depends on the DW core magnetization \mathbf{m}_{DW} (the unit magnetization vector at the DW core). We express \mathbf{T}_{DL} as $\mathbf{T}_{DL} \sim [\mathbf{m}_{DW} \times (\mathbf{J} \times \mathbf{u}_z)] \times \mathbf{m}_{DW}$ with \mathbf{u}_z the unit vector which gives the normal to the film along which the inversion symmetry is broken (SIA). The relative orientation between the injected electric current \mathbf{J} and \mathbf{m}_{DW} defines then the amplitude of \mathbf{T}_{DL} . Thus, by varying the angle ϕ_J between \mathbf{J} and \mathbf{m}_{DW} , we can study the action of a spatial dependent SOT on the DW. This is the non-collinear DW motion with respect to the current: we fix the direction of the current while rotating the DW in the (x, y) plane (**Figure III.1.b**).

[Safeer et al., 2015] were the first to propose the investigation of the current-induced DW motion in the non-collinear geometry. They fabricated wires of Co/AlOx on top of a Pt pad (**Figure III.2.a**). The current is injected in the Pt electrode with a fixed horizontal direction while the wires have different orientations with respect to the current direction. Each wire has its long axis at an angle that varies clockwise from 0° to 90° in steps of $\sim 15^\circ$. The measurements of the DW velocity v_{DW} as a function of the tilt angle, for the DW_{U-D} under positive and negative currents, are given in **Figure III.2.b**. The DW motion shows a strong dependence on the angle between the current and the DW. For a positive current, it moves asymmetrically with respect to the current direction and has its maximum velocity at a finite angle ϕ_J^{max} . In the manuscript, we refer to ϕ_J^{max} as the angle of the maximum velocity or the angle of the largest displacement. As for the DW_{D-U} , we obtain the variation of its velocity by applying the (x, z) plane mirror symmetry operation to the DW_{U-D} that has been studied in the tilted wires (in **Figure III.2.a**). Following this symmetry operation, the DW_{D-U} motion under a positive (negative) current in wires at angles varying clockwise from 0° to 90° is the same as the DW_{U-D} motion under a negative (positive). Consequently, in a tilted wire at $\phi_J = +45^\circ$ (anti-clockwise rotation) only the DW_{D-U} moves under a positive current whereas only the DW_{U-D} moves in a tilted wire at $\phi_J = -45^\circ$ (clockwise rotation) (**Figure III.3.a**).

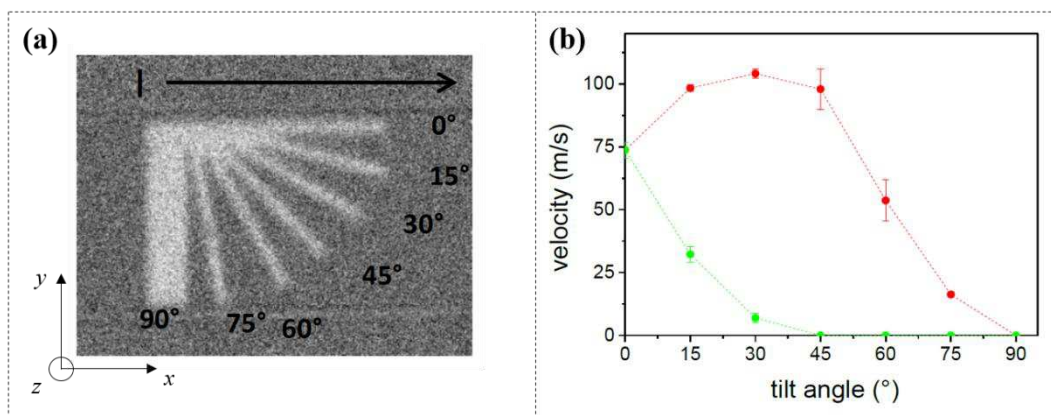


Figure III.2 First observation of the non-collinear DW motion in Pt/Co/AlOx. (a) MOKE image of the magnetic wires (500 nm width) of Co/AlOx on top of a Pt layer. The bright contrast, corresponding to a saturated down magnetization, highlights these wires. (b) The DW velocity versus the tilt angle. These measurements correspond to the DW_{U-D} under a positive (negative) current in red (green) with a density of $1.81 \cdot 10^{12} \text{ A.m}^{-2}$. The tilt angle is the angle between the wire axis and the current direction. (a) extracted from [Safeer et al., 2015] and (b) from [Chenattukuzhiyil, 2016].

Even though their physical mechanisms are not clear, [Safeer et al., 2015] have introduced an interesting concept of magnetic devices based on the specific properties of the non-collinear DW motion. It is the shape-controlled SOT magnetization switching, i.e. the geometry of the device dictates the magnetization reversal scheme. An example of such a device is the “u-shape” device (**Figure III.3.c**) that is made by joining two tilted wires at opposite angles ($\phi_J = \pm 45^\circ$) at the two ends of a straight wire ($\phi_J = 0^\circ$) [Safeer et al., 2015]. For a functional SOT-MRAM, the read element (the top part of the MTJ) would be placed on top of the straight wire. The tilted wire at $\phi_J = \pm 45^\circ$ selects the polarity of the moving DW (either DW_{D-U} or DW_{U-D}) thus it determines the polarity of the magnetization switching (either from up to down or from up to down) depending on the direction of the injected current (either positive or negative). The reversed domains are nucleated in the narrower parts of the tilted wires by the first current pulse. Due to the selectivity in the tilted wires (**Figure III.3.b**), a “u-shape” device with an initial up magnetization switches to the down state only under a consecutive positive current (the bottom panel in **Figure III.3.c**). If the magnetization is already down, no switching takes place (the top panel in **Figure III.3.c**). In fact, only the selected DW_{D-U} in the wire at $\phi_J = +45^\circ$ moves under a positive current from left to right into the straight wire thus resulting in the expansion of the down domain. Following this, in order to switch from down to up, we have to apply a negative current (**Figure III.3.d**). In this case, only the DW_{D-U} , moving from right to left, is selected in the wire at $\phi_J = -45^\circ$. Beyond this example, it is possible to imagine various geometries opening the way for a wide range of magnetic switching schemes. More particularly, the design proposed by [Safeer et al., 2015] is not dictated by any magnetic in-plane field

which is beneficial from the application point of view. As long as the magnetic device size remains larger than the DW width Δ , the magnetic switching scheme remains based on the nucleation-propagation scenario. Therefore, it is still crucial to have a better understanding of the non-collinear current-induced DW motion. This experiment should be extended into many multilayered structures with different SIA since we expect the DW motion to be strongly dependent on the materials.

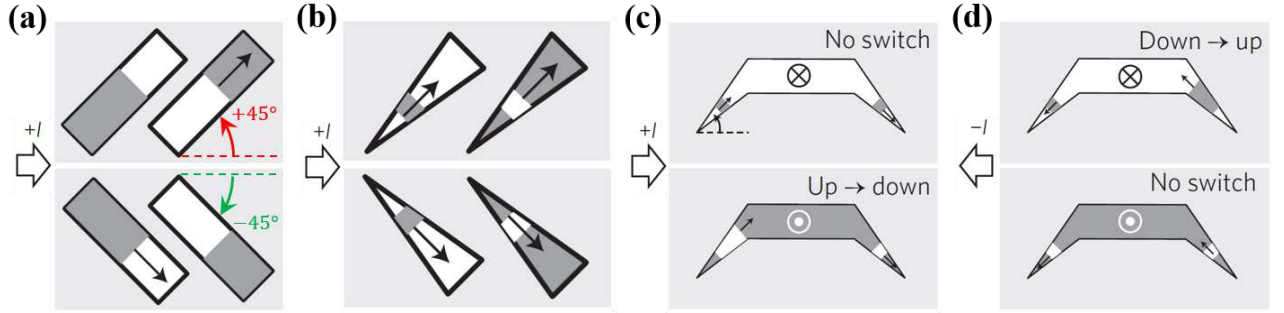


Figure III.3 The shape-controlled magnetic switching devices. (a) The asymmetric DW motion in tilted wires. The devices are based on the specific feature consisting in a single DW type moving in a wire tilted at 45°. (b) The DW selection in a pin-shaped tilted wire. In the narrow region of the pin-shaped wire, a reversed domain is nucleated due to Joule heating. Following (a), only one DW of the reversed domain is selected to move under the current. The operation mode of the ‘u-shape’ device under a positive (negative) current in (c) ((d)). The dark and white colors represent the up and down magnetic domains, respectively. The light grey rectangle is the heavy metal conductive layer. The black arrows indicate the DW motion. Extracted and adapted from [Safeer et al., 2015].

We can apply also an external in-plane magnetic field H_x to tune the action of SOT. This method has been widely used to determine the sign and the amplitude of the DMI (cf. section I.5.5.2). The equilibrium orientation of the DW core magnetization \mathbf{m}_{DW} is set by the effective magnetic fields within the DW: the magnetostatic ‘shape’ anisotropy field H_K that favors the Bloch configuration and the DMI field H_{DMI} that promotes the Néel configuration (cf. I.5.2). The in-plane field H_x can modify the orientation of the DW core magnetization \mathbf{m}_{DW} . By varying the amplitude of H_x , the angle between \mathbf{m}_{DW} and the current \mathbf{J} changes similarly to the DW motion in the non-collinear geometry. For instance, a positive in-plane field H_x reverses the chirality of the Néel wall from the left-handed (the top panel in **Figure III.4.a**) to the right-handed chirality (the bottom panel in **Figure III.4.b**). The angle ϕ_J between \mathbf{m}_{DW} and \mathbf{J} has been then changed from 0° to 180°. Consequently, the SOT-induced direction of the DW motion reverses between the two cases. It is possible to combine the two methods to tune the action of SOT: the non-collinear DW motion in the presence of H_x . This provides a more comprehensive picture of the CIDWM in SIA materials. In the absence of H_x , the motion of the DW sitting at a finite angle ϕ_J with respect to the current (the left panel in **Figure III.4.b**) is not similar to the DW motion in a straight wire. On the contrary, a large negative H_x saturates \mathbf{m}_{DW} (the right panel in **Figure III.4.b**). In this case, the SOT action is expected to be the same whether the DW is in a collinear or a non-collinear geometry. Therefore, this study allows verifying the validity of the DMI + SOT mechanism that was experimentally founded on the basis of the DW motion in a one-dimensional geometry. If the DW motion asymmetry persists, it indicates that new and complex physical mechanisms are involved in the CIDWM.

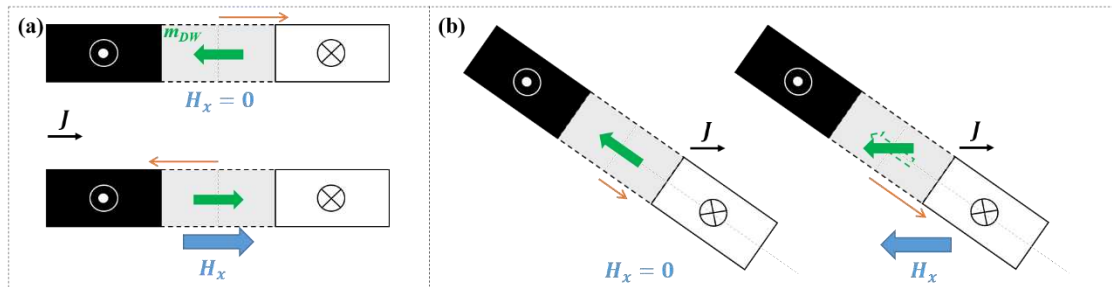


Figure III.4 The modulation of the DW core magnetization \mathbf{m}_{DW} by the in-plane magnetic field H_x . (a) Effect of H_x on Néel walls in a straight wire. By assuming a motion in the current direction for the left-handed chirality, a positive H_x reverses the direction of motion of the NW. (b) Effect of H_x on the non-collinear DW motion. A large negative H_x saturates \mathbf{m}_{DW} for the DW sitting in a tilted wire. Thus, the SOT action is similar to that on the NW in a straight wire ((a)). The orange arrows give the direction and the amplitude of the SOT-induced DW motion.

However, the extent of the modulation of the DW core magnetization \mathbf{m}_{DW} by \mathbf{H}_x depends strongly on the amplitude of the DMI, which in turn depends on SIA. A large SIA induces strong and robust effects: e.g. a large interfacial DMI that stabilizes homochiral NWs. It is then very difficult to modulate \mathbf{m}_{DW} . In contrast, it is expected to be less difficult to modulate \mathbf{m}_{DW} in a low SIA material. The characteristics of the non-collinear DW motion can thereby differ between a large SIA and a low SIA structures. The Pt/Co/AlOx stack has large SIA since bottom and top interfaces are totally different. It exhibits large DMI ($|D| = 2.71 \text{ mJ.m}^{-2}$ via BLS measurements [Belmeguenai et al., 2015]) and large SOT (torque-to-current ratios for T_{FL} and T_{DL} about -4.0 and $+6.9 \text{ mT per } 10^{11} \text{ A.m}^{-2}$, respectively [Garello et al., 2013]). The Pt/Co/AlOx stack has attracted a lot of attention after the report of fast CIDWM, up to a velocity of 400 m.s^{-1} , in the current direction without any Walker breakdown [Miron et al., 2011] (Figure III.5.a). As for the Pt/Co/Pt stack, it has low SIA. It is almost a symmetric structure as the Co layer is sandwiched between two layers made of the same element Pt. The low SIA is produced by crystallographic differences between top and bottom interfaces, inherent in the growth of the layers by sputtering. Unlike Pt/Co/AlOx, the SIA does not induce strong effects. Indeed, we have measured smaller DW velocities in Pt/Co/Pt (Figure III.5.b). Similarly to the creep (current density $J < 1.45 \cdot 10^{12} \text{ A.m}^{-2}$) and the depinning regime ($1.45 < J < 2 \cdot 10^{12} \text{ A.m}^{-2}$) seen in the FIDWM (cf. section I.3.4), the DW mobility increases with the current density. In the flow regime ($J > 2 \cdot 10^{12} \text{ A.m}^{-2}$), the DW velocity reaches a saturation plateau. Whereas for comparable current densities, the DW mobility is constant in Pt/Co/AlOx, which allows achieving larger velocities. Moreover, the ingredients of the DW dynamics under magnetic fields, in Pt/Co/Pt, are better understood so far after the proposal of the Chiral Damping mechanism. The Pt/Co/Pt stack gives then the opportunity to uncover the Chiral Damping role in the non-collinear DW motion.

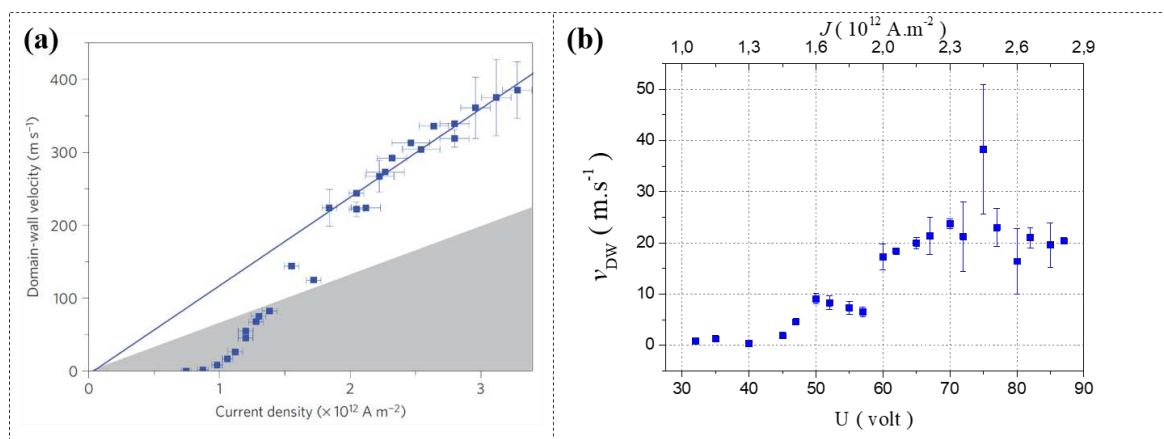


Figure III.5 Measurements of CIDWM in straight wires in different SIA materials. The DW velocity v_{DW} versus the current density J in (a) the Pt/Co/AlOx structure and in (b) the Pt/Co/Pt structure. (a) Extracted from [Miron et al., 2011].

The objective of this work is to have a better understanding of the current induced non-collinear DW motion. We propose thereby to study the non-collinear DW motion in the presence of a bias in-plane magnetic field in materials with different SIA. This chapter contains two main parts. After describing the procedure used to study the non-collinear DW motion, I will first present the experimental results obtained in Pt/Co/AlOx (large SIA) and next in Pt/Co/Pt (low SIA). I will discuss also the possible mechanisms that can explain these results.

III.2. Asymmetric distortion of magnetic circular domains

In my experiments, I have studied the non-collinear DW motion using a different method from that described in [Safeer et al., 2015]. The DW motion in a 2D geometry or in a non-collinear geometry means that the current is not injected perpendicular to the DW but in an oblique injection. Consequently, instead of fabricating tilted wires on top of the HM layer, I have investigated the effects of the current on a magnetic circular domain. In a $10 \mu\text{m} \times 20 \mu\text{m}$ magnetic wire, we inject a current density \mathbf{J} in the presence of a magnetic field \mathbf{H}_x . This allows us to nucleate reversed DWs at the four wire corners. An out-of-plane field \mathbf{H}_z is subsequently applied to propagate these DWs towards the wire center. By controlling their motion so that different DWs do not collapse into each other, a circular domain is formed in the wire center, away from edges, with a diameter of $4\text{--}8 \mu\text{m}$. We then assume a uniform current-distribution for the circular domain that we probe using a MOKE. **Figure III.6.a** shows, on the left, a representative sketch of a circular domain with an up magnetization (black or dark contrast). On the right, a MOKE image gives an example of a prepared up circular domain in the magnetic wire.

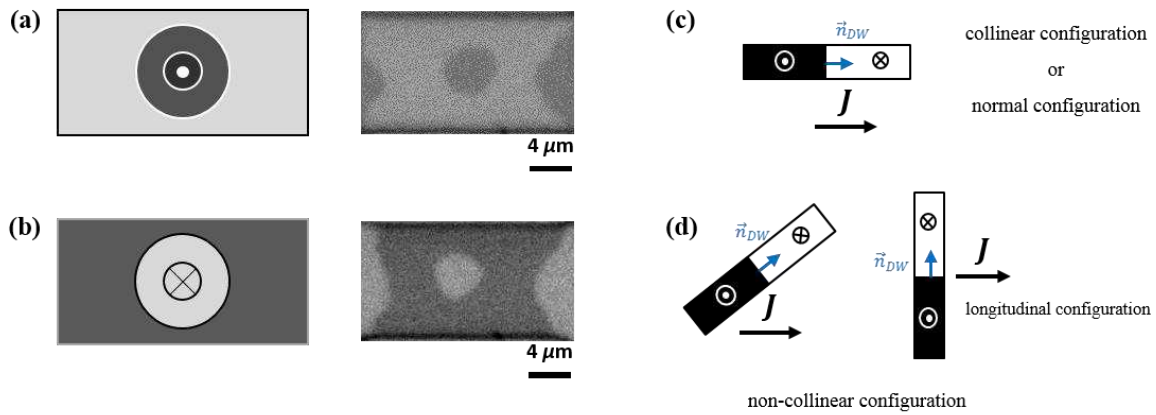


Figure III.6 Magnetic circular domains for the study of the non-collinear DW motion. (a) ((b)) Sketch of a prepared up (down) circular domain with the corresponding MOKE image. Sketch of a: (c) collinear and (d) non-collinear configuration for CIDWM. In the MOKE images, a dark (or a black) contrast represents the up magnetization and a white (or a bright) contrast corresponds to the down magnetization.

This method allows the DW propagation to be simultaneously monitored in the collinear and the non-collinear configurations. In the collinear configuration, the DW stands normal to the current flow, i.e. \mathbf{n}_{DW} , the DW normal vector that is parallel or anti-parallel to the current density vector \mathbf{J} (the straight wire in **Figure III.6.c**). In the non-collinear configuration, \mathbf{n}_{DW} has a nonzero angle ϕ_J with respect to \mathbf{J} (the tilted wires in **Figure III.6.d**). In addition, this method enables following the behavior of the two different DWs, i.e. the DW_{U-D} and the DW_{D-U} , at the same time. Each side of the magnetic circular domain corresponds to a different DW. **Figure III.7** emphasizes the advantage of studying the motion of a semi-circle shaped DW in a continuous film. Furthermore, since the DW spans continuously all angles (from -90° to $+90^\circ$), it is then possible to measure accurately the angle ϕ_J^{max} as a function of the current density and/or the applied in-plane field \mathbf{H}_x . This is valuable for a more complete picture of the non-collinear DW motion.

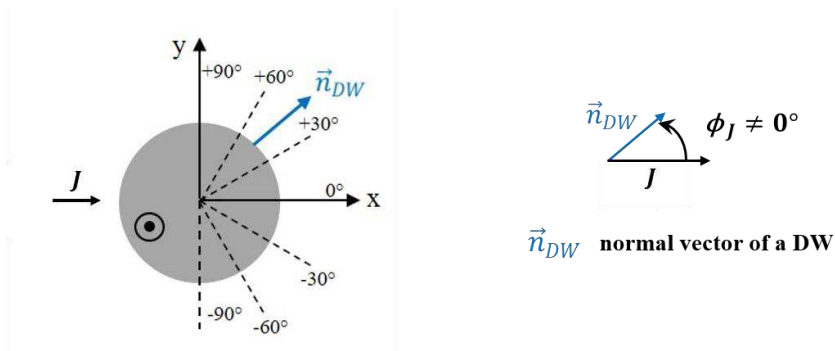


Figure III.7 Schematic diagram of the semi-circle shaped DW in a continuous film. The dark grey circle corresponds to an up circular magnetic domain under a positive current density J . The DW_{U-D} spans all the angles ϕ_J from -90° to $+90^\circ$ while crossing the position at $\phi_J = 0^\circ$ (collinear configuration). At the same time, the other side of the magnetic circular domain gives the DW_{D-U} motion.

The study of the magnetic circular domains helps also removing some artefacts associated with the study based on the patterned wires. The ferromagnet wires are patterned separately on top of the HM layer. This may distort the rectilinear current flow distribution so that it contributes to the observed DW motion asymmetry. Moreover, the DW can be tilted so that it is no longer sitting perpendicular to the wire (cf. chapter IV). In that case, the angle ϕ_J between the wire and the current direction is not necessarily the angle between the DW normal vector \mathbf{n}_{DW} and the current direction.

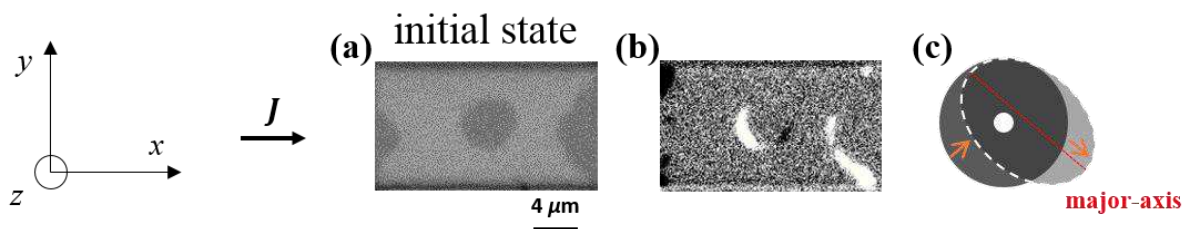


Figure III.8 Asymmetric current-induced distortion of the up magnetic circular domain in SIA materials. (a) Initial MOKE image. (b) Differential MOKE image after the current injection. (c) Illustration of the elliptical distortion obtained in (b). The dashed line emphasizes the final elliptical shape of the magnetic domain. The displacements of the semi-circle shaped DWs (magnetic contrast regions towards the center of the wire) are not symmetric with respect to the horizontal axis in (b). The orange arrows indicate the largest DW displacements in (c). In a differential MOKE image, a bright (dark) contrast corresponds to the magnetization that has been reversed from the up (down) to the down (up) orientation.

As observed in the Pt/Co/AlOx stack [Safeer et al., 2015], the largest current-induced DW displacement is towards positive and negative angles for the DW_{D-U} and the DW_{U-D} , respectively. The displacements of the semi-circle shaped DWs are not then symmetric with respect to the current direction (the x -axis). Therefore, the magnetic circular domain is distorted by the electric current and shows an elliptical shape (Figure III.8.c). We call this effect the asymmetric distortion of the magnetic domains. We have then followed the asymmetric distortion of the magnetic domains under MOKE to study of the non-collinear DW motion in Pt/Co/AlOx and Pt/Co/Pt.

III.3. Non-collinear DW motion in Pt/Co/AlOx

In Pt/Co/AlOx, a down magnetic circular domain is distorted asymmetrically as depicted in Figure III.9. This behavior takes place at different DW regimes of motion with the DW velocity v_{DW} increasing from $v_{DW} \sim 0.02 \text{ m.s}^{-1}$ (the creep regime) for a current density of $J \sim 0.7$ (Figure III.9.a) to $v_{DW} \sim 100 \text{ m.s}^{-1}$ (the flow regime) for a current density of $J \sim 2.73 \cdot 10^{12} \text{ A.m}^{-2}$ (Figure III.9.d).

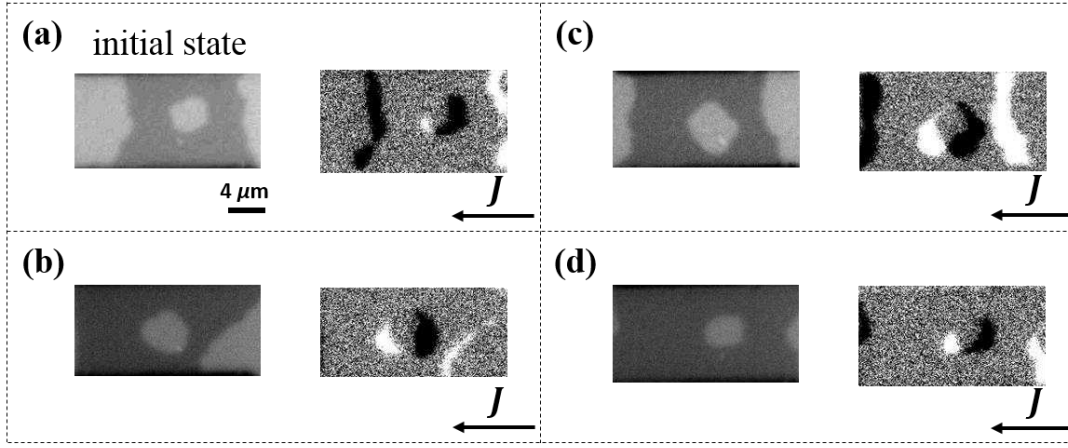


Figure III.9 Asymmetric distortion of the down magnetic domain for different current densities in Pt/Co/AlOx. We have applied different current density amplitudes, number of current pulses and current pulse lengths. (a) $J \sim -0.70 \cdot 10^{12} \text{ A.m}^{-2}$, 5000 pulses, 20 ns each. (b) $J \sim -0.83 \cdot 10^{12} \text{ A.m}^{-2}$, 500 pulses, 20 ns each. (c) $J \sim -1.45 \cdot 10^{12} \text{ A.m}^{-2}$, 80 pulses, 5 ns each. (d) $J \sim -2.73 \cdot 10^{12} \text{ A.m}^{-2}$, 40 pulses, 1 ns each. All MOKE differential images exhibit qualitatively the same asymmetry.

From the MOKE images in **Figure III.9**, we are able to deduce the asymmetric variation of the DW displacement, as schematized in **Figure III.10**. We observe opposite asymmetries between the DW_{U-D} and the DW_{D-U} in a good agreement with [Safeer et al., 2015]. Moreover, this asymmetric non-collinear DW motion is independent of the DW regime of motion because it is qualitatively the same for different current densities (**Figure III.9**). Actually, the DW dynamic deformation by the DMI + SOT mechanism predicts this kind of asymmetric motion but only in the flow regime.

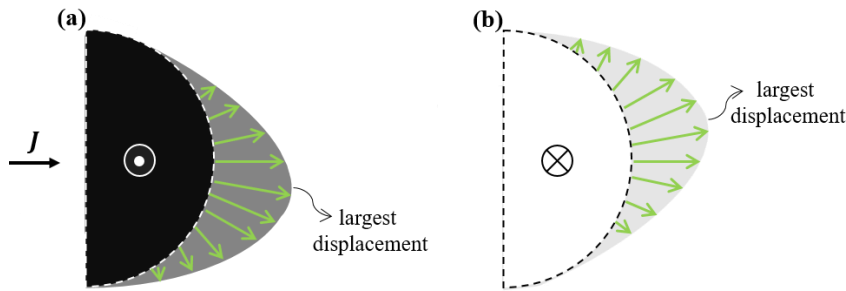


Figure III.10 Schematic diagrams of the asymmetric non-collinear DW motion observed in Pt/Co/AlOx. (a) for the DW_{U-D} and (b) for the DW_{D-U} . The dashed circular lines give the initial position of the semi-circle shaped DWs. The green arrows highlight the asymmetric variation of the DW displacement as a function of the angle ϕ_J .

III.3.1. The DMI + SOT mechanism in the flow regime

In non-collinear DW motion, the electric current effects are not linear. According to **Figure III.2.c**, at $\phi_J \neq 0^\circ$, series of positive current pulses followed by identical series of negative pulses do not bring the DW back to its initial position. If these effects were linear, the total displacement would be equal to zero. Following Eqs. **I.33** and **I.34**, the action of the damping-like torque T_{DL} on \mathbf{m}_{DW} is nonlinear either. Upon reversal of the current polarity, the extent of the canting of \mathbf{m}_{DW} by T_{DL} is not necessarily the same. This is due to the variation of the x -component (m_x) of \mathbf{m}_{DW} during the DW distortion. One is then tempted to interpret the asymmetric DW motion with ϕ_J in terms of the DMI + SOT mechanism.

In Pt/Co/AlOx, the strong DMI stabilizes left-handed chiral NWs. The distortion of such NWs by SOT results in the asymmetric motion with ϕ_J in the flow regime. To visualize this mechanism, we consider the action of the damping-like torque T_{DL} on the DW core magnetization \mathbf{m}_{DW} (**Figure III.11**). In the left-handed NW configuration, the DW core magnetization \mathbf{m}_{DW} sits

perpendicular to the DW plane, pointing from the down towards the up magnetic domain. While injecting the current, \mathbf{T}_{DL} cant away \mathbf{m}_{DW} from its equilibrium orientation inducing a terminal deformation angle \mathcal{E} of the DW internal structure.

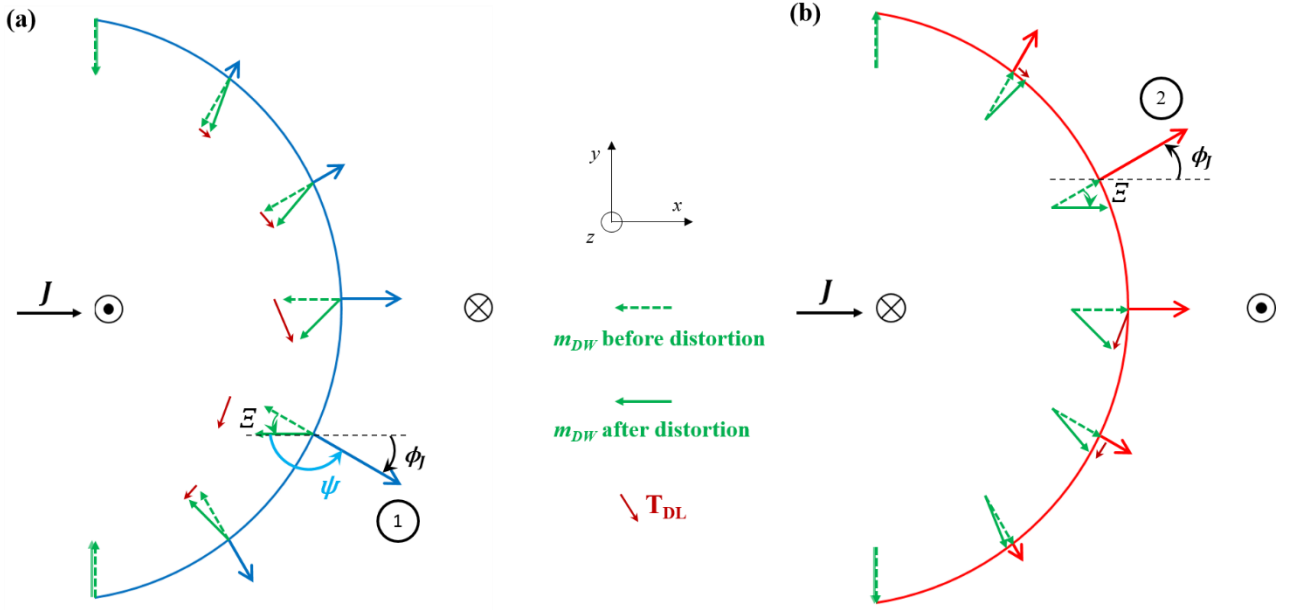


Figure III.11 Schematic diagram of the distortion of left-handed NWs by SOT in the non-collinear configuration. (a) The DW_{U-D} and (b) the DW_{D-U} . \mathbf{T}_{DL} cant away \mathbf{m}_{DW} with a deformation angle \mathcal{E} . At ϕ_J^{max} , the deformation angle \mathcal{E} aligns \mathbf{m}_{DW} with the current thus the maximum DW velocity. The angle ψ is the angle between \mathbf{m}_{DW} and \mathbf{n}_{DW} with \mathbf{n}_{DW} parallel to \mathbf{v}_{DW} for any angle ϕ_J . The blue (red) arrows represent the velocity vector of the DW_{U-D} (DW_{D-U}). The dark red arrows corresponds to the damping-like torque \mathbf{T}_{DL} . The DW core magnetization \mathbf{m}_{DW} is given by a (dotted) straight green arrow (before) after being distorted by \mathbf{T}_{DL} .

By analogy with FIDWM, the DW velocity v_{DW} is dictated by the damping-like field \mathbf{H}_{DL} in the steady-state regime. According to Eq. I.19, the DW_{U-D} velocity v_{UD} can be written as (Figure III.11.a):

$$v_{UD} = \frac{\gamma\Delta}{\alpha} |\mathbf{H}_{DL}| \quad (\text{III.1})$$

where $\mathbf{H}_{DL} = J\mathbf{H}_{DL}(\mathbf{u}_y \times \mathbf{m}_{DW})$. Thus, \mathbf{T}_{DL} rotates \mathbf{m}_{DW} anti-clockwise with an angle $\mathcal{E} > 0$ giving $\mathbf{m}_x = -\cos(\mathcal{E} + \phi_J)\mathbf{u}_x$ in the non-collinear configuration. Eq. III.1 is rewritten as:

$$v_{UD} = \frac{\gamma\Delta}{\alpha} JH_{DL} \cos(\mathcal{E} + \phi_J) \quad (\text{III.2})$$

On the upper half of the DW_{U-D} ($0^\circ \leq \phi_J \leq +90^\circ$), v_{UD} decreases monotonously due to the term $\cos(\mathcal{E} + \phi_J)$. At $\phi_J = 0^\circ$, v_{UD} is not maximum since the distortion by \mathbf{T}_{DL} reduces the component \mathbf{m}_x ($\cos \mathcal{E} < 1$). Instead, the fastest motion occurs on the lower half of the DW_{U-D} ($-90^\circ \leq \phi_J < 0$) at the position 1 where the distortion makes \mathbf{m}_{DW} collinear with the current \mathbf{J} (for $\mathcal{E} = -\phi_J$). This is in line with the obtained negative angle ϕ_J^{max} for the DW_{U-D} . The distortion of \mathbf{m}_{DW} is clockwise for the DW_{D-U} thus a maximum velocity at the position 2 as shown in Figure III.11.b (a positive angle ϕ_J^{max}).

Micromagnetic simulations, in literature, confirm such a scenario. Without disorder and for a high current density of $2 \cdot 10^{12}$ A.m⁻² (the flow regime of motion), [Eduardo et al., 2016] fitted the normalized DW displacement $d(J, \phi_J)$ by its maximum d_{max} as a function of $(\phi_J - \mathcal{E})$ following the equation:

$$\frac{d(J, \phi_J)}{d_{max}} = \cos(\phi_J - \mathcal{E}) \quad (\text{III.3})$$

where ϕ_J and \mathcal{E} are expressed in their absolute values. The dependence on $(\phi_J - \mathcal{E})$ is in line with Eq. III.2 expressed for the DW velocity v_{DW} . Accordingly, the angle of the largest displacement is determined as $\phi_J^{max} = \mathcal{E}$ for chiral NWs. It depends on both the initial DW structure and the amplitude of the distortion by T_{DL} . Therefore, ϕ_J^{max} is expected to be a function of the current density J , material parameters (the DMI constant $|D|$ and the spin Hall angle θ_{SH} of the HM layer) and the injection time of the current. In addition, ϕ_J^{max} can be a function of the applied in-plane magnetic field H_x if the latter is capable to modify the initial DW structure through the modulation of the DW core magnetization m_{DW} . We propose then to test the validity of the DMI + SOT mechanism by examining the variation of the angle ϕ_J^{max} as a function of the current density J and of H_x . To that end, we have studied the non-collinear DW motion in the presence of H_x .

III.3.2. The DW motion in the presence of an in-plane magnetic field

III.3.2.1. Effects of the in-plane magnetic field

Here, we present the effects induced by the magnetic field H_x on the asymmetric distortion of magnetic circular domains in Pt/Co/AlOx. Asymmetric DW motion with ϕ_J is maintained up to $|H_x| = 150$ mT. The up magnetic domain, in **Figure III.12**, loses its round shape to adopt an elliptical form similar to that obtained at $H_x = 0$. Thus, the angle ϕ_J^{max} keeps the same symmetry for the two different DWs in the presence of H_x .

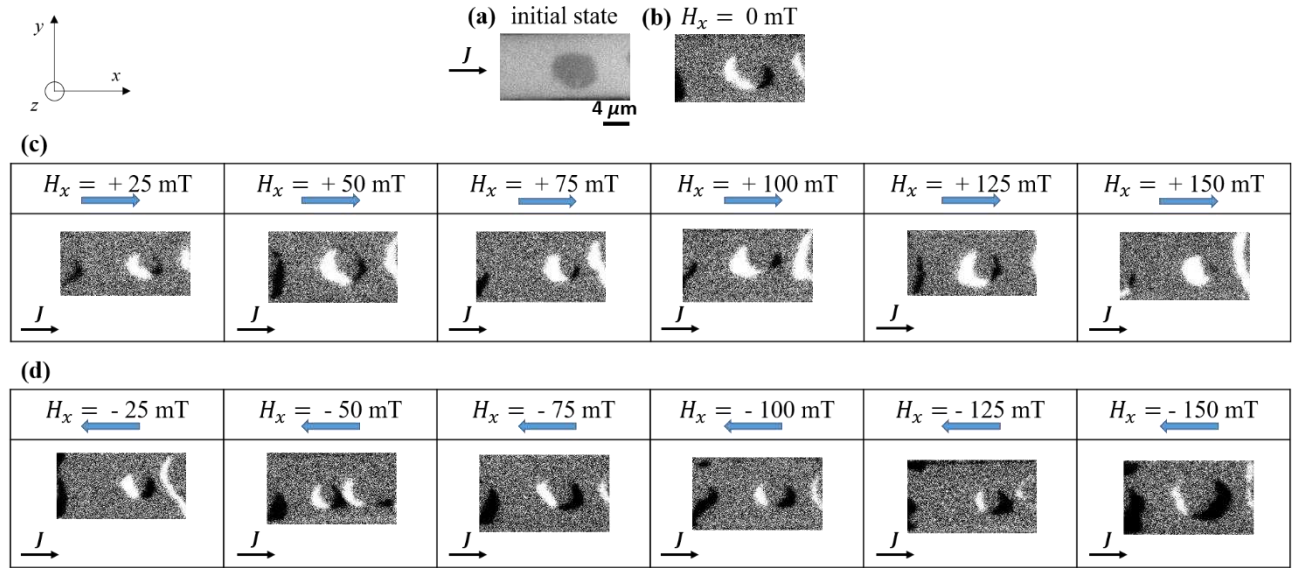


Figure III.12 Asymmetric distortion of the up domain in Pt/Co/AlOx in the presence of H_x under a positive current. (a) Initial MOKE image of the up domain before the injection of current. (b) Differential MOKE images of the final state of the up domain after current injection at $H_x = 0$ in (b), at a positive (respect. negative) H_x in (c) (respect. (d)). The current density is $J \sim + 2.75 \cdot 10^{12} \text{ A.m}^{-2}$.

From the MOKE images (**Figure III.12**), we can detect the effects of H_x by following the motion of the center of the magnetic circular domain. Due to the asymmetric non-collinear DW motion, the center has a vertical motion (along the y-axis) along with the horizontal motion (along the x-axis). To determine the direction of motion of these two components, we compare the position of the center of the final magnetic domain state with that of the initial magnetic domain state in the differential MOKE image. In all the MOKE differential images, we focus on the magnetic contrast regions towards the wire center. The magnetic contrast region on the left gives the displacement of the semi-circle shaped DW_{D-U} while the magnetic contrast region on the right corresponds to that of the semi-circle shaped DW_{U-D} . Whether H_x is positive or negative, the DW_{D-U} contrast is always

bright while the DW_{U-D} contrast is dark. Thus, according to the description of the MOKE microscopy in section II.2, the center of the up domain moves horizontally in the current direction for any applied in-plane field. In addition, each contrast region has an asymmetry with respect to the x -axis, similar to that obtained at $H_x = 0$. This confirms that the angle ϕ_J^{max} does not change its sign for both DWs. In **Figure III.12**, the initial up magnetic domain is then represented by the bright contrast region associated with the central grey textured region. The central grey textured region associated with the dark contrast region gives the final up magnetic domain state. We infer then that the center of the up domain moves upwards (downwards) for a positive (negative) H_x . Such a vertical motion can be accounted for by the competition between H_x and the DMI effective magnetic field H_{DMI} within each DW. Since DMI stabilizes left-handed NWs in Pt/Co/AlOx, a positive H_x is parallel to H_{DMI} within the DW_{D-U} whereas they are anti-parallel inside the DW_{U-D} . The action of the damping-like torque T_{DL} is then less effective on the DW_{U-D} than on the DW_{D-U} . This results in an asymmetric motion between the two DWs with the semi-circle shaped DW_{D-U} being faster. As its largest displacement takes place at a positive angle ϕ_J^{max} , the size of the up magnetic domain reduces for a positive H_x (**Figure III.12.c**) and the center moves in the $+y$ -axis direction. It is the opposite situation for a negative H_x that is parallel and anti-parallel to H_{DMI} inside the DW_{U-D} and DW_{D-U} , respectively. Thereby, since the angle ϕ_J^{max} is negative for the DW_{U-D} , the up magnetic domain increases its size for a negative H_x with its center moving in the $-y$ -axis direction as obtained in **Figure III.12.d**. These different scenarios of the asymmetric distortion of the up magnetic circular domain under a positive current in Pt/Co/AlOx are summarized in **Figure III.13**.

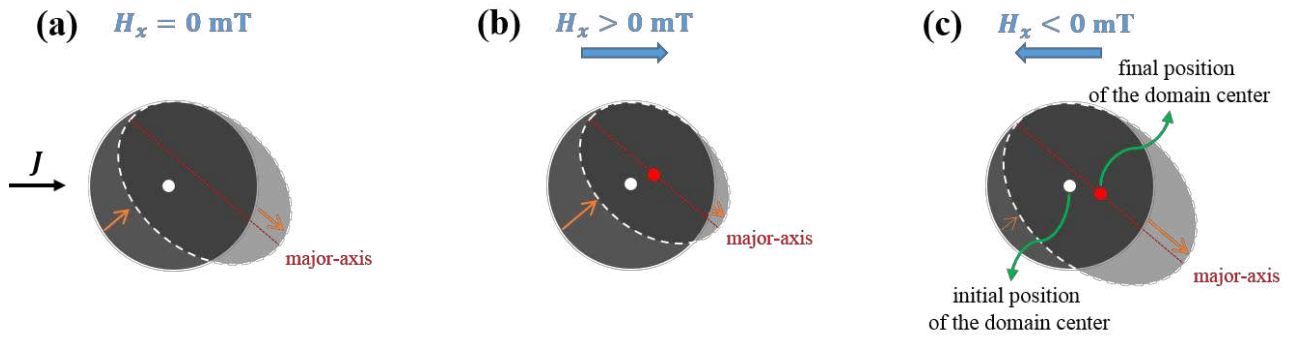


Figure III.13 Schematic diagram of the asymmetric distortion of the up magnetic circular domain under a positive current in the presence of H_x in Pt/Co/AlOx. $H_x = 0$ in (a), positive in (b) and negative in (c).

To confirm that the observed phenomenon is not an artifact, we have checked the domain distortion for the other magnetization and/or current polarities. An up domain under a negative current is equivalent to an up domain under a positive current by the 180° rotation symmetry operation around the z -axis. Their respective distortions should follow the symmetry operation as illustrated in **Figure III.14.a-d**. Under a negative current, the up domain is expected to expand with its center moving upwards at a positive H_x while it shrinks with its center moving downwards at negative H_x , which has been found to be in agreement with the experiment (**Figure III.14.e-f**).

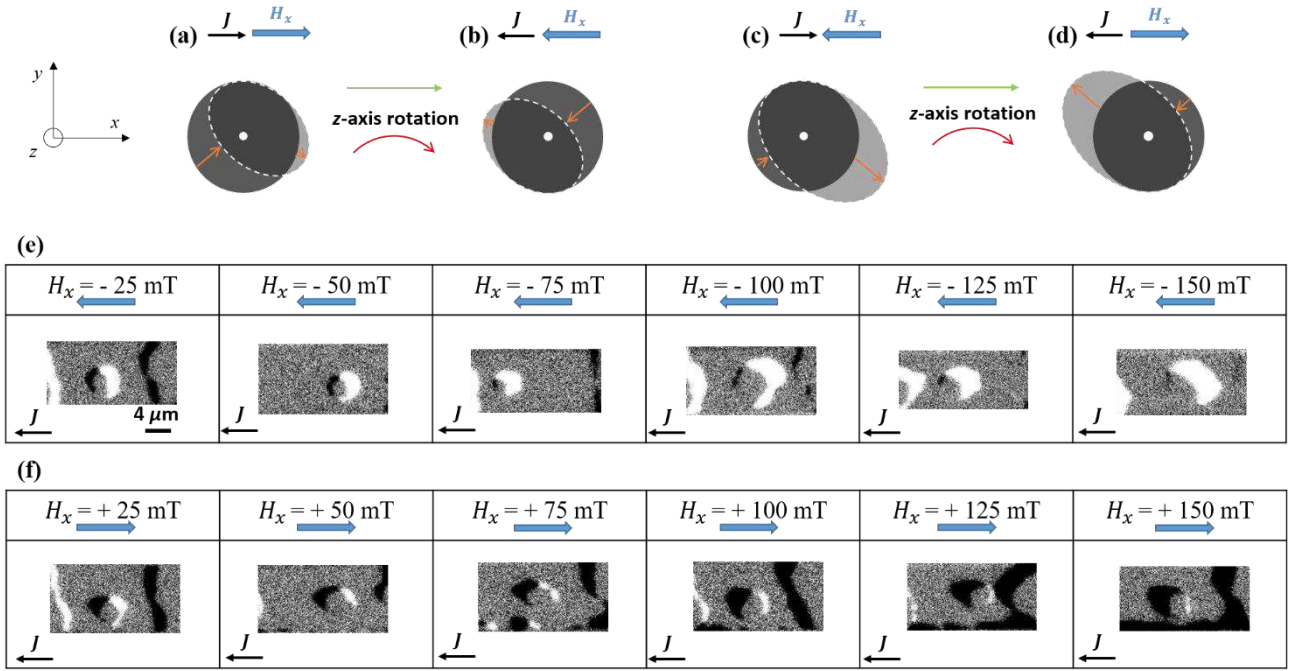


Figure III.14 Asymmetric distortion of the up magnetic domain in Pt/Co/AlOx in the presence of H_x under a negative current. (a)-(d) The image of the distortion of an up domain under a positive current by the 180° rotation symmetry operation around the z-axis in Pt/Co/AlOx. The image of an up domain under a positive current at a positive H_x in (a) (respect. negative (c)) is an up domain under a negative current at a negative H_x in (b) (respect. positive (d)). The obtained distortion of the up domain under $J \sim -2.73 \cdot 10^{12}$ A.m⁻² at a negative (respect. positive) H_x in (e) (respect. (f)).

As for the down magnetic domain, **Figure III.15** (respect. **Figure III.16**) gives the effect of H_x under a positive (respect. negative) current. In both cases, the observed distortion follows, by the corresponding symmetry operation, the image of the distortion of the up magnetic domain under a positive current in **Figure III.12**.

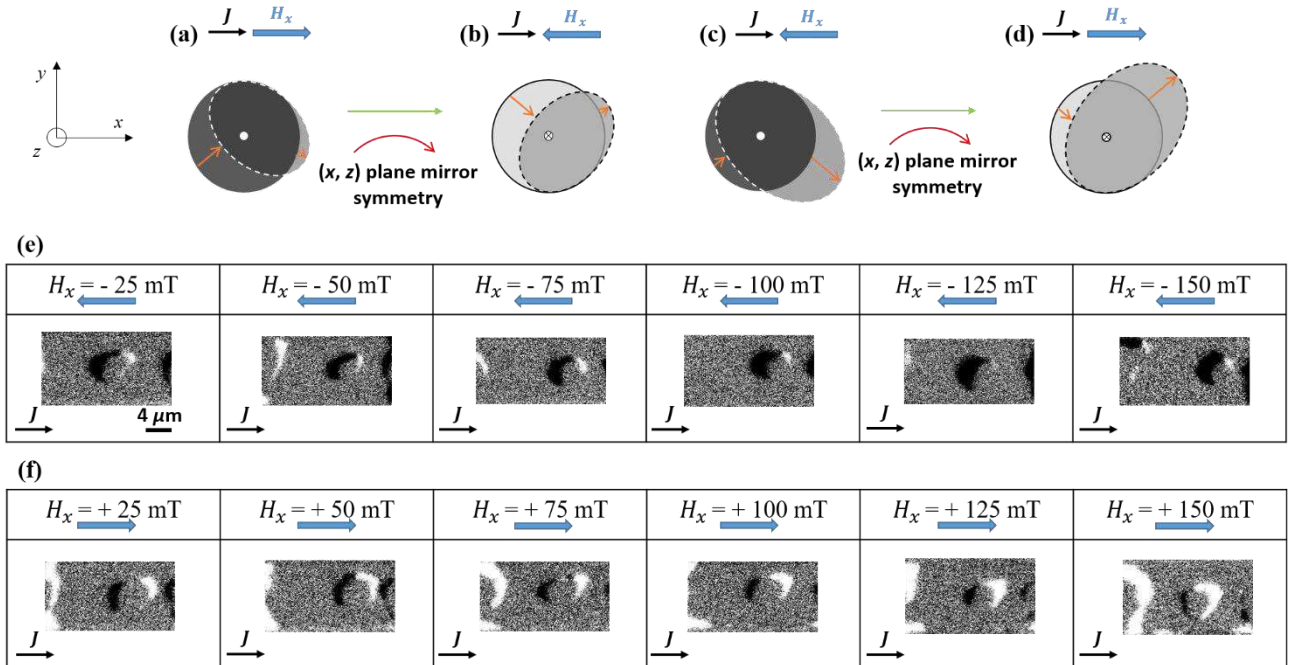


Figure III.15 Asymmetric distortion of the down magnetic domain in Pt/Co/AlOx in the presence of H_x under a positive current. (a)-(d) The image of the distortion of an up domain by the (x, z) plane mirror symmetry operation in Pt/Co/AlOx. The image of an up domain under a positive current at a positive H_x in (a) (respect. negative (c)) is a down domain under a positive at a negative H_x in (b) (respect. positive (d)). The obtained distortion of the down domain under $J \sim +2.75 \cdot 10^{12}$ A.m⁻² at a negative (respect. positive) H_x in (e) (respect. (f)).

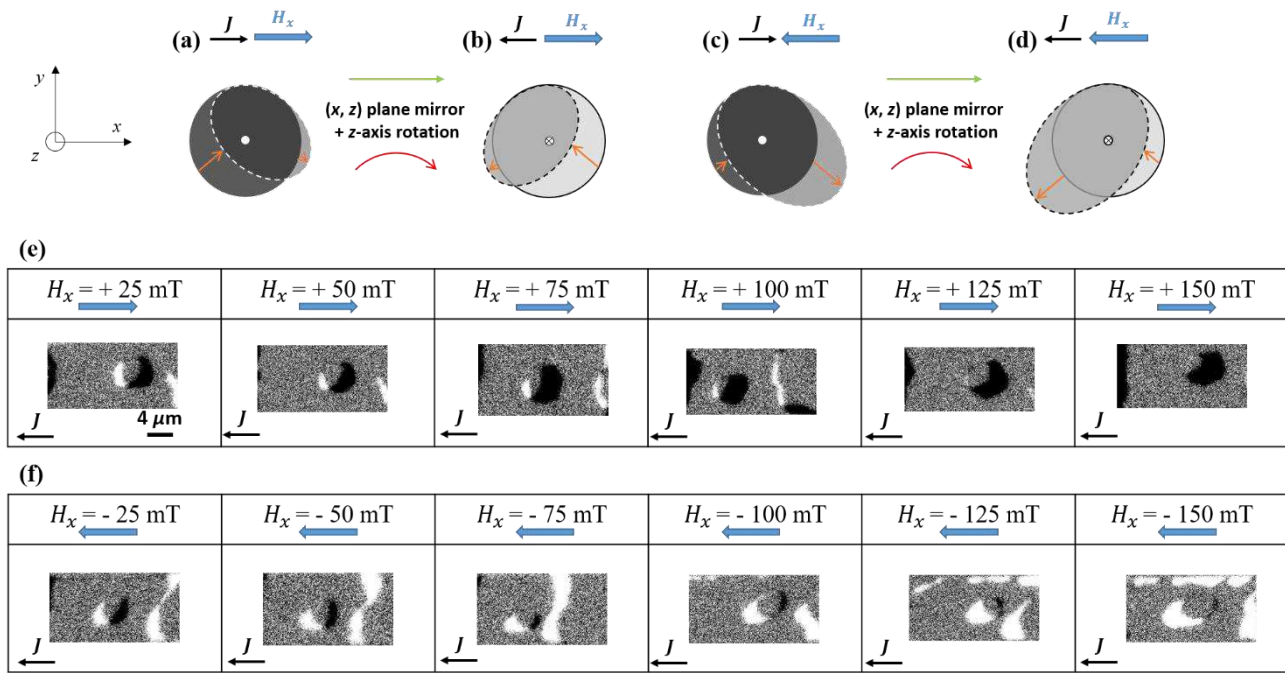


Figure III.16 Asymmetric distortion of the down magnetic domain in Pt/Co/AlOx in the presence of H_x under negative current. (a)-(d) The image of the distortion of an up domain by the (x, z) plane mirror symmetry operation followed by the 180° rotation around the z -axis in Pt/Co/AlOx. The image of an up domain under a positive current at a positive H_x in (a) (respect. negative (c)) is a down domain under a negative current at a positive H_x in (b) (respect. negative (d)). The obtained distortion of the down magnetic domain under $J \sim -2.73 \cdot 10^{12} \text{ A.m}^{-2}$ at a positive (respect. negative) H_x in (e) (respect. (f)).

We have seen that for all polarities for the magnetization and/or the current, the distortion of the magnetic circular domain follows well the symmetry operations. This rules out any possible contribution from artefacts. The in-plane field H_x does not then alter the asymmetric DW motion with ϕ_J in Pt/Co/AlOx.

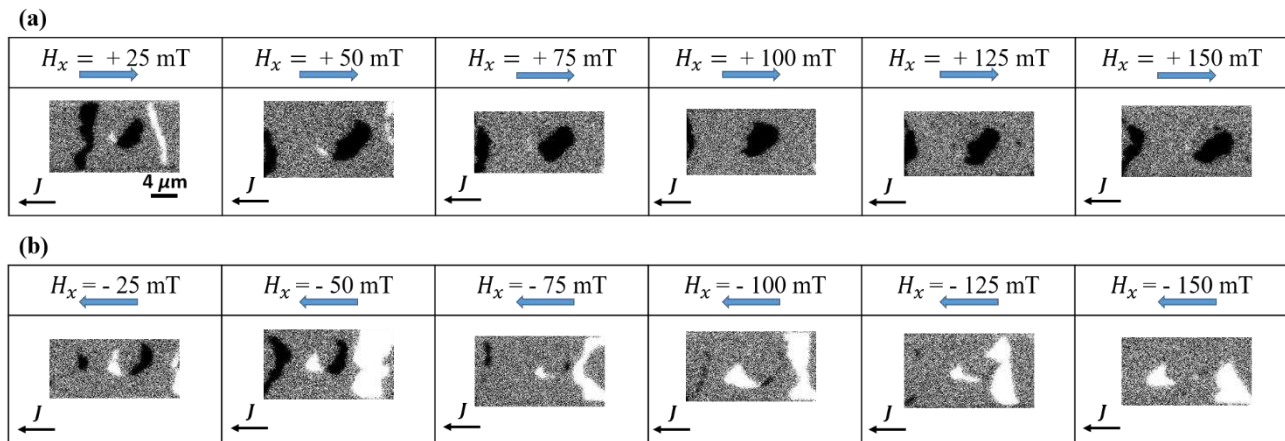


Figure III.17 Asymmetric distortion of the down magnetic domain under $J \sim -0.70 \cdot 10^{12} \text{ A.m}^{-2}$ in the presence of H_x in Pt/Co/AlOx. The obtained distortion at a positive (respect. negative) H_x in (a) (respect. (b)).

These observations were obtained for current densities of $J \sim +2.75 \cdot 10^{12} \text{ A.m}^{-2}$ and $J \sim -2.73 \cdot 10^{12} \text{ A.m}^{-2}$, which corresponds to the high velocity regime (the flow regime). We obtained the same features for $J \sim 0.70 \cdot 10^{12} \text{ A.m}^{-2}$ (the creep regime according to **Figure III.5.a**) in **Figure III.17** and for $J \sim 1.45 \cdot 10^{12} \text{ A.m}^{-2}$ (the depinning regime according to **Figure III.5.a**) in **Figure III.18**. Therefore, the asymmetric DW motion with ϕ_J in the presence of H_x is independent of the DW regime of motion.

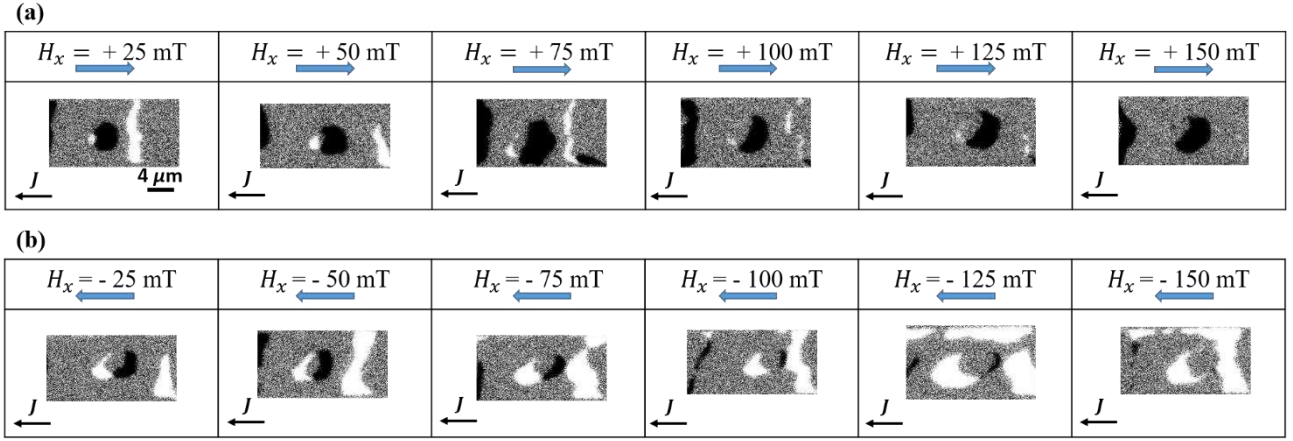


Figure III.18 Asymmetric distortion of the down magnetic domain under $J \sim -1.45 \cdot 10^{12} \text{ A.m}^{-2}$ in the presence of H_x in Pt/Co/AlOx. The obtained distortion at a positive (respect. negative) H_x in (a) (respect. (b)).

Even though H_x induces an asymmetric motion between the two different DWs, we did not obtain any reversal of the DW direction up to $|H_x| = 150 \text{ mT}$. In addition, the angle ϕ_J^{max} keeps the same symmetry at any in-plane field for both DWs. These features indicate that it is difficult to modulate the DW core magnetization \mathbf{m}_{DW} by H_x which is expected since the DMI is large in the Pt/Co/AlOx stack. According to Eq. I.38 and parameters for similar nominal structures ($|D| = 2.71 \text{ mJ.m}^{-2}$ [Belmeguenai et al., 2015], $M_s = 1090 \text{ kA.m}^{-1}$ [Miron et al., 2010] and $\Delta = 5.64 \text{ nm}$ [Jué, 2013]), a rough estimation gives $|H_{DMI}| \approx 690 \text{ mT}$ which lies far beyond the available experimental range of H_x . In the meantime, the DW displacement varies significantly in the presence of H_x . This indicates that the action of SOT in the non-collinear DW motion has been significantly modified. Thus, we expect the angle ϕ_J^{max} to show a net quantitative variation in the presence of H_x .

III.3.2.2. Measurement of the angle ϕ_J^{max}

In this work, I have not carried out quantitative measurements of current-induced DW motion. Since it is the similar Pt/Co/AlOx system, I refer to measurements of the CIDWM in the presence of an in-plane magnetic field done in the previous works of [Jué, 2013] in straight nanowires ($\phi_J = 0^\circ$) and of [Safeer et al., 2015] in tilted nanowires ($\phi_J \neq 0^\circ$) (Figure III.19). [Jué, 2013] observed that H_x changes significantly the DW velocity v_{DW} . In the flow regime, even at a moderate amplitude of the in-plane field ($|H_x| = 75 \text{ mT}$), the DW velocity v_{DW} changes with more than a factor of two compared to the velocity at $H_x = 0$ (Figure III.19.a). [Safeer et al., 2015] obtained a similar trend for the DW displacements, measured in wires placed at different angles ϕ_J in steps of $\sim 15^\circ$ (Figure III.19.b). According to the DMI + SOT mechanism, these observations indicate that the action of SOT is significantly dependent on H_x . [Safeer et al., 2015] reported an estimation of ϕ_J^{max} in the flow regime of motion only at $H_x = 0$ with $\phi_J^{max} \approx 20^\circ$. For H_x varying from -150 up to +150 mT, the largest DW displacement is always situated between $\phi_J = 15^\circ$ and $\phi_J = 30^\circ$ (Figure III.19.b). Following the DMI + SOT mechanism, the angle ϕ_J^{max} is expected to vary between these two values in the presence of H_x . We have performed then exact measurements of the angle ϕ_J^{max} at different H_x and under different current densities J .

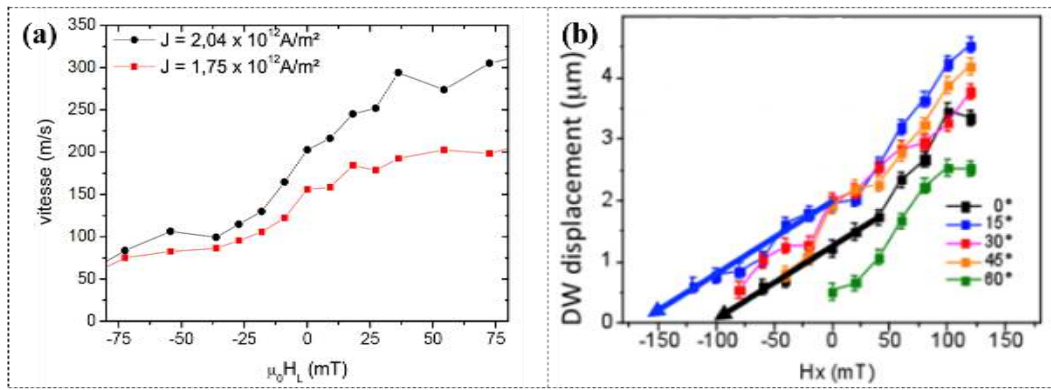


Figure III.19 The CIDWM in the presence of an in-plane magnetic field in the Pt/Co/AlOx structure. (a) The DW velocity v_{DW} versus H_L for the DW_{D-U} measured in a straight wire. Here, H_L stands for a longitudinal in-plane field that is equivalent to H_x . (b) DW displacement (in μm) versus H_x under a current density of $1.6 \cdot 10^{12} \text{ A.m}^{-2}$ at different angles ϕ_j . Each color corresponds to a value of ϕ_j . The wires tilted at 15° (blue) and 30° (red) exhibit the largest DW displacement independently of H_x . (a) extracted from [Jué, 2013] and (b) from [Safeer et al., 2015].

In fact, the first detected DW displacement gives the angle ϕ_j^{max} (Figure III.20.a). It corresponds to the first region under MOKE that yields a magnetic contrast. ϕ_j^{max} is then the angle between the wire axis and the line connecting the center of the initial circular domain to the magnetic contrast region. Here, the angle ϕ_j^{max} is taken as the angle of the first and largest displacement of the DW and can be considered then as the angle of maximum velocity.

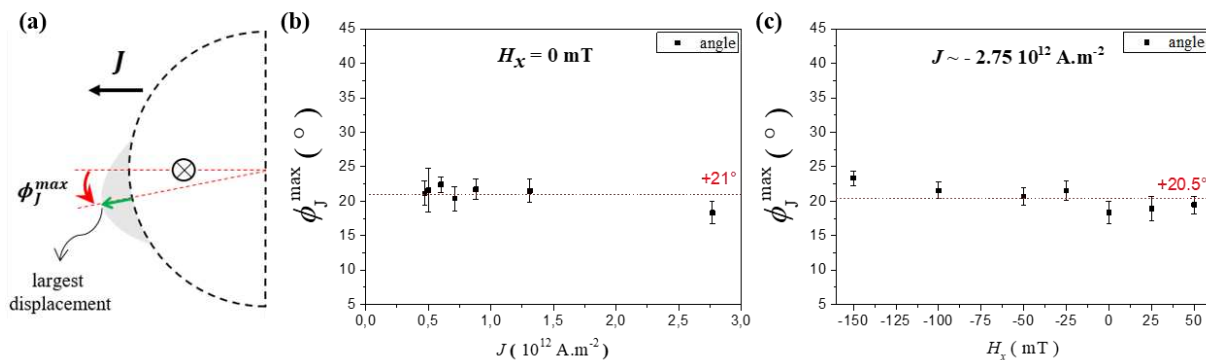


Figure III.20 Measurement of the angle ϕ_j^{max} in the non-collinear DW motion in Pt/Co/AlOx. (a) Schematic diagram describing the estimation procedure of ϕ_j^{max} via MOKE. The light grey area corresponds to the first DW displacement induced by the current. Here, the measurements are performed for the DW_{U-D} driven by a negative current. (b) The angle ϕ_j^{max} versus the current density J at $H_x = 0 \text{ mT}$. (c) The angle ϕ_j^{max} versus H_x under $J \sim -2.75 \cdot 10^{12} \text{ A.m}^{-2}$. Dashed red lines in (b) and (c) give the average ϕ_j^{max} .

In the absence of H_x , the estimation of the angle ϕ_j^{max} was conducted for different current densities varying from $\sim 0.47 \cdot 10^{12} \text{ A.m}^{-2}$ to $\sim 2.77 \cdot 10^{12} \text{ A.m}^{-2}$ (from the creep to the flow regime of motion). We have obtained a constant ϕ_j^{max} with an average value of $\approx 21^\circ$ (Figure III.20.b). In the presence of H_x , the angle ϕ_j^{max} does not show any net variation (considering the error bars) in the flow regime (for $J \sim 2.75 \cdot 10^{12} \text{ A.m}^{-2}$) (Figure III.20.c). We can estimate an average angle ϕ_j^{max} equal to $\approx 20.5^\circ$. These measurements are in a good agreement with measurements in the flow regime at $H_x = 0$ done by [Safeer et al., 2015]. We note that we were not able to measure the angle ϕ_j^{max} at $H_x > +50 \text{ mT}$ as the faster DW_{D-U} rapidly collapses into the DW_{U-D}. The estimation of the angle ϕ_j^{max} as a function of H_x in the creep regime was not performed. Due to pinning effects, more statistics are needed to conduct this kind of measurements in this regime. This is beyond the scope of this thesis.

These findings are in conflict with the DMI + SOT mechanism in Pt/Co/AlOx. We deduce that such a mechanism is incomplete and cannot explain all the features of the DW motion in the flow regime in large SIA materials. There is a need to consider other mechanisms. Besides these

incompatibilities in the flow regime, the DMI + SOT mechanism show limitations with the experimental observations in the creep regime of motion.

III.3.3. Asymmetric DW motion in the creep regime

In the DMI + SOT mechanism, the DW velocity depends on the terminal deformation angle of the DW core magnetization \mathbf{m}_{DW} that is induced by the damping-like torque \mathbf{T}_{DL} . A significant DW distortion gives a large velocity whereas a limited velocity is synonym of a small distortion. In the creep regime, we cannot describe the DW dynamics by simply considering the DMI + SOT mechanism. The DWs need to be considered as elastic interfaces in a disordered medium so that they are sensitive to imperfections or defects. These defects act as local pinning centers. While being driven by the current, the DW is either pinned or hopping between the pinning centers. Therefore, the average velocity of the DW can be written as:

$$\langle v_{DW} \rangle \approx \frac{\Delta l}{\Delta t} = \frac{\Delta l}{\Delta t_{depinning} + \Delta t_{hopping}} \quad (\text{III.4})$$

where Δl is the total displacement of the DW and Δt the integrated time or the current injection time. The DW spends a large time trying to depin itself from the pinning centers and moves only for a short period; $\Delta t_{depinning} \gg \Delta t_{hopping}$. The DW velocity v_{DW} is then largely determined by the depinning time even though $\Delta t_{hopping}$ depends, in principle, on the angle ϕ_J between the current direction \mathbf{J} and the DW normal vector \mathbf{n}_{DW} . Following such a scenario, the DW velocity is small and its variation with the angle ϕ_J is not as visible as it is in the flow regime. Therefore, the asymmetry of the DW motion is expected to reduce in the creep regime and the angle ϕ_J^{max} of the largest DW displacement to approach the angle $\phi_J = 0^\circ$ (the collinear configuration).

Micromagnetic simulations have confirmed that the angle ϕ_J^{max} decreases in the creep regime by incorporating the thermal fluctuations, edge roughness and a random distribution of the anisotropy K_u in grains in 512 nm-wide stripes to mimic the pinning landscape [Eduardo et al., 2016]. The angle ϕ_J^{max} is reduced from 45° in perfect wires to 30° in realistic wires for a large current density (Figure III.21.b).

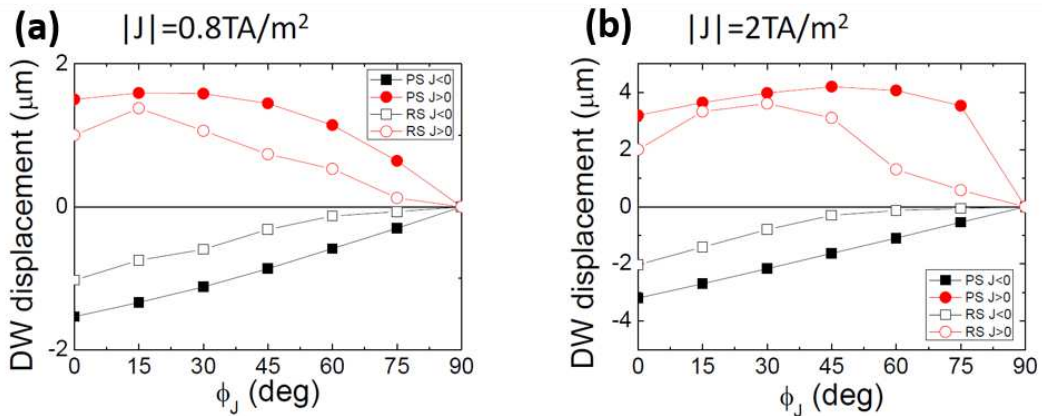


Figure III.21 The DW_{U-D} displacements versus the tilt angle ϕ_J for different current densities from micromagnetic simulations based on the DMI + SOT mechanism. The comparison between PS (perfect stripes with no imperfections) and RS (stripes at room temperature with disorder) for an injected current density of (a) $0.8 \cdot 10^{12} \text{ A.m}^{-2}$ and (b) $2 \cdot 10^{12} \text{ A.m}^{-2}$. The disorder and thermal effects reduce ϕ_J^{max} . Decreasing the current reduces also ϕ_J^{max} . Extracted and adapted from [Eduardo et al., 2016].

Moreover, simulations did not yield any DW displacement without taking into account the thermal fluctuations under $J = 0.8 \cdot 10^{12} \text{ A.m}^{-2}$. The regime of the DW motion corresponds then to the thermally activated regime with the angle ϕ_J^{max} equal to 15° (Figure III.21.a). This tendency

confirms that the angle ϕ_j^{max} is expected to show a notable reduction when decreasing current density. This is not in line with our experimental measurements of the angle ϕ_j^{max} shown in **Figure III.20.b**.

To conclude, we have pursued the study of the non-collinear DW motion in the Pt/Co/AlO_x structure that has a large SIA. By providing a comprehensive picture thanks to our experimental results, we have confirmed that the DMI + SOT mechanism fails to explain all the DW motion features in the flow regime. The asymmetric motion in the non-collinear geometry is not altered neither by the current nor by the in-plane magnetic field. These results are difficult to analyze since it is difficult to modulate the DW core magnetization in this kind of structures. Next, I present the results of the study carried out in the Pt/Co/Pt structure. In this low SIA material, the non-collinear DW motion is expected to exhibit different behaviors since the DW core magnetization can be manipulated by the in-plane magnetic field.

III.4. Non-collinear DW motion in Pt/Co/Pt

In this section, I will address the current-induced non-collinear DW motion in Pt/Co/Pt. The SIA is low in this material. Nonetheless, the FIDWM in the presence of a bias in-plane field is asymmetric between the two different DWs implying that a significant chiral mechanism, originating from SIA, acts on the DW motion. This investigation has led to the proposal of a novel phenomenon: the Chiral Damping [Jué et al., 2015]. Initially, the goal behind our study was to verify if the Chiral Damping (CD) mechanism has a role to play in the CIDWM.

Our preliminary investigations of the CIDWM have suggested an acting DMI and SOT in the Pt/Co/Pt structure. I have thus determined the sign of both the DMI and the damping-like torque T_{DL} by means of a qualitative study of the CIDWM. We have then studied the non-collinear DW motion in the presence of an in-plane field H_x . To explain our results, we have included the Chiral Damping in the used numerical model. Our investigation have evidenced the important interplay between chiral energy (DMI) and chiral dissipation (Chiral Damping) for the DW motion in SIA materials.

III.4.1. The presence of the DMI in Pt/Co/Pt

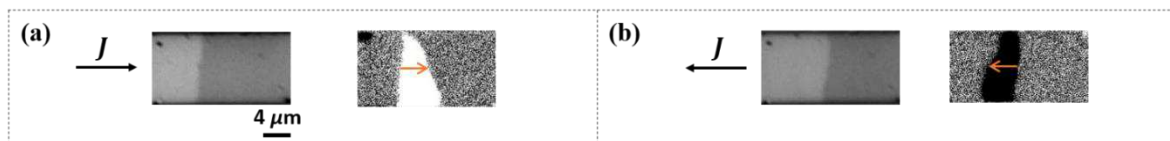


Figure III.22 The current-induced DW motion in Pt/Co/Pt. The DWs move in the current direction. MOKE images of the DW_{D-V} motion under a current density of $J \sim +1.13 \cdot 10^{12} \text{ A.m}^{-2}$ in (a) and $J \sim -1.09 \cdot 10^{12} \text{ A.m}^{-2}$ in (b). In (a) and (b), on the left, an image of the initial state of the DW_{D-V}. On the right, a differential MOKE image of the DW displacement. The orange arrows highlight the direction of the DW motion.

In the Pt/Co/Pt structure, the CIDWM is in the current direction as shown in **Figure III.22**. This is contrary to what is expected in the case of STT-driven DWs. As discussed in section I.5.4.2, the damping-like torque T_{DL} can induce such a unidirectional motion only if the DW core magnetization m_{DW} has a chiral in-plane component m_x . Thereby, the interfacial DMI is present in spite of the low SIA of the Pt/Co/Pt stack. These observations suggest that the DMI + SOT mechanism plays a main role in the CIDWM similarly to the Pt/Co/AlO_x stack. We need then to determine the sign of both T_{DL} and DMI in Pt/Co/Pt.

The action of T_{DL} on the DWs is equivalent to an out-of-plane local effective field H_{DL} that alternates its sign between the two different DWs. This effective field is written as

$\mathbf{H}_{DL} = H_{DL} \cdot (\mathbf{u}_z \times \mathbf{J}) \times \mathbf{m}_{DW}$. The orientation of the DW core magnetization \mathbf{m}_{DW} then fixes the sign of \mathbf{H}_{DL} . In order to identify the chirality of the DWs in Pt/Co/Pt, we need to determine the exact sign of \mathbf{H}_{DL} for each orientation of \mathbf{m}_{DW} . To that end, we have followed the DW motion under a positive electric current in the presence of a large in-plane field \mathbf{H}_x . The orientation of \mathbf{m}_{DW} saturates parallel to a large \mathbf{H}_x . In **Figure III.23**, the down magnetic domain in the wire shrinks for a negative applied \mathbf{H}_x . Then, \mathbf{H}_{DL} points upwards for $m_x < 0$. For a positive applied \mathbf{H}_x , the down domain expands so that \mathbf{H}_{DL} points downwards for $m_x > 0$.

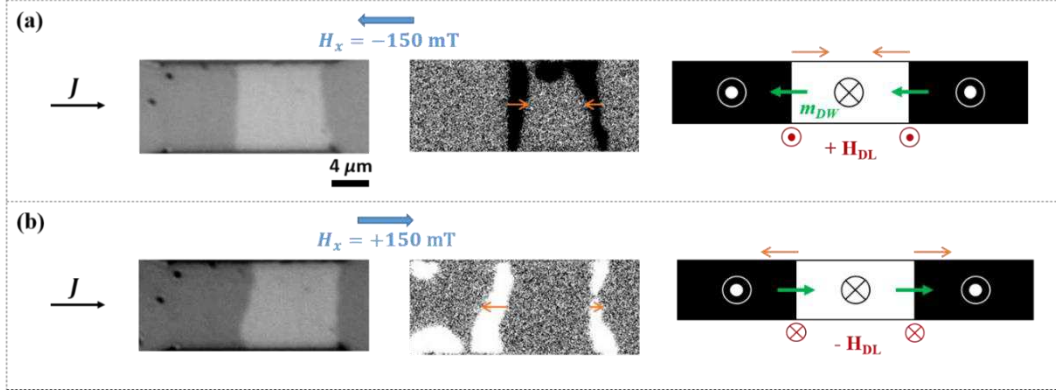


Figure III.23 The sign of the damping-like effective field \mathbf{H}_{DL} in Pt/Co/Pt. MOKE images of the down magnetic domain reduction (respect. expansion) in (a) (respect. in (b)) for a positive current in the presence of the in-plane field \mathbf{H}_x . The current density is $J \sim +2.75 \cdot 10^{12} \text{ A.m}^{-2}$ and $|\mathbf{H}_x| = 150 \text{ mT}$. \mathbf{H}_x is large enough so that it saturates \mathbf{m}_{DW} along its direction. Sketches, on the right in (a) and (b), show the dependence of \mathbf{H}_{DL} on the orientation of \mathbf{m}_{DW} (green arrow). The orange arrows highlight the direction of motion of the DWs. In (a), \mathbf{H}_{DL} reduces the down magnetic domain (dark contrast). It is then pointing upwards. Whereas in (b), the down magnetic domain expands (bright contrast) so that \mathbf{H}_{DL} is pointing downwards.

Based on these observations, we can deduce the chirality of m_x , whether left-handed, .i.e. pointing from the down magnetic domain towards the up magnetic domain, or right-handed, .i.e. pointing from the up domain towards the down domain. As highlighted in **Figure III.24**, the DWs must have the left-handed chirality for the current-induced motion to occur in the current direction as obtained experimentally. The sign of the DMI and of the damping-like torque \mathbf{T}_{DL} are similar to that in the Pt/Co/AlOx structure [Garello et al., 2013; Belmeguenai et al., 2015].

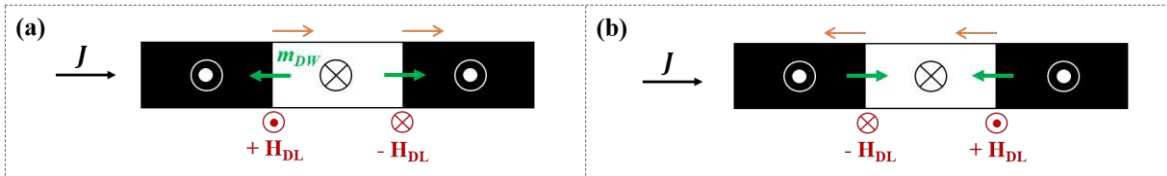


Figure III.24 Schematic diagrams of the DW chirality effects on the CIDWM. The orientation of \mathbf{H}_{DL} with respect to \mathbf{m}_{DW} is deduced from the reasoning presented above (**Figure III.23**). The left-handed chirality gives a motion in the current direction (a) as observed experimentally in Pt/Co/Pt whereas the right-handed chirality gives a motion in the electron flow (b).

The exact measurement of the amplitude of the DMI was not possible via the techniques available at hand. The measurements based on the FIDWM proved to be not suitable since the Chiral Damping was found to be the governing mechanism. As for the CIDWM, it is difficult to determine the exact in-plane field that stops the DW motion (cf. section I.5.5.2.1). During our investigation, the DW has remained pinned for a wide range of applied \mathbf{H}_x . Nonetheless, as we have started to observe the DWs moving in the opposite direction beyond $|\mathbf{H}_x| = 20 \text{ mT}$. We may consider this amplitude to be the upper limit of the DMI effective magnetic field $|\mathbf{H}_{DMI}|$. Consequently, the DMI is weak in the Pt/Co/Pt stack. This is confirmed by comparing the measured DW velocity v_{DW} (shown in **Figure III.5.b**) with predictions of [Thiaville et al., 2012] based on the DMI + SOT mechanism (**Figure I.20**). In fact, the v_{DW} curve in Pt/Co/Pt follows the scenario of a weak DMI ($|D| < 0.4 \text{ mJ.m}^{-2}$ in **Figure I.20**). The DW velocity v_{DW} increases with the current density J and then saturates in the flow regime. Indeed, the BLS measurements, carried out in the Pt/Co/Pt stack, did not yield any fingerprints of a sizeable DMI. Moreover, the magnetostatic ‘shape’ anisotropy effective field was estimated to be around $|\mathbf{H}_K| \sim 40 \text{ mT}$ [Jué et al., 2015]. Therefore, the DMI is not

strong enough to stabilize homochiral NWs and the DWs should be in an intermediate configuration between the Bloch and the Néel configurations in the Pt/Co/Pt structure.

The Pt/Co/Pt structure is then very interesting. On the one hand, it presents many similarities with the Pt/Co/AlOx structure (same sign of the DMI and T_{DL}). On the other hand, the DW core magnetization \mathbf{m}_{DW} can be easily manipulated by an in-plane field \mathbf{H}_x . Furthermore, the DW motion ingredients are better understood in Pt/Co/Pt after the evidence of the Chiral Damping mechanism. It offers then the possibility to have a better understanding of the non-collinear DW motion.

III.4.2. Asymmetric non-collinear DW motion

Like in the Pt/Co/AlOx structure, we have followed the current-induced non-collinear DW motion by studying the asymmetric distortion of the magnetic circular domains (cf. section III.2) in the Pt/Co/Pt stack. We have started by examining the evolution of an up magnetic circular domain under a positive current $J \sim + 1.13 \cdot 10^{12} \text{ A.m}^{-2}$. The obtained asymmetric distortion is shown in **Figure III.25.d**. The magnetic circular domain is no longer circular after the current injection and shows an elliptical shape that is similar to that obtained in Pt/Co/AlOx. The asymmetry of the non-collinear DW motion is then the same in the two structures. These same effects have been observed upon the reversal of the current polarity and/or the magnetization orientation in agreement with the associated symmetry operations, excluding then any possible contributions from a non-uniform current distribution, pinning or any other artefact.

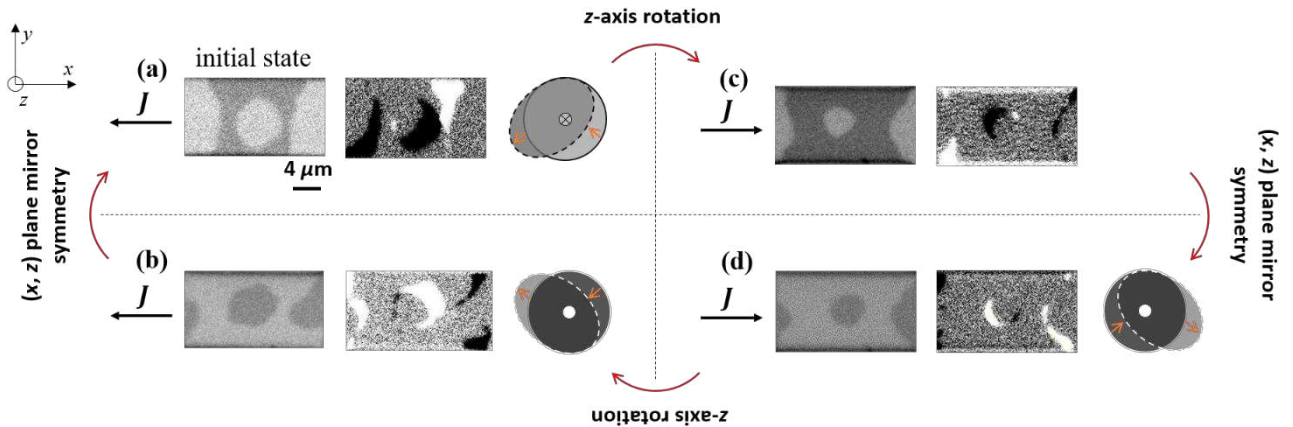


Figure III.25 Asymmetric current-induced distortion of the magnetic circular domains in Pt/Co/Pt. All the possible magnetization/current polarities are shown. The positive current density is $J \sim + 1.13 \cdot 10^{12} \text{ A.m}^{-2}$ and the negative is $J \sim -1.09 \cdot 10^{12} \text{ A.m}^{-2}$. MOKE images for (a) an initial down domain and a negative current, (b) an initial up domain and a negative current, (c) an initial down domain and a positive current and (d) an initial up domain and a positive current.

For current densities of $J \sim - 1.09 \cdot 10^{12} \text{ A.m}^{-2}$ and $J \sim + 1.13 \cdot 10^{12} \text{ A.m}^{-2}$, the DW motion takes place in the depinning regime. We have then investigated the distortion of the magnetic domains for other current densities, each one corresponding to a different DW regime of motion based on the v_{DW} curve (cf. **Figure III.5.b**). For $J \sim 0.90 \cdot 10^{12} \text{ A.m}^{-2}$, the DW motion is in the creep regime whereas it is in the flow regime for $J \sim 1.92 \cdot 10^{12} \text{ A.m}^{-2}$. The DW velocity v_{DW} reaches the saturation plateau of the flow regime for $J \sim 2.58 \cdot 10^{12} \text{ A.m}^{-2}$. From $J \sim 0.90 \cdot 10^{12} \text{ A.m}^{-2}$ to $J \sim 1.92 \cdot 10^{12} \text{ A.m}^{-2}$, the DW velocity v_{DW} increases by about four orders of magnitude (from $v_{DW} \sim 0.002 \text{ m.s}^{-1}$ to $v_{DW} \sim 10 \text{ m.s}^{-1}$). We have observed that the asymmetric DW motion with respect to ϕ_J is still the same (**Figure III.26**), which means that it does not depend on the DW regime of motion. It should be noted that quantitative measurements of ϕ_J^{max} were not possible in Pt/Co/Pt. Unlike in Pt/Co/AlOx where the asymmetry is more pronounced, it is difficult to determine the position of the largest DW displacement from the first injected current pulses in Pt/Co/Pt.

To summarize, we have obtained similarities in the non-collinear DW motion between Pt/Co/AlO_x and Pt/Co/Pt. It is then possible that, in Pt/Co/Pt, the asymmetric non-collinear DW motion comes also from the DMI + SOT mechanism. However, we have seen that the DWs are not stabilized in the Néel configuration. Besides that, another mechanism, originating from SIA, is present, i.e. the Chiral Damping (CD). To establish the physical mechanisms behind the asymmetric DW motion in Pt/Co/Pt, we have calculated the DW velocity v_{DW} as a function of the angle ϕ_J using the numerical collective coordinate model.

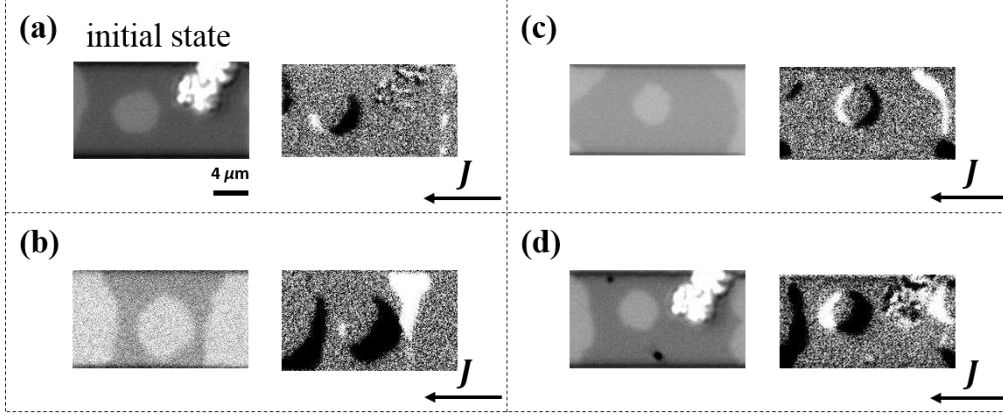


Figure III.26 Asymmetric current-induced distortion of the down magnetic circular domain in Pt/Co/Pt for different current density amplitudes, number of current pulses and current pulse lengths: (a) $J \sim -0.90 \cdot 10^{12} \text{ A.m}^{-2}$, 30000 pulses, 20 ns. (b) $J \sim -1.09 \cdot 10^{12} \text{ A.m}^{-2}$, 540000 pulses, 20 ns. (c) $J \sim -1.92 \cdot 10^{12} \text{ A.m}^{-2}$, 80 pulses, 5 ns. (d) $J \sim -2.58 \cdot 10^{12} \text{ A.m}^{-2}$, 750 pulses, 2.4 ns. All differential MOKE images exhibit qualitatively the same asymmetry.

III.4.3. The numerical collective coordinate model

To determine the DW chirality in Pt/Co/Pt, we have considered the DW motion in a straight wire within the DMI + SOT (or DMI + \mathbf{T}_{DL}) mechanism. In order to model our results in the non-collinear configuration, we have included the Chiral Damping mechanism (CD). We refer to the combined action of all of these mechanisms as the DMI + SOT + CD mechanism (or DMI + \mathbf{T}_{DL} + CD). We use the numerical collective coordinate model $q - \phi$ that we describe in this section.

In Pt/Co/Pt, the DWs are in an intermediate configuration with a Bloch component and a Néel component \mathbf{m}_x whose chirality is left-handed. In the model, this configuration is represented by the internal DW angle $\phi(t)$ (the azimuthal angle of \mathbf{m}_{DW}). $\phi(t)$ is defined with respect to the +x-axis (**Figure III.27**). The DW dynamics is described by the two collective coordinates; The DW azimuthal angle $\phi(t)$ and the DW position $q(t)$. This model was initially introduced by [Schryer & Walker 1974] and [Slonczewski, Graham and Rhyne, 1972; Malozemoff and Slonczewski, 1979]. It consists in solving the coupled differential equations numerically in order to obtain the time-dependent variables $\dot{q}(t)$ and $\dot{\phi}(t)$. We consider here the DMI, the damping-like torque \mathbf{T}_{DL} (or \mathbf{H}_{DL}) and the Chiral Damping while neglecting STT and the field-like component of SOT. The thermal fluctuations were taken into account via the thermal field $\mathbf{H}_{th}(t)$ as proposed in [Brown 1963] and [Martinez et al. 2007]. The phenomenological $\mathbf{H}_{th}(t)$ models a form of disorder in our calculations (cf. Appendix section A.1.1).

In our study, we divide the circle-shaped DW into small portions, called cells, in which the DW is straight. We apply the collective coordinate model in each cell to obtain the corresponding $\dot{\phi}(t)$ and $\dot{q}(t)$. The thermal field, noted \mathbf{H}_{th}^i , is computed at each time step Δt in the cell i whose volume is expressed as $V^i = L^i \times t_{FM} \times \Delta$ with Δ the DW width parameter and t_{FM} the FM layer thickness. L^i is a phenomenological parameter that gives the DW length in each cell i . The oblique injection of the current is set by the angle ϕ_J^i between the current density vector \mathbf{J} and the DW normal

vector \mathbf{n}_{DW}^i . The current flow has been chosen to be from left to right (positive current) and ϕ_j^i varies as $\phi_j^i = 2i$ (in degrees) with i an integer going from 0 to 179. We have reproduced then the circle-shaped domain by varying ϕ_j^i from 0° to 358° in steps of 2° (cf. **Figure III.27.c**). Afterwards, the asymmetric distortion under current is obtained by calculating ϕ and q for each ϕ_j^i (in each cell i).

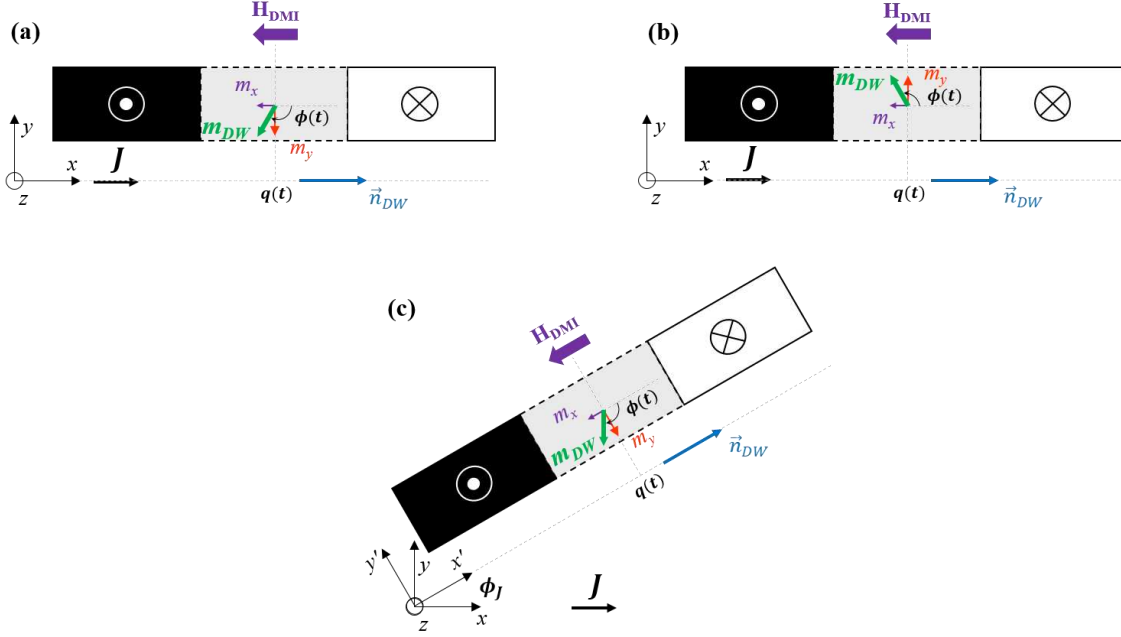


Figure III.27 The intermediate Bloch-Néel configuration of the DW_{U-D} in Pt/Co/Pt considered in the numerical collective coordinate model. \mathbf{m}_{DW} is represented by the green arrow. \mathbf{H}_{DMI} induces a left-handed Néel component of the DW_{U-D} ($m_x < 0$). \mathbf{H}_K is the magnetostatic ‘shape’ effective field oriented along the y -axis (not shown here) that favors a Bloch DW. We assume $|\mathbf{H}_{DMI}| < |\mathbf{H}_K|$ so that the DW is in an intermediate configuration between Bloch and Néel DW. \mathbf{H}_K does not have a preferential orientation thus the Bloch component (m_y) is either left-handed (a) or right-handed (b). In (a) and (b), the DW is in the collinear configuration. (c) The frame (x', y', z) of the DW_{U-D} has an angle ϕ_J with respect to the reference frame (x, y, z) . The DW_{U-D} is then in the non-collinear configuration.

In principle, three configurations are possible for the semi-circle shaped DW. They differ in terms of the chirality of the Bloch component of \mathbf{m}_{DW} and are depicted in **Figure III.28**. In PMA materials, the chirality of the Bloch wall is degenerate so there is no preference between left-handed ($m_y < 0$ in **Figure III.27.a**) and right-handed ($m_y > 0$ in **Figure III.27.b**) chiralities. The chirality can then be defined, either left-handed or right-handed, but it may also not exist with a random orientation of \mathbf{m}_{DW} along the DW as shown in **Figure III.28.c** although this configuration is less favorable due to uncompensated magnetostatic charges. In the absence of the thermal fluctuations ($T = 0$ K), we need to introduce the coupling parameter between neighboring \mathbf{m}_{DW} (i.e. neighboring cells) to model this configuration, which is not the case in the study presented here.

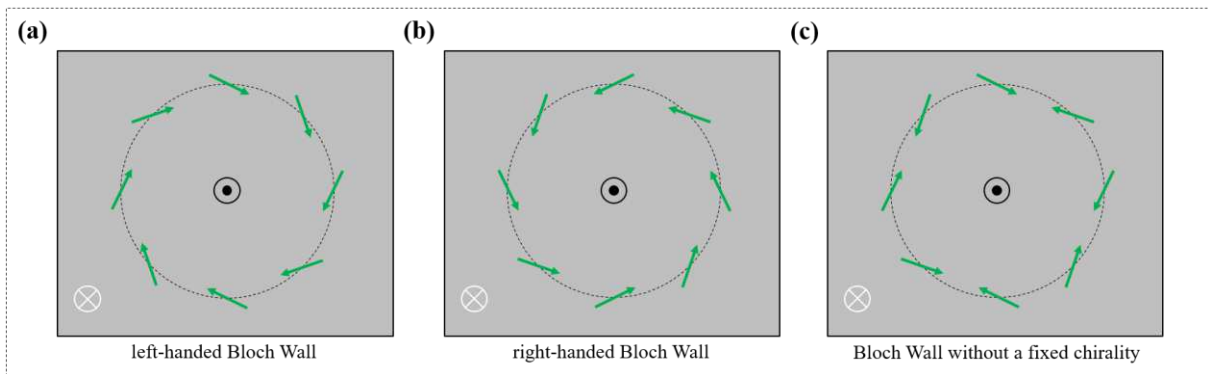


Figure III.28 Different configurations of the DW for an up circular magnetic domain in Pt/Co/Pt. Across the boundary of the domain, the chirality of the Bloch component is left-handed (a), right-handed (b) or random (c). The green arrows correspond to \mathbf{m}_{DW} .

In the model, some of the magnetic parameters come from the previous experimental works such as the saturation magnetization $\mu_0 M_s = 1.3$ T, the isotropic Gilbert damping $\alpha_0 = 0.5$, the CD coefficient $\alpha_c = 0.3$, $H_K = 40$ mT, $\Delta = 5$ nm [Jué et al. 2015] and $t_{FM} = 0.6$ nm. The total damping is expressed as $\alpha = \alpha_0 + \alpha_c(\mathbf{m}_{DW} \cdot \nabla m_z)$ (cf. Eq. I.54). The presence of DMI was accounted for by $|\mathbf{H}_{DMI}| = 20$ mT, smaller than $|\mathbf{H}_K|$ so that to not induce a NW. The action of SOT is taken into account by the effective damping-like field \mathbf{H}_{DL} . We have set $|\mathbf{H}_{DL}| = 10$ mT for high current densities (which corresponds to the saturation plateau of the DW velocity v_{DW} according to **Figure III.5.b**) and $|\mathbf{H}_{DL}| = 1$ mT for low current densities. The time step is taken as $\Delta t = 5 \cdot 10^{-12}$ seconds (5 ps) for a total current injection time of 200 ns. Finally, we chose $L^i = 50$ nm (which gives a circular magnetic domain of about $3 \mu\text{m}$ in diameter).

In what follows, we give calculations for the up circular domain under a positive applied current \mathbf{J} and, when mentioned, at a negative in-plane field \mathbf{H}_x . All the other situations (the other magnetization/current/in-plane field orientations) can be obtained by the symmetry operations. Using our model, we have evidenced the key role of the thermal fluctuations in the DW motion. For that purpose, we compare the DW velocity calculations in the non-collinear geometry in the absence and in the presence of the thermal fluctuations.

III.4.4. The role of the thermal fluctuations

III.4.4.1. The DW motion in the absence of the thermal fluctuations

Initially, the thermal fluctuations were not included ($T = 0$ K) for a low current density ($H_{DL} = 1$ mT). The DMI + \mathbf{T}_{DL} + CD mechanism gives an asymmetric DW motion as illustrated by the results of the calculation of the DW velocity v_{DW} as a function of the angle ϕ_J , depicted in **Figure III.29**. The calculated asymmetries in the DW motion depend on the chirality of the Bloch component of the DW, left-handed or right-handed. The two asymmetries are opposite to each other. Three major contradictions emerge from the comparison with our experimental observations. First, the DW moves in the normal geometry with respect to the current ($v_{DW} \neq 0$ at $\phi_J = 90^\circ$ and 270°). Secondly, the motion is against the current flow at certain non-collinear positions along the semi-circle shaped DW. This is not expected as we have not considered yet any external in-plane field. For instance, the DW velocity v_{DW} is pointing inwards (towards the center of the up domain) at $30^\circ \leq \phi_J \leq 90^\circ$ for the semi-circle shaped DW_{U-D} (**Figure III.29.a**). Finally, the asymmetry (simply; the sign of the angle ϕ_J^{max}) depends on the chirality whereas no such discrepancy is reported in the experiment. A more detailed discussion of the mechanism behind the asymmetry at $T = 0$ K is available in Appendix A.1.2.1.

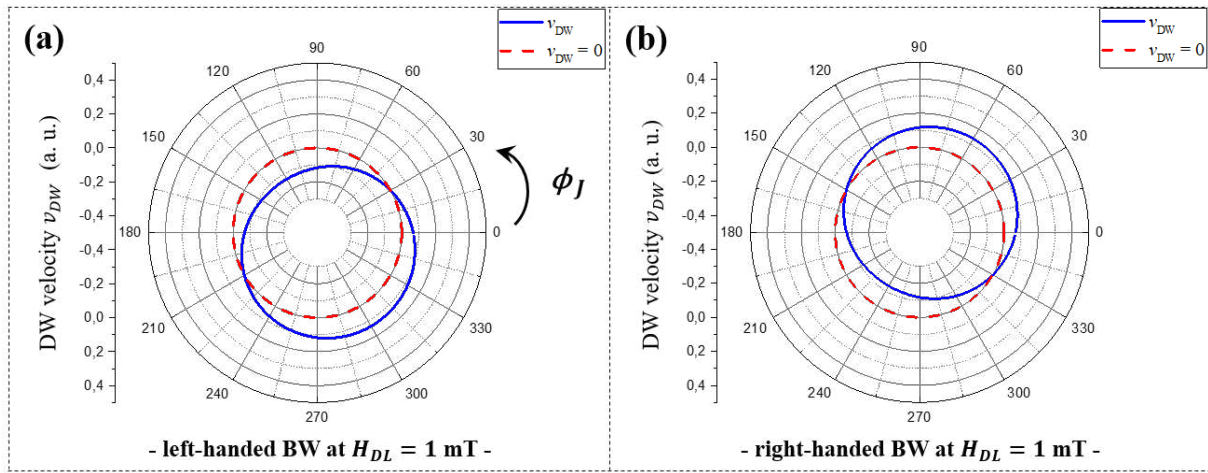


Figure III.29 The DW velocity v_{DW} versus the angle ϕ_J from calculations at $T = 0$ K using the DMI+SOT+CD mechanism in the collective coordinate model under low current ($H_{DL} = 1$ mT). The current is positive, flowing from left to right and ϕ_J goes from 0° to 360° in the anticlockwise direction. For the DW_{U-D} , ϕ_J is between $0^\circ \leq \phi_J \leq 90^\circ$ and $270^\circ \leq \phi_J \leq 360^\circ$. For the DW_{D-U} , ϕ_J is between $90^\circ \leq \phi_J \leq 270^\circ$. The DW_{U-D} is moving along (against) the current flow when v_{DW} is positive or pointing outwards (negative or pointing inwards) and vice versa for the DW_{D-U} . The reference $v_{DW} = 0$ (no motion) is represented by the red dashed line and the blue line gives the calculated v_{DW} at ϕ_J for a left- and a right-handed BWs, respect. in (a) and (b).

This discrepancy between the model and the experiment could mean that we are still missing a key ingredient to describe the CIDWM that is the thermal fluctuations.

III.4.4.2. The DW motion in the presence of the thermal fluctuations

The thermal field $\mathbf{H}_{th}(t)$ is included for the injected high current densities (modeled by $H_{DL} = 10$ mT). The **Figure III.30** shows the calculated DW velocity v_{DW} as a function of the angle ϕ_J in green (in blue) when considering the DMI (the DMI and the CD). The two curves merge practically indicating that the DMI governs the DW motion. The CD does not induce any significant change in the amplitude of the DW velocity v_{DW} . According to our calculations, the DMI + SOT + CD mechanism gives the maximum DW velocity at the angle $\phi_J^{max} \approx \pm 34^\circ$ (– for the DW_{U-D} and + for the DW_{D-U}). Unlike the previous case at $T = 0$ K, the two chiralities of the Bloch component of the DW give the same DW velocity v_{DW} . The calculations are in a good qualitative agreement with the experiment results (cf. **Figure III.25.d**) revealing the key role of the thermal fluctuations.

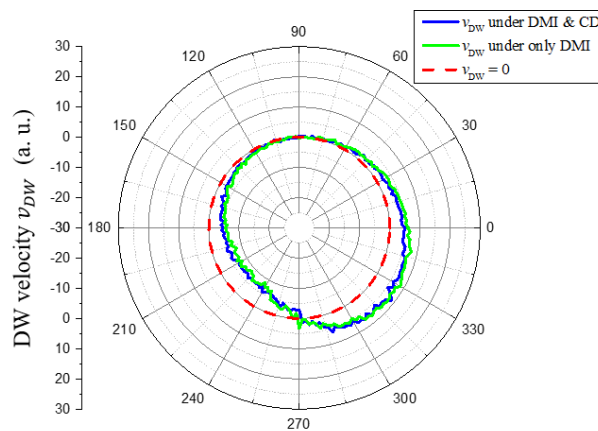


Figure III.30 The DW velocity v_{DW} versus the angle ϕ_J calculated at $T = 300$ K using the collective coordinate model under high current density ($H_{DL} = 10$ mT). The model uses the DMI + \mathbf{T}_{DL} only (in green) or the DMI + \mathbf{T}_{DL} + CD (in blue). The shown data are the average of 5 different calculations. The DW velocity v_{DW} does not show any dependence on the chirality of the Bloch component of the DW.

The stochastic thermal field \mathbf{H}_{th} demagnetizes the DWs. The action of the current, on average, is then equivalent to that exerted on homochiral NWs. In other terms, the thermal fluctuations mix the two chiralities of the Bloch component of the DW. In fact, during the injection of the current, the DW core magnetization \mathbf{m}_{DW} precesses around \mathbf{H}_{th} which has a random orientation at each time step Δt . As the BW magnetostatic ‘shape’ field \mathbf{H}_K does not have any preferential orientation, the y -component of \mathbf{m}_{DW} has a zero mean value ($\langle m_y \rangle = 0$). On the contrary, the distribution of m_x is skewed due to the DMI. \mathbf{H}_{DMI} points inwards (outwards) for the DW_{U-D} (the DW_{D-U}) so that we have $\langle m_x \rangle < 0$ ($\langle m_x \rangle > 0$). This results in the DWs in Pt/Co/Pt having an equivalent configuration of NWs like it is depicted in **Figure III.11**. Without the injected current, the DW core magnetization \mathbf{m}_{DW} sits normal to the DW pointing inwards (outwards) for the DW_{U-D} (the DW_{D-U}). \mathbf{m}_x is anti-parallel (parallel) to the current \mathbf{J} . The DW motion, induced by \mathbf{T}_{DL} , is then in the current direction for any angle ϕ_J as obtained by the calculations and observed experimentally. In the absence of an in-plane field ($\mathbf{H}_x = 0$ mT), the mechanism responsible for the asymmetric non-collinear DW motion in Pt/Co/Pt is then the same as the mechanism described in **Figure III.11** (cf. section III.3.1) for the DWs in Pt/Co/AlOx. As the signs of the DMI and \mathbf{T}_{DL} are identical, the asymmetric DW motion with the angle ϕ_J is then qualitatively comparable in Pt/Co/Pt and Pt/Co/AlOx with a maximum v_{DW} at a finite angle $\phi_J^{max} \neq 0^\circ$.

In principle, the CD mechanism has a contribution to the asymmetry with respect to the angle ϕ_J ($v_{DW} \propto 1/\alpha$ in Eq. III.2). By substituting the DW normal vector \mathbf{n}_{DW} for the magnetization gradient ∇m_z in Eq. I.54, we unveil the dependence of the chiral component α_c on the angle ψ (the angle between \mathbf{n}_{DW} and \mathbf{m}_{DW} in **Figure III.11**). For instance, we write α for the arc-shaped DW_{U-D} as:

$$\alpha = \alpha_0 + \alpha_c \mathbf{m}_{DW} \cdot \nabla m_z = \alpha_0 - \alpha_c \mathbf{m}_{DW} \cdot \mathbf{n}_{DW} = \alpha_0 - \alpha_c \cos \psi \quad (\text{III.5})$$

Consequently, the damping α varies across the semi-circle shaped DW and is not symmetric with respect to $\phi_J = 0^\circ$ (due to the modification of the angle ψ induced by the distortion of \mathbf{m}_{DW}). However, the CD contribution is not significant, in comparison to the DMI contribution, as shown in **Figure III.30**. In fact, for large current densities, the DW velocity v_{DW} reaches the saturation plateau for which the DW distortion is at its maximum (cf. section I.5.4.2 and [Thiaville et al., 2012]). The DW velocity v_{DW} is then largely determined by the out-of-plane torque \mathbf{T}_{DMI} , induced by the DMI, on which the variations of the damping α have little impacts.

Finally, according to Eq. III.2, the maximum DW velocity is linked to the amount of the distortion and the initial DW internal structure. Therefore, the angle ϕ_J^{max} is expected to be a function of the current density \mathbf{J} and the in-plane magnetic field \mathbf{H}_x in Pt/Co/Pt. However, we were not able to verify these assumptions as it was not possible to conduct measurements of the angle ϕ_J^{max} .

By including the thermal fluctuations, we are able to account for the asymmetric non-collinear DW motion by the DMI + SOT + CD mechanism in Pt/Co/Pt in the flow regime. We apply, next, an external in-plane field \mathbf{H}_x in order to investigate the interplay between the DMI and the CD.

III.4.5. The interplay between the DMI and the Chiral Damping

III.4.5.1. Effects of the in-plane magnetic field

Here, the magnetic circular domains are examined under the current along with the longitudinal field H_x . By varying the amplitude of H_x , we tune the DW configuration. We are able then to observe the effects induced by the variation of the DW internal structure on the non-collinear DW motion in Pt/Co/Pt. The **Figure III.31** gives a summary of the effects induced by H_x on the asymmetric distortion of the up magnetic circular domain under $J \sim +1.13 \cdot 10^{12} \text{ A.m}^{-2}$. From $H_x = 0$ up to +65 mT, the DW_{D-U} (the semi-circle shaped DW on the left) is faster as its magnetic contrast region (its displacement), in the MOKE differential images, is larger than that of the DW_{U-D} (the semi-circle shaped DW on the right). These effects can be related to the interplay between H_x and the local H_{DMI} inside each DW as discussed in section III.3.2.1, since the DMI has the same sign in both Pt/Co/AlOx and Pt/Co/Pt structures. In the case of a weak DMI, like in the Pt/Co/Pt stack, it is possible to reverse the chirality of the Néel component of the DW by an in-plane field hence the motion against the current observed for the DW_{U-D} starting from $H_x = +37$ mT.

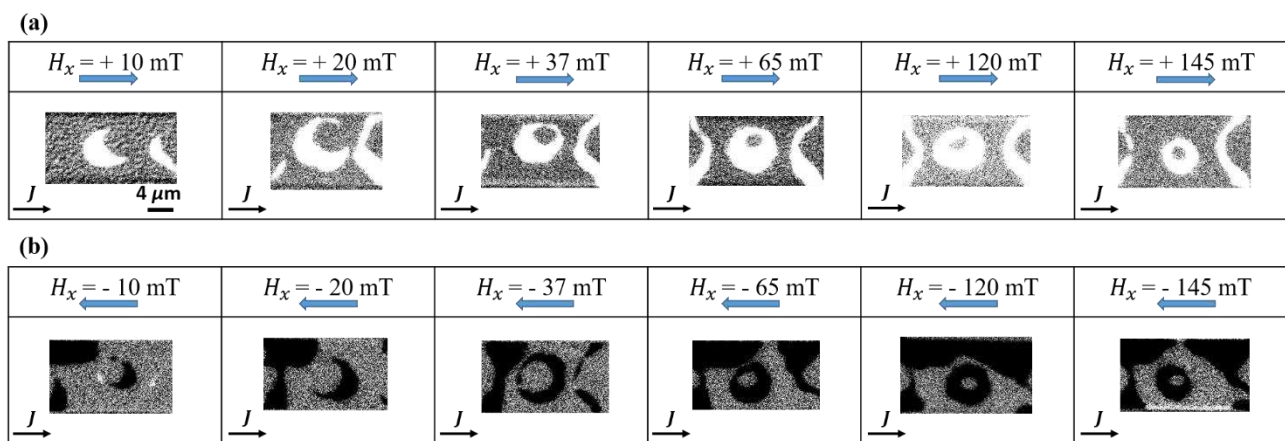


Figure III.31 Asymmetric distortion of the up domain in Pt/Co/Pt in the presence of H_x under a positive current. (a) (respect. (b)) MOKE differential images at a positive (respect. negative) H_x . The injected current density is $J \sim +1.13 \cdot 10^{12} \text{ A.m}^{-2}$.

Similarly to the Pt/Co/AlOx structure, we follow the asymmetric distortion by studying the motion of the center of the up magnetic circular domain in **Figure III.31**. For a positive (respect. negative) H_x , the round grey-textured area towards the center of the wire, surrounded by a bright (respect. dark) contrast, corresponds to the final (respect. initial) state of the up domain. The larger round area, enclosing it, corresponds to the initial (respect. final) state of the up domain. By comparing the initial and final states of the magnetic domain, we determine the direction of motion of its center. From $H_x = 0$ up to +65 mT, the center has a horizontal motion in the current direction even though the DW_{U-D} moves against the current direction. This results from the asymmetric motion between the two DWs that is induced by the DMI. However, at $H_x > +65$ mT, the center shows a motion against the current flow. This is an unexpected effect that indicates a reversal of the asymmetric motion between the two DWs at large H_x . In fact, following the DMI mechanism, the asymmetric motion should maintain the same sign as long as H_x is not reversed and regardless of the amplitude of H_x . Besides these effects, the center has a vertical motion. For a positive H_x , its final position is always located on top of its initial position. As seen in the Pt/Co/AlOx, this is a signature of the asymmetric non-collinear DW motion. The asymmetric non-collinear DW motion is then maintained in the presence of H_x . Even though the DW_{U-D} reverses its direction of motion, it keeps the same symmetry for the angle ϕ_J^{max} .

The DWs interchange their roles for a negative H_x , as depicted in **Figure III.31.b**. The DW_{U-D} is, initially, faster than the DW_{D-U} and the center of the domain moves in the current direction. Similarly, for a large H_x , the asymmetric motion between the two DWs is reversed and the center moves against the current flow. The presence of a vertical motion of the center indicates also that the asymmetric DW motion with ϕ_J is maintained (the center is now located below its initial position). To confirm these effects, we have verified their presence for all the magnetization and/or the current polarities.

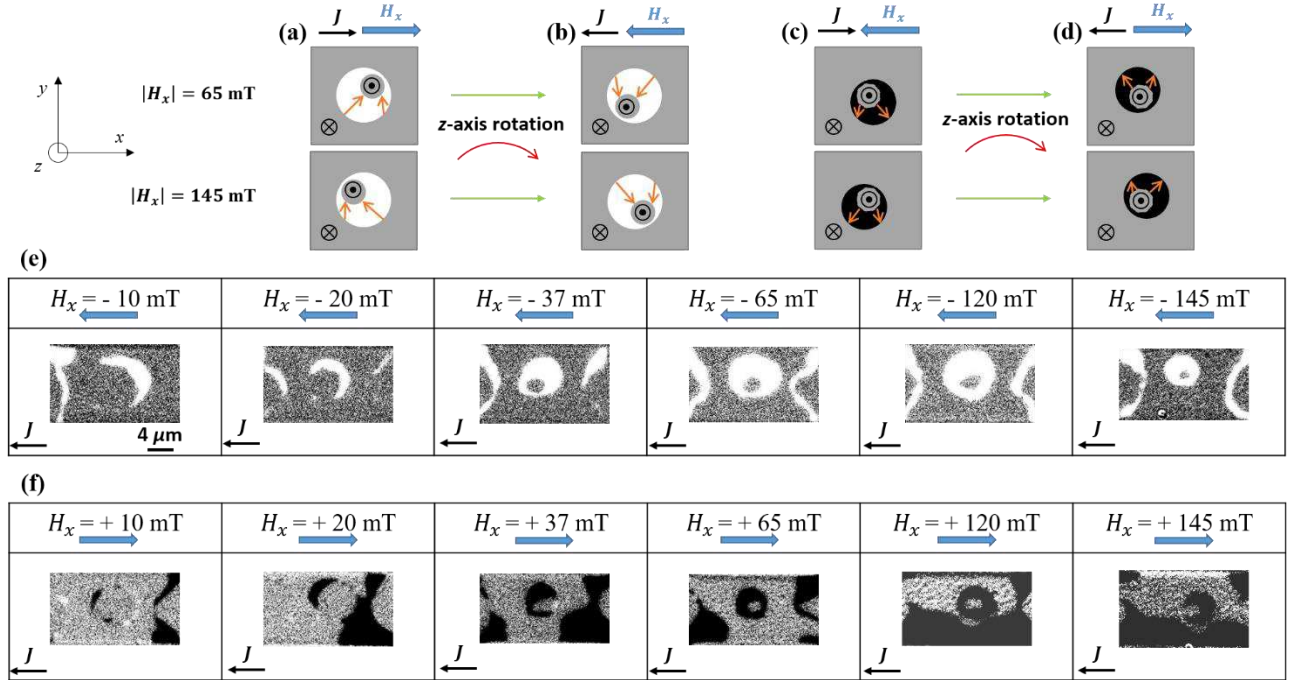


Figure III.32 Asymmetric distortion of the up domain in Pt/Co/Pt in the presence of H_x under a negative current. (a)-(d) The image of the asymmetric distortion of the up domain by the 180° rotation symmetry operation around the z-axis. The image of an up domain under a positive current at a positive (respect. negative) H_x in (a) (respect. (c)) is an up domain under a negative current at a negative (respect. positive) H_x in (b) (respect. (d)). The experimentally obtained distortion of an up domain under $J \sim -1.09 \cdot 10^{12}$ A.m⁻² at a negative (respect. positive) H_x in (e) (respect. (f)).

In **Figure III.32**, we show the distortion of the up domain under a negative current in Pt/Co/Pt. In this case, the effects induced by H_x should be the image by the 180° rotation symmetry around the z-axis of the up domain under a positive current as depicted in **Figure III.32.a-d**. We show diagrams only at $|H_x| = 65$ and 145 mT since they are representative of the two opposite horizontal motions of the center of the domain in the presence of H_x . Indeed, the obtained results in **Figure III.32.e-f** are in a good agreement with the symmetry operation.

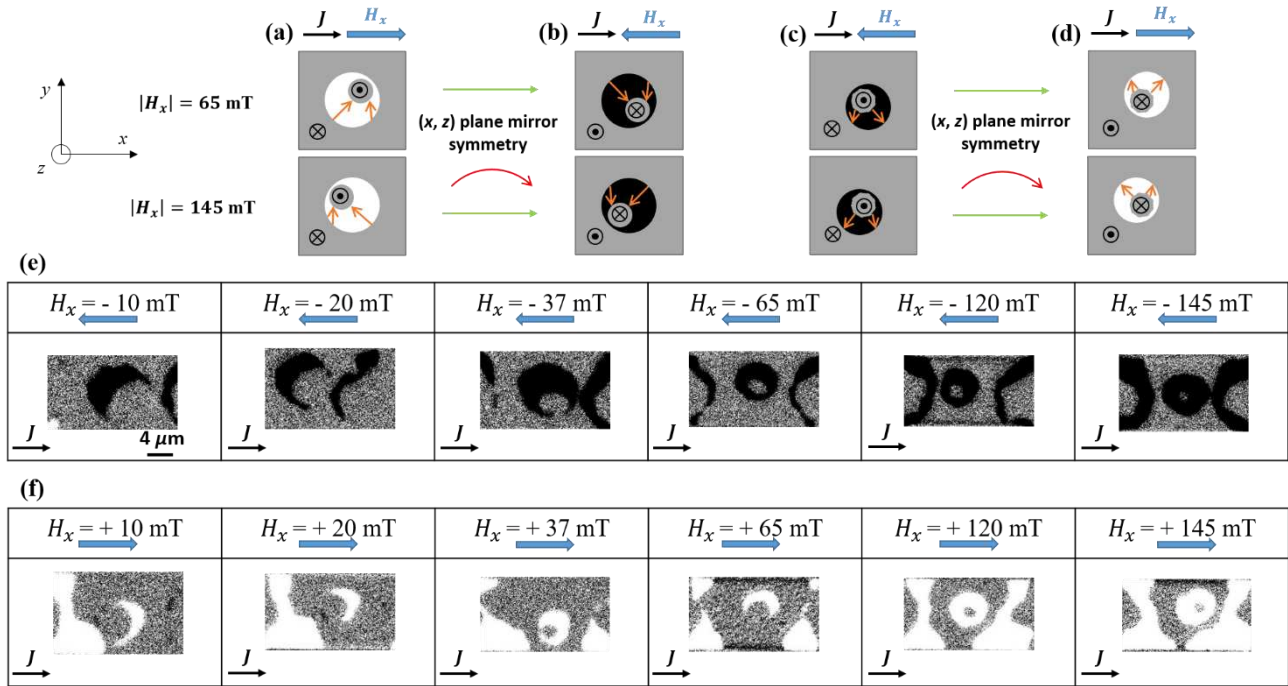


Figure III.33 Asymmetric distortion of the down domain in Pt/Co/Pt in the presence of H_x under a positive current. (a)-(d) The image of the asymmetric distortion of the up domain by the (x, z) plane mirror symmetry operation. The image of an up domain under a positive current at a positive H_x (respect. negative) in (a) (respect. (c)) is a down domain under a positive current at a negative H_x (respect. positive) in (b) (respect. (d)). The experimentally obtained distortion of down magnetic domain under $J \sim +1.13 \cdot 10^{12} \text{ A.m}^{-2}$ at a negative (respect. positive) H_x in (e) (respect. (f)).

As for the down magnetic domain, **Figure III.33** (respect. **Figure III.34**) gives the effects induced by H_x under a positive (respect. negative) current. In both cases, the observed distortion follows the image by the corresponding symmetry operations of the distortion of the up domain under a positive current in **Figure III.31**.

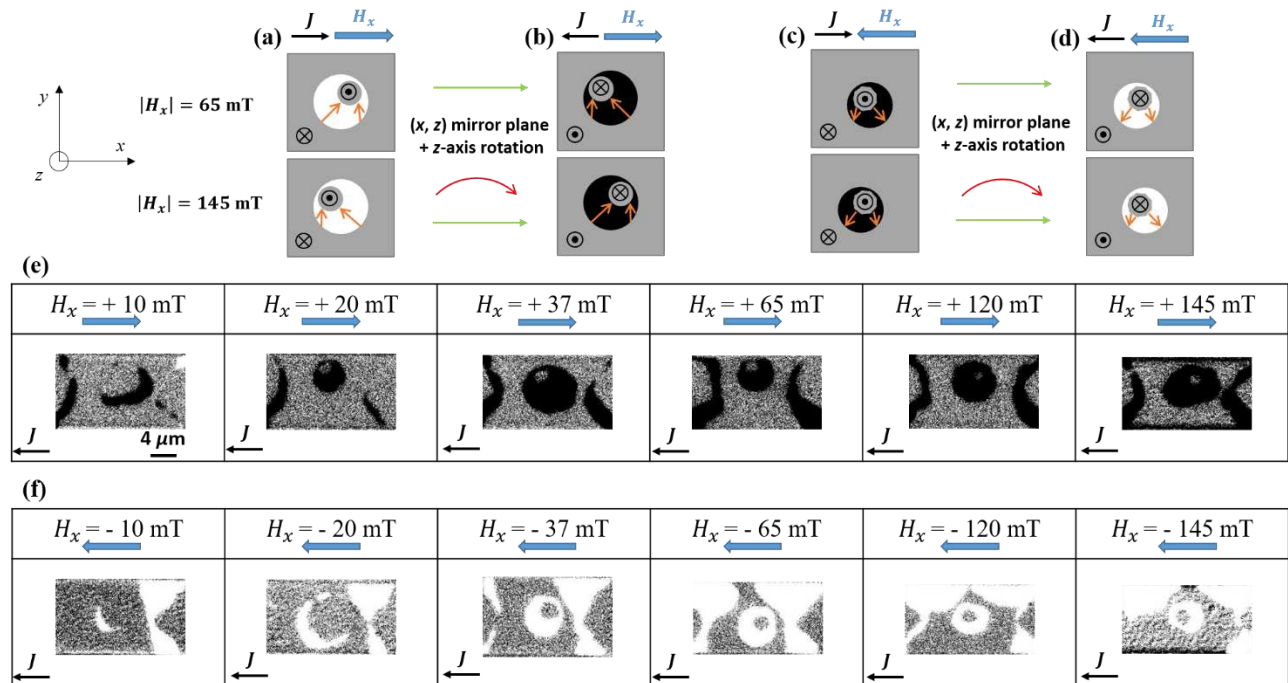


Figure III.34 Asymmetric distortion of the down domain in Pt/Co/Pt in the presence of H_x under a negative current. (a)-(d) The image of the asymmetric distortion of the up domain by the (x, z) plane mirror followed by the 180° rotation symmetry operation around the z -axis. The image of an up domain under a positive current at a positive H_x (respect. negative) in (a) (respect. (c)) is a down domain under a negative current at a positive H_x (respect. negative) in (b) (respect. (d)). The obtained distortion of an up domain under $J \sim -1.09 \cdot 10^{12} \text{ A.m}^{-2}$ at a positive (respect. negative) H_x in (e) (respect. (f)).

We have seen that for all the polarities of the magnetization and/or the current, the asymmetric distortion of the magnetic circular domains in the presence of H_x follows with a good agreement the symmetry operations. This rules out any possible contribution from artefacts. It is evident then that H_x does not alter the asymmetric non-collinear DW motion in Pt/Co/Pt, like in Pt/Co/AlOx. Unlike Pt/Co/AlOx, the asymmetric motion between the two DWs is reversed for large in-plane fields ($|H_x| > 65$ mT).

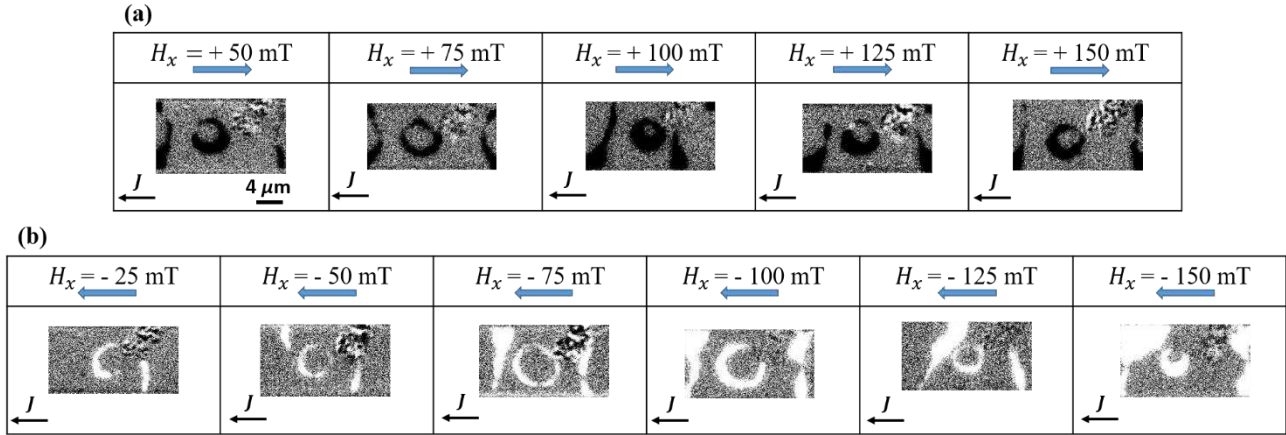


Figure III.35 Asymmetric distortion of the down magnetic circular domain under $J \sim -0.90 \cdot 10^{12} \text{ A.m}^{-2}$ in the presence of H_x in Pt/Co/Pt. The experimentally obtained distortion at a positive (respect. negative) H_x in (a) (respect. (b)).

The distortion of circular magnetic domains in the presence H_x has been also examined for different current densities. In **Figure III.35** (respect. **Figure III.36**), we show MOKE differential images of the down magnetic domain for $J \sim -0.90 \cdot 10^{12} \text{ A.m}^{-2}$ (respect. $J \sim -1.92 \cdot 10^{12} \text{ A.m}^{-2}$). In both figures, we have obtained effects that are similar to that for $J \sim -1.09 \cdot 10^{12} \text{ A.m}^{-2}$ in **Figure III.34**. We deduce that the H_x -modulation of the asymmetric non-collinear DW motion is independent of the DW regime of motion in Pt/Co/Pt.

We note that the amplitude of H_x , above which the center of the magnetic domain moves against the current direction, increases with the current density. For $J \sim -0.90 \cdot 10^{12} \text{ A.m}^{-2}$, such a field is about 100 mT (**Figure III.35**). For $J \sim -1.09 \cdot 10^{12} \text{ A.m}^{-2}$ and $J \sim +1.13 \cdot 10^{12} \text{ A.m}^{-2}$, the reversal of the motion takes place for a larger field, about 120 mT. In contrast, for $J \sim -1.92 \cdot 10^{12} \text{ A.m}^{-2}$, no motion against the current direction is observed. For the largest applied field ($|H_x| = 150$ mT), the center of the domain does not exhibit any horizontal motion (**Figure III.36**) indicating that the two DWs have the same displacement. This implies that the center of the domain might move against the current direction for $|H_x| > 150$ mT for high current densities.

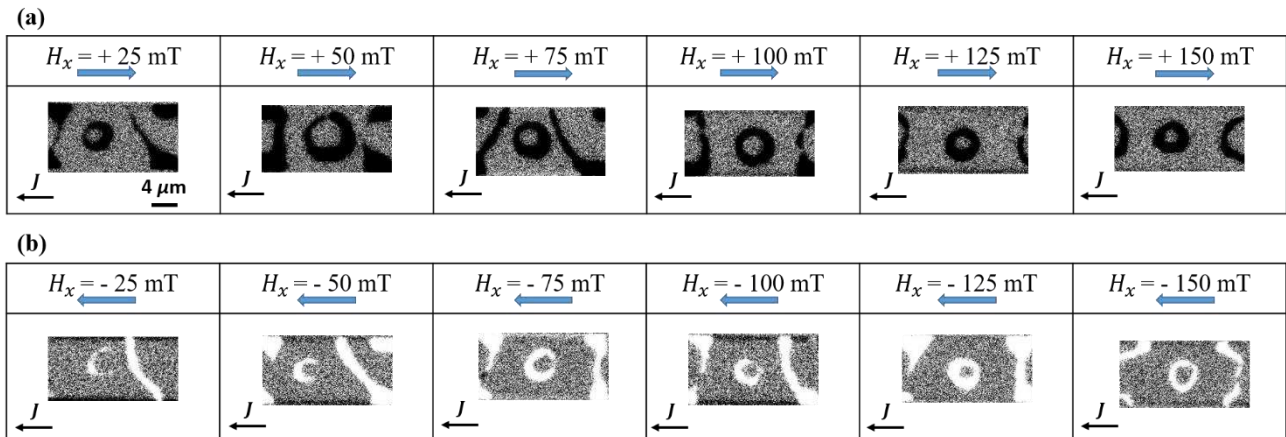


Figure III.36 Asymmetric distortion of the down magnetic circular domain under $J \sim -1.92 \cdot 10^{12} \text{ A.m}^{-2}$ in the presence of H_x in Pt/Co/Pt. The obtained distortion at a positive (respect. negative) H_x in (a) (respect. (b)).

In summary, the effects induced by \mathbf{H}_x on the non-collinear DW motion in Pt/Co/Pt have showed some similarities with the Pt/Co/AlO_x structure. In fact, these effects do not depend on the injected current density. Like in Pt/Co/AlO_x, the symmetry of the angle ϕ_J^{max} is not altered for both DWs. On the contrary, the asymmetric motion between the two DWs have been found to reverse in the presence of \mathbf{H}_x in the Pt/Co/Pt stack. A possible explanation behind this asymmetry reversal in the flow regime of motion can be given by the Chiral Damping contribution that we have included in our numerical model.

III.4.5.2. The role of the Chiral Damping in CIDWM

We were able to explain qualitatively the asymmetric non-collinear DW motion with the angle ϕ_J at $\mathbf{H}_x = 0$ in the flow regime using the DMI + SOT + CD mechanism along with the thermal fluctuations in the numerical model. We have then employed the same method to try to understand the effects induced by \mathbf{H}_x . In what follows, the calculations represent the up magnetic circular domain under a positive current at a negative \mathbf{H}_x (pointing to the left) (corresponding to the experimental results shown in **Figure III.31.b**).

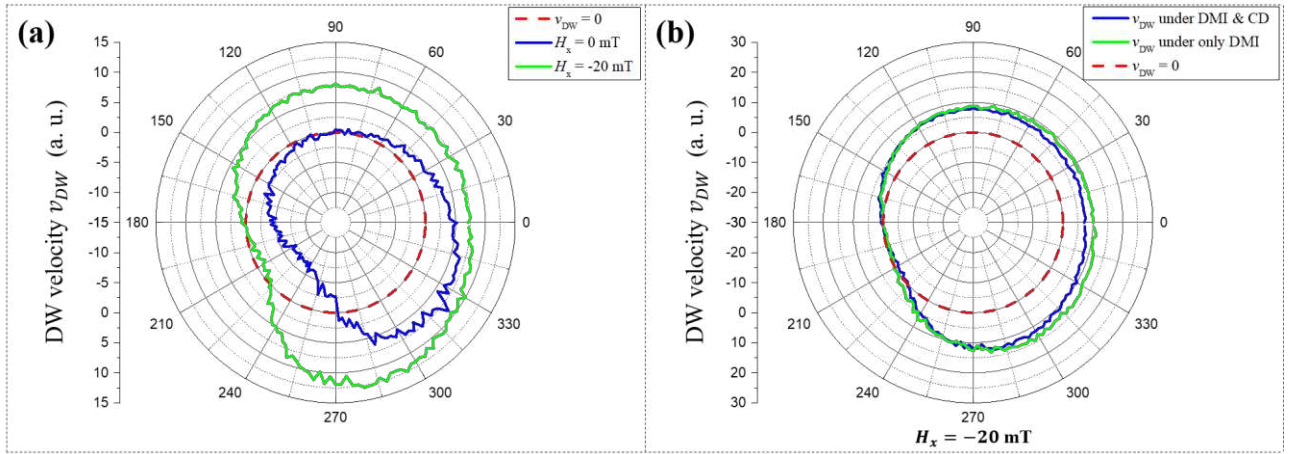


Figure III.37 The calculated DW velocity in the non-collinear configuration at $\mathbf{H}_x = -20$ mT in Pt/Co/Pt. (a) The DW velocity v_{DW} versus the angle ϕ_J at $T = 300$ K with $\mathbf{H}_x = 0$ mT (in blue) and $\mathbf{H}_x = -20$ mT (in green). The calculations are based on the DMI + SOT + CD mechanism. (b) The DW velocity v_{DW} versus the angle ϕ_J at $T = 300$ K with $\mathbf{H}_x = -20$ mT from different mechanisms. The calculations are based either on DMI + SOT + CD (in blue) or only on DMI+SOT (in green). The used model is the numerical collective coordinate model under a high ($H_{DL} = 10$ mT) positive current density, flowing from left to right, at a negative \mathbf{H}_x (pointing to the left). The shown data are the average of 5 and 7 different calculations at $\mathbf{H}_x = 0$ mT and $\mathbf{H}_x = -20$ mT, respectively.

For the DW_{U-D}, the negative $\mathbf{H}_x = -20$ mT is parallel to \mathbf{H}_{DMI} so that the DW velocity is larger than that at $\mathbf{H}_x = 0$ as given by the numerical model (**Figure III.37.a**). In the meantime, \mathbf{H}_x and \mathbf{H}_{DMI} are anti-parallel within the DW_{D-U}. For $180^\circ < \phi_J \lesssim 225^\circ$, the DW_{D-U} still propagates in the current direction (the DW velocity v_{DW} points inwards) but with limited velocities compared to the velocity at $\mathbf{H}_x = 0$. In fact, the in-plane field \mathbf{H}_x , by modulating the DW internal structure, reduces $|\mathbf{m}_x|$ thus the action of SOT is less effective in this range of the angle ϕ_J . In the remaining configurations (other values of the angle ϕ_J), the DW_{D-U} moves against the current direction (the DW velocity v_{DW} points outwards). This can be explained by the reversal of the DW chirality, induced by \mathbf{H}_x . Although it has reversed its direction of motion, the DW_{D-U} shows a larger velocity v_{DW} than that at $\mathbf{H}_x = 0$ at some configurations (e.g. the angle $\phi_J = 120^\circ$). This can be explained by the increase in $|\mathbf{m}_x|$, thanks to $\mathbf{H}_x = -20$ mT, that enhances the efficiency of SOT. To summarize, the variation of the DW velocity v_{DW} with the angle ϕ_J from the numerical model is asymmetric which gives a center of the up domain moving horizontally in the current direction (in the $+x$ -axis direction) and vertically in the $-y$ -axis direction at $\mathbf{H}_x = -20$ mT. The asymmetric motion between

the two different DWs and the asymmetric non-collinear motion are in a good qualitative agreement with the experimental observations.

In order to determine which mechanism governs the non-collinear DW motion for $H_x = -20$ mT, we compare the calculations based on the DMI + SOT + CD mechanism to those based on the DMI + SOT mechanism in **Figure III.37.b**. The two v_{DW} curves nearly coincide indicating that the DMI is still dominant over the CD similarly to the case for $H_x = 0$. Nevertheless, by including the CD, the velocity of the DW_{U-D} is reduced. We infer that the CD contribution cannot anymore be totally neglected and it is competing with the DMI contribution. Indeed, the calculations based on the CD + SOT mechanism (without the DMI) have yielded the opposite asymmetric motion between the two DWs for $H_x = -20$ mT (cf. **Figure A.5** in Appendix) with the DW_{D-U} having a larger velocity than the DW_{U-D}.

The numerical calculations demonstrate that the DMI governs the asymmetric non-collinear DW motion for a small H_x (cf. **Figure A.4**). However, when H_x is larger, a transition in the DW motion takes place. It is the outcome of the interplay between the DMI and the CD contributions.

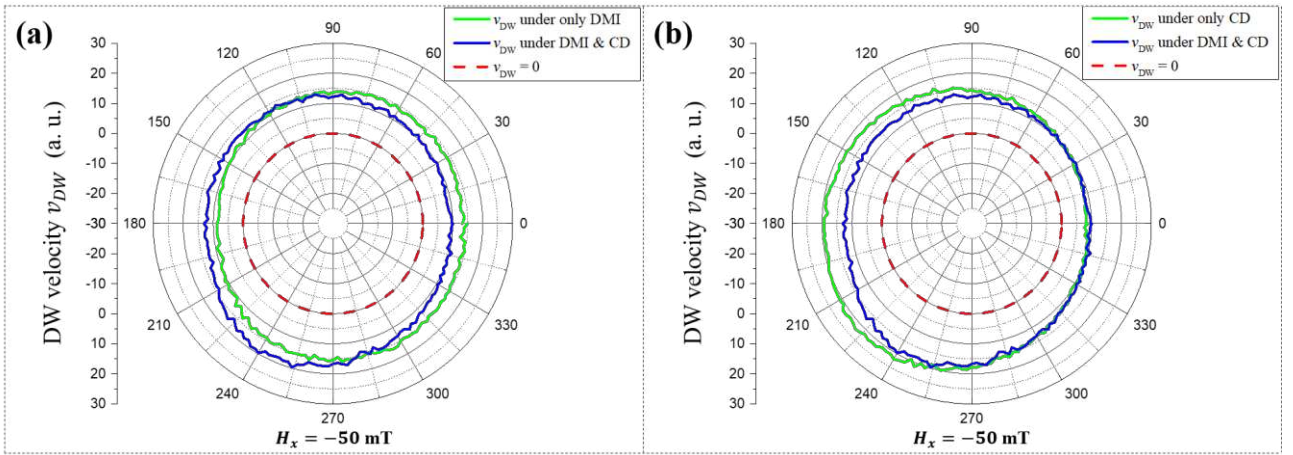


Figure III.38 The calculated DW velocity in the non-collinear configuration at $H_x = -50$ mT in Pt/Co/Pt. The DW velocity v_{DW} versus the angle ϕ_j at $T = 300$ K in the presence of $H_x = -50$ mT under a positive current with a high current density ($H_{DL} = 10$ mT) using the numerical collective coordinate model. Here, we compare the calculations using the DMI + SOT + CD mechanism (in blue) with the calculations using only the DMI in (a) and using only the CD in (b). The shown data are the average of 5 different calculations.

From the calculations shown in **Figure III.38**, neither the DMI nor the CD dictates the amplitude of the DW velocity v_{DW} at $H_x = -50$ mT. The calculations that are based on the combined action of the DMI and the CD (in blue in **Figure III.38**) do not coincide with the calculations based on the DMI or the CD alone. At $H_x = -50$ mT, the DMI alone still promotes a sizeable chiral energetic contribution that gives a faster DW_{U-D} than the DW_{D-U} (in green in **Figure III.38.a**). In the meantime, the CD contribution has increased yielding alone DW velocities with comparable amplitudes (in green in **Figure III.38.b**). On the contrary, the asymmetry between the two DWs, induced by the CD, is opposite to that induced by the DMI. Consequently, by including both the DMI and the CD, the calculations give a quasi-symmetric expansion of the up magnetic domain. The center of the domain does not show any net horizontal motion. The asymmetric non-collinear DW motion, in contrast, is maintained at $H_x = -50$ mT. In fact, the center of the domain still has a vertical motion in the $-y$ -axis direction. This is in agreement with the experimental observations for $|H_x|$ between 65 mT and 120 mT (in **Figure III.31**) where the MOKE images do not exhibit any horizontal motion of the center of the magnetic domain. Our numerical model has evidenced then a transition in CIDWM that takes place when the contributions from the DMI and the CD become comparable. The asymmetric motion between the two different DWs vanishes whereas the asymmetric non-collinear motion is still present. This transition occurs for H_x that is larger H_{DMI} and comparable to H_K , the DW magnetostatic ‘shape’ anisotropy effective field that favors a Bloch configuration.

The increase in the amplitude of the CD contribution from $H_x = 0$ mT to $H_x = -50$ mT implies that it may dominate over the DMI for larger H_x . Indeed, the numerical model evidences that the CD is the governing mechanism of CIDWM in Pt/Co/Pt at $H_x = -150$ mT (**Figure III.39**).

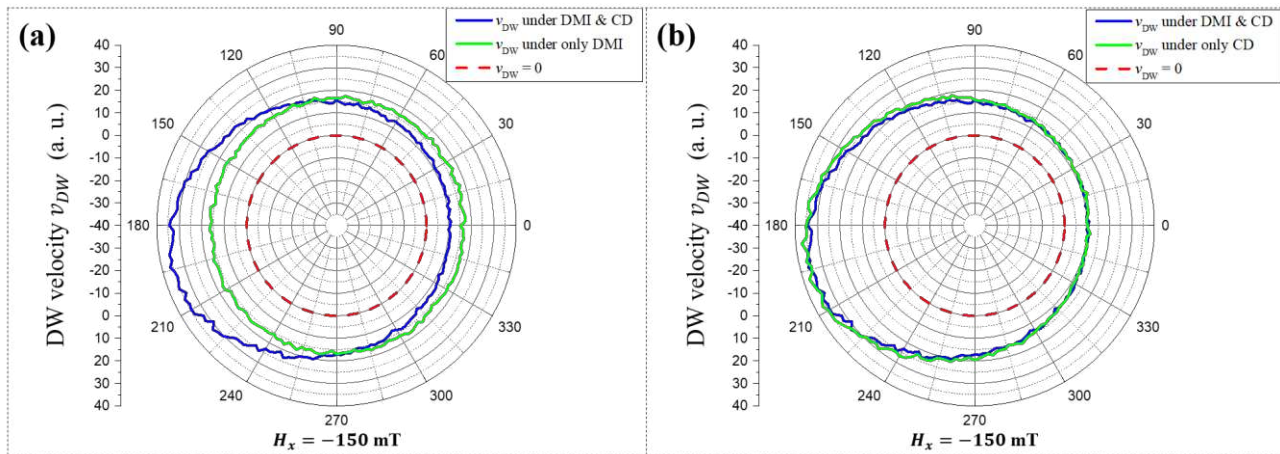


Figure III.39 The calculated DW velocity in the non-collinear configuration at $H_x = -150$ mT in Pt/Co/Pt. The DW velocity v_{DW} versus the angle ϕ_J at $T = 300$ K in the presence of $H_x = -150$ mT under a positive current with a high current density ($H_{DL} = 10$ mT) using the numerical collective coordinate model. Here we compare the calculations using the DMI + SOT + CD mechanism (in blue) with the calculations using only the DMI in (a) and using only the CD in (b). The asymmetric distortion of the up magnetic circular domain is dictated by the Chiral Damping mechanism. The shown data are the average of 5 different calculations.

At $H_x = -150$ mT, the DMI does not induce any asymmetric motion between the two DW as illustrated in **Figure III.39.a** (in green). The center of the domain does not exhibit any motion which is in contradiction with the experimental results. In contrast, the v_{DW} curves coincide in **Figure III.39.b**. Both asymmetries, between the two DWs and with the angle ϕ_J , are dictated by the CD at $H_x = -150$ mT. On the one hand, the asymmetry between the DW_{U-D} and the DW_{D-U} is reversed so that the center of the domain moves against the current direction. On the other hand, the asymmetric non-collinear DW motion remains qualitatively the same. The vertical motion of the center of the domain is, as previously, in the $-y$ -axis direction. These calculations are in a good agreement with the experimental observations at $|H_x| = 145$ mT for $J \sim +1.13 \cdot 10^{12}$ A.m⁻² and for $J \sim -1.09 \cdot 10^{12}$ A.m⁻². An intermediate situation ($H_x = -100$ mT), at which the DMI contribution is still significant according to the numerical model, is shown in Appendix section A.1.3.

In order to illustrate the role of the CD, we resort to a simplistic picture of the motion of the DW_{D-U} (depicted in **Figure III.40**). Across the semi-circle shaped DW, the DW core magnetization \mathbf{m}_{DW} points in the $-x$ -axis direction for a large negative H_x . The damping-like torque \mathbf{T}_{DL} is then uniform and it rotates \mathbf{m}_{DW} anticlockwise in the (x, y) plane with an angle \mathcal{E} . According to Eq. III.1, considering only the isotropic damping, the DW velocity v_{DW} is symmetric with respect to the angle $\phi_J = 180^\circ$ (the collinear configuration).

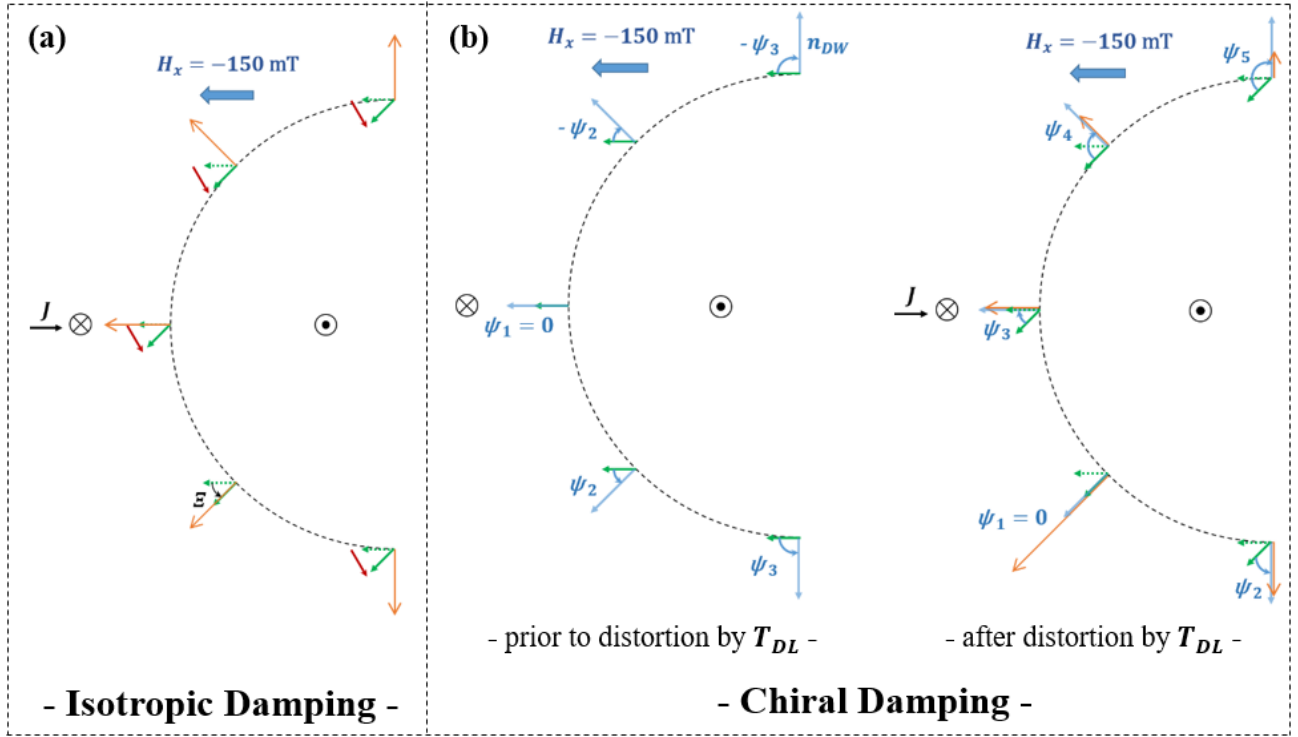


Figure III.40 The asymmetric non-collinear DW motion induced by the Chiral Damping at large H_x in Pt/Co/Pt. Schematic diagram of the velocity across the semi-circle shaped DW_{D-U} induced by the distortion of \mathbf{m}_{DW} by \mathbf{T}_{DL} at $H_x = -150$ mT based on; (a) the DMI with isotropic damping and on (b) the Chiral Damping (CD). The straight (dashed) green arrows correspond to \mathbf{m}_{DW} after (before) the distortion by \mathbf{T}_{DL} at the angle ϕ_J . The red arrows indicate the in-plane anti-clockwise rotation of \mathbf{m}_{DW} by \mathbf{T}_{DL} . The blue arrows correspond to the DW normal vector \mathbf{n}_{DW} at ϕ_J with ψ the angle between \mathbf{m}_{DW} and \mathbf{n}_{DW} . The orange arrows give the DW velocity at each angle ϕ_J . In (a), uniform velocity with ϕ_J . In (b), the distortion of \mathbf{m}_{DW} gives rise to a non-uniform damping with ϕ_J , which results in an asymmetric non-collinear motion.

In the presence of the chiral damping component α_c , the uniform action of SOT gives an asymmetric motion with the angle ϕ_J . Based on the proposal of the phenomenological equation for the CD by [Jué et al., 2015] (Eq. I.54 in Chapter I) and by substituting the DW normal vector \mathbf{n}_{DW} for the magnetization gradient ∇m_z , we express the damping for the DW as:

$$\alpha = \alpha_0 - \alpha_c \mathbf{m}_{DW} \cdot \mathbf{n}_{DW} = \alpha_0 - \alpha_c \cos \psi \quad (\text{III.6})$$

with ψ the angle between \mathbf{m}_{DW} and \mathbf{n}_{DW} (Figure III.40.b). α_{DU} (α_{UD}) refers to the damping for the DW_{D-U} (the DW_{U-D}). At the collinear configurations with respect to the current \mathbf{J} ($\phi_J = 0^\circ$ for the DW_{U-D} and $\phi_J = 180^\circ$ for the DW_{D-U}), $\cos \psi$ has opposite signs between the DW_{D-U} and the DW_{U-D} resulting in $\alpha_{DU} < \alpha_{UD}$. Based on the Eq. III.1, one obtains $v_{DU} > v_{UD}$. The CD mechanism promotes then the asymmetric motion between the two DWs at $H_x = -150$ mT that is opposite to the asymmetric motion induced by the DMI. Concerning the asymmetric motion with the angle ϕ_J , we focus on the semi-circle shaped DW_{D-U} ($90^\circ \leq \phi_J \leq 270^\circ$) prior to and after the distortion by \mathbf{T}_{DL} . Initially, the angle ψ variation is symmetric with respect to the angle $\phi_J = 180^\circ$. However, while distorting the DW, SOT makes the angle ψ asymmetric. Thereby, the minimum of α_{DU} , corresponding to the largest v_{DU} , becomes located at a non-collinear configuration ($180^\circ < \phi_J < 270^\circ$) where $\psi = 0^\circ$. This scheme applies also for the DW_{U-D} . Therefore, the CD mechanism is behind the asymmetric DW motion in the non-collinear configuration. The numerical model based on the DMI + SOT + CD mechanism predicts that the angle ϕ_J^{max} varies in the presence of H_x (Figure III.41). The angle ϕ_J^{max} is taken here as the angle of the maximum velocity. It saturates near -90° for the DW_{U-D} and shows a drastic decrease for the DW_{D-U} at large H_x . Since we were not able to extract any exact measurements of the angle ϕ_J^{max} in Pt/Co/Pt, the predictions shown in Figure III.41 could not be verified.

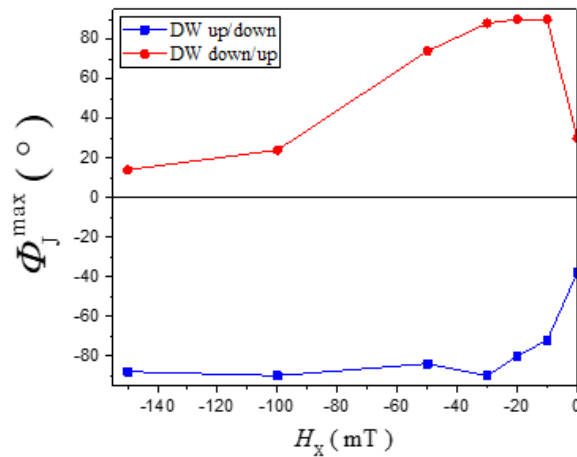


Figure III.41 The angle ϕ_J^{\max} versus the in-plane field H_x using the numerical collective coordinate model. The model is based on the DMI + SOT + CD mechanism and the angle ϕ_J^{\max} is taken as the angle of the maximum velocity for each DW. Blue (red) symbols correspond to the DW_{U-D} (the DW_{D-U}).

We have also included the Thiele DW width parameter in our numerical model (not shown). It did not modify the general trend of the DW velocity with the angle ϕ_J in the presence of H_x . Its contribution is symmetric and induces an increase in the DW velocity v_{DW} . This confirms that the asymmetry in CIDWM in the flow regime in Pt/Co/Pt is governed by the interplay between the DMI and the CD.

The DMI + SOT + CD mechanism is related to the action of SOT. Whether it results from the DMI and/or the CD, the asymmetry in the CIDWM is associated to the distortion of the DW core magnetization \mathbf{m}_{DW} by the damping-like torque \mathbf{T}_{DL} . We are then able to model our experimental results only in the flow regime of motion. As seen in **Figure III.26** and **Figure III.35**, the same features of the CIDWM are obtained in the creep regime of motion where the DMI + SOT + CD fails as discussed in section III.3.3. The physical mechanisms of the CIDWM are still then mysterious and call for additional theoretical and experimental efforts.

In this section, we have evidenced experimentally in Pt/Co/Pt an asymmetric non-collinear DW. This asymmetry is present whether a bias in-plane H_x field is applied or not. We have as well observed a reversal in the asymmetry between the two different DWs upon the increase of the amplitude of H_x . We were able to account for these observations in the flow regime of motion by considering the action of SOT in the presence of both the DMI and the CD. A good qualitative agreement between the numerical calculations and the experimental results was only achieved after taking into account the thermal fluctuations. The numerical model shows that the motion of the DWs is the outcome of the interplay between the DMI and the CD. At small H_x , the DMI dominates and imposes the sign of the asymmetry whereas the CD induces the opposite asymmetry at large H_x . These results demonstrate the relevance of the CD mechanism in CIDWM in SIA materials.

Conclusions

We have studied the current-induced non-collinear DW motion in Pt/Co/AlO_x and Pt/Co/Pt. Both materials exhibit the structural inversion asymmetry (SIA): a large SIA in Pt/Co/AlO_x and a low SIA in Pt/Co/Pt. In both structures, it is the Pt/Co bottom interface that has the dominant contribution to two of the phenomena that originate from SIA; DMI and SOT. This might explain the observed similarities in the non-collinear DW motion. These similarities consist in the DWs having a preferential motion at a finite angle ϕ_j^{max} with respect to the current direction independently of both the current density and the bias in-plane field. The angle ϕ_j^{max} is negative for the up/down DW and positive for the down/up DW.

The DMI + SOT mechanism in the flow regime predicts an asymmetric non-collinear DW motion in Pt/Co/AlO_x. However, this model is not in line with our experimental measurements of the angle ϕ_j^{max} as a function of the in-plane field. Actually, we have found a constant angle $\phi_j^{max} \approx 21^\circ$.

In the Pt/Co/Pt structure, we were also able to explain qualitatively our experimental results only in the flow regime. Nevertheless, we needed to include the thermal fluctuations and the Chiral Damping mechanism. Thanks to the thermal fluctuations, the current action is equivalent to the action of SOT on homochiral Néel walls though DWs are likely to stabilize in an intermediate configuration between Bloch and Néel since DMI is weak. We have evidenced that both the DMI and the Chiral Damping contribute to the asymmetric non-collinear DW motion. For a small in-plane field H_x , the DMI is the governing mechanism and dictates the asymmetric motion between the two different DWs. Whereas for a large in-plane field H_x , the Chiral Damping dominates and induces the opposite asymmetry between the two DWs. These findings are the evidence of the interplay between chiral energy and chiral dissipation in CIDWM in SIA materials.

The observation of the asymmetric motion in the creep regime in both materials suggests that the standard model based on the SOT action is limited. Therefore, to understand fully DWs dynamics in SIA materials, a broad and complex model of physical mechanisms, besides SOT, DMI and Chiral Damping, is still required.

Even though we do not understand its exact physical mechanisms, the non-collinear DW motion in SIA materials induces some intriguing consequences. We propose, in the following chapters, to examine these consequences on the DW motion and on the skyrmion bubble motion.

IV. The DW tilt in SIA materials

In this chapter, I will discuss about the formation of the DWs tilt during their current-induced motion in nanowires in SIA materials. I will address, in particular, the possible connection between the DW tilt and the current-induced non-collinear DW motion, described in the previous chapter. For that end, I have studied the DW tilt in Pt/Co/AlO_x and Pt/Co/Pt. From these investigations, we have shown that the non-collinear DW motion can be responsible for the DW tilt in large SIA materials.

IV.1. The formation of a DMI-induced DW tilt

In order to minimize its energy by reducing its length, the DW sits perpendicular to the wire. However, numerous studies in SIA materials showed a tilt of the DWs during their motion. [Ryu et al., 2012] reported, in the Pt/Co/Ni/Co/TaN structure, a DW tilt that is opposite to the tilt expected from the Oersted field (**Figure IV.1**). Later, a DW tilt was also reported in the Pt/Co/AlO_x structure [Lo Conte et al., 2017]. This suggests a common origin of the DW tilt in PMA materials with large SIA. Similarly, [Kwon et al., 2017] reported a sizeable DW tilt angle χ while the DWs are driven by an out-of-plane field H_z . Although in the latter case the authors suggested a significant role of the edge roughness, all of these observations are believed to be a consequence of the DMI. Some theoretical studies based on analytical models and micromagnetic simulations proposed an explanation for the formation of such DMI-induced DW tilt [Bouille et al., 2013; Martinez et al., 2014]. It results from the energy minimization process of the chiral NWs while being distorted by the driving mechanism, e.g. the out-of-plane field H_z or the damping-like torque T_{DL} . The DW core magnetization \mathbf{m}_{DW} is canted away from the normal to the DW. Therefore, in order to recover its favored Néel configuration, the DW tilts its surface. This effect scales with the DMI hence it is not significant in weak-DMI structures. Micromagnetic simulations showed that even under pinning in thermally activated motion, the DWs develop a net DMI-induced tilt angle χ . It has been evidenced that this effect is established after a time constant that is proportional to w^2 (w is the width of the wire).

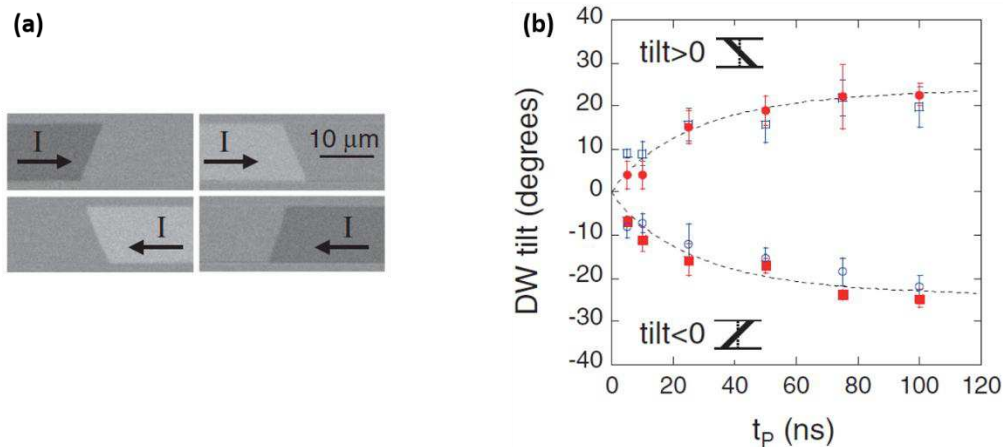


Figure IV.1 The DW tilt in the Pt/Co/N/Co/TaN structure. (a) MOKE images of the DW tilt in CIDWM. Dark (bright) contrast corresponds to down (up) magnetization. The tilt is opposite between the DW_{D-U} (left-side) and the DW_{U-D} (right-side). (b) The DW tilt angle vs the current pulse length t_p . Square (circle) symbols are for the DW_{D-U} (the DW_{U-D}). Solid (open) symbols represent the positive (negative) current pulses. A positive current flows from left to right in (a). The positive (negative) tilt angle corresponds to anti-clockwise (clockwise) rotation of the DW surface. The tilt angle increases and saturates for long pulses. Extracted from [Ryu et al., 2012].

IV.2. The DW tilt and the non-collinear DW motion

The asymmetric non-collinear DW motion was observed in tilted wires and in circular domains that are located in the center of a large wire and away from the edges. This rules out any possible contributions from complex current flow distributions. Still, one can ascribe the asymmetric non-collinear DW motion to the DW tilt. Indeed, the symmetry of the DW tilt angle in the Pt/Co-based structures (**Figure IV.1**) is similar to the symmetry of the angle ϕ_J^{max} observed in Pt/Co/Pt and Pt/Co/AlOx. It is possible that the DW tilt plays a role in the emergence of the asymmetric motion of the DWs with the angle ϕ_J . [Safeer et al., 2015] examined the dependence of the DW depinning current with ϕ_J in 500 nm-wide stripes. It yielded a dependence similar to that of the DW velocity v_{DW} with the angle ϕ_J . In these measurements, the current pulses are too short to enable a DW motion over large distances. Consequently, no DW tilt takes place. Moreover, the time resolved X-ray measurements of the DWs dynamics in dots of 500-nm-diameter in Pt/Co/AlOx revealed a fast and a preferential DW motion at a finite angle with respect to the current [Baumgartner et al., 2017] (**Figure IV.2**). The symmetry of that angle follows the angle ϕ_J^{max} . This technique (time resolution of 100 ps) probes the transient magnetic configuration during the application of sub-nanosecond current pulses. These are time scales that are shorter than the DW tilt time constant [Ryu et al., 2012; Boulle et al., 2013]. Therefore, these two experiments confirm that the asymmetric non-collinear DW motion is an intrinsic property of the DWs dynamics in Pt/Co structures and is not induced by the DW tilt mechanism.

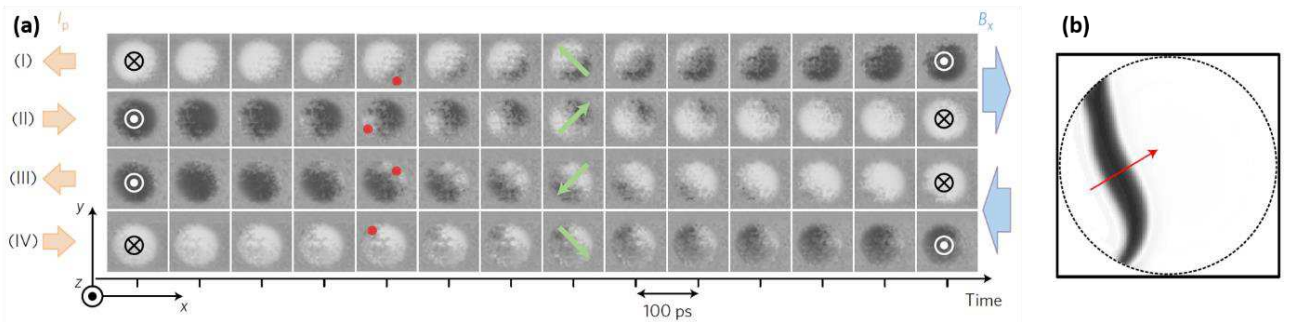


Figure IV.2 Time resolved X-ray measurements of the DW dynamics in Pt/Co/AlOx. (a) X-ray images of the magnetization switching in a 500-nm-dot of Co/AlOx on a Pt line by a 2-ns-long current pulse. \mathbf{I}_p and \mathbf{B}_x indicate, respectively, the current direction and the in-plane field. The current density is $2-4 \cdot 10^{12} \text{ A.m}^{-2}$. The applied \mathbf{B}_x is +94 mT and -124 mT. The red dots give the DW nucleation point and the green arrows its propagation direction. (b) Micromagnetic simulations of the tilt and motion of the DW_{D-U} between two frames separated by 200 ps under a positive current. The black area represents the area swept by the DW_{D-U} and the red arrow highlights the direction of the fastest motion. Note that the asymmetric motion of the DWs is in the presence of \mathbf{B}_x . Extracted from [Baumgartner et al., 2017].

In an alternative way, the DW tilt angle χ can be a consequence of the asymmetric non-collinear DW motion rather than being induced by the DW energy minimization process that aims to restore the DMI-induced Néel configuration, by analogy to suggestions in [Baumgartner and Gambardella, 2018; Kim et al., 2018]. The variation of the pinning forces in a wire transforms a straight DW into an arc-shaped DW during the motion. Due to the asymmetry of the DW velocity v_{DW} with the angle ϕ_J , the upper half of the DW is faster than the lower half or vice versa depending on whether the DW is the DW_{D-U} or the DW_{U-D} . The DW faster front is then expelled from the wire and the DW tilt takes place. The angle χ is fixed by the angle of the DW slower front (**Figure IV.3**).

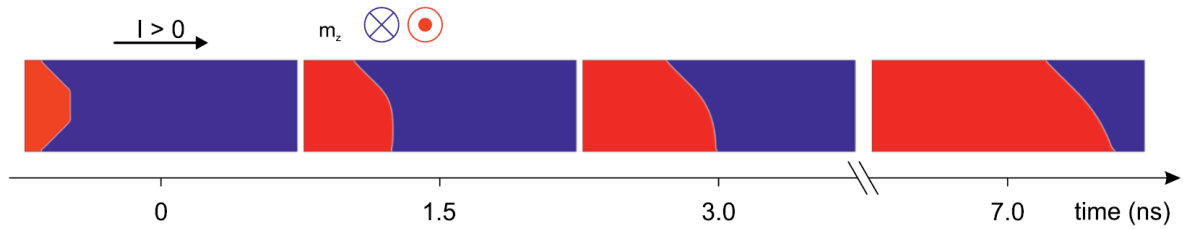


Figure IV.3 Snapshots from micromagnetic simulations of the arc-shaped DW_{U-D} driven by electric current. The current density is $4.5 \cdot 10^{12} \text{ A.m}^{-2}$. The wire is $4.5\text{-}\mu\text{m}$ -length and $1.5\text{-}\mu\text{m}$ -width. After $\approx 1.5 \text{ ns}$, the fastest DW is expelled from the wire. The final tilt angle corresponds to the DW slowest front and is in agreement with previous studies of the Pt/Co structures. Extracted from [Baumgartner and Gambardella, 2018].

IV.3. The DW tilt in Pt/Co/AlOx

We have investigated the formation of the DW tilt in our samples. For the Pt/Co/AlOx stack, it has only been observed in the low current density regime (or the creep regime) (**Figure IV.4.a**). It seems that it is rather induced by the asymmetric non-collinear DW motion. If the DMI were behind the emergence of the DW tilt under low current, the DW tilt would be as well present under a larger current while keeping the same pulse duration. Within this scenario, a pulse duration of 18 ns, sufficient to establish the DW tilt in **Figure IV.4.a**, is larger than the DMI-induced tilt time constant. However, the DW tilt is absent under a larger current density with 18-ns-long pulses in **Figure IV.4.b**. Following the description in **Figure IV.3**, the asymmetric non-collinear DW motion can be behind the DW tilt in the creep regime (note that **Figure IV.3** represents the DW_{U-D} whereas **Figure IV.4.a** shows the DW_{D-U} hence the opposite signs of the tilt angle). As the motion is no longer in the creep regime while increasing the current density, the DW profile remains straight. The DW tilt is then less apparent under large current densities since the arc-shaped DW profile is absent.

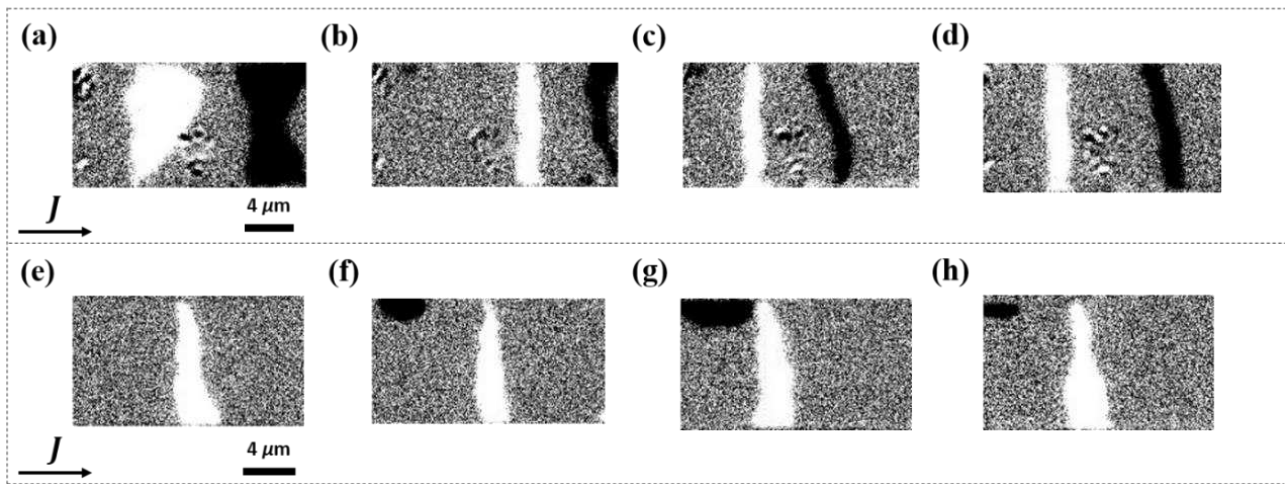


Figure IV.4 MOKE images of the DW_{D-U} tilt. (a)-(d) in Pt/Co/AlOx and (e)-(h) in Pt/Co/Pt. We have applied multiple current pulses with different number of pulses, pulse time lengths and current density amplitudes. (a) 2500 pulses, 18 ns, $J \sim +0.59 \cdot 10^{12} \text{ A.m}^{-2}$. (b) 4 pulses, 18 ns, $J \sim +0.99 \cdot 10^{12} \text{ A.m}^{-2}$. (c) 5 pulses, 2.4 ns, $J \sim +2.00 \cdot 10^{12} \text{ A.m}^{-2}$. (d) 10 pulses, 1.0 ns, $J \sim +2.75 \cdot 10^{12} \text{ A.m}^{-2}$. (e) 1000 pulses, 20 ns, $J \sim +1.09 \cdot 10^{12} \text{ A.m}^{-2}$. (f) 300 pulses, 9.4 ns, $J \sim +1.58 \cdot 10^{12} \text{ A.m}^{-2}$. (g) 850 pulses, 3.6 ns, $J \sim +2.24 \cdot 10^{12} \text{ A.m}^{-2}$. (h) 10000 pulses, 2.0 ns, $J \sim +2.73 \cdot 10^{12} \text{ A.m}^{-2}$.

IV.4. The DW tilt in Pt/Co/Pt

In the Pt/Co/Pt wires, the DW tilt is present in CIDWM (**Figure IV.4.e-h**). Unlike Pt/Co/AlOx, the tilt angle χ follows the symmetry of the Oersted field and is opposite to the expected DMI-induced tilt. In Pt/Co/Pt, the DMI has the same sign as in the Pt/Co-based structures with large SIA. Since the motion is along the current direction, the symmetry of the DMI-induced DW tilt in Pt/Co/Pt would follow the example shown in **Figure IV.1**. The absence of such a tilt corroborates then with a weak DMI in Pt/Co/Pt. Actually, other studies argued that in Pt/Co/Pt the Oersted field can lead to large effects in wires with large widths [Yoo, Moon and Choe, 2013]. According to [Yamanouchi et al., 2006], in a thin uniform metallic conductor ($t \ll w$), the Oersted field generated by the current is concentrated on the two edges of the wire and its averaged out-of-plane component writes:

$$H_z = \mp \frac{Jt}{4\pi} [3 + 2\ln\left(\frac{w}{t}\right)] \quad (\text{IV.1})$$

As $t = 5.1$ nm in Pt/Co/Pt, the Oersted field can reach values up to 9.3 mT under $J = 1 \cdot 10^{12}$ A.m⁻² for a 10 μ m-width wire. These values are not negligible and can contribute to the DW motion at the edges. The Oersted field effect in Pt/Co/Pt exceeds probably the DW speed asymmetry that might result from the non-collinear geometry with respect to current. Therefore, unlike Pt/Co/AlOx, the DW tilt might be induced by the Oersted field in Pt/Co/Pt.

Conclusions

In this chapter, I have mainly examined the formation of the DW tilt during its motion in different SIA structures: Pt/Co/AlO_x and Pt/Co/Pt. Initially, the DW tilt that was observed in several large SIA structures was attributed to the DMI effect. The current-induced torques distort the DW internal structure so that the counter effect consists on the DW tilting its surface to recover its DMI-stabilized Néel configuration. In the meantime, there have been other proposals suggesting a possible role of the asymmetric non-collinear DW motion in the emergence of such a DW tilt. I have then verified these two possible scenarios by investigating the DW motion in wires. In the Pt/Co/AlO_x structure, the DW tilt is significant only in the creep regime motion. We have then proposed the combination of the asymmetric non-collinear motion and the arc-shaped DW profile to be responsible for the formation of the DW tilt. In the flow regime, the DW remains straight so that no tilt emerges. In the Pt/Co/Pt structure, we have evidenced that the DW tilt is induced by the Oersted field effect. Following our study, it appears that the mechanism of the non-collinear DW motion does not lead systematically to the emergence of the DW tilt in the SIA materials.

V. The extrinsic mechanism of the Skyrmion Hall Effect

In Chapter III, we have evidenced the asymmetric non-collinear DW motion with respect to the injected electric current in Pt/Co/Pt and Pt/Co/AlO_x. The DWs have a preferential direction of motion at an oblique finite angle ϕ_J^{max} . Interestingly, the angle ϕ_J^{max} exhibits striking similarities with the skyrmion Hall Effect (SkHE) (**Figure V.1**). The SkHE is the deflection of the magnetic skyrmions from their trajectories, while being driven by the current along a nanowire, by an angle called the Skyrmion Hall angle (SkHA) θ_{SkH} . As for the asymmetric non-collinear DW motion, it distorts a magnetic circular domain into an ellipse whose the major-axis direction is fixed by the angle ϕ_J^{max} of the front DW. Thereby, the major-axis of the down (up) domain rotates anti-clockwise (clockwise) with respect to the current direction. As for the SkHE, a Néel down (up) magnetic skyrmion is deflected anti-clockwise (clockwise). The angles ϕ_J^{max} and θ_{SkH} have then the same symmetry. It is noteworthy to remind that Pt/Co/Pt and Pt/Co/AlO_x contain the required ingredients for the formation and the manipulation of Néel magnetic skyrmions, namely the interfacial DMI and SOT, both originating from SIA. Therefore, it is legitimate to imagine a causal connection (gyration) between these two phenomena since the motion of magnetic skyrmions is analogous to chiral NWs dragged by SOT [Sampaio et al., 2013]. We have then studied the current-induced motion of the chiral magnetic bubbles, or the skyrmion bubbles, in Pt/Co/Pt and Pt/Co/AlO_x. This experimental investigation has allowed us to demonstrate the extrinsic mechanism of the SkHE. It consists in a well-defined deflection of the skyrmion bubbles that is induced by the asymmetric non-collinear DW motion.

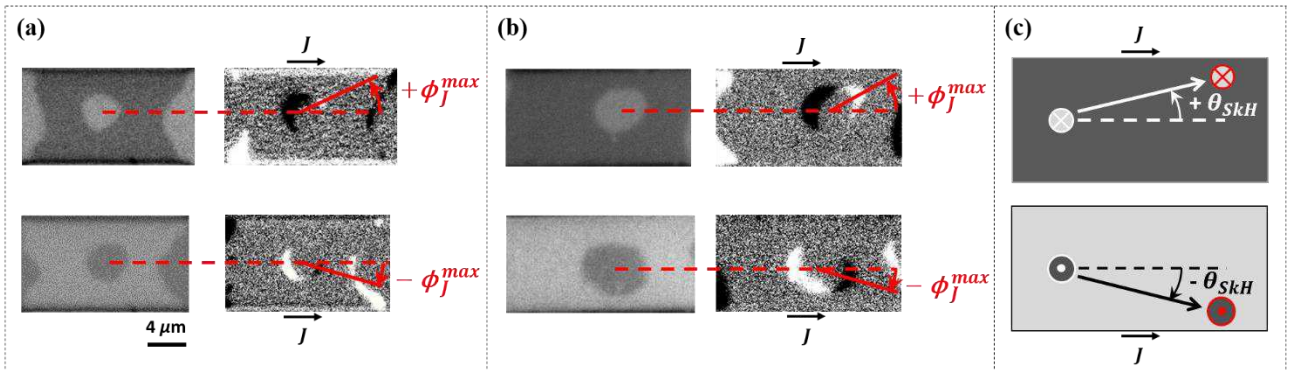


Figure V.1 Similarities between the non-collinear DW motion and the Skyrmion Hall Effect. (a) and (b) are the MOKE images of the asymmetric non-collinear DW motion in Pt/Co/Pt and Pt/Co/AlO_x, respectively. The angle ϕ_J^{max} of the front DW of the magnetic circular domain is highlighted. On the left, MOKE image of the initial state of the magnetic circular domain. On the right, differential MOKE image of the final state of the magnetic circular domain after the current injection where bright (dark) contrast gives the DW_{D-U} (DW_{U-D}) displacement. (c) Schematic diagram of the SkHE for the Néel skyrmion moving in the current direction. The up (down) panels correspond to the domain/skyrmion with the down (up) magnetization. The angles ϕ_J^{max} and θ_{SkH} follow the same symmetry with respect to the magnetization and to the current polarity (negative current not shown here).

In order to evidence the extrinsic SkHE, we first introduce the conventional SkHE mechanism or the intrinsic SkHE. This will enable us to emphasize that the mechanism of the asymmetric non-collinear DW motion and the intrinsic SkHE are independent. Next, we will describe the procedure used to stabilize and manipulate the chiral magnetic bubbles in Pt/Co/Pt and Pt/Co/AlO_x. As the intrinsic SkHE is vanishingly small, the sizeable deflection of these skyrmion bubbles reveals the extrinsic contribution to the SkHE. To account for such contribution, we propose a mechanism based on the asymmetric non-collinear DW motion. Finally, we will discuss the relevance of the extrinsic SkHE for the compact magnetic skyrmions.

V.1. The intrinsic SkHE

V.1.1. Magnetic skyrmions

Skyrmions are smooth magnetic objects that resemble the DWs [Skyrme, 1962]. The interest in the magnetic skyrmions had surged after the observation of a skyrmion lattice in a bulk MnSi due to the symmetry breaking in the structure by the DMI [Mühlbauer, 2009]. Upon crossing a skyrmion, the magnetic texture corresponds to a 360° Bloch or Néel wall. We speak for the former of the Bloch-type skyrmion and for the latter of the hedgehog or the Néel-type skyrmion (Figure V.2). The difference between the Bloch-type and the Néel-type skyrmions comes from the microscopic mechanism responsible for the DMI in the system. The bulk DMI induces a DMI vector \mathbf{D}_{ij} usually parallel to the vector \mathbf{r}_{ij} that connects the neighboring magnetic moments at the atomic sites i and j . It favors the helical magnetization spirals with a fixed chirality (Bloch-type skyrmion) [Yu et al., 2010]. In contrast, the interfacial DMI (cf. section I.5.1) induces the cycloidal magnetization spiral (Néel-type skyrmion). In the presence of the DMI, the skyrmions have a fixed chirality: either left-handed or right-handed whereas both chiralities are possible for trivial magnetic bubbles in dipolar systems. In this work, we only focus on the Néel-type skyrmions because the DMI in our ultrathin ferromagnetic layers has an interfacial origin.

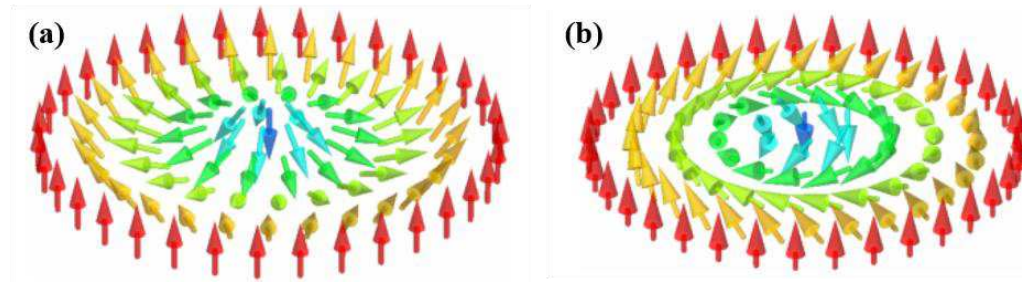


Figure V.2 Magnetic skyrmions in systems with Structural Inversion Asymmetry. (a) Hedgehog or Néel-type skyrmion with a left-handed chirality. (b) Bloch-type skyrmion with a right-handed helical spiral. The magnetization of the skyrmion core is pointing down. Extracted from [Everschor-Sitte, 2012].

Skyrmions are topologically protected magnetic objects. The topological protection is associated to the topological quantization parameter n (the winding number). It is expressed as [Chen, 2018]:

$$n = \frac{1}{4\pi} \iint \mathbf{m} \left(\frac{\partial \mathbf{m}}{\partial x} \times \frac{\partial \mathbf{m}}{\partial y} \right) dx dy \quad (\text{V.1})$$

n is the number that counts how many times the local magnetization \mathbf{M} is wrapped around a unit sphere. Thanks to the chiral structure of the skyrmion, n is an integer that depends on the orientation of the magnetization at the skyrmion center ($n = +1$ for \mathbf{M} pointing up and $n = -1$ for \mathbf{M} pointing down). We refer to n also as the topological charge. The skyrmion is topologically not equivalent to the other magnetic configurations like the uniform magnetization state with $n = 0$. It is not possible to deform these configurations continuously into each other without having to overcome an infinite energy barrier (topological classification). As a picture, the skyrmion resembles a knot tied into a rope that cannot be untied without using the ends or by cutting the rope. However, the energy barrier is finite in real magnetic systems and skyrmions can be annihilated at the sample edges or distorted by defects [Braun, 2018]. We note that the definition of n is independent of the skyrmion size. In this manuscript, we use the term “skyrmion bubble” to describe a skyrmion that has a plateau region in their center in opposition to a compact skyrmion where a single spin is reversed. The competition between the DMI and the other magnetic interactions sets the skyrmion size. Large or compact, skyrmions are topologically equivalent like it is demonstrated by micromagnetic simulations [Jiang et al., 2017]. In literature, the reported size of a skyrmion can go from sub-100 nm up to $2 \mu\text{m}$.

Owing to their small size and their stability, the magnetic skyrmions have emerged as promising candidates for spintronic devices [Sampaio et al., 2013]. Compared to the DWs, their motion require a reduced critical current density [Iwasaki, Mochizuki and Nagaosa, 2013], which is useful for low-energy cost functionalities. Moreover, the modeling of defects and impurities did not reveal any significant effect on their motion, essential for a better reliability. An intensive research effort has then been conducted to demonstrate the stabilization and the manipulation of magnetic skyrmions at room temperature. Recently, skyrmions were experimentally detected in sputtered Pt/Co/MgO structures [Boulle et al., 2016]. Subsequently, multiple works have reported the manipulation of skyrmions at very high speed by current.

V.1.2. Current-induced motion and the SkHE

In experiments, the skyrmion motion can be strongly hindered by pinning [Jiang et al., 2015; Yu et al., 2016; Jiang et al., 2017; Legrand et al., 2017] and can also be efficient with velocities up to $120 \text{ m}\cdot\text{s}^{-1}$ [Woo et al., 2016, 2017, 2018; Hrabec et al., 2017; Litzius et al., 2017; Juge et al., 2019]. Usually, there is no direct evidence of the chiral magnetic texture of the bubble because a suited imaging technique is difficult to provide. The distinction between skyrmions and trivial bubbles relies on the direction of motion induced by the electric current. Based on the DMI + SOT mechanism, a unidirectional displacement along or opposite to the current flow is a hallmark of the Néel-type skyrmion [Jiang et al., 2015; Woo et al., 2016, 2017, 2018; Yu et al., 2016; Litzius et al., 2017]. The Bloch-skyrmion would have a transverse motion with respect to the current flow [Tomasello et al., 2015]. The observation of the current-induced deflection is also considered as an indication of the topological charge, characteristic of the hedgehog skyrmions [Hrabec et al., 2017; Wang et al., 2019].

This deflection is usually identified as the intrinsic SkHE that was predicted from several theoretical works [Zang et al., 2011; Nagaosa and Tokura, 2013] and micromagnetic simulations [Tomasello et al., 2015; Zhang, Zhou and Ezawa, 2016]. It results from the emergent electromagnetism that can be important for the moving skyrmion.

V.1.2.1. The emergent electromagnetism

In a conductor, the moving charged particles are deflected perpendicularly to their velocities in the presence of a magnetic field. This is the Hall Effect from the Lorentz force. By analogy, the skyrmion has a nonzero topological charge n that plays the role of a local finite fictitious field (corresponding to the central magnetization \mathbf{M}) for conduction electrons in a thin magnetic field. We can then expect a mechanism similar to the classical Hall effect to be related to the intrinsic SkHE. This mechanism is the Berry phase curvature [Everschor-Sitte and Sitte, 2014].

In fact, the state of the spin of a conduction electron is characterized by a wave with an amplitude and a phase. When these two parameters change simultaneously and adiabatically following a cyclic variation (going back to the initial configuration), the system recovers the initial eigenstate but with a phase factor. The phase factor has two contributions. The first comes from the time evolution whilst the second from the variation of the eigenstate with the changing Hamiltonian. This second contribution is the so-called Berry phase and it is nonzero for a system undergoing an adiabatic cyclic variation. It has a major effect on many observed properties in solid-state physics such as electric polarization, orbital magnetism, quantum Hall Effect and anomalous Hall Effect. In the adiabatic limit, a free conduction electron crossing a spatially inhomogeneous magnetic structure adjusts constantly its spin to the direction of the local magnetization \mathbf{M} . Consequently, the spin of the electron picks up a Berry phase while flowing through a magnetic skyrmion. The Berry phases are

opposite for the up and the down skyrmions and they act as emergent fields felt by an electron traveling in a uniform magnetic state. These emergent fields are the orbital magnetic field \mathbf{B}^e and the electrical field \mathbf{E}^e whose components are expressed as follows [Everschor-Sitte and Sitte, 2014]:

$$B_i^e = \frac{\hbar}{2} \epsilon_{ijk} \mathbf{m} \cdot \left(\frac{\partial \mathbf{m}}{\partial j} \times \frac{\partial \mathbf{m}}{\partial k} \right) \quad (\text{V.2})$$

$$E_i^e = \hbar \mathbf{m} \cdot \left(\frac{\partial \mathbf{m}}{\partial i} \times \frac{\partial \mathbf{m}}{\partial t} \right) \quad (\text{V.3})$$

with \hbar the reduced Planck constant or the quantum of angular momentum. The topological charge n of the skyrmion ensures a net emergent magnetic flux as can be obtained after integration of Eq. V.2:

$$\int \mathbf{B}^e \cdot d\boldsymbol{\sigma}_P = 4\pi\hbar n \quad (\text{V.4})$$

with σ_P denoting the Pauli matrix. The emergent electric field is only finite for a time-dependent spin profile. A skyrmion moves with a drift velocity \mathbf{v}_d . Since $\partial \mathbf{m} / \partial t = -(\mathbf{v}_d \cdot \nabla) \mathbf{m}$, the magnetic and the electric fields are coupled as [Everschor-Sitte and Sitte, 2014]:

$$\mathbf{E}^e = -\mathbf{v}_d \times \mathbf{B}^e \quad (\text{V.5})$$

The Eq. V.5 reflects the Faraday's law of induction, i.e. a change of the magnetic flux causes an electric field. These emergent fields lead to Lorentz forces acting on the conduction electrons and giving a contribution to the Hall signal. Since the magnetization texture enters in the expressions of \mathbf{B}^e and \mathbf{E}^e , the Hall signal is called the topological Hall effect. There are several reports of measurements of the emergent topological Hall effect [Schulz et al., 2012; Soumyanarayanan et al., 2017; Leroux et al., 2018; Maccariello et al., 2018; Zeissler et al., 2018].

The back reaction (the counter-force) of the topological Hall effect is the intrinsic SkHE [Everschor-Sitte and Sitte, 2014]. The gyrotropic force or the "Magnus force" emerges and deflects the skyrmions perpendicularly to their velocities. The notion of the Magnus force is taken by analogy with classical mechanics. The Magnus force acts on a spinning ball in the air bending its path like a soccer ball. Accelerated air on one side of the spinning ball and decelerated air on the other side give rise to a force acting on the air. Consequently, the ball experiences the opposite force that is the Magnus force. As for the skyrmion, the emergent fields from the Berry phase induce the Lorentz forces deflecting the current that in turn lead to the counter-effect, the "topological Magnus force".

These emergent fields give a canonical conjugate relation between the coordinates X and Y of the skyrmion core center (Eq. V.5). This relation helps to describe analytically the intrinsic SkHE through the Thiele Equation of motion. Multiple theoretical works have demonstrated the good agreement between micromagnetic results and the Thiele Equation [Iwasaki, Mochizuki and Nagaosa, 2013; Tomasello et al., 2015].

V.1.2.2. The Thiele Equation of motion

We consider the motion of the magnetic skyrmion within the framework of the soliton dynamics with a mass \mathcal{M} and a position vector \mathbf{R} . Its equation of motion is given as [Thiele, 1973; Tretiakov et al., 2008; Tveten et al., 2013]:

$$\mathcal{M}\ddot{\mathbf{R}} - \mathbf{G} \times \dot{\mathbf{R}} - \alpha\mathcal{D} \cdot \dot{\mathbf{R}} = \mathbf{F} \quad (\text{V.6})$$

The time-resolved X-ray investigations of SOT-driven excitations, on the nanosecond time scale, suggest the absence of inertial effects for skyrmions in quasi-infinite geometries [Litzius et al., 2017; Woo et al., 2017]. They demonstrated that the skyrmion velocity follows the current pulses without any delay. In contrast, other observations reported strong inertial effects for trivial bubbles in narrow confined geometries [Büttner et al., 2015]. In fact, the mass \mathcal{M} scales inversely with the rigidity of the spin structure. Thanks to the DMI, the spin structure of a skyrmion is rigid thus lowering the effective mass. In addition, we usually manipulate skyrmions in wide and long patterned tracks. Therefore, the assumption of a rigid massless-particle is valid. The Eq. V.6 is simplified to obtain the Thiele Equation of motion:

$$\mathbf{G} \times \mathbf{v} - \alpha\mathcal{D} \cdot \mathbf{v} + \mathbf{F} = 0 \quad (\text{V.7})$$

with $\dot{\mathbf{R}} = \mathbf{v} \equiv (v_x, v_y)$ the velocity of the skyrmion center. The first term is the transverse force acting on the skyrmion called the ‘‘topological Magnus force’’ or the gyrotropic term. The second term is the ‘‘frictional force’’ and the third term \mathbf{F} represents the sum of effective forces acting on the skyrmion.

The topological Magnus force

This force ($\mathbf{G} \times \mathbf{v}$) is nonzero for magnetic objects with a nonzero topological charge n . It is characterized by the gyromagnetic coupling vector \mathbf{G} :

$$\mathbf{G} \equiv \left(0, 0, -4\pi n \frac{\mu_0 M_s t_{FM}}{\gamma}\right) \quad (\text{V.8})$$

\mathbf{G} changes then sign between the opposite orientations of the skyrmion magnetization. Skyrmions with opposite orientations are thereby deflected in opposite directions. The intrinsic SkHE is then attributed to the presence of the gyromagnetic coupling vector \mathbf{G} . In the absence of the DMI, there is no unique topological charge for the magnetic bubbles so the random transverse motion is expected.

The frictional force

It is the force ($-\alpha\mathcal{D} \cdot \mathbf{v}$) that is due to the magnetic damping mechanism represented by the dissipative tensor \mathcal{D} . The components of \mathcal{D} are given by [Hrabec et al., 2017]:

$$\mathcal{D}_{xx} = \mathcal{D}_{yy} = \frac{\mu_0 M_s t_{FM}}{\gamma} \int \left(\frac{\partial m}{\partial x}\right)^2 dx dy \quad (\text{V.9})$$

$$\mathcal{D}_{xy} = \mathcal{D}_{yx} = 0 \quad (\text{V.10})$$

The equations V.9 and V.10 are derived under the assumptions that the skyrmion maintains its rotational symmetry during the motion. Subsequently, the exact numerical evaluation of \mathcal{D}_{xx} for the Néel skyrmion can be well approximated to the following analytical formula for $d > 2\Delta$ where d is the skyrmion diameter and Δ the DW width parameter [Hrabec et al., 2017]:

$$\mathcal{D}_{xx} \approx \frac{\mu_0 M_s t_{FM}}{\gamma} \pi \left(\frac{d}{\Delta} + \frac{4\Delta}{d} \right) \quad (\text{V.11})$$

As for the effective force \mathbf{F} , we write it as follows:

$$\mathbf{F} = \mathbf{F}^u + \mathbf{F}_{STT} + \mathbf{F}_{Oe} + \mathbf{F}_{SOT} \quad (\text{V.12})$$

The first term \mathbf{F}^u on the right side assembles forces due to the changes in the potential energy of the skyrmion. We define it as $\mathbf{F}^u = -\nabla U$ with U the potential energy at the coordinates (X, Y) of the skyrmion center. In principle, \mathbf{F}^u can have a component transverse to the current direction, which can have an impact on the SkHE. In the present work, we do not consider the action of any possible \mathbf{F}^u . \mathbf{F}_{STT} is the force that results from the action of the adiabatic \mathbf{T}_A and the nonadiabatic \mathbf{T}_{NA} torques from the STT mechanism (cf. section I.4.1). As the STT mechanism is neglected in thin layers with SIA, \mathbf{F}_{STT} is not taken into account. The third term \mathbf{F}_{Oe} is the force originating from the Oersted-field gradient in the wire and is always transverse to the current direction. Therefore, \mathbf{F}_{Oe} contributes to the skyrmion deflection. For a uniform current along the x -axis, \mathbf{F}_{Oe} is given by [Yu et al., 2016, 2017; Hrabec et al., 2017]:

$$\mathbf{F}_{Oe} = \frac{\pi}{2} d^2 t_{FM} M_s \frac{\partial H_z^{Oe}}{\partial y} \mathbf{u}_y \quad (\text{V.13})$$

with $\partial H_z^{Oe}/\partial y$ the change in the out-of-plane component of the Oersted field across the skyrmion diameter.

The effective SOT force

The fourth term \mathbf{F}_{SOT} is due to SOT induced by the current flowing in the adjacent HM layer. We neglect the field-like component and only the damping-like contribution from the SHE is taken into account (cf. section I.4.2). We write then [Jiang et al., 2017]:

$$\mathbf{F}_{SOT} = 4\pi \mathbf{B} \cdot \mathbf{J} \quad (\text{V.14})$$

Here, \mathbf{B} is the tensor that quantifies the efficiency of the damping-like torque over the spin profile of the skyrmion [Wang et al., 2019]. The components of \mathbf{B} for the rigid Néel skyrmion are given by:

$$\mathcal{B}_{xx} = \mathcal{B}_{yy} = \eta \int \left(\frac{\partial \mathbf{m}}{\partial x} \times \mathbf{m} \right)_y dx dy \quad (\text{V.15})$$

$$\mathcal{B}_{xy} = \mathcal{B}_{yx} = 0 \quad (\text{V.16})$$

with η the parameter characterizing the strength of the damping-like torque \mathbf{T}_{DL} . Upon applying a uniform current along the x -axis, the generated \mathbf{F}_{SOT} from the bottom HM layer writes [Hrabec et al., 2017]:

$$\mathbf{F}_{SOT} = 4\pi \mathcal{B}_{xx} \mathbf{J} \mathbf{u}_x = \pm \frac{\pi \hbar}{2e} b \theta_{SH} \mathbf{J} \mathbf{u}_x \quad (\text{V.17})$$

where b is a skyrmion characteristic length (half its perimeter when $d \gg \Delta$) and the orientation of \mathbf{F}_{SOT} is set by the spin Hall angle θ_{SH} and the magnetic texture chirality by the symbol \pm (+ for the left-handed and – for the right-handed chirality).

We note that the Thiele Equation of motion does not include neither pinning nor modifications of the internal degrees of freedom (the mass) of the skyrmion. It allows us to characterize the intrinsic SkHE by the skyrmion Hall angle (SkHA) θ_{SkH} ; the angle between the current flow and the skyrmion position.

V.1.2.3. The Skyrmion Hall angle (SkHA)

Based on the Thiele Equation of motion and upon neglecting $\mathbf{F}_{\mathbf{0e}}$, we express components of the skyrmion velocity, v_x and v_y , as:

$$v_x = \frac{\alpha \mathcal{D}_{xx}}{G^2 + \alpha^2 \mathcal{D}_{xx}^2} F_{SOT} \quad (\text{V.18})$$

$$v_y = \frac{G}{G^2 + \alpha^2 \mathcal{D}_{xx}^2} F_{SOT} \quad (\text{V.19})$$

The SkHA θ_{SkH} is then expressed as:

$$\theta_{SkH} = \tan^{-1} \left(\frac{v_y}{v_x} \right) = \tan^{-1} \left(\frac{G}{\alpha \mathcal{D}_{xx}} \right) \quad (\text{V.20})$$

Based on Eq. V.11, we have:

$$\theta_{SkH} = \tan^{-1} \left[-\frac{4n}{\alpha} \left(\frac{d}{\Delta} + \frac{4\Delta}{d} \right)^{-1} \right] \quad (\text{V.21})$$

In the limit of large skyrmion bubbles ($d \gg \Delta$), θ_{SkH} is simplified to [Hrabec et al., 2017; Litzius et al., 2017]:

$$\theta_{SkH} = \tan^{-1} \left(-\frac{4\Delta}{\alpha d} n \right) \quad (\text{V.22})$$

We should note here the difference in the approximated formula of θ_{SkH} in literature. It results from different assumptions concerning the spin profile of the skyrmion in order to evaluate the dissipative tensor component \mathcal{D}_{xx} . For instance, in [Jiang et al., 2017], θ_{SkH} writes:

$$\theta_{SkH} = \tan^{-1} \left(-\frac{8\Delta}{\alpha \pi^2 d} n \right) \quad (\text{V.23})$$

Finally, the SkHE is detrimental from the application point of view since it pushes skyrmions towards the edges of the patterned devices resulting in their annihilation. Nevertheless, it can be useful for novel applications like the topological sorting as up and down skyrmions are deflected in opposite directions. In the meantime, there are proposals to use the ferrimagnets or the antiferromagnets to inhibit or even make disappear the intrinsic SkHE [Zhang, Zhou and Ezawa, 2016; Woo et al., 2018]. The direct observation of the SkHE was reported recently in several experimental works.

V.1.2.4. Experimental observations of the intrinsic SkHE

By evidencing the vertical motion that follows the symmetry of the topological Magnus force (Eq. V.8), many groups have confirmed the direct observation of the intrinsic SkHE [Yu et al., 2016; Hrabec et al., 2017; Wang et al., 2019]. Nonetheless, only a few were able to perform quantitative measurements of the SkHA allowing the confrontation of the theory predictions with the experimental findings [Jiang et al., 2017; Litzius et al., 2017; Juge et al., 2019].

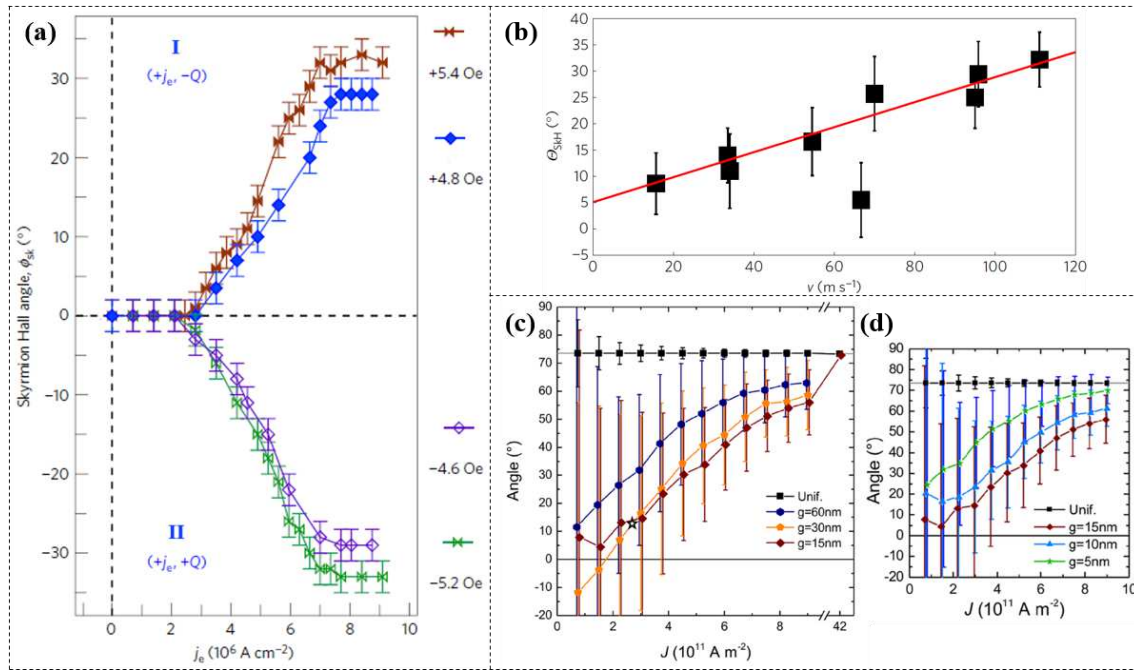


Figure V.3 Observations of the drive-dependent skyrmion Hall effect. (a) The measured SkHA versus electron flow density j_e in Ta (5 nm)/CoFeB (1.1 nm)/TaOx (3 nm). Above the threshold current density, the SkHA exhibits a linear dependence and then saturates. Here, skyrmions, with a topological charge Q , move along the electron flow j_e . The up (down) panel I (II) corresponds to skyrmions with down (up) magnetization driven by a positive j_e . The SkHA decreases by increasing (decreasing) the skyrmion diameter (out-of-plane field) from $d = 800 \pm 300$ nm (+5.4 Oe, blue symbols/-5.2 Oe, green symbols) to $d = 1100 \pm 300$ nm (+4.8 Oe, red symbols/-4.6 Oe, purple symbols). (b) The measured SkHA θ_{skH} as a function of the skyrmion velocity in [Pt (3.2 nm)/CoFeB (0.7 nm)/MgO (1.4 nm)]₁₅ for a skyrmion with $d = 110$ nm. The linear fit (red line) is a guide to the eye. (c)-(d) The mean SkHA as a function of the current density J from micromagnetic simulations where the magnetic film is modeled as a granular system in which grains positions and sizes are random. DMI has a Gaussian distribution within grains. The uniform case (constant DMI) in black symbols is fitted to a line showing a constant SkHA. In (c), different grain sizes are $g = 60$ nm (blue symbols), $g = 30$ nm (gold symbols) and $g = 15$ nm (red symbols). In (d), $g = 15$ nm (red symbols), $g = 10$ nm (blue symbols) and $g = 5$ nm (green symbols). Extracted and adapted from (a) [Jiang et al., 2017], (b) [Litzius et al., 2017], (c) and (d) [Legrand et al., 2017].

In fact, some observations have evidenced a strong dependence of the SkHE on the regime of motion (Figure V.3) [Jiang et al., 2017; Woo et al., 2018; Juge et al., 2019]. This is not in line with the predictions of a constant SkHA. The Eq.V.22 does not contain any term connected neither to the current density nor to the velocity of motion. Under low current densities (the creep regime of motion), there is a cancellation of the SkHE. Skyrmions move in a hopping-like mode without a net deflection angle (Figure V.3.a). The SkHA is observed under larger current densities and it increases with current/velocity. Eventually, the angle θ_{skH} saturates at its expected theoretical value when the skyrmion is driven in the flow regime. Such behavior is reminiscent of a strong pinning effect. The competition between the topological Magnus force and disorder leads to a drive-dependent SkHA. Under low current densities, skyrmions are pinned. As they become able to overcome defects, the SkHA emerges. These variations of the SkHA can be reproduced in micromagnetic simulations that include pinning as random distributions of magnetic parameters within the film grains [Kim and Yoo, 2017; Legrand et al., 2017]. The non-uniformity of the magnetic parameters between neighboring grains makes skyrmions suffer from a dispersion of their equilibrium diameter. They even get a transverse motion opposite to the expected SkHA. In Figures V.3.c and .b, we show the SkHA variation with the current density from micromagnetic simulations where the DMI is the only parameter randomly distributed in the granular system. For any given mean grain size g , the reduction of the SkHA is qualitatively the same. The most significant suppression of the SkHA is obtained for $g = 15$ nm that is comparable to the average skyrmion diameter d considered in the study [Legrand et al., 2017]. For a smaller grain size, the local variations of the magnetic parameters are averaged over the skyrmion size whereas for a larger grain size the gradient of local variations is weak so that in both cases the reduction of the SkHA is less stressed. Micromagnetic simulations show that the variations of M_s induce the strongest SkHA reduction whilst the weakest effects come from DMI distributions [Legrand et al., 2017].

V.1.3. The intrinsic SkHE and the asymmetric DW motion in the non-collinear configuration

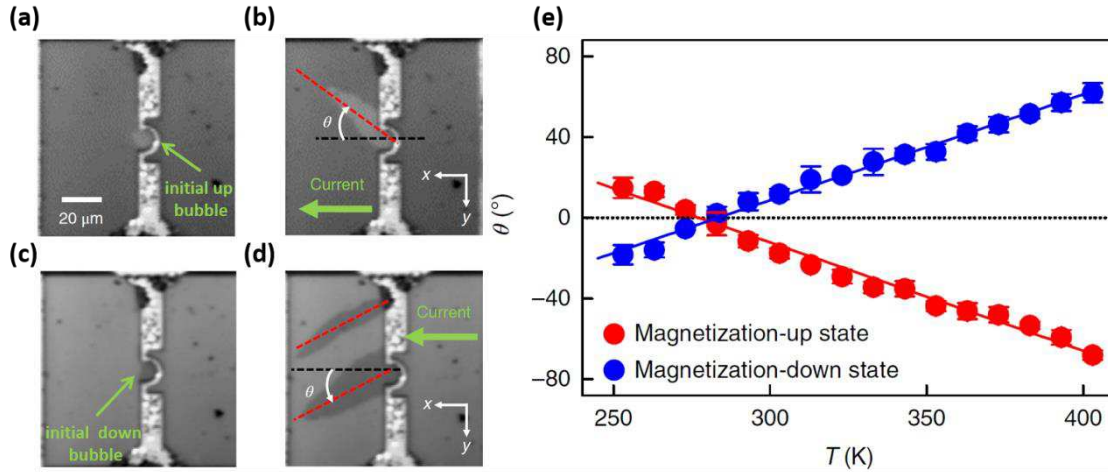


Figure V.4 Oblique elongation of the magnetic bubbles in GdFeCo/Pt ferrimagnet structure. (a) MOKE image of a nucleated circular up bubble. Dark and bright areas correspond to down and up magnetizations, respectively. (b) The oblique elongation of the up bubble obtained after the current injection into (a). (c) MOKE image of a nucleated circular down bubble. (d) The oblique elongation of the down bubble. (e) The elongation angle θ as a function of temperature T of the ferrimagnet. The angle θ vanishes near the compensation temperature of the ferrimagnet. Extracted from [Hirata et al., 2019].

As they have the same symmetry with the topological charge n , the intrinsic SkHE and the asymmetric non-collinear DW motion can be two linked phenomena. In fact, the magnetic circular domains are skyrmion-like objects thanks to the DMI in Pt/Co/Pt and Pt/Co/AlOx. In principle, the intrinsic SkHE is expected for these objects. It contributes then to or even might be responsible for the observed asymmetric non-collinear DW motion. However, the asymmetric non-collinear DW motion has been initially evidenced for magnetic domains with relatively large diameters $d \sim 4 - 8 \mu\text{m}$.

According to the analytical formula (Eq. V.22 or .23), the angle θ_{SkH} is determined by the skyrmion size d , the DW width Δ and the damping parameter α . The dependence on $1/d$ imposes a decreasing θ_{SkH} for an increasing d , which is confirmed by micromagnetic simulations. They give a ratio $|v_y/v_x|$ ($\theta_{SkH} = \tan^{-1}(v_y/v_x)$) that varies with the ratio of d/Δ for a constant current density [Legrand et al., 2017]. For a compact skyrmion (at the limit $d \approx \pi\Delta$), the SkHA is very large and increases initially with d . Once $d \gg \Delta$, the SkHA reduces drastically and vanishes for micrometer-sized magnetic bubbles. This trend of the angle θ_{SkH} was confirmed experimentally by [Litzius et al., 2017] where the increase in d , at a constant skyrmion velocity, from $d = 96 \text{ nm}$ to $d = 130 \text{ nm}$ reduces the SkHA from $\theta_{SkH} = 21^\circ$ to $\theta_{SkH} = 6^\circ$. [Jiang et al., 2017] observed the same effect for different current densities (cf. Figure V.3.a). Nonetheless, despite a large $d \approx 10 \mu\text{m}$, [Hirata et al., 2019] reported a sizeable intrinsic SkHE in a GdFeCo ferrimagnetic film (Figure V.4). Similarly to the effect of the asymmetric non-collinear DW motion, [Hirata et al., 2019] observed an oblique elongation of magnetic domains at an angle θ . On one hand, the angle θ changes sign with the topological charge n of the magnetic domain. On the other hand, it is equal to zero at the compensation temperature that corresponds to the zero net magnetization of the ferrimagnet, i.e. the zero topological charge n . Thereby, [Hirata et al., 2019] attributed these observations to an intrinsic SkHE. Such a sizeable angle θ_{SkH} is possible since the DW width parameter Δ is large ($\Delta \approx 15 \text{ nm}$) and the magnetic damping α is ultra low ($\alpha \approx 0.003$) in the ferrimagnetic film. In Eqs V.22 and .23, these values compensate the decrease in the angle θ_{SkH} from the factor $1/d$ for the magnetic bubbles with large diameters.

In contrast, the DWs are short ($\Delta \approx 5$ nm) and the damping is strong ($\alpha \approx 0.5$) in Pt/Co/Pt and Pt/Co/AlOx. Consequently, the SkHA is negligible for $d \sim 4 - 8 \mu\text{m}$ (maximum $\theta_{SkH} \approx 0.6^\circ$ for $d = 4 \mu\text{m}$). Therefore, the asymmetric non-collinear DW motion and the intrinsic SkHE are two independent phenomena. In the meantime, we can rule out that the mechanism of the asymmetric non-collinear DW motion can be relevant for magnetic skyrmions. We examine therefore the current-induced motion of small chiral magnetic bubbles in Pt/Co/Pt and Pt/Co/AlOx.

V.2. Chiral magnetic bubbles in Pt/Co/Pt and Pt/Co/AlOx

V.2.1. Formation of chiral magnetic bubbles

To obtain chiral magnetic bubbles in our samples, we have followed the same procedure already described in section III.2. At first, we form a magnetic circular domain with a large size in the center of the wire. Subsequently, by applying short pulses of an out-of-plane field H_z , we reduce the domain diameter down to a minimum of $1 \mu\text{m}$. Due to the MOKE resolution limit, we are not able to reach smaller sizes. For a similar investigation in the TbFeCo ferrimagnet film, [Tanaka et al., 2015, 2017] used an assisted-heating nucleation technique with a laser beam. Their technique is less time consuming and allows to choose freely the magnetic bubble nucleation site. The bubble diameter distributions in Pt/Co/Pt and Pt/Co/AlOx are shown in **Figure V.5.a-b**. In both samples, the average diameter is $1.6 \mu\text{m}$.

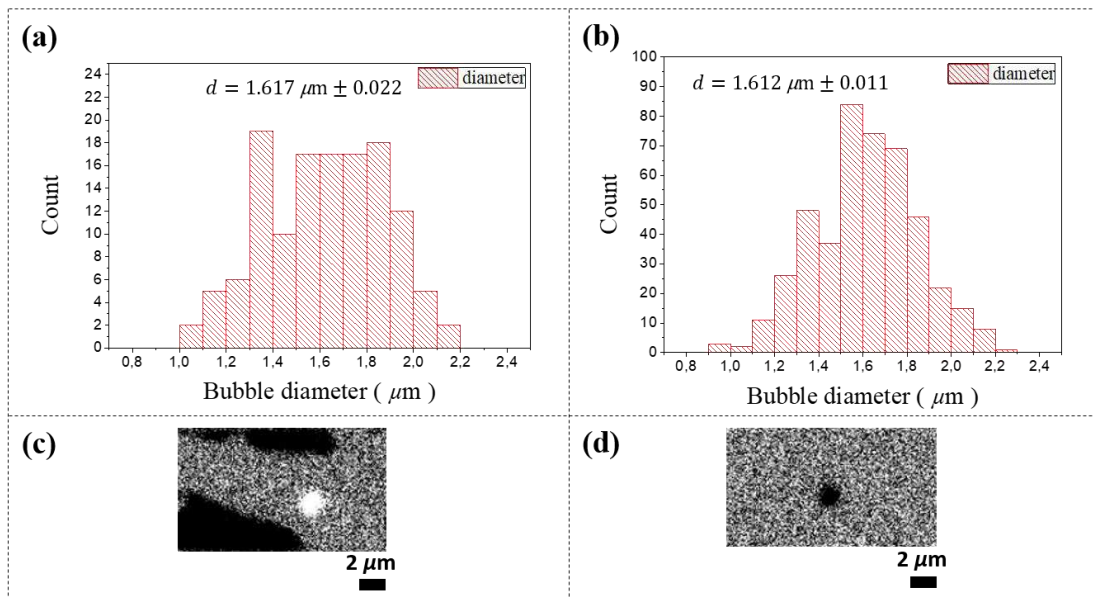


Figure V.5 Chiral magnetic bubbles diameter distributions (in μm). (a) For Pt/Co/Pt and (b) for Pt/Co/AlOx. (c) - (d) MOKE differential images of the initially prepared chiral magnetic bubbles. The images are taken after moving or collapsing the bubbles. The initial up (down) magnetic bubble is the round region with a bright (dark) contrast in (c) ((d)).

We have followed the magnetic bubble motion using MOKE in the differential mode. In these static measurements, we detect the motion by comparing final and initial positions of the bubble. For the up bubble, the magnetization located at its initial position has been reversed to the down orientation whereas the magnetization at the final position has been reversed from down to up. Consequently, these two positions exhibit different contrasts. Based on the description of our MOKE in Chapter II, the final position has a dark contrast whilst the initial position has a bright contrast (**Figure V.5.c**). It is the inverse for the down magnetic bubble. When MOKE differential mode exhibits just one circular region with a magnetic contrast, it means that the magnetic bubble has been annihilated after the current injection. To ensure a stable bubble for a sustainable motion, we apply an easy-axis magnetic field along with the current.

V.2.2. Stabilization of chiral magnetic bubbles with an out-of-plane field

We have controlled the current-induced magnetic bubbles using an external out-of-plane field H_z . Otherwise, the bubbles have a high collapse rate. The applied H_z is parallel to the bubble core magnetization. Depending on its amplitude, the bubble dynamics differ. At a critical amplitude H_z^{mb} , the bubble is stable and moves without a substantial change in its size. Below H_z^{mb} , the bubble collapses whereas it grows without moving above H_z^{mb} . The amplitude of H_z^{mb} depends strongly on the current pulse. It varies with the current density, the pulse duration, the total number of pulses and the pulse period. Therefore, for each current density J , we have to determine the exact corresponding H_z^{mb} in order to reproduce the magnetic bubble motion. Afterwards, we are able to extract characteristics of the current-induced motion from significant amounts of statistics. For instance, **Figure V.6** gives an example of the parameters determined to obtain a sustainable up bubble motion in Pt/Co/AlOx under a current density of $J \sim 1.95 \cdot 10^{12} \text{ A.m}^{-2}$. In Appendix section A.2, we give the chosen parameters for all the possible current/magnetization polarities in each sample. In **Figure V.6**, the sequence consists of 7 positive current pulses with 6.6 ns time width each. The time elapsed between two consecutive pulses (the pulse period) is varied from $10 \mu\text{s}$ up to 100 ms. We adjust then the time width of H_z (H_z and H_z^{mb} are used interchangeably in the rest of the manuscript). We take as a constraint that all the current pulses must be injected while H_z is applied. This is crucial in order to reduce the annihilation rate of the bubbles when the current is injected. Consequently, the time width of H_z varies here from 10 ms to 700 ms. The H_z -pulse has a rise/fall time of 2 ms. In order to have the bubble motion under a quasi-constant H_z , we fix the time delay between the onsets of the H_z -pulse and the first current pulse. The same time delay is set between the terminations of the last current pulse and H_z . The time delay can be varied independently. We choose to change it from 5 to 75 ms in the example described in **Figure V.6**. H_z was set in consequence at two different amplitudes, +1.8 and +2.4 mT. A particular attention is taken to keep its amplitude smaller than the DW propagation field. We verify that H_z , applied during the same time width, does not induce any notable growth of the bubbles. We consider then that the contribution of H_z to the bubble motion is negligible.

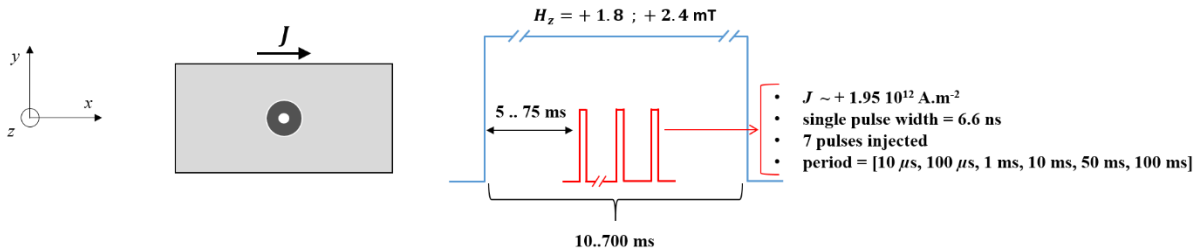


Figure V.6 The determined parameters for the up magnetic bubble motion under a current density of $J \sim +1.95 \cdot 10^{12} \text{ A.m}^{-2}$ in Pt/Co/AlOx. The fixed parameters are the pulse time width and the total number of current pulses. The other parameters can be adjusted and varied.

The action of H_z helps extending the lifetime of the magnetic bubbles during the injection of the multiple current pulses. It counteracts the interactions that cause the bubble collapse. The bubble phase formation in PMA films is attributed to the interplay between the long range (dipolar) and the short range (exchange) interactions [Ng and Vanderbilt, 1995]. We use then a simplistic picture to emphasize the role of H_z . These different energies induce effective forces acting on the magnetic bubble edges (the DWs) (**Figure V.7**). On the one hand, the formation of a bubble with a diameter d costs exchange and anisotropy terms (the DW energy σ_{DW}). They are proportional to d thereby compressing the bubble through the effective force F_σ . On the other hand, the dipolar energy favors opposite domains so that the effective force F_{dip} tends to expand the bubble. These effective forces act normally to the DWs and the bubble is stable when F_σ and F_{dip} compensate each other. F_{dip} is M_s -dependent thus it is sizeable in our materials since the Co thin film has a large saturation value ($M_s = 1090 \text{ emu.cm}^{-3}$ [Miron et al., 2010]). The dipolar interaction can then stabilize the magnetic bubbles (**Figure V.7.a**). Due to the thermal fluctuations and pinning, one effective force can dominate

over the other during the current injection. Let us assume that the current action on the magnetic moments of the DW is equivalent to an effective force \mathbf{F}_J (from SOT). A dominant \mathbf{F}_{dip} opposes \mathbf{F}_J on the bubble left edge and adds up to it on the right edge (**Figure V.7.b**). The amplitude of \mathbf{F}_{Left} , the sum of the forces acting on the left edge of the bubble, is smaller than its counterpart \mathbf{F}_{Right} hence the right edge of the bubble moves faster leading to the bubble elongation during its motion (**Figure V.7.e**). As for a dominant \mathbf{F}_σ (**Figure V.7.c**), the left edge becomes faster. It may then catch up with the slower right edge resulting in the bubble collapse. The action of \mathbf{H}_z adds up to \mathbf{F}_{dip} compensating the dominant \mathbf{F}_σ . This way, the difference between \mathbf{F}_{Left} and \mathbf{F}_{Right} is waned so the bubble moves without any notable change in its size (**Figure V.7.d**). The worst-case scenario is a decrease in d rather than the bubble collapse (**Figure V.7.f**). **Figures V.7.e** and **.f** are subsequent states of the same bubble moving under the same current density in the presence of the same field \mathbf{H}_z , which evidences the stochastic effect of the thermal fluctuations and pinning on the balance between \mathbf{F}_{dip} and \mathbf{F}_σ . \mathbf{H}_z^{mb} is the field that ensures a sustainable bubble motion along with its size fluctuation (either a slight decrease or a minor increase of d). Above \mathbf{H}_z^{mb} , \mathbf{F}_{Left} is either zero or flips its orientation so the bubble expands without any motion. Below \mathbf{H}_z^{mb} , the bubble has a high annihilation rate.

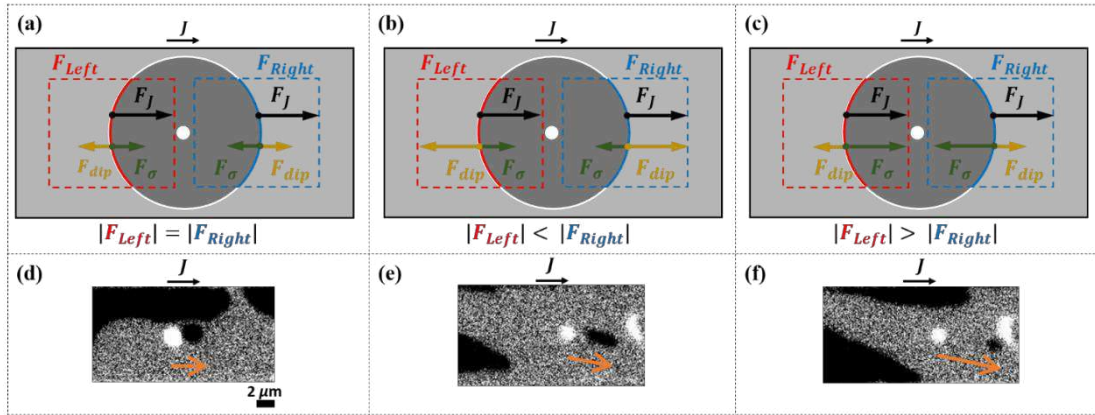


Figure V.7 The stabilization of the magnetic bubbles for the study of their current-induced motion. (a)-(c) Schematics of the total effective forces acting on the left edge (\mathbf{F}_{Left}) and the right edge (\mathbf{F}_{Right}) of the up magnetic bubble. \mathbf{F}_{Left} and \mathbf{F}_{Right} include the current-induced force \mathbf{F}_J , the DW energy σ force \mathbf{F}_σ and the dipolar force \mathbf{F}_{dip} . MOKE images of a moving up magnetic bubble while maintaining its size (d), growing (e) and shrinking (f). The bright (dark) round contrast corresponds to the initial (final) position of the up bubble. (f) is the image that follows (e) for the same initial bubble. The orange arrows give the bubble direction of motion (pointing from the initial to the final position of the bubble).

After identifying \mathbf{H}_z^{mb} , we have studied the magnetic bubble motion by applying subsequent trains of multiple current pulses. We are able to displace bubbles along distances as large as $10 \mu\text{m}$ with velocities as high as $100 \text{ m}\cdot\text{s}^{-1}$. We keep injecting the current pulses until the bubble collapses, expands considerably, merges with a neighboring magnetic domain or reaches the end of the wire. The current-induced bubble motion exhibits properties similar to those of the Néel skyrmions.

V.2.3. Vanishing intrinsic SkHE in Pt/Co/Pt and Pt/Co/AIOx

The magnetic bubbles have a unidirectional motion in the current direction in Pt/Co/Pt and Pt/Co/AIOx. Thanks to the presence of the interfacial DMI and by following the discussions in section V.1.2, we can consider these magnetic bubbles as chiral skyrmion bubbles in Pt/Co/Pt and Pt/Co/AIOx. They have then a nonzero topological charge n corresponding to their core magnetization. Therefore, they are expected to experience the topological Magnus force hence the intrinsic SkHE.

In the meantime, these chiral skyrmion bubbles have a large average diameter $d = 1.6 \mu\text{m}$. Even though the intrinsic SkHE is expected to be small for the micrometer-sized magnetic skyrmions, a sizeable angle θ_{SkH} was reported for large skyrmions with $d = 1.1 \mu\text{m}$ (**Figure V.3.a**) and $d = 2 \mu\text{m}$ in [Jiang et al., 2017] and [Yu et al., 2017], respectively. The SkHA reaches a value as high as $\theta_{SkH} \approx 35^\circ$ in the Ta (5 nm)/CoFeB (1.1 nm)/TaOx (3 nm) structure [Jiang et al., 2017]. In a similar structure, [Yu et al., 2017] measured $\theta_{SkH} \approx 13^\circ$. In fact, the observed SkHE results the large DW width $\Delta \approx 12 - 21 \text{ nm}$ and the low damping $\alpha \approx 0.02$ in this kind of structures. On the contrary, [Miron, 2009] extracted, from analysis of the FIDWM, a strong damping parameter ($\alpha = 0.5$) in the Pt/Co-based heterostructures. This large value is due to the nonlocal increase in the magnetic damping in comparison to the measurements through conventional ferromagnetic resonance (FMR) [Gerrits et al., 2006; Weindler et al., 2014]. In addition, the DWs are thin in Pt/Co/Pt and Pt/Co/AlOx with $\Delta \cong 5 \text{ nm}$. Consequently, according to Eqs. V.22 and .23, the angle θ_{SkH} is vanishingly small ($\theta_{SkH} \leq 1.4^\circ$) for the chiral skyrmion bubbles that we have studied in Pt/Co/Pt and Pt/Co/AlOx.

It is not possible to detect such a small angle of deflection using MOKE. The observation of a sizeable deflection of these skyrmions bubbles in our samples results then necessarily from an extrinsic contribution to the SkHE. In the following, we start by presenting our investigations in Pt/Co/Pt and next in Pt/Co/AlOx. The motion of chiral magnetic bubbles were recorded in videos in the differential mode of MOKE. The presented images hereafter are taken from these videos.

V.3. The emergence of the extrinsic SkHE

In the following, I will describe the current-induced motion of the skyrmion bubbles in our samples. First, I will address the experimental results obtained in the Pt/Co/Pt stack. Secondly, I will present the current-induced motion in the Pt/Co/AlOx structure. For each sample, the description will be divided in two parts according to the injected current density amplitudes. I will begin by presenting the experimental results obtained under low injected current densities and next the results obtained under high injected current densities. By low current densities, we refer to the current densities J for which the DW motion occurs in the creep or in the depinning regimes ($J < 2 \cdot 10^{12} \text{ A.m}^{-2}$ in both structures, cf. the DW velocities curves in **Figure III.5** in chapter III). The high current densities correspond to the flow regime of motion ($J \gtrsim 2 \cdot 10^{12} \text{ A.m}^{-2}$). In fact, the characteristics of the current-induced motion of the skyrmion bubbles show a dependence on the DW regime of motion. By comparing the results between Pt/Co/Pt and Pt/Co/AlOx structures, we have evidenced the extrinsic SkHE and proposed a possible mechanism behind its emergence.

V.3.1. The effects of the asymmetric non-collinear DW motion on the skyrmion bubbles

In this section, I will address the effects induced by the mechanism of the asymmetric non-collinear DW motion on the skyrmion bubbles. By studying the current-induced motion of the skyrmion bubbles in Pt/Co/Pt, we have observed their elliptical distortion. Such a distortion is induced by the asymmetric non-collinear DW motion. Moreover, we have evidenced that it can promote a deflection of the skyrmion bubbles. However, this vertical motion is not systematic in the Pt/Co/Pt structure. Furthermore, it is strongly drive-dependent. It shows a well-defined symmetry under low current densities whereas it becomes randomly oriented under high current densities.

V.3.1.1. The distortion of the skyrmion bubbles into ellipses in Pt/Co/Pt

Based on our preliminary observations, the skyrmion bubble does not necessarily maintain its initial round shape during its motion in Pt/Co/Pt. It has the possibility to undergo an elliptical distortion. In **Figure V.8.a**, we give a schematic diagram of the observed elliptical distortion of the up skyrmion bubble under a positive current. The final ellipse has a major-axis (dashed green line) that rotates clockwise with respect to the current direction (i.e. the horizontal axis). The direction of this rotation follows the sign of the angle ϕ_J^{max} of the distorted up magnetic circular domain (**Figure V.8.b**). As discussed in Chapter III, the asymmetric non-collinear DW motion induces this kind of asymmetric distortion of the magnetic circular domains. Thereby, it induces the same effect on the skyrmion bubbles. We have obtained the elliptical skyrmion bubble distortion for all the magnetization/current polarities under low current densities (**Figure V.8.d**). The elliptical distortion follows the symmetry operations as emphasized in **Figure V.8.c** ruling out any possible role from artefacts.

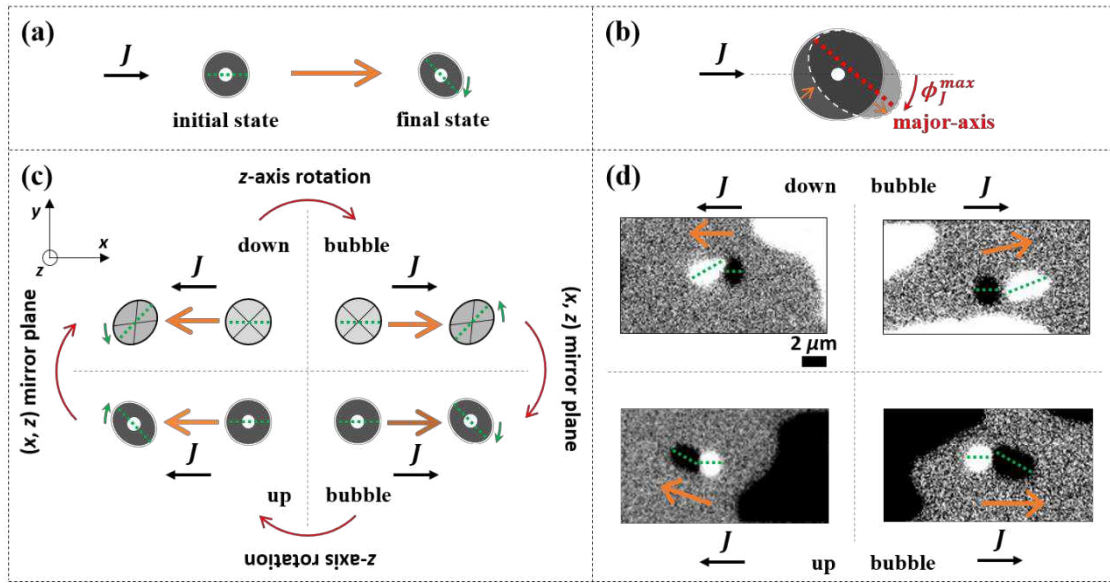


Figure V.8 The distortion of the skyrmion bubbles into an ellipse under low current densities in Pt/Co/Pt. (a) Schematic diagram of the elliptical distortion of the up bubble for a positive current. (b) Asymmetric distortion of the up magnetic circular domain for a positive current in Pt/Co/Pt. (c) Schematic diagram of the elliptical deformation for all the magnetization/current polarities obtained from the symmetry operations and experimentally in (d). The injected current densities are $J \sim -1.09 \cdot 10^{12} \text{ A.m}^{-2}$ and $J \sim +1.13 \cdot 10^{12} \text{ A.m}^{-2}$. In (d), the dashed green line represents the skyrmion bubble major-axis and the orange arrows indicates its direction of motion.

The effect of the asymmetric non-collinear DW motion is also present under high current densities in Pt/Co/Pt. The skyrmion bubble still exhibits a final elliptical shape after the current injection that is similar to that obtained under low current densities (**Figure V.9**). Besides the effects on its shape, we can imagine other effects on the skyrmion bubble motion. In fact, the elliptical distortion drags the skyrmion bubble axis away from the current direction. It is possible that it endows the skyrmion bubble with a vertical motion despite the fact that the intrinsic SkHE is vanishingly small in Pt/Co/Pt as seen in section V.2.3. We have found that the presence of such a well-defined deflection depends on the regime of motion (whether in the creep or in the flow regime) as it is described next.

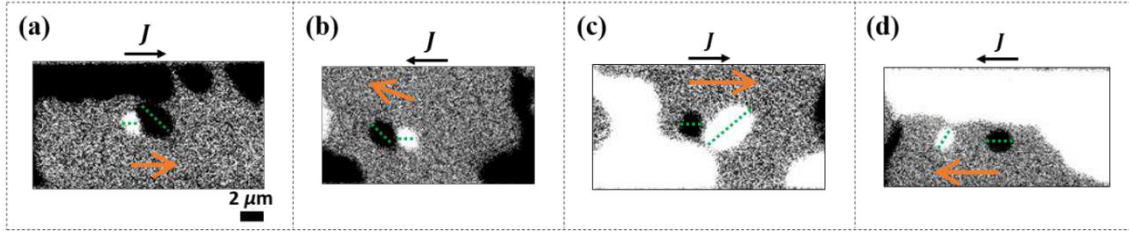


Figure V.9 The distortion of the skyrmion bubble into an ellipse under high current densities in Pt/Co/Pt. The up bubble under $J \sim +2.77 \cdot 10^{12} \text{ A.m}^{-2}$ in (a) and under $J \sim -1.96 \cdot 10^{12} \text{ A.m}^{-2}$ in (b). A down bubble under $J \sim +1.93 \cdot 10^{12} \text{ A.m}^{-2}$ in (c) and under $J \sim -1.96 \cdot 10^{12} \text{ A.m}^{-2}$ in (d). The elliptical distortion under high current densities is similar to that elliptical under low current densities in **Figure V.8**. The asymmetric non-collinear DW motion is relevant also under high current densities in Pt/Co/Pt.

V.3.1.2. The “apparent” SkHE in Pt/Co/Pt under low current densities

We have studied the skyrmion bubbles motion under current densities of $J \sim -1.09 \cdot 10^{12} \text{ A.m}^{-2}$ and $J \sim +1.13 \cdot 10^{12} \text{ A.m}^{-2}$. As expected in the creep regime, the skyrmion bubble velocity v_{Sk} , in the current direction, is small and is in the order of $\sim 0.1 \text{ m.s}^{-1}$. In this regime, we have observed a deflection of the skyrmion bubble with a rate of $\sim 26\%$. In **Table V.1**, we present the data obtained from summing up all the statistics of the current-induced motion for all the magnetization/current polarities. By following symmetry operations, we make the data correspond to the case of the up skyrmion bubble driven by a positive current. The statistics for each single configuration are available in Appendix.


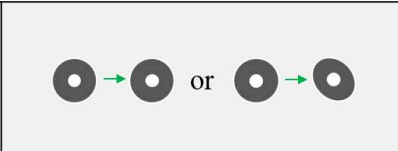
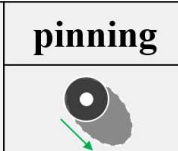
			
number of displacements	53	92	56
Percentage %	26.37	45.77	27.86

Table V.1 The modes of the skyrmion bubble motion in the creep regime in Pt/Co/Pt. Each column corresponds to a distinct mode of motion. From left to right, deflection mode, horizontal mode and pinning mode (no motion and the skyrmion bubble expands). On top, each schematic diagram represents the corresponding mode of motion for the up skyrmion bubble under a positive current.

The obtained deflection of the skyrmion bubble has a well-defined symmetry that depends on the skyrmion bubble magnetization. It is similar to the SkHE, for the Néel skyrmion, that depends on the topological charge n (cf. **Figure V.1.c**). Under a positive (negative) current, the down skyrmion bubble drifts upwards (downwards) whereas the up skyrmion bubble drifts downwards (upwards) (**Figure V.10**).

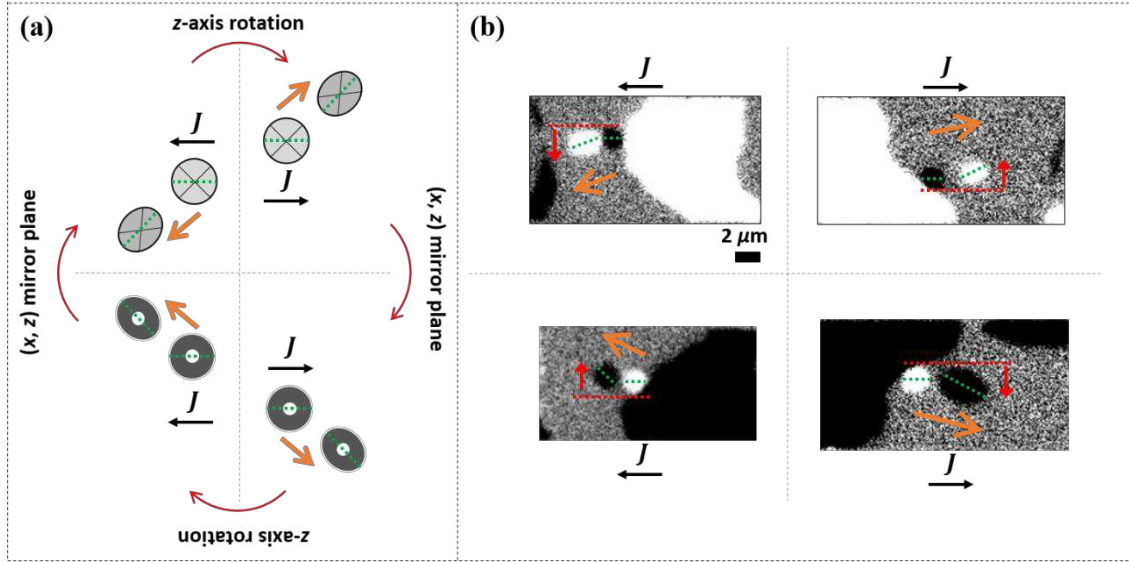


Figure V.10 The skyrmion bubble deflection in the creep regime in Pt/Co/Pt. (a) Schematic diagram of the expected deflections for all the magnetization/current polarities by the symmetry operations and those obtained in the experiment (b). In (b), The MOKE images on the top (bottom) panel correspond to the deflected down (up) skyrmion bubble. The dashed red horizontal line and the red arrow highlight the bubble drift in the MOKE images. The deflection emerges along with the elliptical distortion of the skyrmion bubble (represented by dashed green lines). The injected current densities are $J \sim -1.09 \cdot 10^{12} \text{ A}\cdot\text{m}^{-2}$ and $J \sim +1.13 \cdot 10^{12} \text{ A}\cdot\text{m}^{-2}$.

Figure V.11 shows the drift angle distributions for the up and the down skyrmion bubbles. Despite the insufficient statistics, it is clear that the average finite drift angle ϕ_d is much larger than the expected SkHA θ_{SkH} in Pt/Co/Pt ($\phi_d \gg 1.4^\circ \geq \theta_{SkH}$). The angle ϕ_d cannot then be attributed to the intrinsic SkHE. Moreover, the skyrmion bubbles deflection is always accompanied by the elliptical distortion (**Figure V.10.b**). This suggests that the asymmetric non-collinear DW motion is indeed behind this well-defined deflection in Pt/Co/Pt. However, the skyrmion bubble does not necessarily move with a vertical deflection.

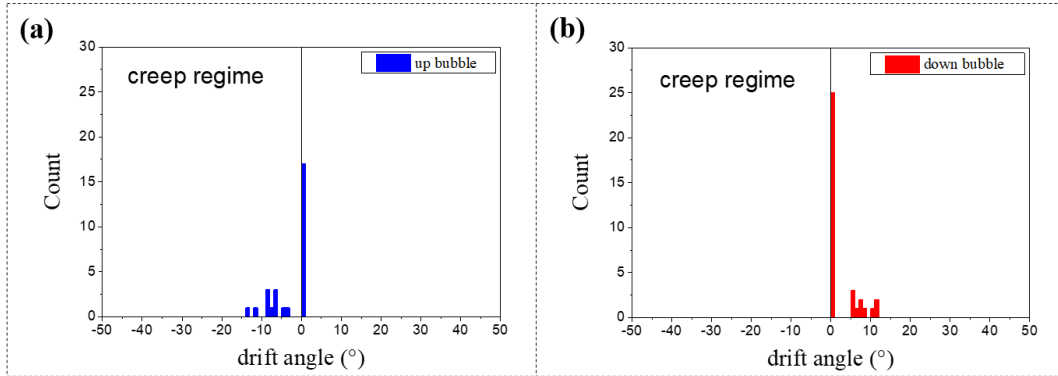


Figure V.11 The drift angle distributions (in degrees) of the skyrmion bubble in the creep regime in Pt/Co/Pt. (a) For the up and (b) for the down skyrmion bubble. The drift angle is the angle between the line connecting the centers of the final and initial positions of the bubble and the current direction.

As shown in **Figure V.12**, the skyrmion bubble moves usually horizontally (the horizontal motion is the major motion mode with a rate of $\sim 46\%$, cf. **Table V.1**) before or after showing a deflection. In the horizontal mode, the elliptical distortion can be either absent (the bubble recovers the round shape **Figure V.12.b** and **.d**) or present (**Figure V.12.e**). Thus, the elliptical bubbles distortion is not stable and does not induce systematically the bubble deflection. It needs to act with another mechanism to provide the bubble deflection. **Figure V.12.f** shows the situation where the pinning promotes an oblique elongation of the bubble following the asymmetric non-collinear DW motion. It is then possible that the enhancement of the bubble elliptical distortion, due to a significant pinning (obtained with a rate of $\sim 27\%$), participates in the emergence of the well-defined deflection.

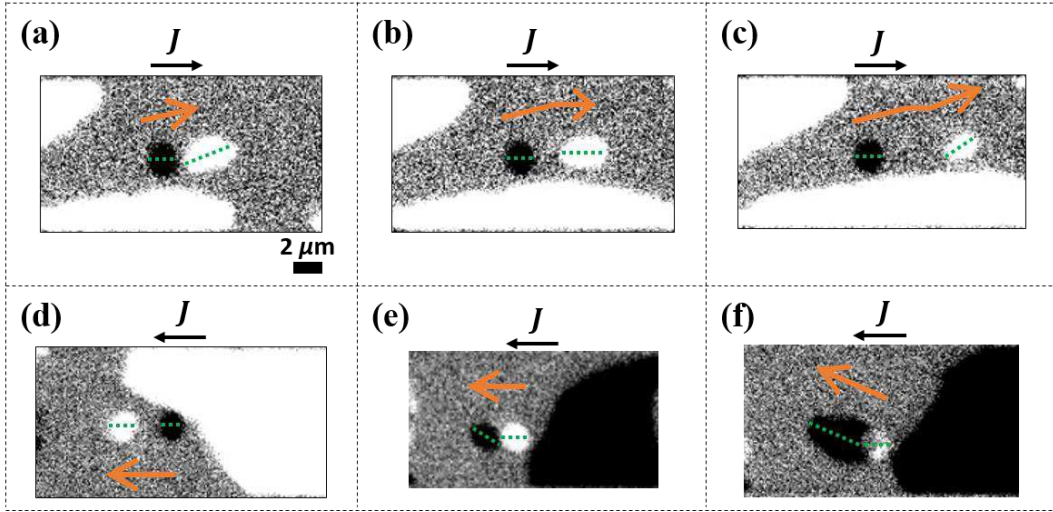


Figure V.12 MOKE images of the different motion modes of the skyrmion bubbles in the creep regime in Pt/Co/Pt. (a)-(c) Subsequent images of the down bubble under $J \sim +1.13 \cdot 10^{12} \text{ A.m}^{-2}$. Initially, a deflection (a) then an horizontal motion (b) and finally a deflection (c). In (b), there is no elliptical distortion. (d)-(f) The up bubble under $J \sim -1.09 \cdot 10^{12} \text{ A.m}^{-2}$. The horizontal motion without (d) and with (e) the elliptical distortion. (f) Oblique elongation due to pinning.

The non-uniformity and the stochastic nature of the pinning can be behind the emergence of the deflection mode. For the up skyrmion bubble under a positive current, there are two possible scenarios. In the first scenario, the strong pinning acts only on the front DW (the right edge of the bubble). The back DW (the left edge of the bubble) moves then faster so that the bubble collapses. With static measurements under MOKE, we are not able to detect if whether the bubble had moved horizontally or had been deflected before its annihilation in this scenario. In the second scenario (**Figure V.13**), the strong pinning acts initially only on the back DW. The bubble undergoes then an oblique elongation following the asymmetric non-collinear motion of the front DW. For the current pulses that are injected afterwards, the pinning becomes stronger on the front DW. The elongated bubble shrinks so that it recovers a size comparable to its initial state. Henceforth, the center of the up skyrmion bubble is located below its initial position. Under MOKE, we observe then an “apparent” SkHE in the creep regime of motion in Pt/Co/Pt. Therefore, the “apparent” SkHE might result from the interplay between the strong pinning and the asymmetric non-collinear DW motion.

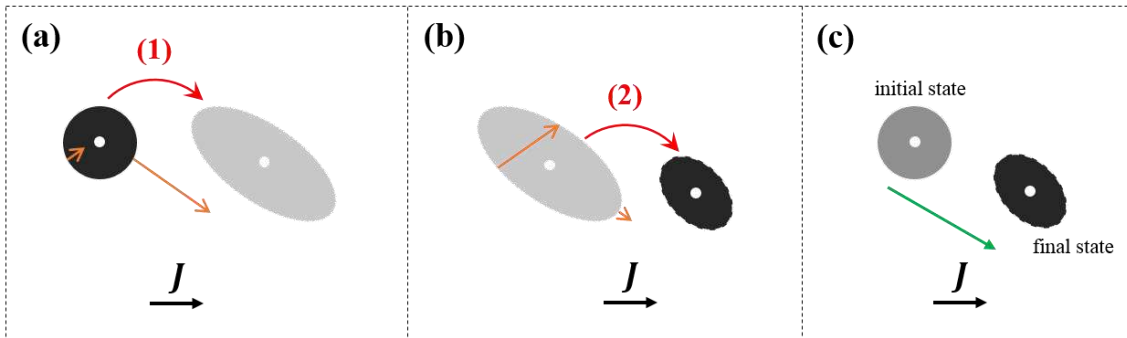


Figure V.13 The possible mechanism responsible for the “apparent” SkHE in the creep regime in Pt/Co/Pt. The represented scenario applies for all the magnetization/current polarities. (a) A first current pulse elongates the up bubble with an oblique angle following the angle ϕ_j^{\max} since the back DW is pinned. (b) For a second pulse, the front DW becomes pinned. (c) Finally, the bubble sits below its initial position. The orange arrows indicate the largest displacements for each DW at the angle ϕ_j^{\max} following the asymmetric non-collinear DW motion.

Following this description, we expect the “apparent” SkHE to occur in less proportions under high current densities, for which the skyrmion bubble is able to overcome the strong pinning. We present next the skyrmion bubbles motion in the flow regime in Pt/Co/Pt.

V.3.1.3. Hopping-like motion in Pt/Co/Pt under large current densities

We have injected current densities for which the DW motion is in the flow regime according to the variation of the DW velocity v_{DW} (cf. **Figure III.5.b** in chapter III), namely $J \sim -1.96 \cdot 10^{12} \text{ A.m}^{-2}$, $J \sim +1.93 \cdot 10^{12} \text{ A.m}^{-2}$, $J \sim -2.73 \cdot 10^{12} \text{ A.m}^{-2}$ and $J \sim +2.77 \cdot 10^{12} \text{ A.m}^{-2}$. For these current densities, the DW velocity v_{DW} saturates in Pt/Co/Pt. Consequently, we have not obtained a notable variation in the skyrmion bubble velocity v_{Sk} between these different injected densities (v_{Sk} in the order of $\sim 1.2 \text{ m.s}^{-1}$). In this regime, the pinning is less significant. The statistics, in **Table V.2**, give the skyrmion bubble oblique elongation, due to the pinning, with a reduced rate of $\sim 7\%$. The rate of the “apparent” SkHE has waned also down to $\sim 11\%$. We note that a new mode of deflection emerges with a non-negligible rate of $\sim 15\%$. It deflects the skyrmion bubble in the direction opposite to the “apparent” SkHE.

				pinning
number of displacements	55	75	335	37
Percentage %	10.96	14.94	66.73	7.37

Table V.2 The modes of the skyrmion bubble motion in the flow regime in Pt/Co/Pt. The columns, from left to right, correspond to the “apparent” SkHE, the new deflection mode, the horizontal motion and the pinning mode.

Figure V.14 illustrates these two types of the deflection in the flow regime. Actually, the elliptical distortion takes also place along with the new mode of deflection. This is an additional confirmation that the asymmetric non-collinear DW motion does not induce systematically the “apparent” SkHE in Pt/Co/Pt. The bubble deflection becomes random and no finite average value can be extracted from the drift angle distributions (**Figure V.15**).

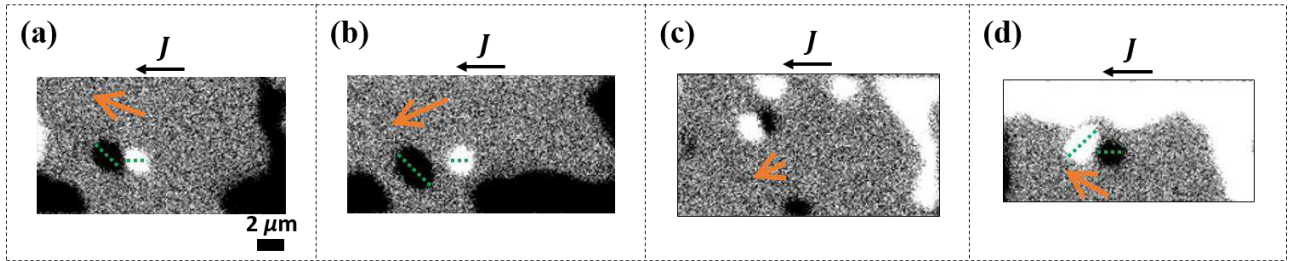


Figure V.14 MOKE images of the random deflection of the skyrmion bubbles in the flow regime in Pt/Co/Pt. The up skyrmion bubble under $J \sim -1.96 \cdot 10^{12} \text{ A.m}^{-2}$ in (a) and (b). The down skyrmion bubble under $J \sim -2.73 \cdot 10^{12} \text{ A.m}^{-2}$ in (c) and under $J \sim -1.96 \cdot 10^{12} \text{ A.m}^{-2}$ in (d). (a) and (c) follow the “apparent” SkHE. (b) and (d) represent the new deflection opposite to the “apparent” SkHE. The elliptical distortion (highlighted by the green dashed line) emerges in both modes of the deflection.

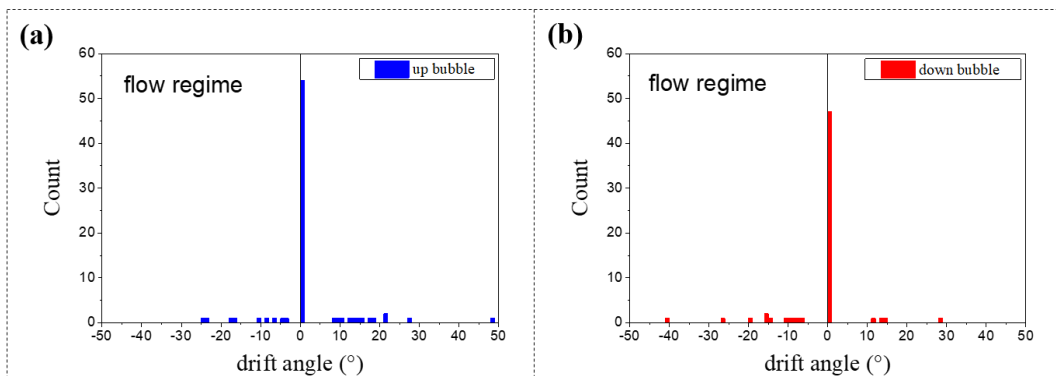


Figure V.15 The drift angle distributions (in degrees) of the skyrmion bubble in the flow regime in Pt/Co/Pt. (a) for the up and (b) for the down skyrmion bubble.

Under large current densities, the pinning is no longer as significant as in the creep regime. It is not able anymore to induce, in concert with the skyrmion bubble elliptical distortion, the “apparent” SkHE. Nevertheless, the pinning effects do not vanish. It prevents the major motion mode that is the horizontal motion (with a rate of $\sim 67\%$ in **Table V.2**) from being sustainable. The skyrmion bubble motion is then a hopping-like motion with random deflections due to pinning in Pt/Co/Pt.

We have evidenced that the asymmetric non-collinear DW motion acts on the skyrmion bubbles in Pt/Co/Pt. It deforms the skyrmion bubbles into ellipses but does not induce systematically the bubble deflection. In fact, the elliptical bubble shape is not favored in Pt/Co/Pt. The bubble deflection or the “apparent” SkHE emerges only when the pinning is significant enough to trap the skyrmion bubble in the elliptical shape preventing it from recovering the round shape. The motion is then mostly horizontal in Pt/Co/Pt. On the contrary, the study of the skyrmion bubbles motion have evidenced a reproducible well-defined deflection in Pt/Co/AlOx.

V.3.2. Evidence of “extrinsic” SkHE in Pt/Co/AlOx

In this section, I will describe the current-induced skyrmion bubbles motion in the Pt/Co/AlOx structure. Like in Pt/Co/Pt, the mechanism of the asymmetric non-collinear DW motion acts on the skyrmion bubbles. The elliptical deformation has been found to be more pronounced and more stable than in the Pt/Co/Pt stack. Interestingly, the skyrmion bubbles motion is exclusively associated with a well-defined deflection in Pt/Co/AlOx.

V.3.2.1. The skyrmion bubbles motion under low current densities

We have begun studying the skyrmion bubbles motion under low current densities of $J \sim + 0.88 \cdot 10^{12} \text{ A.m}^{-2}$ and $J \sim - 0.86 \cdot 10^{12} \text{ A.m}^{-2}$. The skyrmion motion is in the creep regime with a velocity v_{sk} in the order of $\sim 0.2 \text{ m.s}^{-1}$. Similarly to Pt/Co/Pt, the asymmetric non-collinear DW motion changes the skyrmion bubbles into ellipses. On the contrary, unlike Pt/Co/Pt, the skyrmion bubble does not recover its initial round shape. The elliptical distortion is actually more pronounced in Pt/Co/AlOx. **Figure V.16** gives the examples of the skyrmions bubbles turning into moving “flat oblique discs” under low current densities.

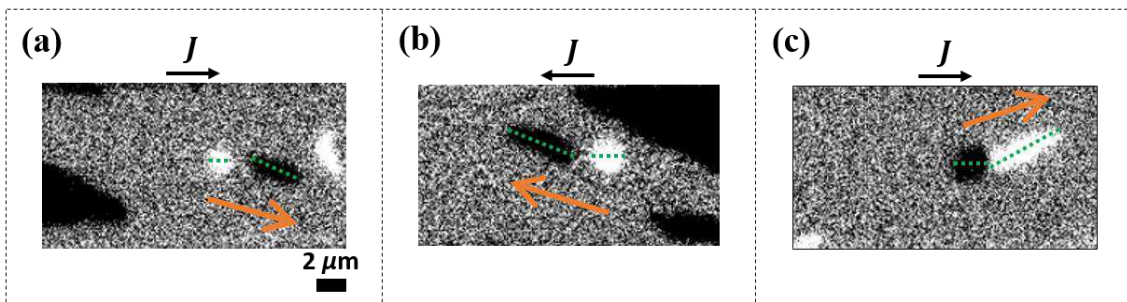


Figure V.16 The distortion of the skyrmion bubbles into an ellipses under low current densities in Pt/Co/AlOx. The up bubble under $J \sim + 0.88 \cdot 10^{12} \text{ A.m}^{-2}$ in (a) and under $J \sim - 0.86 \cdot 10^{12} \text{ A.m}^{-2}$ in (b). (c) The down bubble $J \sim + 0.88 \cdot 10^{12} \text{ A.m}^{-2}$. The distortion is more pronounced than that in Pt/Co/Pt (cf. **Figure V.8.d**).

The elliptic distortion takes place along with the vertical drift of the skyrmion bubble, which is the preferential motion mode as given by the statistics in **Table V.3**. Unlike Pt/Co/Pt, the pinning is not a hurdle to the skyrmion bubbles motion in Pt/Co/AlOx. Indeed, we have obtained the oblique elongation of the bubbles with a rate less than 3% (compare with the rate of $\sim 28\%$ in **Table V.1** for the Pt/Co/Pt stack). When it does not induce the oblique elongation, the acting pinning can prevent the bubble deflection and be behind the rarely obtained horizontal motion (rate of $\sim 1\%$).

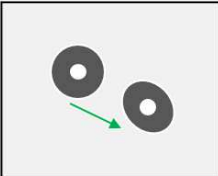
			pinning 
number of displacements	241	3	7
Percentage %	96.02	1.19	2.79

Table V.3 The modes of the skyrmion bubble motion in the creep regime in Pt/Co/AlOx. The columns, from left to right, correspond to the deflection mode, the horizontal motion and the pinning mode.

The deflection motion mode exhibits a well-defined symmetry. It depends on the core magnetization orientation (the topological charge n) of the skyrmion bubble (**Figure V.17**). Its symmetry is similar to that of the intrinsic SkHE for the Néel skyrmion that moves in the current direction. Under a negative current, the down (up) skyrmion bubble drifts downwards (upwards). Under a positive current, the down (up) skyrmion bubble drifts upwards (downwards).

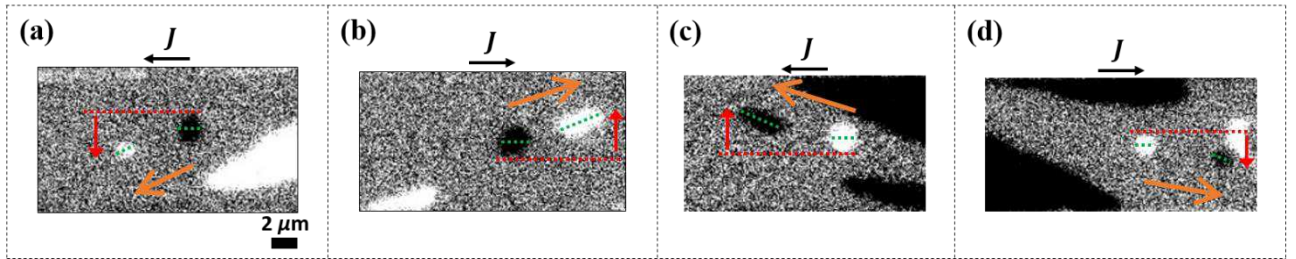


Figure V.17 The skyrmion bubble deflection in the creep regime in Pt/Co/AlOx. (a)-(b) The down skyrmion bubbles. (c)-(d) The up skyrmion bubbles. The current densities are $J \sim -0.86 \cdot 10^{12} \text{ A.m}^{-2}$ and $J \sim +0.88 \cdot 10^{12} \text{ A.m}^{-2}$.

As seen in **Table V.3**, the pinning still has minor effects on the skyrmion bubbles motion in Pt/Co/AlOx under low current densities. We expect then these effects to disappear allowing the deflection motion mode to occur at a rate of $\sim 100\%$ in the flow regime under large injected current densities.

V.3.2.2. The skyrmion bubble motion under large current densities

The injected current densities are $|J| \sim 1.95 \cdot 10^{12} \text{ A.m}^{-2}$ and $|J| \sim 2.75 \cdot 10^{12} \text{ A.m}^{-2}$, which correspond to the steady-state regime of motion for the DWs in Pt/Co/AlOx (cf. **Figure III.5.a** in chapter III). Following the constant DW mobility in this regime, the skyrmion velocities v_{Sk} are large and increase from $\sim 50 \text{ m.s}^{-1}$ under $|J| \sim 1.95 \cdot 10^{12} \text{ A.m}^{-2}$ to $\sim 100 \text{ m.s}^{-1}$ under $|J| \sim 2.75 \cdot 10^{12} \text{ A.m}^{-2}$. We have determined v_{Sk} as the slopes of a linear regression fit of the skyrmion bubble horizontal displacement as a function of the integrated time of the current (**Figure V.18**). The integrated time is equal to the pulse time width multiplied by the total number of the injected pulses. As discussed in Chapter II, this method underestimates the velocities of motion. Therefore, v_{Sk} might reach values as large as 400 m.s^{-1} , the largest DW velocity v_{DW} reported in Pt/Co/AlOx [Miron et al., 2011].

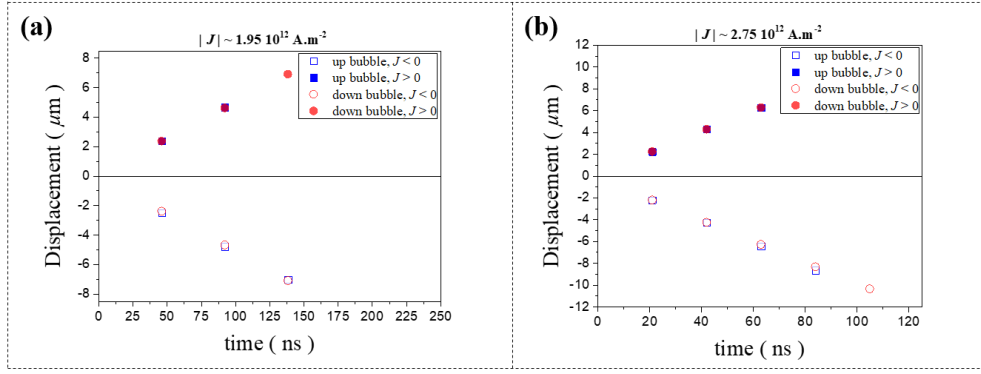


Figure V.18 The skyrmion bubble displacement (in μm) as a function of the current integrated time in the flow regime in Pt/Co/AlOx. (a) Under $|J| \sim 1.95 \cdot 10^{12} \text{ A.m}^{-2}$. (b) Under $|J| \sim 2.75 \cdot 10^{12} \text{ A.m}^{-2}$.

As they are driven in the flow regime, the skyrmion bubbles are not any longer sensitive to pinning and exhibit exclusively (**Table V.4**) a motion with a well-defined deflection following the description in **Figure V.17**.

			pinning
number of displacements	991	0	0
Percentage %	100	0	0

Table V.4 The modes of the skyrmion bubble motion in the flow regime in Pt/Co/AlOx. Only the deflected motion mode is obtained.

The displacements of the skyrmion bubbles are efficient and reproducible. **Figure V.19** gives some examples of the skyrmion bubbles moving away and then returning back to their exact initial positions. Both right-most MOKE images do not show distinguishable round regions with magnetic contrast indicating that the skyrmion bubble has retrieved its initial position. Another important feature is that the elliptical distortion is also pronounced in the flow regime. Thereby, we have determined from the MOKE images analysis the average elliptical shape: the major-axis at an angle of $\sim 48^\circ$ with respect to the current direction and the rate $e \sim 0.6$ with $e = b/a$ (b the minor-axis length and a the major-axis length).

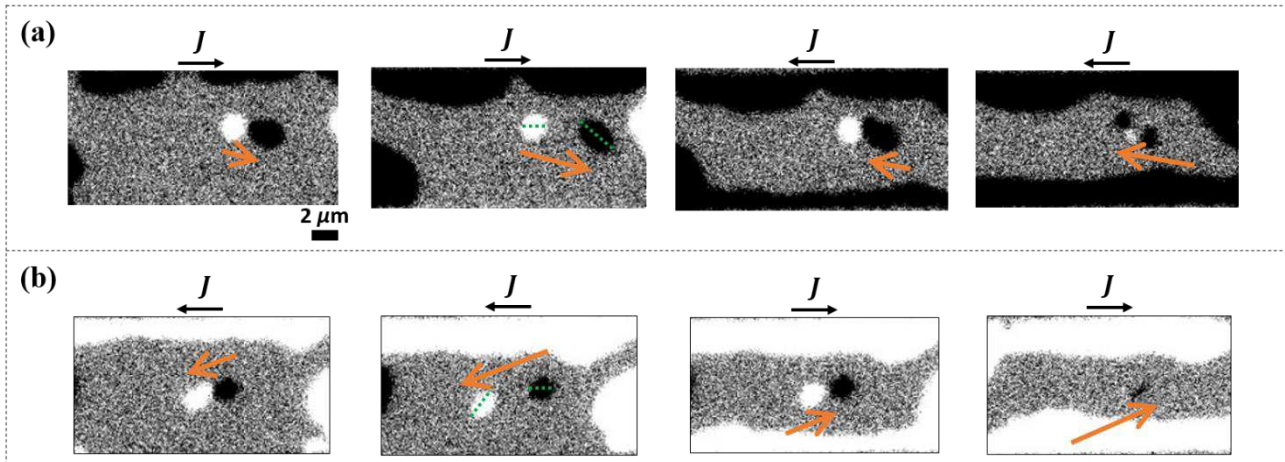


Figure V.19 The reproducible motion of the skyrmion bubbles in the flow regime in Pt/Co/AlOx. Each MOKE image is taken after injecting the same train of the current pulses successively from left to right in (a) and (b). Starting from the third image, we reverse the current polarity. The skyrmion bubble retrieves its initial position in the fourth image. (a) The up skyrmion bubble under $|J| \sim 1.95 \cdot 10^{12} \text{ A.m}^{-2}$. (b) The down skyrmion bubble under $|J| \sim 2.75 \cdot 10^{12} \text{ A.m}^{-2}$. The elliptical deformation of skyrmion bubbles is pronounced in the flow regime.

As the skyrmion bubble motion is sustainable and reproducible, we are able to extract the drift angle ϕ_d . We have found that the angle ϕ_d does not show any dependence on the different parameters used to define the train of the injected current pulses (cf. section V.2.2). In addition, no notable variation with the current density emerges. Therefore, we have assembled all the data of the angle ϕ_d in a single distribution for each magnetization orientation (**Figure V.20**). Indeed, the distributions exhibit a Gaussian-like behavior allowing the estimation of the average ϕ_d . For the up skyrmion bubble, we have estimated $\phi_d = -11.00^\circ \pm 0.14$ and for the down skyrmion bubble $\phi_d = +13.95^\circ \pm 0.16$. These two values are comparable following the symmetry between the up and the down magnetizations.

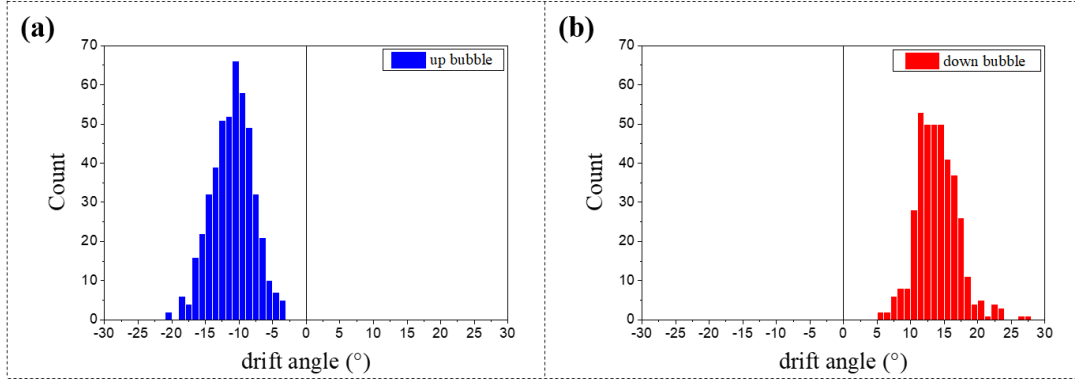


Figure V.20 The drift angle distributions (in degrees) of the skyrmion bubble in Pt/Co/AlOx. (a) For the up and (b) for the down skyrmion bubble. The data include all the extracted values under the different injected current densities.

Firstly, the drift angle ϕ_d is much larger than the expected intrinsic SkHA in Pt/Co/AlOx ($\theta_{SkH} \leq 1.4^\circ$). Secondly, the angle ϕ_d does not exhibit any net variation with the current density J , between the creep and the flow regimes of motion. In contrast, it has been demonstrated that the intrinsic SkHA is strongly drive-dependent (depends on the skyrmion velocity) (cf. section V.1.2.4). Therefore, the observed well-defined deflection and the intrinsic SkHE are not compatible. They are two independent effects.

Moreover, the possible contribution of the effective Oersted field force \mathbf{F}_{Oe} cannot account for the estimated angle ϕ_d . \mathbf{F}_{Oe} is only significant at the wire edges where the gradient ($\partial H_z^{Oe} / \partial y$) is large. Actually, the skyrmion bubbles motion takes place at the center of the wire where \mathbf{F}_{Oe} is negligible. On top of that, the skyrmion bubble would shift towards the edge where the Oersted field is parallel to its core magnetization for a significant action of \mathbf{F}_{Oe} . Under a positive current, the up skyrmion bubble would drift upwards and the down skyrmion bubble downwards. Such a scenario does not follow our experimental observations. Therefore, the Oersted field does not play any role in the net deflection of the skyrmion bubbles in Pt/Co/AlOx. We have evidenced thereby a new mechanism of a well-defined deflection in the skyrmion bubbles dynamics that we call the “extrinsic” SkHE.

In Pt/Co/AlOx where the intrinsic SkHE is vanishingly small, the skyrmion bubbles experience a sizeable “extrinsic” SkHE. This unexpected effect is always accompanied by the skyrmion bubbles elliptical distortion generated by the asymmetric non-collinear DW motion. Therefore, as predicted by [Baumgartner and Gambardella, 2018], the asymmetric non-collinear DW motion is potentially behind the emergence of the extrinsic SkHE. Interestingly, the asymmetric non-collinear DW motion is present in both Pt/Co/AlOx and Pt/Co/Pt. However, the extrinsic SkHE has been only evidenced in the former structure. An additional key ingredient is needed to explain the difference in the skyrmion bubbles dynamics between the two materials.

V.3.3. The mechanism of the extrinsic SkHE

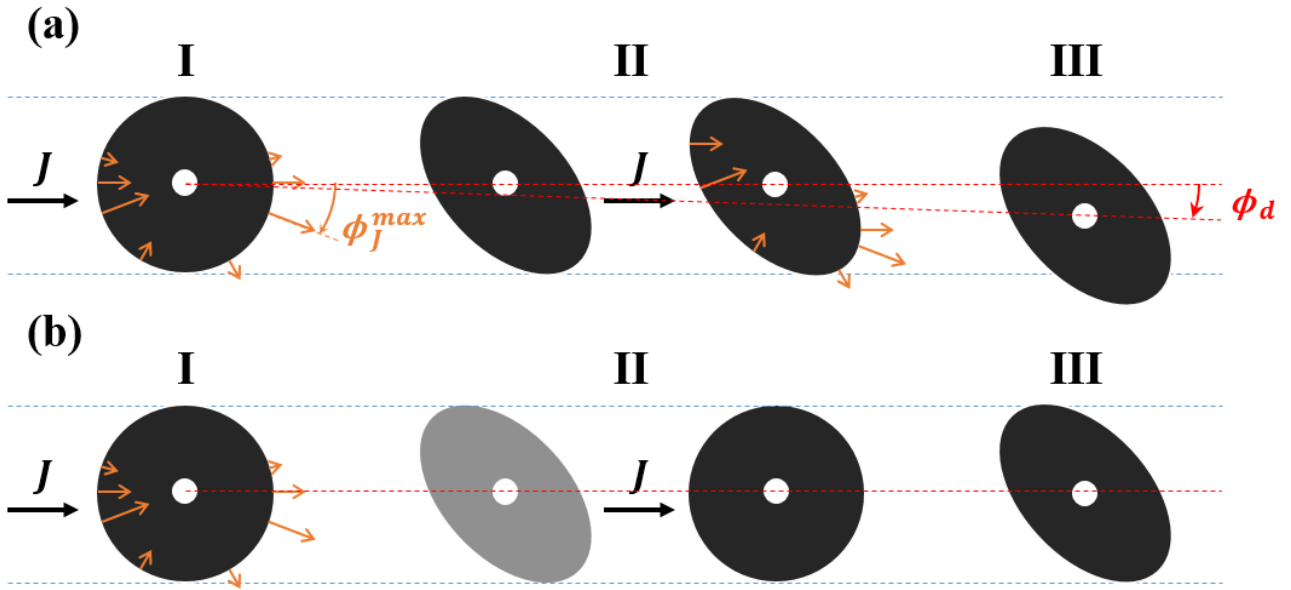


Figure V.21 The mechanism responsible for the emergence of the extrinsic SkHE. Schematic diagrams correspond to the up skyrmion bubble under a positive current in (a) Pt/Co/AlOx and in (b) Pt/Co/Pt. In (I), the skyrmion is initially circular and gets deformed into an ellipse while moving horizontally. In (II), the elliptical shape is stable in Pt/Co/AlOx while the skyrmion recovers the round shape in Pt/Co/Pt. In (III), the subsequent current pulses induce a drift with an angle ϕ_d for the skyrmion in Pt/Co/AlOx whereas they only distort again the skyrmion bubble in Pt/Co/Pt. The orange arrows represent the DW velocity v_{DW} in the non-collinear geometry with respect to the injected current. The maximum v_{DW} is obtained at the angle ϕ_J^{max} .

Actually, the main difference in the skyrmion bubble dynamics, between Pt/Co/AlOx and Pt/Co/Pt, is the stability of the elliptical distortion. As observed under MOKE, the elliptical shape is not the preferential bubble's shape during the skyrmion bubble motion in Pt/Co/Pt. The skyrmion bubble has a tendency to recover its circular profile between the injected current pulses. Besides that, the bubble's shape is sensitive to the pinning sites since it exhibits irregular and random profiles. Thereby, the elliptical shape is not maintained throughout the skyrmion bubble motion. On the contrary, the elliptical shape is stable in Pt/Co/AlOx. Under MOKE, we observe only the elliptical skyrmion bubbles after the current injection. The differences in the DW energy between the two structures can explain the difference in the stability of the elliptical bubble shape. The magnetic interactions differ (the DMI, the magnetic anisotropy, the dipolar energy, etc.) thus the DW energy profile changes from Pt/Co/AlOx to Pt/Co/Pt. In fact, the interfacial DMI is larger in Pt/Co/AlOx than in Pt/Co/Pt. Following the approximation of the DW energy density $\sigma_{DW} \sim \sigma_0 - \pi|D|$ (with $|D|$ the DMI constant, cf. section I.5.2), the tendency to have circular shaped DWs so that they have a reduced energy is stronger in Pt/Co/Pt than in Pt/Co/AlOx. We suggest that the stability of the elliptical distortion plays an important role in the emergence of the extrinsic SkHE. To illustrate its action in concert with the asymmetric DW motion in the non-collinear configuration, we use the simplistic picture depicted in **Figure V.21**.

In Pt/Co/AlOx, we move the skyrmion bubbles by means of trains of multiple current pulses. The mechanism of the asymmetric non-collinear DW motion acts on the DWs of these skyrmion bubbles. Consequently, the initial injected current pulses drive the skyrmion bubble horizontally while distorting it into an ellipse. The subsequent injected current pulses encounter then an elliptical skyrmion bubble instead of the initial round shape. For the up bubble under a positive current (**Figure V.21.a**), the acting mechanism of the asymmetric DW motion drags the lower half of the front DW downwards. In fact, the front DW is the DW_{U-D} for which the largest displacement occurs at a finite negative angle ϕ_J^{max} . In the meantime, it pushes the upper half of the back DW towards the front DW. For the back DW, the angle ϕ_J^{max} is positive so that its upper half merges with the front DW upper half. As a result, the center of the bubble becomes located below its initial position.

Such a mechanism ensures the skyrmion bubble deflection, perpendicularly to the current direction, with the angle ϕ_d that follows the symmetry of the angle ϕ_f^{max} of the front DW. This is similar to the SkHE hence the label of the ‘‘extrinsic’’ SkHE. On the contrary, the DWs recover their circular profiles between the consecutive current pulses in Pt/Co/Pt. As they do not encounter an elliptical DW shape, the subsequent current pulses are not able to generate the deflection of the bubble. The skyrmion bubbles moves thereby only horizontally in the flow regime. However, the pinning sites can promote the elliptical distortion by preventing the DWs from restoring their circular shapes. That is why the ‘apparent’ SkHE is observed in the creep regime of motion in Pt/Co/Pt.

The extrinsic SkHE emerges from the asymmetric non-collinear DW motion and the stable distorted skyrmion bubbles shape. Though an advanced theoretical effort is needed to verify such a mechanism, the presence of the two ingredients in a material where compact magnetic skyrmions are stabilized suggests that the intrinsic and the extrinsic contributions to the SkHE can coexist.

V.3.4. The extrinsic SkHE and magnetic skyrmion dynamics

For the compact skyrmions ($d \sim 100$ nm), the intrinsic SkHE can be significant. However, if the extrinsic SkHE is relevant also, it is required to reconsider the skyrmion dynamics. Actually, we have evidenced the asymmetric non-collinear DW motion in two different SIA materials, Pt/Co/AIOx and Pt/Co/Pt. This suggests that the asymmetric DW motion is an inherent effect that originates from the SIA in heterostructures and is not just specific to our studied samples. No evidence of the asymmetric non-collinear DW motion has been reported yet in a different material. Nevertheless, some observations of the DW dynamics, in literature, are reminiscent of the asymmetric non-collinear DW motion like in [Tanaka et al., 2015, 2017;]. In the $\text{SiO}_2/[\text{Tb} (0.6 \text{ nm})/\text{Co} (0.31 \text{ nm})]_7/\text{Pt} (2 \text{ nm})$ structure, [Tanaka et al., 2017] have observed that the magnetic bubbles, with $d \sim 2 \mu\text{m}$, deform into ellipses by injecting the electric current (Figure V.22). Such a distortion is similar to the distortion of the magnetic domains that is induced by the asymmetric non-collinear DW motion (cf. Figure III.8 in chapter III). In addition, the symmetry of the elliptical distortion with respect to the orientation of the Co magnetization in the ferrimagnet is similar to that observed in the Co ferromagnetic layer in Pt/Co/AIOx and Pt/Co/Pt. These observations indicate that the asymmetric non-collinear DW motion can be relevant in any multilayered structure with SIA, especially the materials where we take advantage of the interfacial DMI to stabilize compact magnetic skyrmions [Moreau-Luchaire et al., 2016; Woo et al., 2016; Legrand et al., 2017; Litzius et al., 2017].

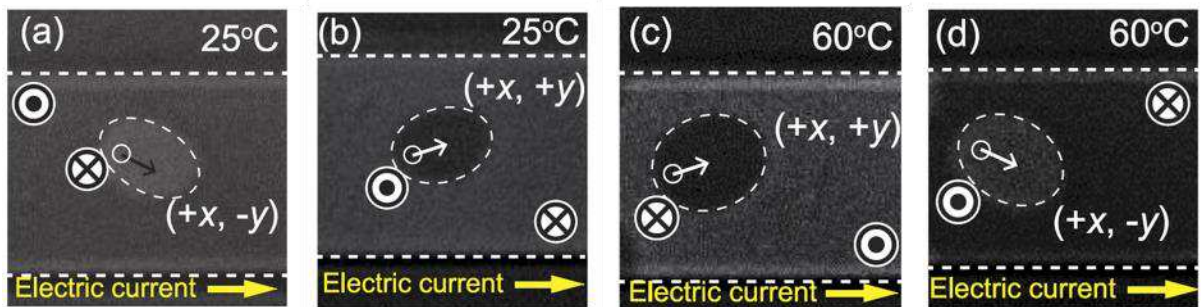


Figure V.22 MOKE images of the elliptical distortion of the magnetic bubbles in $\{\text{Tb}/\text{Co}\}_7\text{Pt}$ ferrimagnet multilayers. The down (a) and the up (b) bubbles are at 25°C at which the net magnetization is Tb dominant. The down (c) and the up (d) bubbles are at 60°C at which the net magnetization is Co dominant. The bubbles have initially a diameter of $2 \mu\text{m}$. The solid and the dashed lines, respectively, show the initial and the final states of the bubble. Here, the bubbles expand without moving. The expansion is along an oblique direction. The net magnetization from (a) to (d) has been reversed but the Co magnetization has kept the same orientation. With respect to the Co magnetization, the oblique angle has the same sign in (a) and (d) (also in (b) and (c)). Extracted from [Tanaka et al., 2017].

The triggering of the internal degrees of freedom is also relevant for the compact skyrmions. The time-resolved X-ray imaging during the current injection has revealed the dynamic excitations on the nanosecond time scale for skyrmions with $d \sim 100$ nm [Woo et al., 2017]. Depending on the

current density, the skyrmion motion is accompanied by a breathing mode consisting in the skyrmion diameter that varies continuously during the current pulse. Several theoretical works have predicted the dynamic distortions of the round compact skyrmion shape. Among them, we can have the excitation of the spin profile by the field-like component of SOT [Litzius et al., 2017], the disorder [Kim and Yoo, 2017], the variation of the magnetic anisotropy [Roy, Otxoa and Moutafis, 2019] and the thermal fluctuations [Tomasello et al., 2018]. Therefore, by analogy with our observations in Pt/Co/AlOx, the compact magnetic skyrmions can experience a non-negligible extrinsic SkHE in the reported measurements of the SkHA [Jiang et al., 2017; Litzius et al., 2017; Woo et al., 2018; Juge et al., 2019].

As an example, the variations of the angle θ_{SkH} as a function of the skyrmion velocity (cf. **Figure V.3.b**) in the [Pt (3.2 nm)/CoFeB (0.7 nm)/MgO (1.4 nm)]₁₅ structure are unlikely induced by the pinning/disorder effects [Litzius et al., 2017]. In fact, the CoFeB layer is amorphous and the skyrmion velocity varies from ~ 20 to ~ 120 m.s⁻¹. The regime of motion is likely the flow regime where the pinning action is not significant. The variation of the angle θ_{SkH} can be related to the distortion of the skyrmion profile. [Litzius et al., 2017] have considered a strong field-like torque \mathbf{T}_{FL} ($T_{FL} = 5 \cdot T_{DL}$) to qualitatively account for the unexpected strong drive-dependence of θ_{SkH} as \mathbf{T}_{FL} would distort the skyrmion profile. However, in various Pt/FM/Ox structures, the field-like torque \mathbf{T}_{FL} is usually smaller or at most comparable to the damping-like torque \mathbf{T}_{DL} . Thereby, the emergence of an extrinsic SkHE in this structure could be behind these variations of θ_{SkH} instead.

Conclusions

The deflection of the magnetic skyrmions, perpendicular to their direction of motion, has been usually attributed to the action of the topological Magnus force. This conventional or intrinsic SkHE is negligible in Pt/Co/AlOx and Pt/Co/Pt. In spite of that, by studying the current-induced motion of skyrmion bubbles in these structures, we have evidenced a sizeable well-defined deflection that we have identified as the new extrinsic contribution to the skyrmion Hall Effect (SkHE). The emergence of this extrinsic SkHE comes, in part, from the action of the mechanism of the asymmetric non-collinear DW motion on the skyrmion bubbles.

The mechanism of the asymmetric non-collinear DW motion in the non-collinear, demonstrated in Pt/Co/AlOx and Pt/Co/Pt, distorts the round skyrmion bubbles into ellipses. Nonetheless, it does not generate necessarily the extrinsic SkHE due to the difference in the skyrmion bubbles dynamics between both structures. In Pt/Co/Pt, the skyrmion bubbles move horizontally in a hopping-like mode with random deflections whereas they exhibit a systematic well-defined drift in Pt/Co/AlOx. We suggest that the remaining requisite condition for a relevant extrinsic SkHE is the stability of a skyrmion in a distorted profile.

In principle, this extrinsic SkHE can be relevant for compact skyrmions along with the intrinsic SkHE. This suggests that the current-induced motion of magnetic skyrmions in SIA materials ought to be reconsidered under the scope of the asymmetric non-collinear DW motion. Additional experimental and theoretical efforts are required to have a better understanding of the extrinsic SkHE.

General conclusions

The ultrathin ferromagnetic films with the inversion asymmetry (SIA) have attracted a lot of interest in the nanomagnetism community. This thesis has intended to pursue the investigation of the various effects that originate from SIA on the magnetization dynamics. The objective was to examine the current-induced magnetic domain wall (DW) motion, in particular in the two-dimensional geometry, while taking into account the recent proposal of the Chiral Damping mechanism.

A previous study of the magnetic field-induced DW motion in Pt/Co/Pt proposed the existence of the Chiral Damping mechanism. In the meantime, the current-induced DW motion has been widely attributed to the combined action of the interfacial Dzyaloshinskii-Moriya interaction (DMI) and the spin-orbit torques (SOT). The DMI stabilizes homochiral Néel walls that are driven by the damping-like component T_{DL} of SOT. Therefore, in order to have a comprehensive picture of the DW dynamics, I have pursued and studied the current-induced DW motion in a non-collinear geometry in magnetic multilayers with different (SIA). These structures are the Pt/Co/AlOx stack that exhibits a large SIA since the two Co interfaces are different and the Pt/Co/Pt stack with a low SIA brought by the difference in the thicknesses between the two Pt layers.

The action of SOT depends on the angle between the DW core magnetization m_{DW} and the current direction. We can tune this angle in two different ways: by applying a longitudinal in-plane magnetic field H_x or by injecting the current in an oblique direction with respect to the DW. In fact, H_x modulates the DW core magnetization m_{DW} . Thus, m_{DW} rotates in the plane upon the variation of the amplitude of H_x so that the action of T_{DL} varies. Under an oblique injection, the DW propagates in a direction at a finite angle ϕ_j with respect to the current direction which gives a different T_{DL} than that in the conventional geometry where the current is injected normal to the DW. During this thesis, I have chosen to combine these two methods in order to examine the variation of the action of SOT on the DWs. To avoid possible artifacts due to the nanofabrication of the nanowires, I have studied the action of the current in the presence of H_x on magnetic circular domains in the center of a 10- μm -wide wire. The circular profile of the DWs allows to study the DW motion at every angle ϕ_j (from -90° to $+90^\circ$). In the first experiment, the magnetic circular domains have a large diameter ranging between 4 and 8 μm . In the second experiment, I have reduced the diameter to an average value of 1.6 μm corresponding to the stabilized magnetic bubbles or the skyrmion bubbles. The aim was to unveil the impacts of the observed features of the non-collinear DW motion on the current-induced motion of the skyrmion bubbles.

In the Pt/Co/AlOx structure, the current-induced non collinear DW motion is asymmetric. The largest displacement of the DW takes place at a finite angle ϕ_j^{max} that is negative for the up/down DW and positive for the down/up DW. I have observed such asymmetry by following the asymmetric distortion of the magnetic circular domains. In fact, these domains are deformed into ellipses by the electric current. Moreover, this asymmetric DW motion is qualitatively in agreement with the predictions from the DMI and SOT mechanism in the DW flow regime of motion. Due to the presence of the large DMI, it is very difficult for the in-plane field H_x to modulate the DW internal structure in Pt/Co/AlOx. Thereby, the external field is not expected to alter significantly the current-induced DW motion. Indeed, we have not obtained a net variation of the angle ϕ_j^{max} for the non-collinear DW motion in the presence of H_x . However, numerous reports have evidenced significant effects on the DW displacements for the same range of H_x , which implies that the action of SOT has been tuned. These two contradictory results are not compatible with the DMI +SOT mechanism. The presence of the DMI is then not sufficient to explain all the features of the current-induced DW motion in the flow regime in Pt/Co/AlOx. It is possible that H_x triggers another unknown physical mechanism responsible for the observed chiral effects in Pt/Co/AlOx.

I have next studied the asymmetric distortion of the magnetic circular domains in Pt/Co/Pt. By observing the DW motion in the current direction, we have demonstrated that the DMI and the damping-like component T_{DL} of SOT have the same sign as in the Pt/Co/AlOx structure. This can be behind the similar asymmetric non-collinear DW motion in the two structures (the sign of the angle ϕ_j^{max} , for each DW, is the same in the two structures). Like in Pt/Co/AlOx, the asymmetric non-collinear DW motion is maintained in the presence of H_x even though H_x is able to modulate efficiently the DW core magnetization m_{DW} in Pt/Co/Pt. Indeed, the application of H_x has yielded chiral effects on the DW displacements as expected from the modulation of m_{DW} . The DW motion becomes asymmetric between the two different DWs in the presence of H_x . Interestingly, upon the increase of the amplitude of H_x , the asymmetry between the two DWs has been reversed. By including the Chiral Damping mechanism in the numerical collective coordinate model, we were able to account for the inversion of the asymmetric motion between the two DWs. This analysis have evidenced the role of the Chiral Damping and its interplay with the DMI. On the one hand, the Chiral Damping and the DMI contribute both to the asymmetric non-collinear DW motion. On the other hand, they give rise to opposite asymmetries between the two DWs. The DMI dominates for small applied H_x whereas the Chiral Damping prevails for large applied H_x . These results indicate that chiral energy and chiral dissipation from SIA can contribute on an equal footing to the current-induced DW. They can open the way to tune at will the properties of the DW motion for exotic functionalities in future spintronic devices.

Nevertheless, the models based on the action of SOT fail to explain all of our experimental observations. Actually, the asymmetric non-collinear DW motion is still present in the creep regime of motion in both structures. For instance, the angle ϕ_j^{max} has the same average value between the flow regime and the creep regime in Pt/Co/AlOx. Moreover, the reversal of the asymmetric motion between the two DWs is also present in the creep regime in Pt/Co/Pt. On the contrary, the models based on the action of SOT predict that such effects diminish for a reduced DW velocity like in the creep regime. These observations evidence that the DW motion is still a very complex and mysterious phenomenon.

The angle ϕ_j^{max} , for the current-induced non-collinear DW motion, exhibits striking similarities with the angle of the skyrmion Hall effect (SkHE). They have the same symmetry with respect to the current direction and the magnetization orientation. I have therefore investigated the current-induced motion of small magnetic bubbles in Pt/Co/Pt and Pt/Co/AlOx. These magnetic bubbles have a unidirectional motion in the current direction. Thereby, they can be considered as skyrmion bubbles whose chirality is dictated by the DMI and the motion is driven by SOT. While the skyrmion bubble motion is mainly horizontal with random deflections in Pt/Co/Pt, it has a well-defined deflection in Pt/Co/AlOx. This well-defined deflection follows the expected SkHE for a Néel skyrmion moving in the current direction. By quantitatively studying the skyrmion bubble deflection, we were not able to explain our observations by the conventional SkHE. They actually evidence a new extrinsic contribution to the SkHE. By comparing the skyrmion bubble motion in the two structures, we propose that the extrinsic SkHE is a consequence of the mechanism of the asymmetric non-collinear DW motion that distorts the skyrmion bubble shape.

The different results of this thesis give a more complete picture of the DW and the skyrmion motion in ultrathin magnetic layers with SIA. They have evidenced interesting effects, like the reversal of the asymmetric motion between the DWs and the extrinsic SkHE, which can bring novel ideas and concepts for spintronic devices. The development of such devices requires the understanding of the physical mechanisms responsible for these effects. They actually call for a more complex mechanism than the actual models based on the action of SOT. The future perspectives of this study will be to propose and evidence what possible new mechanisms can play a role in the magnetic textures interaction with the electric current in SIA materials. For that end, it is interesting to include the pinning and imperfections in our numerical calculations. We can then verify the validity of the combined action of SOT, the DMI and the Chiral Damping in a more realistic system. It is as well desirable to pursue our experimental study in order to get the quantitative measurements of the

angle ϕ_J^{max} as a function of the current density J and the longitudinal field \mathbf{H}_x in the Pt/Co/Pt structure. During this thesis, I was not able to evidence the Chiral Damping in Pt/Co/AlOx. The importance of the Chiral Damping contribution to the current-induced DW motion has only been demonstrated in structures with weak SIA like Pt/Co/Pt. It is important to find a technique that helps to probe and quantify the Chiral Damping in large SIA structures. In fact, measuring the contribution of the Chiral Damping in different magnetic systems can bring more insights of the DW motion. Furthermore, static spin-torque-meter measurements in a similar non-collinear geometry can help further understand the DW motion. A magnetic dot with a constriction in the middle can be placed on top of a Hall bar. By stabilizing the DW on the constriction and by measuring the Extraordinary Hall effect for an oblique current injection, it is possible to extract the amplitude of SOT as a function of the angle ϕ_J . It is as well desirable to follow the non-collinear DW motion with a time-resolved imaging technique. Measuring the magnetization dynamics with the required spatial and temporal resolution is still missing. The ongoing development of a near field magneto-optical microscopy, a pump probe MOKE-SNOM, with a spatial resolution below 50 nm and a time resolution of the order of 10 ps can be a possible alternative.

Appendix

A.1. Asymmetric distortion of the magnetic circular domains

This section intends to complete the interpretation of the asymmetric distortion of the magnetic domains by an electric current in the structure of Pt (3 nm)/Co (0.6 nm)/Pt (1.56 nm) in Chapter III section 3.

A.1.1. The phenomenological thermal field

In the numerical model, the thermal fluctuations were taken into account by a thermal field $\mathbf{H}_{th}(t)$ as proposed in [Brown 1963] and [Martinez et al. 2007]. \mathbf{H}_{th}^i is computed at each time step Δt for a DW represented by a cell i whose volume is expressed as $V^i = L^i \times t_{FM} \times \Delta$ with Δ the DW width and t_{FM} the FM layer thickness. L^i is a phenomenological parameter giving the length of the straight DW. \mathbf{H}_{th}^i follows a random Gaussian-distributed stochastic process with zero mean value. In addition, the different \mathbf{H}_{th}^i are uncorrelated in time and in space:

$$\mathbf{H}_{th}^i(t) = \boldsymbol{\eta}^i(t) \sqrt{\frac{2\alpha_0 k_B T}{\gamma_0 \mu_0 M_s V^i \Delta t}}$$

$$\langle \boldsymbol{\eta}^i(t) \rangle = 0$$

$$\langle \boldsymbol{\eta}_i^i(t) \boldsymbol{\eta}_k^j(t') \rangle = \delta_{lk} \delta_{ij} \delta(t - t')$$

Here, α_0 is the isotropic Gilbert damping constant, δ_{ij} the Kronecker delta function and $\boldsymbol{\eta}^i(t)$ is a unit stochastic vector ($|\boldsymbol{\eta}^i(t)| = 1$) whose Cartesian components $l: x, y, z$ are also randomly distributed.

In principle, L^i depends on the temperature T and on the magnetic parameters (A_{ex} , M_s , t_{FM} , K_u , etc...). It is therefore difficult to define such a parameter. Nevertheless, two conditions may allow to fix the L^i phenomenologically, thus obtaining a realistic calculation from the numerical model. The first condition is $(L^i/R) \ll 1$ with R the radius of the domain (i.e. a small curvature of the circular domain). Then, we can still assume that the circumference of the domain is equivalent to the succession of the straight DWs. The second condition is that L^i has to be large enough for the DW not to be in a superparamagnetic-like state. As long as the model saturates \mathbf{m}_{DW} for an external in-plane field \mathbf{H}_x with an amplitude in a good agreement with the experimental observations, we consider the chosen value as a suitable L^i for our calculations. There is in fact a wide range of suitable values of L^i .

A.1.2. The asymmetric distortion at $H_x = 0$

A.1.2.1. The non-collinear DW motion under low current density ($|H_{DL}| = 1$ mT) at $T = 0$ K

In **Figure A.1**, we depict a graphical construction of the DW_{U-D} motion within the DMI + T_{DL} + CD scenario in Pt/Co/Pt in a straight wire ($\phi_J = 0^\circ$). We do not take into account the thermal fluctuations in this section. The Néel component \mathbf{m}_x of the DW is left-handed. In addition, the Bloch component of the DW is left-handed ($m_y < 0$). The effective field \mathbf{H}_{DL} (along the $+z$ -axis) distorts \mathbf{m}_{DW} away from its equilibrium orientation. Therefore, the action of \mathbf{H}_{DMI} creates an out-of-plane torque \mathbf{T}_{DMI} that displaces the DW.

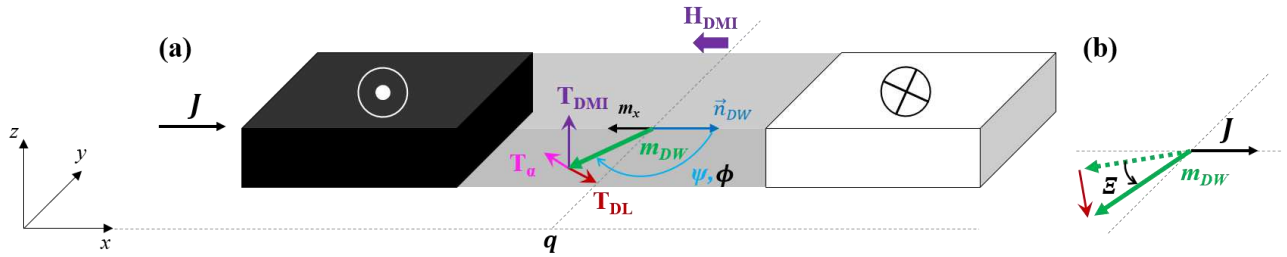


Figure A.1 Schematic representation of the DW dynamics within the DMI + T_{DL} + CD mechanism using the collective coordinate model $q - \phi$. The DW has an intermediate configuration like in Pt/Co/Pt in a straight wire. (a) Schematics of the different torques acting on \mathbf{m}_{DW} at the center of the DW. The Bloch component of the DW is left-handed and the Néel component is given by \mathbf{m}_x . \mathbf{m}_x is oriented against the current. Thus, the current-induced T_{DL} rotates \mathbf{m}_{DW} anti-clockwise in the plane. The balance between the dissipative torque T_α and T_{DL} fixes the steady-state motion of the DW. The motion of the DW is dictated by T_{DMI} . (b) Schematic diagram of the distorted \mathbf{m}_{DW} by T_{DL} . \mathcal{E} is the angle between the distorted \mathbf{m}_{DW} and its initial equilibrium position and ψ is the angle between \mathbf{m}_{DW} and \mathbf{n}_{DW} .

According to the LLG equation, the damping torque \mathbf{T}_α , associated to the DW motion, writes:

$$\mathbf{T}_\alpha = \alpha \mathbf{m}_{DW} \times \frac{\partial \mathbf{m}_{DW}}{\partial t} = \alpha \mathbf{m}_{DW} \times (\mathbf{T}_{DL} + \mathbf{T}_{DMI})$$

For the steady-state DW, the in-plane component of \mathbf{T}_α opposes \mathbf{T}_{DL} until they cancel each other at a certain angle ($\phi - \mathcal{E}$) where

$$T_{\alpha/in-plane} = T_{DL} = \alpha T_{DMI}$$

Thus, the out-of-plane torque \mathbf{T}_{DMI} dictates the velocity of the DW within this mechanism.

$$v_{DW} \propto T_{DMI}$$

Herein, both of T_{DL} and T_{DMI} depend on \mathcal{E} , the static angle between the actual DW magnetization core \mathbf{m}_{DW} , after being distorted, and its initial equilibrium position.

$$T_{DMI} = \gamma |\mathbf{H}_{DMI} \times \mathbf{m}_{DW}| = \gamma |\mathbf{H}_{DMI} \cdot \mathbf{m}_y| = \gamma H_{DMI} \sin(\phi - \mathcal{E})$$

$$T_{DL} = \gamma H_{DL} |[(\mathbf{u}_z \times \mathbf{J}) \times \mathbf{m}_{DW}] \times \mathbf{m}_{DW}| = -\gamma J H_{DL} \cos(\phi - \mathcal{E})$$

In this case, the deformation angle \mathcal{E} and the DW velocity v_{DW} are defined as:

$$\tan(\phi - \mathcal{E}) = -\frac{\alpha H_{DMI}}{J H_{DL}} \quad \text{and} \quad v_{DW} \propto -\frac{\gamma J H_{DL} \cos(\phi - \mathcal{E})}{\alpha}$$

The DW velocity v_{DW} depends proportionally on two terms related to the current density J . The first term is simply the current density J itself. The second term is $\cos(\phi - \mathcal{E})$. It converges towards 0 as we increase J , based on the expression of $\tan(\phi - \mathcal{E})$ ($\phi - \mathcal{E}$ converges towards -90°). These two

terms account, qualitatively, for the shape of the curve of the DW velocity v_{DW} as a function of J within the DMI + T_{DL} mechanism, in **Figure III.5.b**. We get the initial increase with J , as the distortion of \mathbf{m}_{DW} is still small, followed by a saturation plateau due to the competition between these two terms, as \mathcal{E} becomes larger.

If we only consider a constant applied current density J , we have a maximum displacement for the DW when the angle $(\phi - \mathcal{E})$ is equal to 180° (\mathbf{m}_{DW} gets aligned with the direction of the current J after being distorted by T_{DL}). Thus, the displacement is reduced as we cant away \mathbf{m}_{DW} from its alignment in the current direction.

Indeed, if we include the distortion of \mathbf{m}_{DW} , as described above, into the semi-circle shaped DW, the asymmetry of the motion calculated using the numerical model (shown in **Figure III.29**) can be explained (**Figure A.2**). The DW velocity is proportional to \mathbf{m}_x , the component of \mathbf{m}_{DW} that is aligned in the current direction (the x -axis). For the left-handed Bloch wall DW_{U-D}, as we tilt \mathbf{n}_{DW} from the collinear configuration ($\phi_J = 0^\circ$) towards $\phi_J = -90^\circ$ (corresponds to 270° in **Figure A.2.b**), $|\mathbf{m}_x|$ increases. Consequently, the DW velocity gets larger. Since the DW is in an intermediate configuration in Pt/Co/Pt. At $\phi_J = 0^\circ$, \mathbf{m}_{DW} is not aligned in the current direction. In fact, it is initially aligned in the current direction at a finite angle ϕ_J^1 , at point 1 in **Figure A.2.a**. Since we consider the left-handed chirality for both the Néel and the Bloch DW components, the angle ϕ_J^1 is located at the bottom-half side of the semi-circle shaped DW_{U-D} ($-90^\circ < \phi_J^1 < 0^\circ$). However, T_{DL} deviates \mathbf{m}_{DW} from its alignment. Thus, the displacement is not maximum at ϕ_J^1 . Instead, the maximum is reached at the point 2 (the angle ϕ_J^2 with $-90^\circ < \phi_J^2 < \phi_J^1$) where \mathbf{m}_{DW} aligns in the current direction after being distorted. Therefore, it is clear that the DW displacement is maximum at an angle that is different from the collinear configuration ($\phi_J = 0^\circ$). Beyond point 2, $|\mathbf{m}_x|$ starts to decrease resulting in the reduction of the DW velocity. Concerning the top-half side of the DW_{U-D}, $0^\circ < \phi_J < +90^\circ$ so that $|\mathbf{m}_x|$ is initially reduced. At point 3 (angle ϕ_J^3), \mathbf{m}_{DW} becomes orthogonal to the current J . In this case, $T_{DL} = 0$ so that there is no DW motion. Beyond the point 3, $|\mathbf{m}_x|$ starts to increase while becoming parallel to the current ($m_x > 0$). Therefore, the DW starts to move against the current with an increasing velocity. As for the DW_{D-U}, by analogy we obtain the opposite asymmetric motion. This scenario is given by the calculations depicted in final **Figure A.2.b**. For the right-handed Bloch wall, the mechanism is the same. Due to the opposite chirality of the Bloch DW component, each DW exhibits the opposite asymmetry (shown in **Figure III.29.b**). Moreover, $|\mathbf{m}_x|$ is not equal to zero at the normal configurations of the DW ($\phi_J = 90^\circ$ and 270° in **Figure A.2.b**) (due to the Bloch component of the DW). Thus, the model yields a non-zero velocity in these situations in opposition with the experimental results.

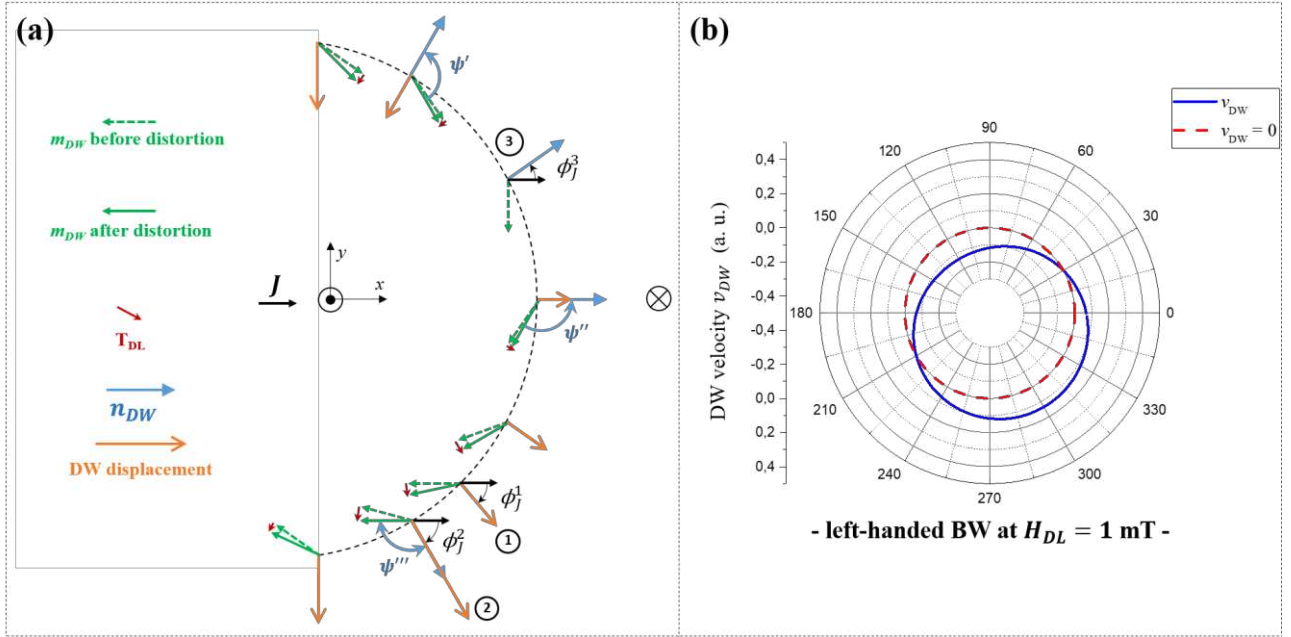


Figure A.2 The asymmetric non-collinear DW motion at $T = 0$ K in Pt/Co/Pt. We consider the DW_{U-D} with a left-handed Bloch chirality. (a) Schematic picture of the distortion of \mathbf{m}_{DW} across the semi-circle shaped DW_{U-D}. When the current is applied, \mathbf{T}_{DL} cants \mathbf{m}_{DW} anti-clockwise if \mathbf{m}_x is anti-parallel to \mathbf{J} . The DW moves then in the current direction. This situation corresponds to the side of the DW located at the bottom of the point 3. Above this point, \mathbf{m}_x becomes parallel to \mathbf{J} . Thus, \mathbf{T}_{DL} cants \mathbf{m}_{DW} clockwise and the DW moves against the current direction. At the point 3, no torque is exerted on \mathbf{m}_{DW} . At the point 2, \mathbf{m}_{DW} becomes aligned with the direction of \mathbf{J} yielding the largest displacement. Here, \mathbf{m}_x is exaggerated for purpose of clarity. (b) DW velocity v_{DW} versus ϕ_J at $T = 0$ K. The calculations (in blue) were obtained using the numerical collective coordinate model within the DMI + SOT + CD mechanism and under low current density ($H_{DL} = 1$ mT).

The CD contributes to the non-collinear asymmetric DW motion since the DW velocity depends on the damping parameter ($v_{DW} \propto 1/\alpha$). For the DW_{U-D} and according to Eq. I.54, one can express the damping as:

$$\alpha = \alpha_0 + \alpha_c \mathbf{m}_{DW} \cdot \nabla m_z = \alpha_0 - \alpha_c \mathbf{m}_{DW} \cdot \mathbf{n}_{DW} = \alpha_0 - \alpha_c \cos \psi$$

Therefore, the direction of the CIDWM (sign of v_{DW}) is only dictated by \mathbf{T}_{DL} . However, α depends on ψ that varies across the semi-circle shaped DW (see **Figure A.2**). Consequently, the damping is not symmetric with respect to $\phi_J = 0^\circ$. It contributes then to the asymmetry of the DW motion.

Indeed, by considering the DMI + \mathbf{T}_{DL} + CD mechanism, we obtain an asymmetry of the DW motion in the non-collinear configuration in Pt/Co/Pt. However, this asymmetry does not correspond to our experimental observations. As seen in the main manuscript, the thermal fluctuations should be considered to model our results.

A.1.2.2. The non-collinear DW motion under high current density ($|H_{DL}| = 10$ mT) at $T = 300$ K

By including the thermal fluctuations, the DMI + SOT + CD mechanism accounts, in a good qualitative agreement, for the asymmetric DW motion in the non-collinear configuration observed experimentally in Pt/Co/Pt. The presence of the DMI is crucial as it makes the current action on the DWs equivalent to that on chiral Néel walls. The numerical model using only the DMI reproduces well the experiment (**Figure A.3.a**) while including CD gives only a correction to the amplitude of the DW velocity (**Figure A.3.b**). The DMI mechanism, in concert with \mathbf{H}_{th} , dictates and governs then the asymmetric DW motion at $\mathbf{H}_x = 0$. The CD also induces an asymmetric DW motion with the angle ϕ_J as evidenced by the calculations of the DW velocity v_{DW} in **Figure A.3.c**. The amplitude

of this asymmetry is limited compared to that induced by the DMI + SOT + CD mechanism as depicted in **Figure A.3.d**, which confirms the dominant role played by the DMI at $H_x = 0$ mT.

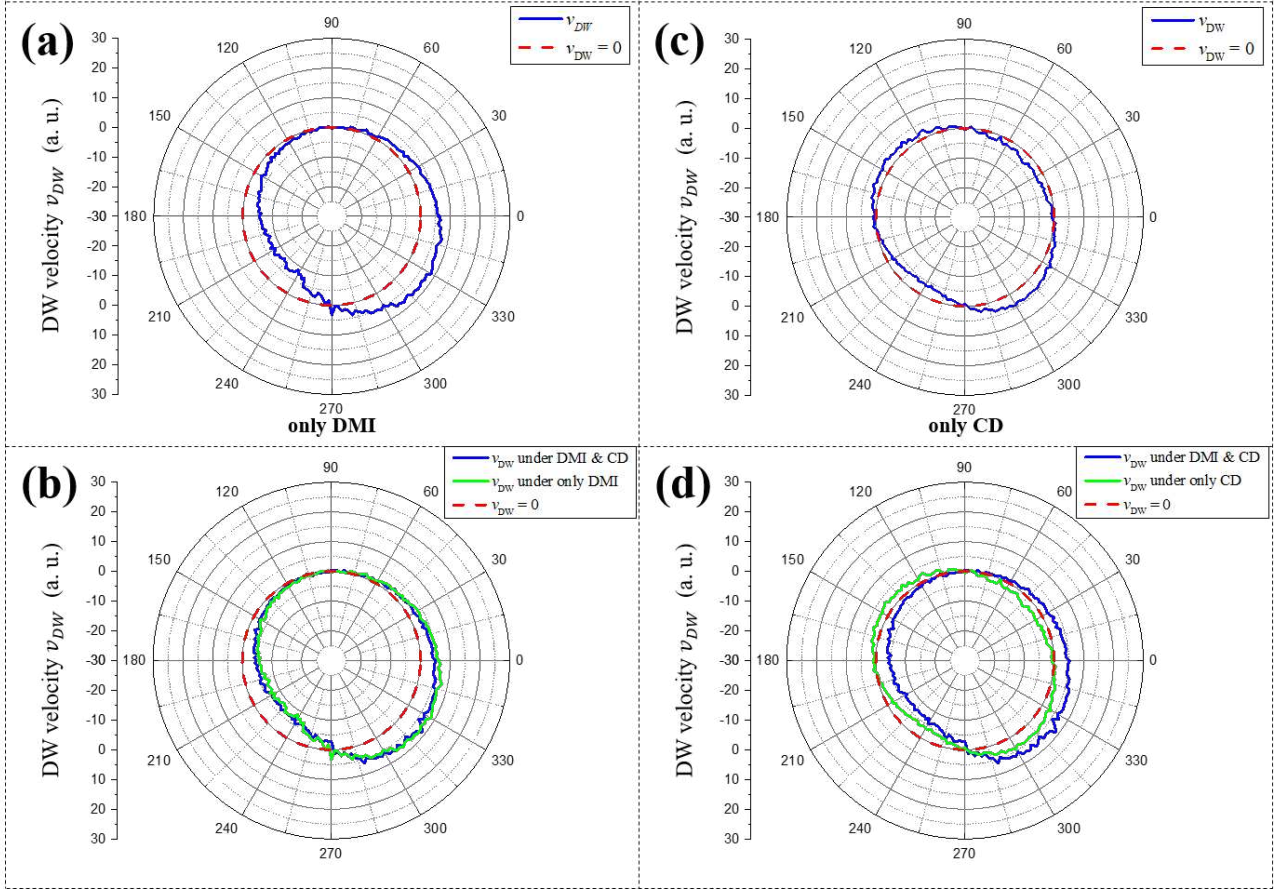


Figure A.3 The comparison of the DW velocity v_{DW} versus the angle ϕ_J at $T = 300$ K between calculations based on different mechanisms using the numerical collective coordinate model. The model is applied to an up circular magnetic domain under a positive current. The model uses the mechanism of DMI + T_{DL} in (a) and of CD + T_{DL} in (c). In (b) (respect. in (d)), we compare the contribution of the DMI (respect. CD) with the DMI + T_{DL} + CD combined action. The shown data are the average of 5 different calculations from the numerical model.

A.1.3. The asymmetric distortion in the presence of H_x

In this section, we present numerical calculations and discussions to complete the interpretation of the asymmetric non-collinear DW motion in the presence of a bias field H_x that we address in section III.4.5.2 of the main manuscript. Due to the thermal field, as discussed above, we consider that the DWs are left-handed NWs during the current injection in Pt/Co/Pt.

The **Figure A.4** aggregates the calculations of the asymmetric distortion of the up magnetic circular domain at H_x with different small amplitudes. The DW_{D-U} moves against the current direction from $H_x = -10$ mT. The reversal of the motion likely starts near the normal configurations with respect to the current ($\phi_J = 90^\circ$ or 270°). Actually, the DW core magnetization \mathbf{m}_{DW} sits along the y -axis at these configurations so a small negative H_x can induce a net $m_x < 0$. Consequently, the damping-like effective field H_{DL} becomes oriented along the $+z$ -axis thus the up domain expands (the DW velocity v_{DW} pointing outwards). As the angle ϕ_J varies from 90° (or 270°) to 180° , \mathbf{m}_{DW} tends gradually to point along to the x -axis with $m_x > 0$. The reversal of the direction of motion of the DW_{D-U}, at these configurations, takes then place at larger H_x . From the numerical model, we get an expansion of the up domain at any ϕ_J at $H_x = -30$ mT. This is comparable to the experiment results that have shown the up domain expansion at $H_x = -37$ mT under $J \sim +1.13 \cdot 10^{12}$ A.m⁻² (**Figure**

III.31.b). In this range of \mathbf{H}_x , for the DW_{U-D} , a negative \mathbf{H}_x is parallel to the local \mathbf{H}_{DMI} thus the DW velocity v_{DW} increases with the amplitude of \mathbf{H}_x and is larger than the velocity of the DW_{D-U} . The calculations confirm that up to $\mathbf{H}_x = -30$ mT, the center of the circular domain moves horizontally in the current direction. It exhibits also a vertical motion (downwards) resulting from the asymmetric motion of DWs with the angle ϕ_J . These asymmetric features of the DW motion are dictated by the DMI at small in-plane field \mathbf{H}_x .

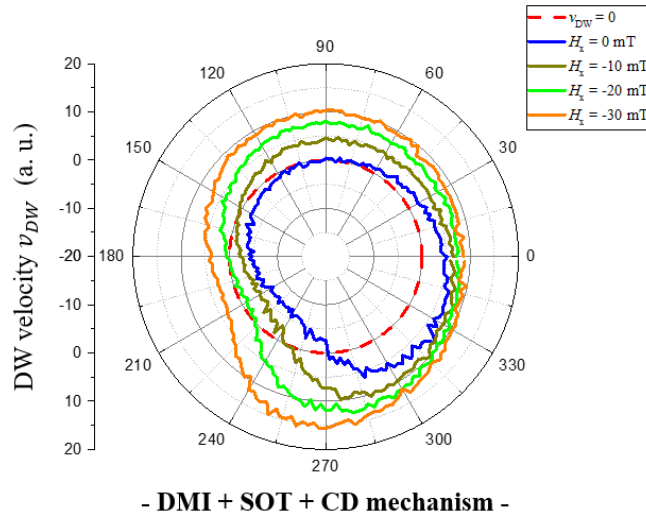


Figure A.4 The calculated DW velocity in the presence of small \mathbf{H}_x in Pt/Co/Pt. The DW velocity v_{DW} versus the angle ϕ_J at $T = 300$ K using the numerical collective coordinate model under high current ($H_{DL}=10$ mT). The calculations are performed at a negative \mathbf{H}_x , pointing to the left, with various amplitudes; $\mathbf{H}_x = 0$ (in blue), $\mathbf{H}_x = -10$ (in brown), $\mathbf{H}_x = -20$ (in green) and $\mathbf{H}_x = -30$ (in orange) (units of \mathbf{H}_x in mT). The DMI + SOT + CD mechanism is applied in the model for the up magnetic circular domain under a positive current (flowing from left to right). In this range of \mathbf{H}_x , the asymmetric distortion of the domain remains qualitatively the same. The shown data are the average of 7 different calculations from the numerical model (of 5 for $\mathbf{H}_x = 0$ mT).

Indeed, in **Figure A.5.a**, the two v_{DW} curves, obtained using DMI +SOT + CD and only DMI in the numerical model, nearly collapse into each other at $\mathbf{H}_x = -20$ mT. Nevertheless, this does not exclude any contribution from the CD mechanism as mentioned in the main manuscript. As depicted in the **Figure A.5.b**, the v_{DW} curve, obtained when considering only the CD in the numerical model, exhibits an asymmetry between the two DWs that is opposite to that induced by the DMI. The DW_{D-U} moves with a velocity larger than the DW_{U-D} . In addition, the CD endows the non-collinear DW motion in the presence of \mathbf{H}_x with an asymmetric feature. The DW velocity v_{DW} , for each DW, has an asymmetric variation with respect to $\phi_J = 0^\circ$ (or 180°) and its maximum is obtained at a finite angle ϕ_J . This is an indication that the asymmetric distortion of the magnetic domains in Pt/Co/Pt is the outcome of the two asymmetries induced by both the DMI and the CD. The DMI is the dominant mechanism at low \mathbf{H}_x .

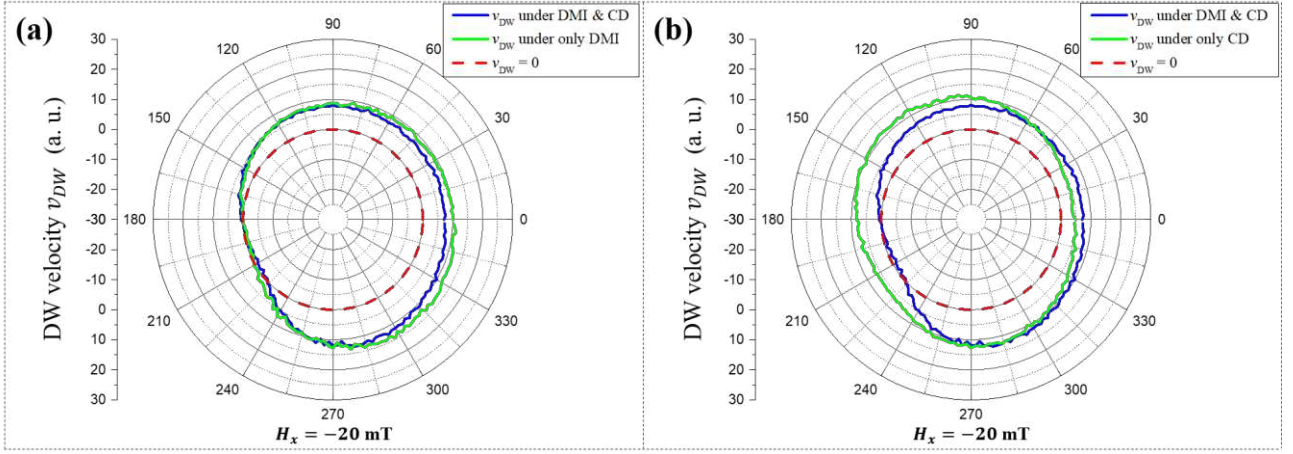


Figure A.5 The Chiral Damping contribution to the non-collinear DW motion at $H_x = -20$ mT. The comparison of the calculations of the DW velocity at $T = 300$ K and at $H_x = -20$ mT using different mechanisms in the numerical collective coordinate model under high current ($H_{DL} = 10$ mT). The model is applied to the up magnetic circular domain under a positive current. In (a), comparison between the DMI + SOT + CD mechanism and the action of DMI. In (b), comparison between the DMI + SOT + CD mechanism and the action of CD in (b). The asymmetric distortion of the up domain is governed by DMI at $H_x = -20$ mT. The shown data are the average of 7 different calculations from the numerical model.

As discussed in the main manuscript, the amplitudes of the DMI and the CD contributions vary with the increase in the amplitude of H_x , respectively decreasing and increasing. The asymmetric distortion of the circular magnetic domain undergoes then a gradual transition under an electric current in Pt/Co/Pt. From $H_x = -20$ mT to $H_x = -100$ mT, the numerical collective coordinate model shows that the asymmetry between the two DWs changes its sign. At $H_x = -100$ mT, the CD mechanism dominates over the DMI (**Figure A.6**). The v_{DW} curve (in blue) from the DMI + SOT + CD mechanism follows the asymmetry imposed by the CD mechanism (in green in **Figure A.6.b**). However, to account for the amplitude of the DW velocity (especially for the DW_{D-U}), we need to consider the DMI contribution that is still present at $H_x = -100$ mT.

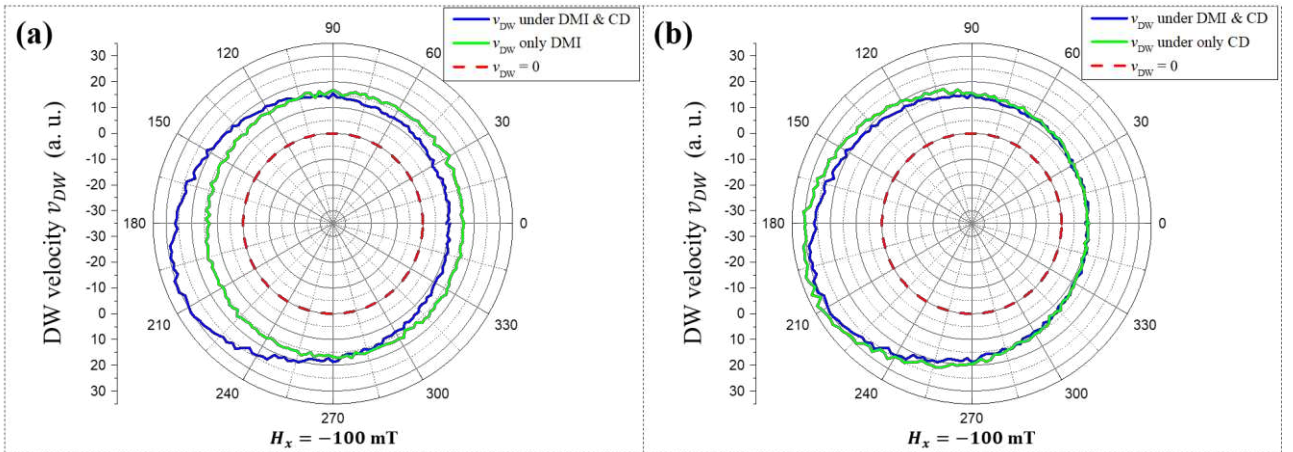


Figure A.6 The calculated DW velocity in the non-collinear configuration at $H_x = -100$ mT in Pt/Co/Pt. The DW velocity v_{DW} versus the angle ϕ_J at $T = 300$ K under a positive current with a high density ($H_{DL} = 10$ mT) using the numerical collective coordinate model. The model is applied to the up magnetic circular domain. Here, we compare the calculations using the DMI + SOT + CD mechanism (in blue) with calculations using only the DMI in (a) and only the CD in (b). The shown data are the average of 5 different calculations.

In **Figure A.7**, we have the v_{DW} curves at different large H_x . Both DWs see their velocities increase with H_x . The rate of this increase is larger for the DW_{D-U}. The velocity of the DW_{U-D} seems to reach a saturation plateau beyond $H_x = -50$ mT. Although the asymmetric motion between the two different DWs has reversed at large H_x , the asymmetric DW motion in the non-collinear configuration is maintained. However, the numerical model gives a varying ϕ_J^{max} (the angle of the largest velocity of a DW) with H_x . For the DW_{D-U}, ϕ_J^{max} tends towards $\phi_J = 180^\circ$ (or 0°) from $H_x = -50$ mT to $H_x = -150$ mT and saturates near -90° (270° in **Figure A.7**) for the DW_{U-D}.

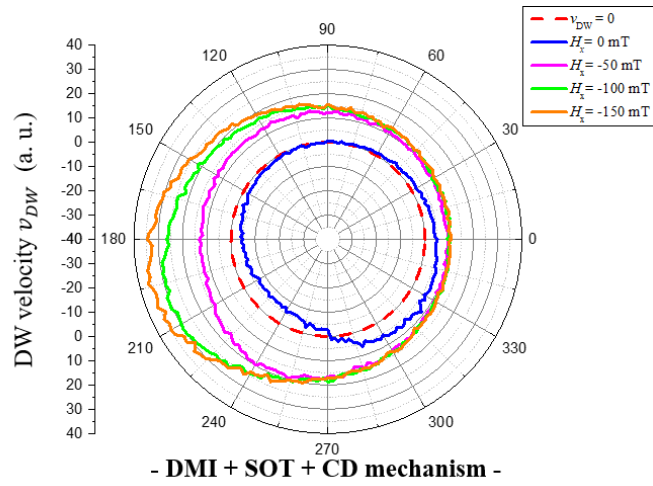


Figure A.7 The calculated DW velocity in the presence of large \mathbf{H}_x in Pt/Co/Pt. The DW velocity v_{DW} versus the angle ϕ_J at $T = 300$ K using the numerical collective coordinate model under a positive current with high density ($H_{DL} = 10$ mT). The calculations are performed at a negative \mathbf{H}_x , pointing to the left, with various amplitudes; $\mathbf{H}_x = 0$ (in blue), $\mathbf{H}_x = -50$ (in purple), $\mathbf{H}_x = -100$ (in green) and $\mathbf{H}_x = -150$ (in orange) (units of \mathbf{H}_x in mT). The DMI + SOT + CD mechanism is applied in the model for the up magnetic circular domain. At large \mathbf{H}_x , the asymmetric motion between the two DWs is reversed. In contrast, the asymmetric non-collinear DW motion remains qualitatively the same to that at low \mathbf{H}_x , the CD becomes the dominant mechanism as $|\mathbf{H}_x|$ increases. The shown data are the average of 5 different calculations from the numerical model.

A.2. The current-induced magnetic bubbles motion

In this section, we detail the different sets of parameters used to induce the coherent magnetic bubble motion in Pt/Co/Pt and Pt/Co/AlO_x. They are given for each injected current density for the different current/magnetization polarities. We accompany each case with a table giving statistics regarding the observed modes of the bubble motion.

A.2.1. Bubble motion in Pt/Co/Pt

A.2.1.1 Bubble motion under current $J \sim + 1.13 \cdot 10^{12}$ A.m⁻²

Up magnetic bubble

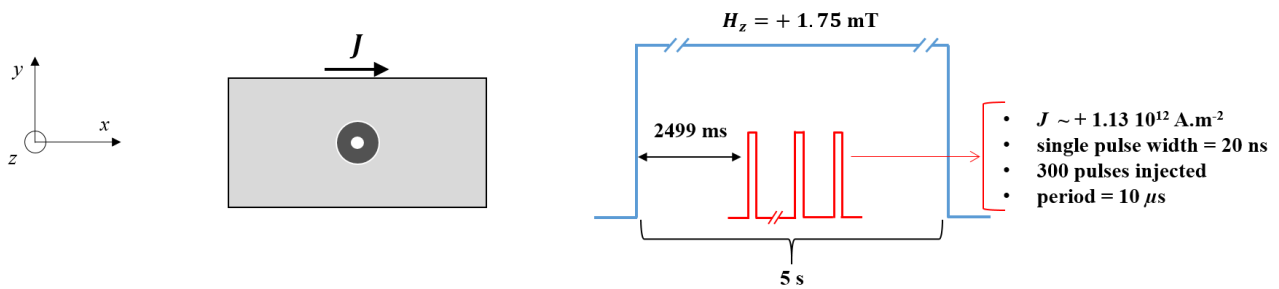


Figure A.8 A diagram summarizing the parameters for an up magnetic bubble motion under $J \sim + 1.13 \cdot 10^{12}$ A.m⁻² in Pt/Co/Pt

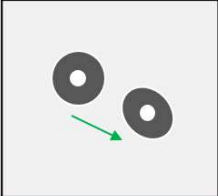
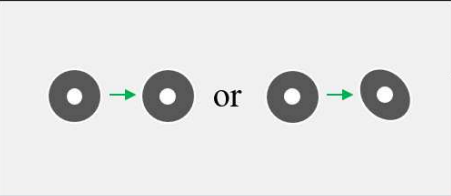
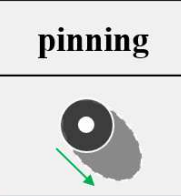
			pinning 
number of displacements	4	23	7
Percentage %	11	68	21

Table A.1 Summary of the up magnetic bubble motion under $J \sim +1.13 \cdot 10^{12} \text{ A.m}^{-2}$ in Pt/Co/Pt.

Down magnetic bubble

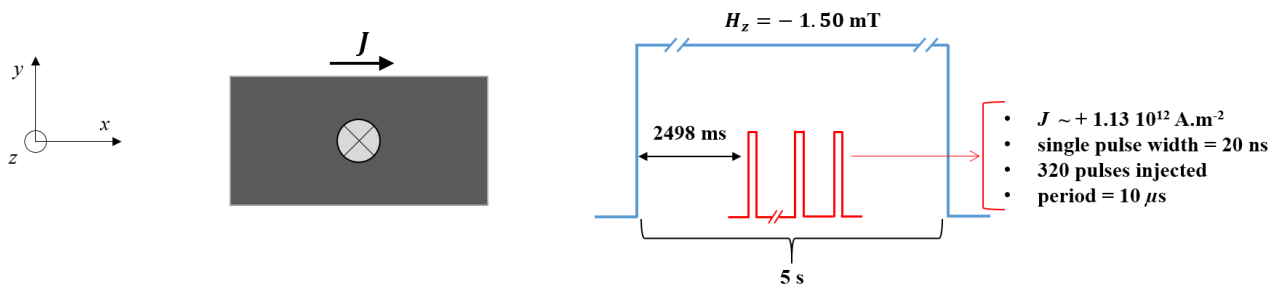


Figure A.9 A diagram summarizing the parameters for a down magnetic bubble motion under $J \sim +1.13 \cdot 10^{12} \text{ A.m}^{-2}$ in Pt/Co/Pt.

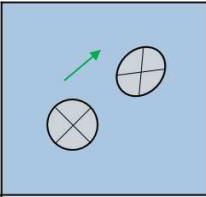
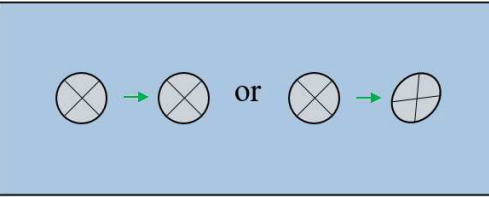
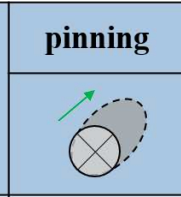
			pinning 
number of displacements	14	38	16
Percentage %	21	56	23

Table A.2 Summary of the down magnetic bubble motion under $J \sim +1.13 \cdot 10^{12} \text{ A.m}^{-2}$ in Pt/Co/Pt.

A.2.1.2. Bubble motion under current $J \sim -1.09 \cdot 10^{12} \text{ A.m}^{-2}$

Up magnetic bubble

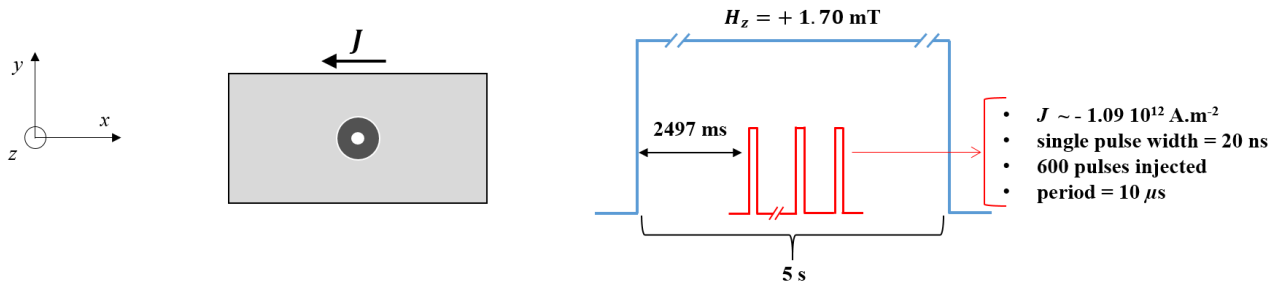


Figure A.10 A diagram summarizing the parameters for an up magnetic bubble motion under $J \sim -1.09 \cdot 10^{12} \text{ A.m}^{-2}$ in Pt/Co/Pt.

			pinning
number of displacements	26	13	15
Percentage %	48	24	27

Table A.3 Summary of the up magnetic bubble motion under $J \sim -1.09 \cdot 10^{12} \text{ A.m}^{-2}$ in Pt/Co/Pt.

Down magnetic bubble

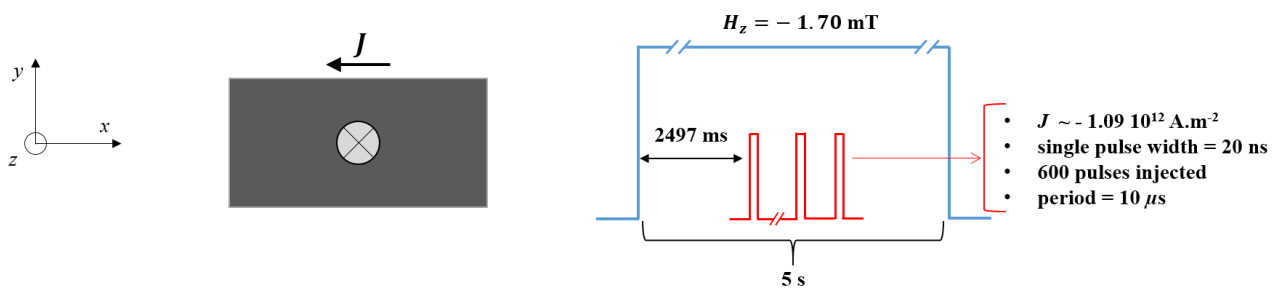


Figure A.11 A diagram summarizing the parameters for a down magnetic bubble motion under $J \sim -1.09 \cdot 10^{12} \text{ A.m}^{-2}$ in Pt/Co/Pt.

			pinning
number of displacements	9	18	18
Percentage %	20	40	40

Table A.4 Summary of the down magnetic bubble motion under $J \sim -1.09 \cdot 10^{12} \text{ A.m}^{-2}$ in Pt/Co/Pt.

A.2.1.3. Bubble motion under current $J \sim +1.93 \cdot 10^{12} \text{ A.m}^{-2}$

Up magnetic bubble

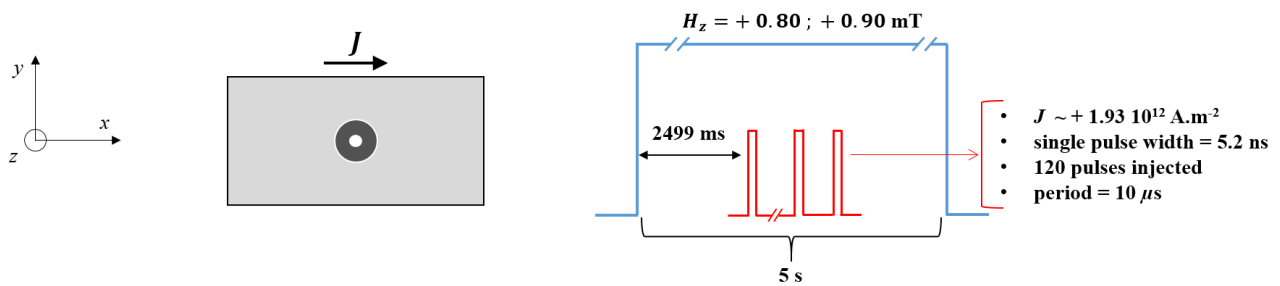


Figure A.12 A diagram summarizing the parameters for the up magnetic bubble motion under $J \sim +1.93 \cdot 10^{12} \text{ A.m}^{-2}$ in Pt/Co/Pt.

				pinning
number of displacements	0	7	28	4
Percentage %	0	18	72	10

Table A.5 Summary of the up magnetic bubble motion under $J \sim +1.93 \cdot 10^{12} \text{ A.m}^{-2}$ in Pt/Co/Pt.

Down magnetic bubble

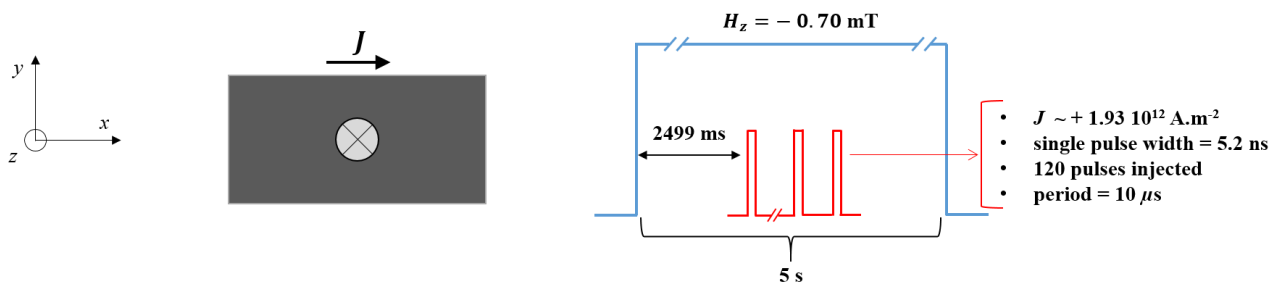


Figure A.13 A diagram summarizing the parameters for the down magnetic bubble motion under $J \sim +1.93 \cdot 10^{12} \text{ A.m}^{-2}$ in Pt/Co/Pt.

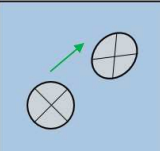
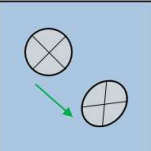
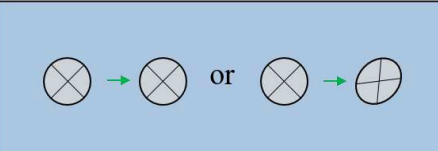
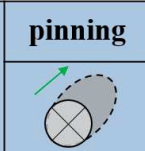
				pinning 
number of displacements	3	7	30	10
Percentage %	6	14	60	20

Table A.6 Summary of the down magnetic bubble motion under $J \sim + 1.93 \cdot 10^{12} \text{ A.m}^{-2}$ in Pt/Co/Pt.

A.2.1.4. Bubble motion under current $J \sim - 1.96 \cdot 10^{12} \text{ A.m}^{-2}$

Up magnetic bubble

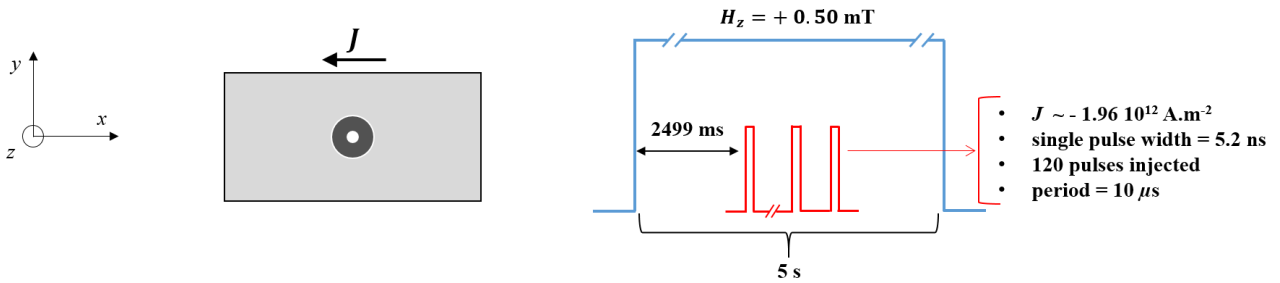


Figure A.14 A diagram summarizing the parameters for the up magnetic bubble motion under $J \sim - 1.96 \cdot 10^{12} \text{ A.m}^{-2}$ in Pt/Co/Pt.

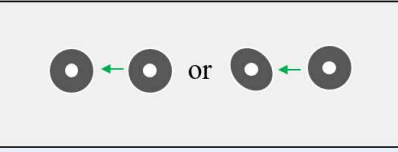
				pinning 
number of displacements	8	14	47	5
Percentage %	11	19	63	7

Table A.7 Summary of the up magnetic bubble motion under $J \sim - 1.96 \cdot 10^{12} \text{ A.m}^{-2}$ in Pt/Co/Pt.

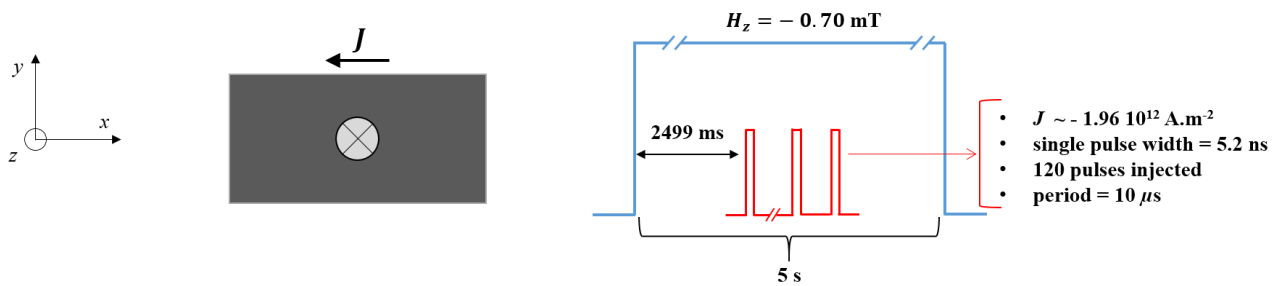
Down magnetic bubble

Figure A.15 A diagram summarizing the parameters for the down magnetic bubble motion under $J \sim -1.96 \cdot 10^{12} \text{ A.m}^{-2}$ in Pt/Co/Pt.

number of displacements	3	11	33	4
Percentage %	6	22	64	8

Table A.8 Summary of the down magnetic bubble motion under $J \sim -1.96 \cdot 10^{12} \text{ A.m}^{-2}$ in Pt/Co/Pt.

A.2.1.5. Bubble motion under current $J \sim +2.77 \cdot 10^{12} \text{ A.m}^{-2}$

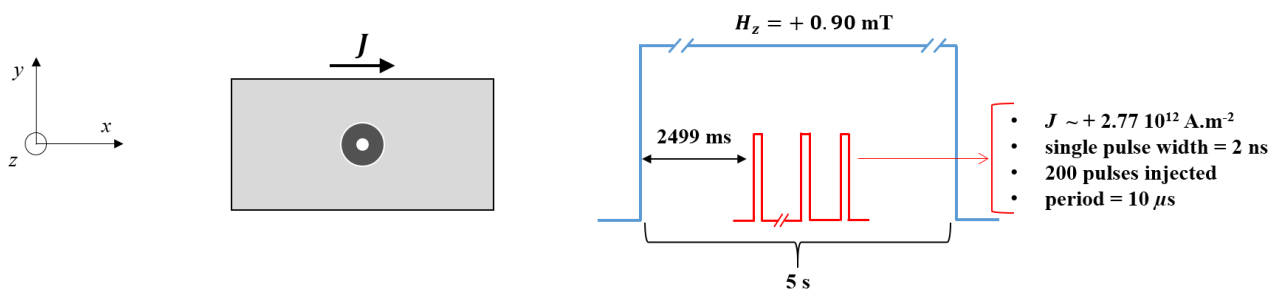
Up magnetic bubble

Figure A.16 A diagram summarizing the parameters for the up magnetic bubble motion under $J \sim +2.77 \cdot 10^{12} \text{ A.m}^{-2}$ in Pt/Co/Pt.

number of displacements	3	16	13	4
Percentage %	8	45	36	11

Table A.9 Summary of the up magnetic bubble motion under $J \sim +2.77 \cdot 10^{12} \text{ A.m}^{-2}$ in Pt/Co/Pt.

Down magnetic bubble

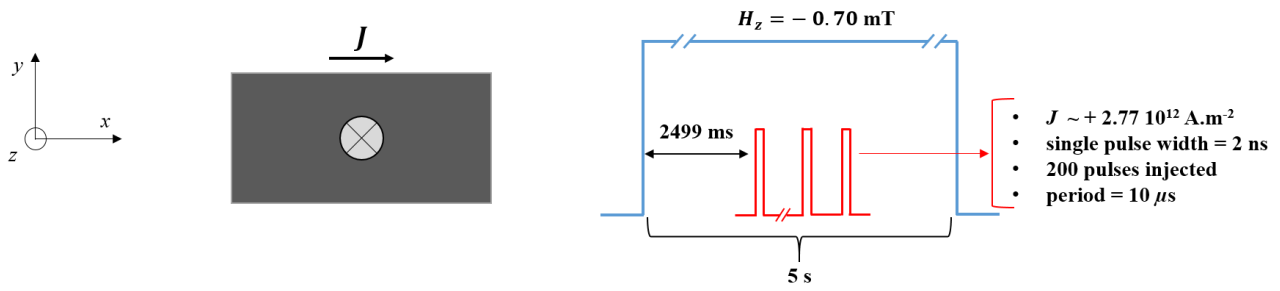


Figure A.17 A diagram summarizing the parameters for the down magnetic bubble motion under $J \sim + 2.77 \cdot 10^{12} \text{ A.m}^{-2}$ in Pt/Co/Pt.

				pinning
number of displacements	5	5	19	10
Percentage %	13	13	49	25

Table A.10 Summary of the down magnetic bubble motion under $J \sim + 2.77 \cdot 10^{12} \text{ A.m}^{-2}$ in Pt/Co/Pt.

A.2.1.6. Bubble motion under current $J \sim - 2.73 \cdot 10^{12} \text{ A.m}^{-2}$

Up magnetic bubble

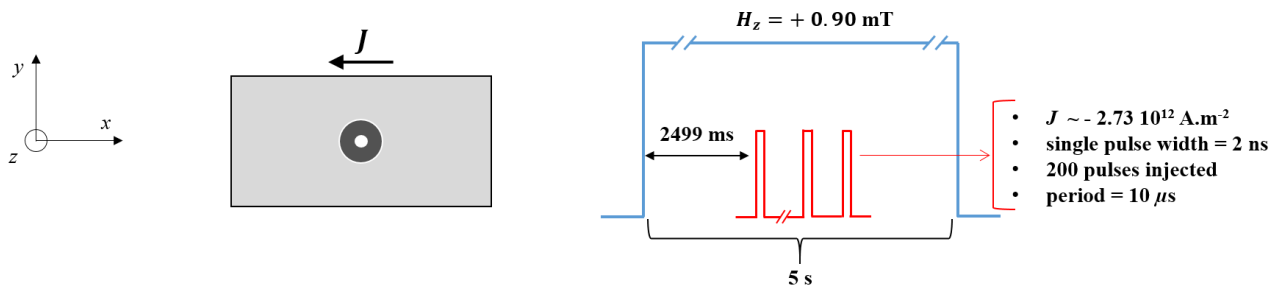


Figure A.18 A diagram summarizing the parameters for the up magnetic bubble motion under $J \sim - 2.73 \cdot 10^{12} \text{ A.m}^{-2}$ in Pt/Co/Pt.

				pinning
number of displacements	29	5	87	4
Percentage %	23	4	70	3

Table A.11 Summary of the up magnetic bubble motion under $J \sim - 2.73 \cdot 10^{12} \text{ A.m}^{-2}$ in Pt/Co/Pt.

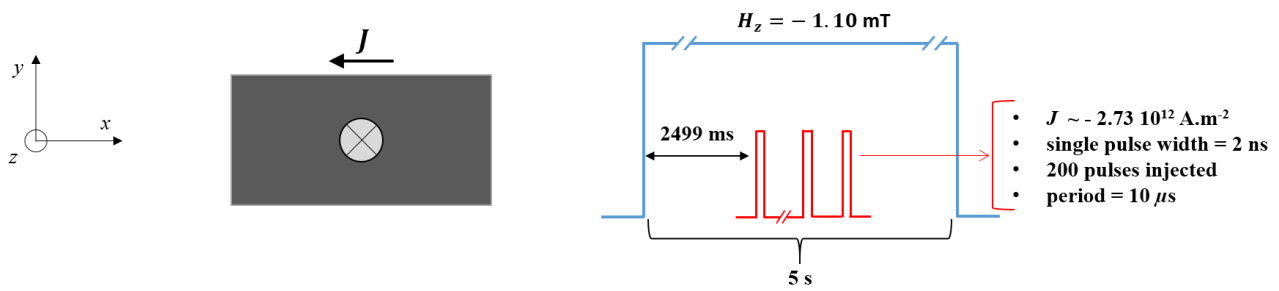
Down magnetic bubble

Figure A.19 A diagram summarizing the parameters for the down magnetic bubble motion under $J \sim -2.73 \cdot 10^{12} \text{ A.m}^{-2}$ in Pt/Co/Pt.

number of displacements	4	10	78	5
Percentage %	4	10	80	6

Table A.12 Summary of the down magnetic bubble motion under $J \sim -2.73 \cdot 10^{12} \text{ A.m}^{-2}$ in Pt/Co/Pt.

A.2.2. Bubble motion in Pt/Co/AlOx

A.2.2.1. Bubble motion under current $J \sim +0.88 \cdot 10^{12} \text{ A.m}^{-2}$

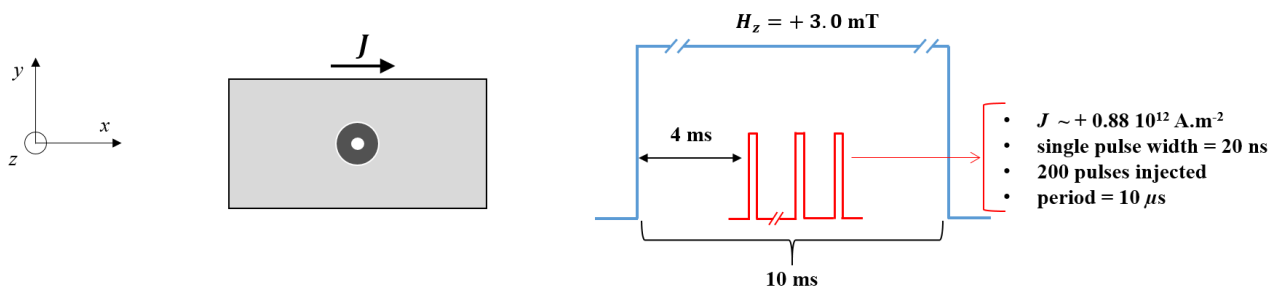
Up magnetic bubble

Figure A.20 A diagram summarizing the parameters for the up magnetic bubble motion under $J \sim +0.88 \cdot 10^{12} \text{ A.m}^{-2}$ in Pt/Co/AlOx.

			pinning
number of displacements	72	1	2
Percentage %	96	1	3

Table A.13 Summary of the up magnetic bubble motion under $J \sim + 0.88 \cdot 10^{12} \text{ A.m}^{-2}$ in Pt/Co/AlOx.

Down magnetic bubble

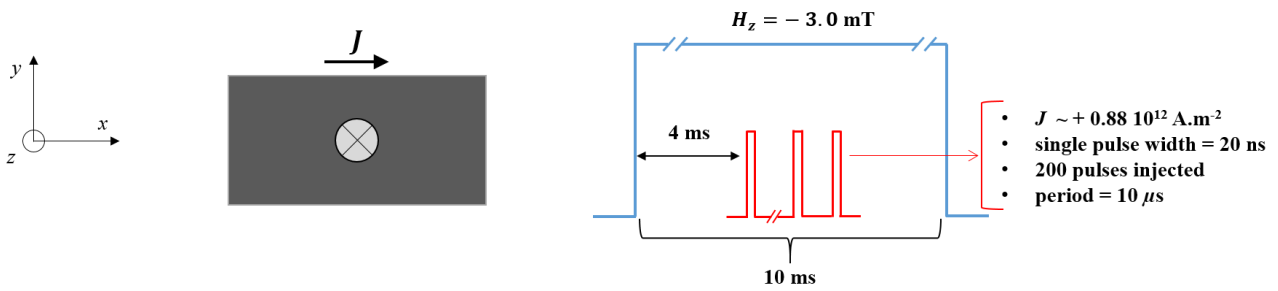


Figure A.21 A diagram summarizing the parameters for the down magnetic bubble motion under $J \sim + 0.88 \cdot 10^{12} \text{ A.m}^{-2}$ in Pt/Co/AlOx.

			pinning
number of displacements	32	1	0
Percentage %	97	3	0

Table A.14 Summary of the down magnetic bubble motion under $J \sim + 0.88 \cdot 10^{12} \text{ A.m}^{-2}$ in Pt/Co/AlOx.

A.2.2.2. Bubble motion under current $J \sim -0.86 \cdot 10^{12} \text{ A.m}^{-2}$

Up magnetic bubble

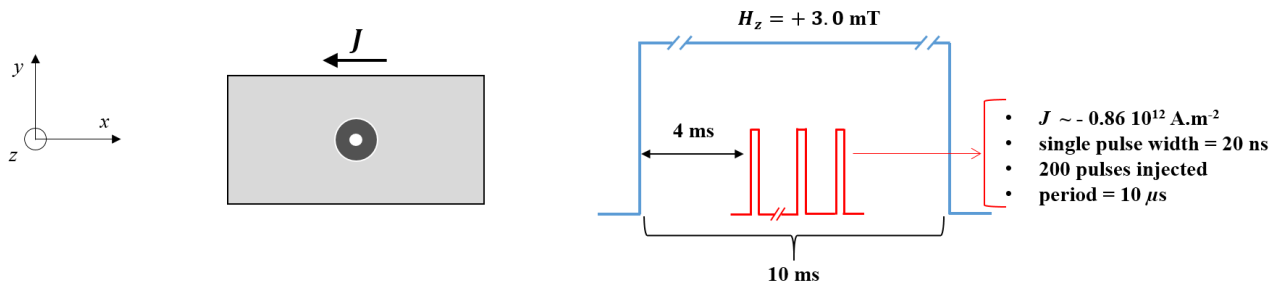


Figure A.22 A diagram summarizing the parameters for the up magnetic bubble motion under $J \sim -0.86 \cdot 10^{12} \text{ A.m}^{-2}$ in Pt/Co/AlOx.

number of displacements	90	0	0
Percentage %	100	0	0

Table A.15 Summary of the up magnetic bubble motion under $J \sim -0.86 \cdot 10^{12} \text{ A.m}^{-2}$ in Pt/Co/AlOx.

Down magnetic bubble

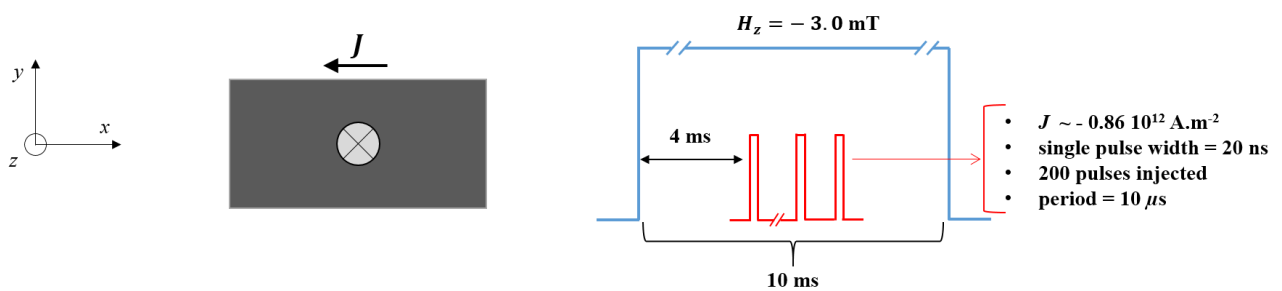


Figure A.23 A diagram summarizing the parameters for the up magnetic bubble motion under $J \sim -0.86 \cdot 10^{12} \text{ A.m}^{-2}$ in Pt/Co/AlOx.

			pinning
number of displacements	47	1	5
Percentage %	89	2	9

Table A.16 Summary of the down magnetic bubble motion under $J \sim -0.86 \cdot 10^{12} \text{ A.m}^{-2}$ in Pt/Co/AlOx.

A.2.2.3. Bubble motion under current $J \sim +1.95 \cdot 10^{12} \text{ A.m}^{-2}$

Up magnetic bubble

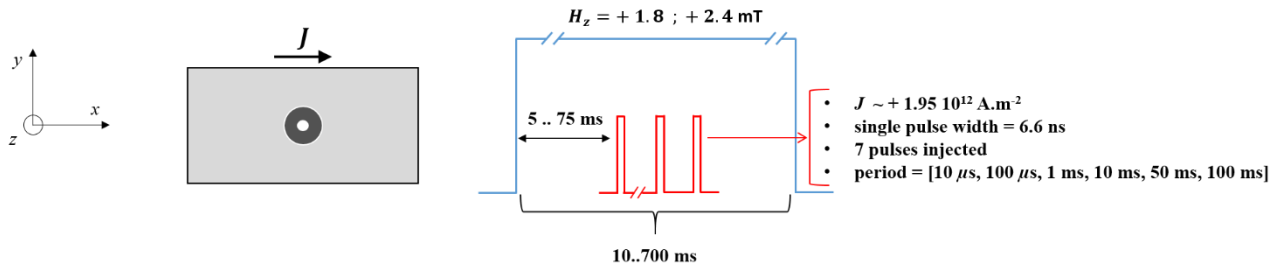


Figure A.24 A diagram summarizing the parameters for the up magnetic bubble motion under $J \sim +1.95 \cdot 10^{12} \text{ A.m}^{-2}$ in Pt/Co/AlOx.

			pinning
number of displacements	40	0	0
Percentage %	100	0	0

Table A.17 Summary of the up magnetic bubble motion under $J \sim +1.95 \cdot 10^{12} \text{ A.m}^{-2}$ in Pt/Co/AlOx.

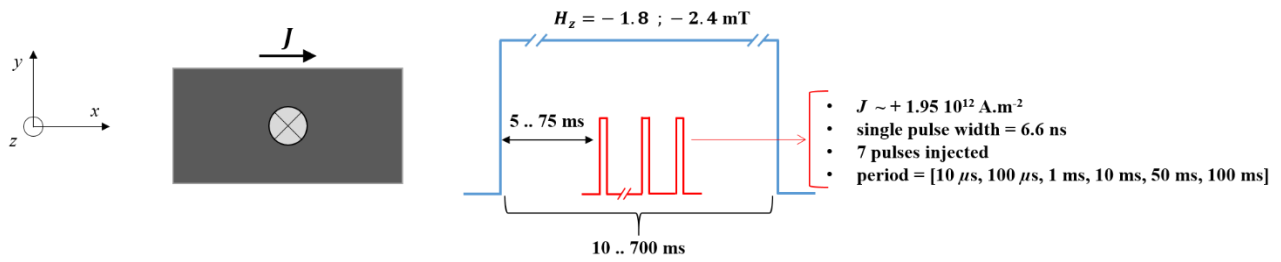
Down magnetic bubble

Figure A.25 A diagram summarizing the parameters for the down magnetic bubble motion under $J \sim +1.95 \cdot 10^{12} \text{ A.m}^{-2}$ in Pt/Co/AlOx.

			pinning
number of displacements	33	0	0
Percentage %	100	0	0

Table A.18 Summary of the down magnetic bubble motion under $J \sim +1.95 \cdot 10^{12} \text{ A.m}^{-2}$ in Pt/Co/AlOx.

A.2.2.4. Bubble motion under current $J \sim -1.95 \cdot 10^{12} \text{ A.m}^{-2}$

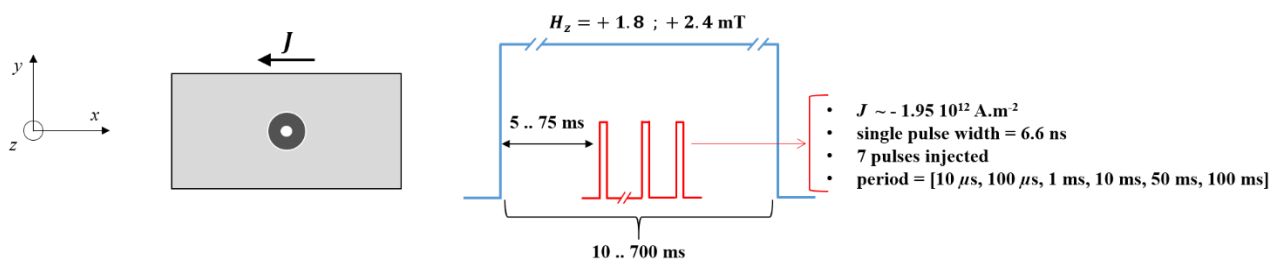
Up magnetic bubble

Figure A.26 A diagram summarizing the parameters for the up magnetic bubble motion under $J \sim -1.95 \cdot 10^{12} \text{ A.m}^{-2}$ in Pt/Co/AlOx.


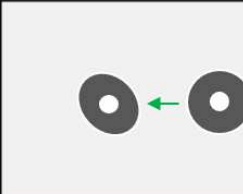
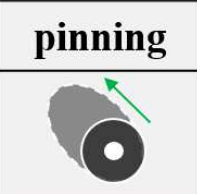
			pinning 
number of displacements	46	0	0
Percentage %	100	0	0

Table A.19 Summary of the up magnetic bubble motion under $J \sim -1.95 \cdot 10^{12} \text{ A.m}^{-2}$ in Pt/Co/AlOx.

Down magnetic bubble

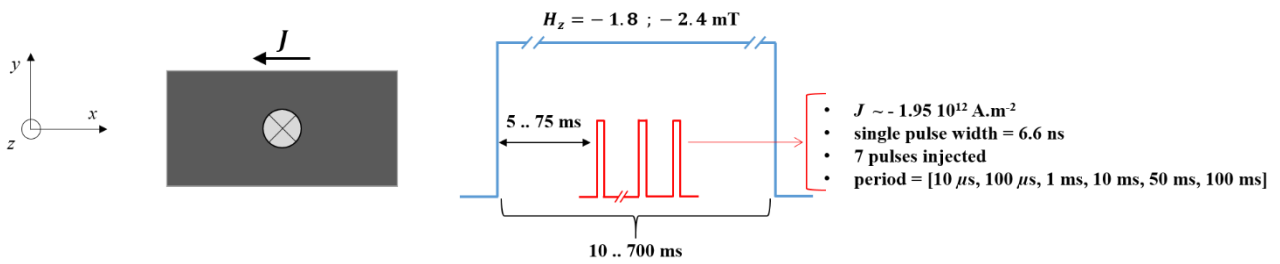


Figure A.27 A diagram summarizing the parameters for the down magnetic bubble motion under $J \sim -1.95 \cdot 10^{12} \text{ A.m}^{-2}$ in Pt/Co/AlOx.

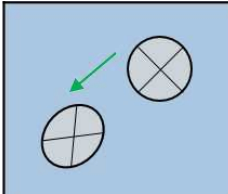
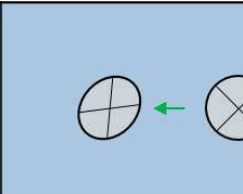
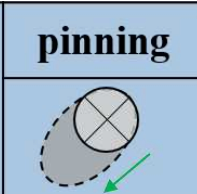
			pinning 
number of displacements	38	0	0
Percentage %	100	0	0

Table A.20 Summary of the down magnetic bubble motion under $J \sim -1.95 \cdot 10^{12} \text{ A.m}^{-2}$ in Pt/Co/AlOx.

A.2.2.5. Bubble motion under current $J \sim + 2.75 \cdot 10^{12} \text{ A.m}^{-2}$

Up magnetic bubble

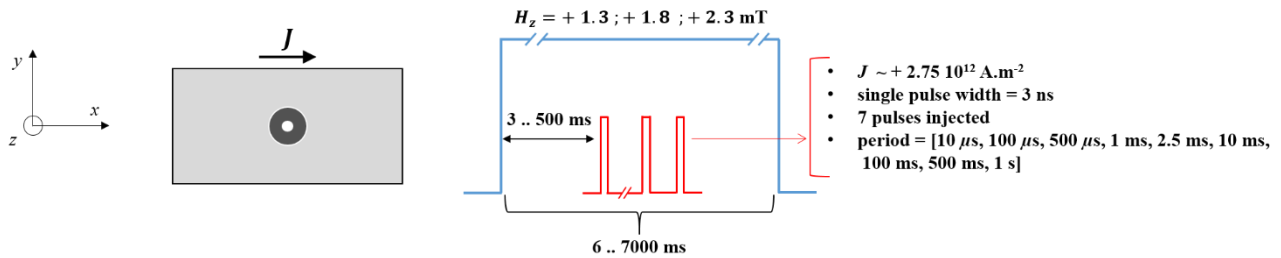


Figure A.28 A diagram summarizing the parameters for the up magnetic bubble motion under $J \sim + 2.75 \cdot 10^{12} \text{ A.m}^{-2}$ in Pt/Co/AlOx.

number of displacements	190	0
Percentage %	100	0

Table A.21 Summary of the up magnetic bubble motion under $J \sim + 2.75 \cdot 10^{12} \text{ A.m}^{-2}$ in Pt/Co/AlOx.

Down magnetic bubble

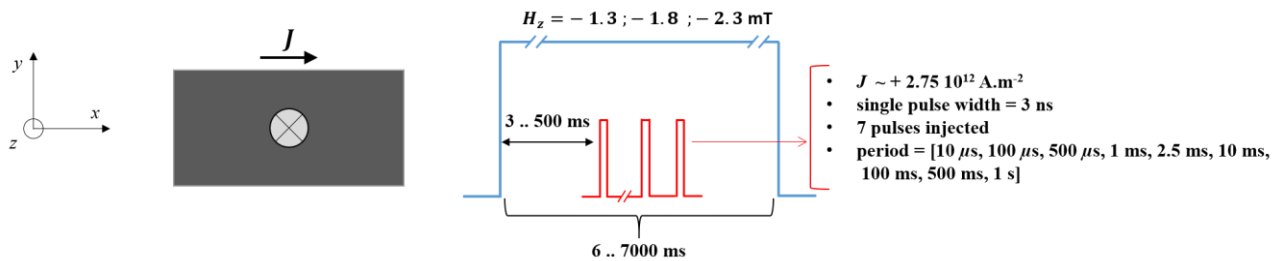


Figure A.29 A diagram summarizing the parameters for the down magnetic bubble motion under $J \sim + 2.75 \cdot 10^{12} \text{ A.m}^{-2}$ in Pt/Co/AlOx.

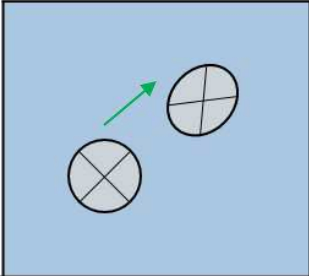
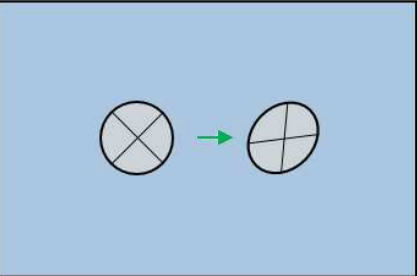
		
number of displacements	201	0
Percentage %	100	0

Table A.22 Summary of the down magnetic bubble motion under $J \sim + 2.75 \cdot 10^{12} \text{ A.m}^{-2}$ in Pt/Co/AlOx.

A.2.2.6. Bubble motion under current $J \sim - 2.75 \cdot 10^{12} \text{ A.m}^{-2}$

Up magnetic bubble

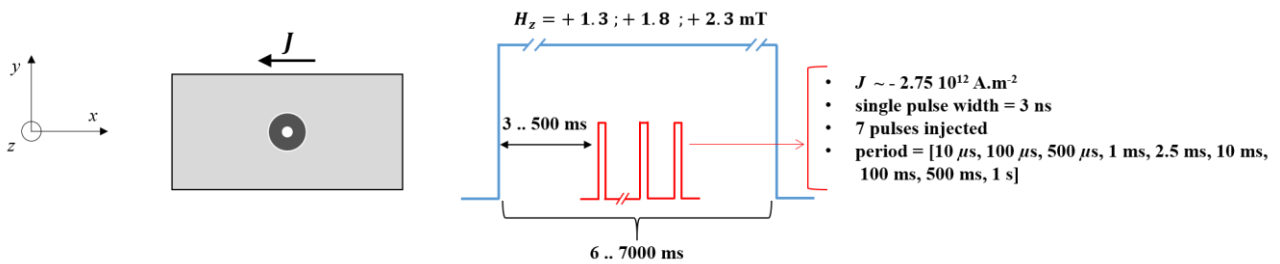


Figure A.30 A diagram summarizing the parameters for the up magnetic bubble motion under $J \sim - 2.75 \cdot 10^{12} \text{ A.m}^{-2}$ in Pt/Co/AlOx.

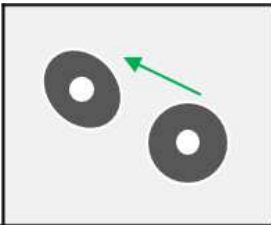
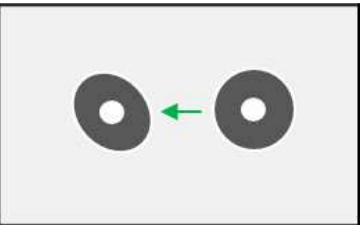
		
number of displacements	234	0
Percentage %	100	0

Table A.23 Summary of the up magnetic bubble motion under $J \sim - 2.75 \cdot 10^{12} \text{ A.m}^{-2}$ in Pt/Co/AlOx.

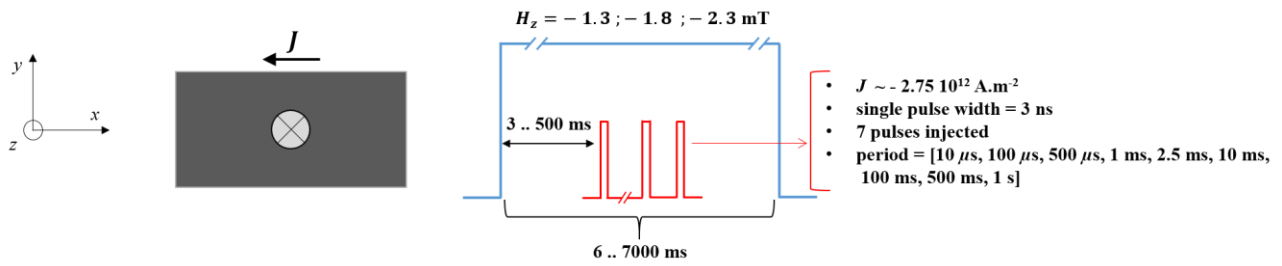
Down magnetic bubble

Figure A.31 A diagram summarizing the parameters for the down magnetic bubble motion under $J \sim -2.75 \cdot 10^{12} \text{ A.m}^{-2}$ in Pt/Co/AlOx.

number of displacements	209	0
Percentage %	100	0

Table A.24 Summary of the down magnetic bubble motion under $J \sim -2.75 \cdot 10^{12} \text{ A.m}^{-2}$ in Pt/Co/AlOx.

References

- Adam, J.-P. *et al.* (2009) ‘Nonadiabatic spin-transfer torque in (Ga,Mn)As with perpendicular anisotropy’, *Physical Review B*, 80(19), p. 193204. doi: 10.1103/PhysRevB.80.193204.
- Aharoni, A. (1998) ‘Demagnetizing factors for rectangular ferromagnetic prisms’, *Journal of Applied Physics*, 83(6), pp. 3432–3434. doi: 10.1063/1.367113.
- Ahn, S.-M. and Beach, G. S. D. (2013) ‘Crossover between in-plane and perpendicular anisotropy in Ta/Co x Fe 100- x /MgO films as a function of Co composition’, *Journal of Applied Physics*, 113(17), p. 17C112. doi: 10.1063/1.4799779.
- Ajejas, F. *et al.* (2017) ‘Tuning domain wall velocity with Dzyaloshinskii-Moriya interaction’, *Applied Physics Letters*, 111(20), p. 202402. doi: 10.1063/1.5005798.
- Akosa, C. A. *et al.* (2016) ‘Phenomenology of chiral damping in noncentrosymmetric magnets’, *Physical Review B*, 93(21), p. 214429. doi: 10.1103/PhysRevB.93.214429.
- Akosa, C. A. *et al.* (2018) ‘Theory of chiral effects in magnetic textures with spin-orbit coupling’, *Physical Review B*. American Physical Society, 98(18), p. 184424. doi: 10.1103/PhysRevB.98.184424.
- Alejos, O. *et al.* (2017) ‘Micromagnetic analysis of geometrically controlled current-driven magnetization switching’, *AIP Advances*, 7(5), p. 055909. doi: 10.1063/1.4973749.
- Ast, C. R. *et al.* (2007) ‘Giant Spin Splitting through Surface Alloying’, *Physical Review Letters*, 98(18), p. 186807. doi: 10.1103/PhysRevLett.98.186807.
- Balk, A. L. *et al.* (2017) ‘Simultaneous control of the Dzyaloshinskii-Moriya interaction and magnetic anisotropy in nanomagnetic trilayers’, *Physical Review Letters*, 119(7), p. 077205. doi: 10.1103/PhysRevLett.119.077205.
- Bandiera, S. *et al.* (2011) ‘Asymmetric Interfacial Perpendicular Magnetic Anisotropy in Pt/Co/Pt Trilayers’, *IEEE Magnetics Letters*, 2, pp. 3000504–3000504. doi: 10.1109/LMAG.2011.2174032.
- Barnes, S. E. and Maekawa, S. (2005) ‘Current-Spin Coupling for Ferromagnetic Domain Walls in Fine Wires’, *Physical Review Letters*, 95(10), p. 107204. doi: 10.1103/PhysRevLett.95.107204.
- Barnes, S. E. and Maekawa, S. (2007) ‘Generalization of Faraday’s Law to Include Nonconservative Spin Forces’, *Physical Review Letters*, 98(24), p. 246601. doi: 10.1103/PhysRevLett.98.246601.
- Baumgartner, M. *et al.* (2017) ‘Spatially and time-resolved magnetization dynamics driven by spin-orbit torques’, *Nature Nanotechnology*. Nature Publishing Group, 12(10), pp. 980–986. doi: 10.1038/nnano.2017.151.
- Baumgartner, M. and Gambardella, P. (2018) ‘Asymmetric velocity and tilt angle of domain walls induced by spin-orbit torques’, *Applied Physics Letters*, 113(24), p. 242402. doi: 10.1063/1.5063456.
- Belabbes, A. *et al.* (2016) ‘Hund’s Rule-Driven Dzyaloshinskii-Moriya Interaction at 3d-5d Interfaces’, *Physical Review Letters*, 117(24), p. 247202. doi: 10.1103/PhysRevLett.117.247202.
- Belmeguenai, M. *et al.* (2015) ‘Interfacial Dzyaloshinskii-Moriya interaction in perpendicularly magnetized Pt/Co/AlOx ultrathin films measured by Brillouin light spectroscopy’, *Physical Review B*, 91(18), p. 180405. doi: 10.1103/PhysRevB.91.180405.
- Berger, L. (1978) ‘Low-field magnetoresistance and domain drag in ferromagnets’, *Journal of*

- Applied Physics*, 49(3), pp. 2156–2161. doi: 10.1063/1.324716.
- Bernard-Mantel, A. *et al.* (2017) ‘The skyrmion-bubble transition in a ferromagnetic thin film’, 027. doi: 10.21468/SciPostPhys.4.5.027.
- Bhowmik, D. *et al.* (2015) ‘Deterministic Domain Wall Motion Orthogonal To Current Flow Due To Spin Orbit Torque.’, *Scientific reports*. Nature Publishing Group, 5, p. 11823. doi: 10.1038/srep11823.
- Bode, M. *et al.* (2007) ‘Chiral magnetic order at surfaces driven by inversion asymmetry’, *Nature*, 447(7141), pp. 190–193. doi: 10.1038/nature05802.
- Boulle, O. *et al.* (2013) ‘Domain Wall Tilting in the Presence of the Dzyaloshinskii-Moriya Interaction in Out-of-Plane Magnetized Magnetic Nanotracks’, *Physical Review Letters*, 111(21), p. 217203. doi: 10.1103/PhysRevLett.111.217203.
- Boulle, O. *et al.* (2014) ‘Current induced domain wall dynamics in the presence of spin orbit torques’, *Journal of Applied Physics*, 115(17), p. 17D502. doi: 10.1063/1.4860946.
- Boulle, O. *et al.* (2016) ‘Room-temperature chiral magnetic skyrmions in ultrathin magnetic nanostructures’, *Nature Nanotechnology*, 11(5), pp. 449–454. doi: 10.1038/nnano.2015.315.
- Braun, H.-B. (2018) ‘Solitons in Real Space: Domain Walls, Vortices, Hedgehogs, and Skyrmions’, in, pp. 1–40. doi: 10.1007/978-3-319-97334-0_1.
- Brown, W. F. (1963) ‘Thermal Fluctuations of a Single-Domain Particle’, *Physical Review*, 130(5), pp. 1677–1686. doi: 10.1103/PhysRev.130.1677.
- Burrowes, C. *et al.* (2013) ‘Low depinning fields in Ta-CoFeB-MgO ultrathin films with perpendicular magnetic anisotropy’, *Applied Physics Letters*, 103(18), p. 182401. doi: 10.1063/1.4826439.
- Buschow, K. H. J. and de Boer, F. R. (2003) *Physics of Magnetism and Magnetic Materials*, *Physics of Magnetism and Magnetic Materials*. Boston, MA: Springer US. doi: 10.1007/b100503.
- Büttner, F. *et al.* (2015) ‘Dynamics and inertia of skyrmionic spin structures’, *Nature Physics*, 11(3), pp. 225–228. doi: 10.1038/nphys3234.
- Cao, A. *et al.* (2017) ‘Tuning the Dzyaloshinskii-Moriya Interaction in Pt/Co/MgO heterostructures through MgO thickness’, *ArXiv e-prints*, (Dmi), pp. 1–18. doi: <http://arxiv.org/abs/1710.09051>.
- Cercellier, H. *et al.* (2006) ‘Interplay between structural, chemical, and spectroscopic properties of Ag/Au(111) epitaxial ultrathin films: A way to tune the Rashba coupling’, *Physical Review B*, 73(19), p. 195413. doi: 10.1103/PhysRevB.73.195413.
- Chen, G. *et al.* (2013) ‘Novel Chiral Magnetic Domain Wall Structure in Fe/Ni/(001) Films’, *Physical Review Letters*, 110(17), p. 177204. doi: 10.1103/PhysRevLett.110.177204.
- Chen, Gong *et al.* (2013) ‘Tailoring the chirality of magnetic domain walls by interface engineering’, *Nature Communications*, 4(1), p. 2671. doi: 10.1038/ncomms3671.
- Chen, G. (2018) ‘Magnetic Skyrmions in Thin Films’, in, pp. 117–150. doi: 10.1007/978-3-319-97334-0_4.
- Chenattukuzhiyil, S. (2016) *Study of domain wall dynamics in the presence of large spin-orbit coupling: chiral damping and magnetic origami*. Université de Grenoble. Available at: <https://tel.archives-ouvertes.fr/tel-01686487>.
- Cho, J. *et al.* (2015) ‘Thickness dependence of the interfacial Dzyaloshinskii–Moriya interaction in inversion symmetry broken systems’, *Nature Communications*, 6(1), p. 7635. doi: 10.1038/ncomms8635.

- Lo Conte, R. *et al.* (2017) ‘Ferromagnetic layer thickness dependence of the Dzyaloshinskii-Moriya interaction and spin-orbit torques in Pt/Co/AlO_x’, *AIP Advances*, 7(6), p. 065317. doi: 10.1063/1.4990694.
- Cormier, M. *et al.* (2010) ‘Effect of electrical current pulses on domain walls in Pt/Co/Pt nanotracks with out-of-plane anisotropy: Spin transfer torque versus Joule heating’, *Physical Review B*, 81(2), p. 024407. doi: 10.1103/PhysRevB.81.024407.
- Cortés-Ortuño, D. and Landeros, P. (2013) ‘Influence of the Dzyaloshinskii–Moriya interaction on the spin-wave spectra of thin films’, *Journal of Physics: Condensed Matter*, 25(15), p. 156001. doi: 10.1088/0953-8984/25/15/156001.
- Crépieux, A. and Lacroix, C. (1998) ‘Dzyaloshinsky–Moriya interactions induced by symmetry breaking at a surface’, *Journal of Magnetism and Magnetic Materials*, 182(3), pp. 341–349. doi: 10.1016/S0304-8853(97)01044-5.
- Demasius, K.-U. *et al.* (2016) ‘Enhanced spin–orbit torques by oxygen incorporation in tungsten films’, *Nature Communications*. Nature Publishing Group, 7(1), p. 10644. doi: 10.1038/ncomms10644.
- Dieny, B. and Chshiev, M. (2017) ‘Perpendicular magnetic anisotropy at transition metal/oxide interfaces and applications’, *Reviews of Modern Physics*, 89(2), p. 025008. doi: 10.1103/RevModPhys.89.025008.
- Drouard, M. (2014) *Etude de l'origine des couples magnétiques induits par le couplage spin-orbite dans des structures asymétriques à base de Co/Pt*. Université de Grenoble Alpes.
- Eduardo, M. *et al.* (2016) ‘Angular dependence of current-driven chiral walls’, *Applied Physics Express*, 9(6), p. 63008. doi: 10.7567/APEX.9.063008.
- Emori, S. *et al.* (2013) ‘Current-driven dynamics of chiral ferromagnetic domain walls.’, *Nature materials*, 12(7), pp. 611–6. doi: 10.1038/nmat3675.
- Emori, S., Bono, D. C. and Beach, G. S. D. (2012) ‘Interfacial current-induced torques in Pt/Co/GdO_x’, *Applied Physics Letters*, 101(4), p. 042405. doi: 10.1063/1.4737899.
- Everschor-Sitte, K. (2012) *Current-Induced Dynamics of Chiral Magnetic Structures, Skyrmions, Emergent Electrodynamics and Spin-Transfer Torques*. Universität zu Köln. Available at: https://kups.ub.uni-koeln.de/4811/1/Thesis_zum_Veroeffentlichen.pdf.
- Everschor-Sitte, K. and Sitte, M. (2014) ‘Real-space Berry phases: Skyrmion soccer (invited)’, *Journal of Applied Physics*, 115(17), p. 172602. doi: 10.1063/1.4870695.
- Fan, X. *et al.* (2013) ‘Observation of the nonlocal spin-orbital effective field’, *Nature Communications*. Nature Publishing Group, 4(1), p. 1799. doi: 10.1038/ncomms2709.
- Ferré, J. *et al.* (2013) ‘Universal magnetic domain wall dynamics in the presence of weak disorder’, *Comptes Rendus Physique*. Elsevier Masson SAS, 14(8), pp. 651–666. doi: 10.1016/j.crhy.2013.08.001.
- Ferriani, P. *et al.* (2008) ‘Atomic-Scale Spin Spiral with a Unique Rotational Sense: Mn Monolayer on W(001)’, *Physical Review Letters*, 101(2), p. 027201. doi: 10.1103/PhysRevLett.101.027201.
- Fert, A., Cros, V. and Sampaio, J. (2013) ‘Skyrmions on the track’, *Nature Nanotechnology*. Nature Publishing Group, 8(3), pp. 152–156. doi: 10.1038/nnano.2013.29.
- Fert, A. R. (1990) ‘Magnetic and Transport Properties of Metallic Multilayers’, *Materials Science Forum*, 59–60, pp. 439–480. doi: 10.4028/www.scientific.net/MSF.59-60.439.
- Freimuth, F., Blügel, S. and Mokrousov, Y. (2014) ‘Spin-orbit torques in Co/Pt(111) and

- Mn/W(001) magnetic bilayers from first principles', *Physical Review B*, 90(17), p. 174423. doi: 10.1103/PhysRevB.90.174423.
- Freimuth, F., Blügel, S. and Mokrousov, Y. (2017) 'Chiral damping, chiral gyromagnetism, and current-induced torques in textured one-dimensional Rashba ferromagnets', *Physical Review B*, 96(10), p. 104418. doi: 10.1103/PhysRevB.96.104418.
- Fukami, S. *et al.* (2011) 'Current-induced domain wall motion in perpendicularly magnetized CoFeB nanowire', *Applied Physics Letters*, 98(8), p. 082504. doi: 10.1063/1.3558917.
- Garanin, D. A. (1997) 'Fokker-Planck and Landau-Lifshitz-Bloch equations for classical ferromagnets', *Physical Review B*, 55(5), pp. 3050–3057. doi: 10.1103/PhysRevB.55.3050.
- Garate, I. *et al.* (2009) 'Nonadiabatic spin-transfer torque in real materials', *Physical Review B*, 79(10), p. 104416. doi: 10.1103/PhysRevB.79.104416.
- Garello, K. *et al.* (2013) 'Symmetry and magnitude of spin-orbit torques in ferromagnetic heterostructures.', *Nature nanotechnology*, 8(8), pp. 587–93. doi: 10.1038/nnano.2013.145.
- Gerrits, T. *et al.* (2006) 'Large-angle magnetization dynamics measured by time-resolved ferromagnetic resonance', *Physical Review B - Condensed Matter and Materials Physics*. doi: 10.1103/PhysRevB.73.094454.
- Gilbert, T. L. (2004) 'Classics in Magnetism A Phenomenological Theory of Damping in Ferromagnetic Materials', *IEEE Transactions on Magnetics*, 40(6), pp. 3443–3449. doi: 10.1109/TMAG.2004.836740.
- Gilmore, K., Idzerda, Y. U. and Stiles, M. D. (2008) 'Spin-orbit precession damping in transition metal ferromagnets (invited)', *Journal of Applied Physics*, 103(7), p. 07D303. doi: 10.1063/1.2832348.
- Gladii, O. *et al.* (2016) 'Frequency nonreciprocity of surface spin wave in permalloy thin films', *Physical Review B*, 93(5), p. 054430. doi: 10.1103/PhysRevB.93.054430.
- Gorchon, J. *et al.* (2014) 'Pinning-Dependent Field-Driven Domain Wall Dynamics and Thermal Scaling in an Ultrathin Magnetic Film', *Physical Review Letters*, 113(2), p. 027205. doi: 10.1103/PhysRevLett.113.027205.
- Gross, I. *et al.* (2016) 'Direct measurement of interfacial Dzyaloshinskii-Moriya interaction in X|CoFeB|MgO heterostructures with a scanning NV magnetometer (X=Ta,TaN, and W) DIRECT MEASUREMENT of INTERFACIAL ... I. GROSS *et al.*', *Physical Review B*, 94(6), p. 064413. doi: 10.1103/PhysRevB.94.064413.
- Guan, Y., Koyama, T. and Chiba, D. (2017) 'Current-induced magnetic domain wall motion in Pt/Co/Pd and Pd/Co/Pt structures with opposite sign of Dzyaloshinskii-Moriya interaction', *AIP Advances*, 7(8), p. 085123. doi: 10.1063/1.4986264.
- Haazen, P. P. J. *et al.* (2013) 'Domain wall depinning governed by the spin Hall effect.', *Nature materials*. Nature Publishing Group, 12(4), pp. 299–303. doi: 10.1038/nmat3553.
- Hals, K. M. D. and Brataas, A. (2014) 'Spin-orbit torques and anisotropic magnetization damping in skyrmion crystals', *Physical Review B*, 89(6), p. 064426. doi: 10.1103/PhysRevB.89.064426.
- Haney, P. M. *et al.* (2013) 'Current induced torques and interfacial spin-orbit coupling: Semiclassical modeling', *Physical Review B*, 87(17), p. 174411. doi: 10.1103/PhysRevB.87.174411.
- Hao, Q., Chen, W. and Xiao, G. (2015) 'Beta (β) tungsten thin films: Structure, electron transport, and giant spin Hall effect', *Applied Physics Letters*, 106(18), p. 182403. doi: 10.1063/1.4919867.

- Hayashi, M. *et al.* (2008) ‘Current-Controlled Magnetic Domain-Wall Nanowire Shift Register’, *Science*, 320(5873), pp. 209–211. doi: 10.1126/science.1154587.
- Heide, M., Bihlmayer, G. and Blügel, S. (2008) ‘Dzyaloshinskii-Moriya interaction accounting for the orientation of magnetic domains in ultrathin films: Fe/W(110)’, *Physical Review B*, 78(14), p. 140403. doi: 10.1103/PhysRevB.78.140403.
- Heinze, S. *et al.* (2011) ‘Spontaneous atomic-scale magnetic skyrmion lattice in two dimensions’, *Nature Physics*. Nature Publishing Group, 7(9), pp. 713–718. doi: 10.1038/nphys2045.
- Hervé, M. *et al.* (2018) ‘Stabilizing spin spirals and isolated skyrmions at low magnetic field exploiting vanishing magnetic anisotropy’, *Nature Communications*. Springer US, 9(1), p. 2198. doi: 10.1038/s41467-018-04680-0.
- Hirata, Y. *et al.* (2019) ‘Vanishing skyrmion Hall effect at the angular momentum compensation temperature of a ferrimagnet’, *Nature Nanotechnology*, 14(3), pp. 232–236. doi: 10.1038/s41565-018-0345-2.
- Hirsch, J. E. (1999) ‘Spin Hall Effect’, *Physical Review Letters*, 83(9), pp. 1834–1837. doi: 10.1103/PhysRevLett.83.1834.
- Hrabec, A. *et al.* (2014) ‘Measuring and tailoring the Dzyaloshinskii-Moriya interaction in perpendicularly magnetized thin films’, *Physical Review B*, 90(2), p. 020402. doi: 10.1103/PhysRevB.90.020402.
- Hrabec, A. *et al.* (2017) ‘Current-induced skyrmion generation and dynamics in symmetric bilayers’, *Nature Communications*, 8(1), p. 15765. doi: 10.1038/ncomms15765.
- Hubert, A. and Schäfer, R. (2009) ‘1.1 What are Magnetic Domains?’, in *Magnetic Domains: The Analysis of Magnetic Microstructures*.
- I.E.Dzialoshinskii (1957) ‘Thermodynamic Theory of “Weak” Ferromagnetism In Antiferromagnetic Substances’, *Soviet Physics JETP*, 5(6), pp. 1259–1272.
- Iwasaki, J., Mochizuki, M. and Nagaosa, N. (2013) ‘Universal current-velocity relation of skyrmion motion in chiral magnets’, *Nature Communications*, 4(1), p. 1463. doi: 10.1038/ncomms2442.
- Je, S.-G. *et al.* (2013) ‘Asymmetric magnetic domain-wall motion by the Dzyaloshinskii-Moriya interaction’, *Physical Review B*, 88(21), p. 214401. doi: 10.1103/PhysRevB.88.214401.
- Je, S.-G. *et al.* (2017) ‘Emergence of Huge Negative Spin-Transfer Torque in Atomically Thin Co layers’, *Physical Review Letters*, 118(16), p. 167205. doi: 10.1103/PhysRevLett.118.167205.
- Jiang, W. *et al.* (2015) ‘Blowing magnetic skyrmion bubbles’, *Science*, 349(6245), pp. 283–286. doi: 10.1126/science.aaa1442.
- Jiang, W. *et al.* (2017) ‘Direct observation of the skyrmion Hall effect’, *Nature Physics*, 13(2), pp. 162–169. doi: 10.1038/nphys3883.
- Jué, E. (2013) *Dynamique du déplacement de parois magnétiques dans les couches ultra-minces à forte interaction spin-orbite*. Université de Grenoble. Available at: <https://hal.archives-ouvertes.fr/tel-01022827/>.
- Jué, E. *et al.* (2015) ‘Chiral damping of magnetic domain walls’, *Nature Materials*, 15(3), pp. 272–277. doi: 10.1038/nmat4518.
- Jué, E. *et al.* (2016) ‘Domain wall dynamics in ultrathin Pt/Co/AlO_x microstrips under large combined magnetic fields’, *Physical Review B*, 93(1), p. 014403. doi: 10.1103/PhysRevB.93.014403.
- Juge, R. *et al.* (2019) ‘Current-driven dynamics of magnetic skyrmions in an ultrathin film:

- experiments and modelling'. Available at: <http://arxiv.org/abs/1904.08275>.
- Kabanov, Y. P. *et al.* (2010) 'In-Plane Field Effects on the Dynamics of Domain Walls in Ultrathin Co Films With Perpendicular Anisotropy', *IEEE Transactions on Magnetics*, 46(6), pp. 2220–2223. doi: 10.1109/TMAG.2010.2045740.
- Karnad, G. V. *et al.* (2018) 'Modification of Dzyaloshinskii-Moriya-Interaction-Stabilized Domain Wall Chirality by Driving Currents', *Physical Review Letters*, 121(14), p. 147203. doi: 10.1103/PhysRevLett.121.147203.
- Kashid, V. *et al.* (2014) 'Dzyaloshinskii-Moriya interaction and chiral magnetism in 3 d – 5 d zigzag chains: Tight-binding model and ab initio calculations', *Physical Review B*, 90(5), p. 054412. doi: 10.1103/PhysRevB.90.054412.
- Kato, Y. K. *et al.* (2004) 'Current-Induced Spin Polarization in Strained Semiconductors', *Physical Review Letters*, 93(17), p. 176601. doi: 10.1103/PhysRevLett.93.176601.
- Kato, Y. K. (2004) 'Observation of the Spin Hall Effect in Semiconductors', *Science*, 306(5703), pp. 1910–1913. doi: 10.1126/science.1105514.
- Khan, R. A. *et al.* (2016) 'Effect of annealing on the interfacial Dzyaloshinskii-Moriya interaction in Ta/CoFeB/MgO trilayers', *Applied Physics Letters*, 109(13), p. 132404. doi: 10.1063/1.4963731.
- Kim, D.-Y., Park, M.-H., Park, Y.-K., Kim, J.-S., Nam, Yune-Seok, *et al.* (2018) 'Chirality-induced antisymmetry in magnetic domain wall speed', *NPG Asia Materials*. Nature Publishing Group, 10(1), p. e464. doi: 10.1038/am.2017.216.
- Kim, D.-Y., Park, M.-H., Park, Y.-K., Yu, J.-S., *et al.* (2018) 'Huge domain-wall speed variation with respect to ferromagnetic layer thickness in ferromagnetic Pt/Co/TiO₂/Pt films', *Applied Physics Letters*, 112(6), p. 062406. doi: 10.1063/1.5009726.
- Kim, D.-Y., Park, M.-H., Park, Y.-K., Kim, J.-S., Nam, Yoon-Seok, *et al.* (2018) 'Magnetic domain-wall tilting due to domain-wall speed asymmetry', *Physical Review B*. American Physical Society, 97(13), p. 134407. doi: 10.1103/PhysRevB.97.134407.
- Kim, D.-Y., Kim, N.-H., *et al.* (2018) 'Quantitative agreement of Dzyaloshinskii-Moriya interactions for domain-wall motion and spin-wave propagation'. Available at: <http://arxiv.org/abs/1810.04375>.
- Kim, J.-S., Nam, Yune-Seok, Kim, D.-Y., Park, Y.-K., Park, Min-Ho and Choe, S.-B. (2018) 'Comparison between spin-orbit torques measured by domain-wall motions and harmonic measurements', *AIP Advances*, 8(5), p. 056009. doi: 10.1063/1.5006868.
- Kim, J.-V. (2015) 'Role of nonlinear anisotropic damping in the magnetization dynamics of topological solitons', *Physical Review B*, 92(1), p. 014418. doi: 10.1103/PhysRevB.92.014418.
- Kim, J.-V. and Yoo, M.-W. (2017) 'Current-driven skyrmion dynamics in disordered films', *Applied Physics Letters*, 110(13), p. 132404. doi: 10.1063/1.4979316.
- Kim, J. *et al.* (2013) 'Layer thickness dependence of the current-induced effective field vector in Ta|CoFeB|MgO', *Nature Materials*, 12(3), pp. 240–245. doi: 10.1038/nmat3522.
- Kim, K.-J. *et al.* (2010) 'Electric Control of Multiple Domain Walls in Pt/Co/Pt Nanotracks with Perpendicular Magnetic Anisotropy', *Applied Physics Express*, 3(8), p. 083001. doi: 10.1143/APEX.3.083001.
- Kim, K.-W., Seo, S.-M., *et al.* (2012) 'Magnetization dynamics induced by in-plane currents in ultrathin magnetic nanostructures with Rashba spin-orbit coupling', *Physical Review B*, 85(18), p. 180404. doi: 10.1103/PhysRevB.85.180404.

- Kim, K.-W., Moon, J.-H., *et al.* (2012) ‘Prediction of Giant Spin Motive Force due to Rashba Spin-Orbit Coupling’, *Physical Review Letters*, 108(21), p. 217202. doi: 10.1103/PhysRevLett.108.217202.
- Kim, K.-W. *et al.* (2013) ‘Chirality from Interfacial Spin-Orbit Coupling Effects in Magnetic Bilayers’, *Physical Review Letters*, 111(21), p. 216601. doi: 10.1103/PhysRevLett.111.216601.
- Kim, K.-W., Lee, Hyun-Woo, Lee, K.-J., Everschor-Sitte, K., Gomony, Olena and Sinova, J. (2018) ‘Roles of chiral renormalization on magnetization dynamics in chiral magnets’, *Physical Review B*. American Physical Society, 97(10), p. 100402. doi: 10.1103/PhysRevB.97.100402.
- Kim, N.-H. *et al.* (2015) ‘Improvement of the interfacial Dzyaloshinskii-Moriya interaction by introducing a Ta buffer layer’, *Applied Physics Letters*, 107(14), p. 142408. doi: 10.1063/1.4932550.
- Kläui, M. *et al.* (2005) ‘Controlled and Reproducible Domain Wall Displacement by Current Pulses Injected into Ferromagnetic Ring Structures’, *Physical Review Letters*, 94(10), p. 106601. doi: 10.1103/PhysRevLett.94.106601.
- Koyama, T. *et al.* (2011) ‘Observation of the intrinsic pinning of a magnetic domain wall in a ferromagnetic nanowire.’, *Nature materials*. Nature Publishing Group, 10(3), pp. 194–7. doi: 10.1038/nmat2961.
- Koyama, T. *et al.* (2013) ‘Current-Induced Magnetic Domain Wall Motion in a Co/Ni Nanowire with Structural Inversion Asymmetry’, *Applied Physics Express*, 6(3), p. 033001. doi: 10.7567/APEX.6.033001.
- Krupin, O. *et al.* (2005) ‘Rashba effect at magnetic metal surfaces’, *Physical Review B*, 71(20), p. 201403. doi: 10.1103/PhysRevB.71.201403.
- Kuświk, P. *et al.* (2018) ‘Asymmetric domain wall propagation caused by interfacial Dzyaloshinskii-Moriya interaction in exchange biased Au/Co/NiO layered system’, *Physical Review B*, 97(2), p. 024404. doi: 10.1103/PhysRevB.97.024404.
- Kwon, J. *et al.* (2017) ‘Asymmetrical domain wall propagation in bifurcated PMA wire structure due to the Dzyaloshinskii-Moriya interaction’, *Applied Physics Letters*, 110(23). doi: 10.1063/1.4984750.
- L. LANDAU, E. L. (1935) ‘On the theory of dispersion of magnetic permeability in ferromagnetic bodies’, *Phys. Zeitsch. der Sow.*, 8, pp. 153–169. Available at: <http://www.ujp.bitp.kiev.ua/files/journals/53/si/53SI06p.pdf>.
- Lacour, D. *et al.* (2007) ‘Magnetic properties of postoxidized Pt/Co/Al layers with perpendicular anisotropy’, *Applied Physics Letters*, 90(19), p. 192506. doi: 10.1063/1.2734378.
- Lacy, F. (2011) ‘Developing a theoretical relationship between electrical resistivity, temperature, and film thickness for conductors’, *Nanoscale Research Letters*, 6, pp. 1–26. doi: 10.1186/1556-276X-6-636.
- Lambert, C.-H. *et al.* (2014) ‘All-optical control of ferromagnetic thin films and nanostructures’, *Science*, 345(6202), pp. 1337–1340. doi: 10.1126/science.1253493.
- LaShell, S., McDougall, B. A. and Jensen, E. (1996) ‘Spin Splitting of an Au(111) Surface State Band Observed with Angle Resolved Photoelectron Spectroscopy’, *Physical Review Letters*, 77(16), pp. 3419–3422. doi: 10.1103/PhysRevLett.77.3419.
- Lau, D. *et al.* (2016) ‘Energetic molding of chiral magnetic bubbles’, *Physical Review B*, 94(6), p. 060401. doi: 10.1103/PhysRevB.94.060401.
- Lau, D. *et al.* (2018) ‘Disentangling factors governing Dzyaloshinskii domain-wall creep in Co/Ni

- thin films using Pt_xIr_{1-x} seed layers', *Physical Review B*, 98(18), p. 184410. doi: 10.1103/PhysRevB.98.184410.
- Lavrijsen, R. *et al.* (2012) 'Asymmetric Pt/Co/Pt-stack induced sign-control of current-induced magnetic domain-wall creep', *Applied Physics Letters*, 100(26), p. 262408. doi: 10.1063/1.4732083.
- Lavrijsen, R. *et al.* (2015) 'Asymmetric magnetic bubble expansion under in-plane field in Pt/Co/Pt: Effect of interface engineering', *Physical Review B*, 91(10), p. 104414. doi: 10.1103/PhysRevB.91.104414.
- Lee, H.-R. *et al.* (2015) 'Spin-orbit torque in a bulk perpendicular magnetic anisotropy Pd/FePd/MgO system', *Scientific Reports*, 4(1), p. 6548. doi: 10.1038/srep06548.
- Lee, J.-C. *et al.* (2011) 'Universality Classes of Magnetic Domain Wall Motion', *Physical Review Letters*, 107(6), p. 067201. doi: 10.1103/PhysRevLett.107.067201.
- Lee, J. *et al.* (2010) 'Roles of adiabatic and nonadiabatic spin transfer torques on magnetic domain wall motion', *Arxiv*, p. 1006.1216.
- Legrand, W. *et al.* (2017) 'Room-Temperature Current-Induced Generation and Motion of sub-100 nm Skyrmions', *Nano Letters*, 17(4), pp. 2703–2712. doi: 10.1021/acs.nanolett.7b00649.
- Lemerle, S. *et al.* (1998) 'Domain Wall Creep in an Ising Ultrathin Magnetic Film', *Physical Review Letters*, 80(4), pp. 849–852. doi: 10.1103/PhysRevLett.80.849.
- Leroux, M. *et al.* (2018) 'Skyrmion Lattice Topological Hall Effect near Room Temperature', *Scientific Reports*, 8(1), p. 15510. doi: 10.1038/s41598-018-33560-2.
- Levy, R. L., Fanter, D. L. and Wolf, C. J. (1972) 'Temperature Rise Time and True Pyrolysis Temperature in Pulse Mode Pyrolysis Gas Chromatography', *Analytical Chemistry*, 44(1), pp. 38–42. doi: 10.1021/ac60309a008.
- Litzius, K. *et al.* (2017) 'Skyrmion Hall effect revealed by direct time-resolved X-ray microscopy', *Nature Physics*, 13(2), pp. 170–175. doi: 10.1038/nphys4000.
- Liu, L. *et al.* (2011) 'Spin-Torque Ferromagnetic Resonance Induced by the Spin Hall Effect', *Physical Review Letters*, 106(3), p. 036601. doi: 10.1103/PhysRevLett.106.036601.
- Liu, L., Lee, O. J., *et al.* (2012) 'Current-Induced Switching of Perpendicularly Magnetized Magnetic Layers Using Spin Torque from the Spin Hall Effect', *Physical Review Letters*, 109(9), p. 096602. doi: 10.1103/PhysRevLett.109.096602.
- Liu, L., Pai, C.-F., *et al.* (2012) 'Spin-Torque Switching with the Giant Spin Hall Effect of Tantalum', *Science*, 336(6081), pp. 555–558. doi: 10.1126/science.1218197.
- Liu, T., Cai, J. W. and Sun, L. (2012) 'Large enhanced perpendicular magnetic anisotropy in CoFeB/MgO system with the typical Ta buffer replaced by an Hf layer', *AIP Advances*, 2(3), p. 032151. doi: 10.1063/1.4748337.
- Maccariello, D. *et al.* (2018) 'Electrical detection of single magnetic skyrmions in metallic multilayers at room temperature', *Nature Nanotechnology*, 13(3), pp. 233–237. doi: 10.1038/s41565-017-0044-4.
- Malozemoff, A. P. and Slonczewski, J. C. (1979) 'Wall Dynamics in One Dimension', in *Magnetic Domain Walls in Bubble Materials*. Elsevier, pp. 123–143. doi: 10.1016/B978-0-12-002951-8.50009-1.
- Manchon, A. *et al.* (2008) 'Analysis of oxygen induced anisotropy crossover in Pt/Co/MO_x trilayers', *Journal of Applied Physics*, 104(4), p. 043914. doi: 10.1063/1.2969711.

- Manchon, A *et al.* (2008) ‘X-ray analysis of the magnetic influence of oxygen in Pt/Co/AlO_x trilayers’, *Journal of Applied Physics*, 103(7), p. 07A912. doi: 10.1063/1.2829896.
- Manchon, A. and Zhang, S. (2008) ‘Theory of nonequilibrium intrinsic spin torque in a single nanomagnet’, *Physical Review B*, 78(21), p. 212405. doi: 10.1103/PhysRevB.78.212405.
- Martinez, E. *et al.* (2007) ‘Thermal effects in domain wall motion: Micromagnetic simulations and analytical model’, *Physical Review B*, 75(17), p. 174409. doi: 10.1103/PhysRevB.75.174409.
- Martinez, E. *et al.* (2014) ‘Current-driven dynamics of Dzyaloshinskii domain walls in the presence of in-plane fields: Full micromagnetic and one-dimensional analysis’, *Journal of Applied Physics*, 115(21). doi: 10.1063/1.4881778.
- Meckler, S. *et al.* (2009) ‘Real-Space Observation of a Right-Rotating Inhomogeneous Cycloidal Spin Spiral by Spin-Polarized Scanning Tunneling Microscopy in a Triple Axes Vector Magnet’, *Physical Review Letters*, 103(15), p. 157201. doi: 10.1103/PhysRevLett.103.157201.
- Metaxas, P. J. *et al.* (2007) ‘Creep and Flow Regimes of Magnetic Domain-Wall Motion in Ultrathin $\text{Pt}/\text{Co}/\text{Pt}$ Films with Perpendicular Anisotropy’, *Physical Review Letters*, 99(21), p. 217208. doi: 10.1103/PhysRevLett.99.217208.
- Miron, I. M. *et al.* (2009) ‘Domain Wall Spin Torquemeter’, *Physical Review Letters*, 102(13), p. 137202. doi: 10.1103/PhysRevLett.102.137202.
- Miron, I. M. (2009) *Etude de l'interaction entre un courant polarisé en spin et une paroi de domaine magnétique dans des matériaux à aimantation perpendiculaire*. Université Grenoble Alpes. Available at: <http://www.theses.fr/2009GRE10054>.
- Miron, I. M. *et al.* (2010) ‘Current-driven spin torque induced by the Rashba effect in a ferromagnetic metal layer.’, *Nature materials*. Nature Publishing Group, 9(3), pp. 230–234. doi: 10.1038/nmat2613.
- Miron, I. M., Moore, T., *et al.* (2011) ‘Fast current-induced domain-wall motion controlled by the Rashba effect.’, *Nature materials*. Nature Publishing Group, 10(6), pp. 419–423. doi: 10.1038/nmat3020.
- Miron, I. M., Garello, K., *et al.* (2011) ‘Perpendicular switching of a single ferromagnetic layer induced by in-plane current injection’, *Nature*, 476(7359), pp. 189–193. doi: 10.1038/nature10309.
- Monso, S. *et al.* (2002) ‘Crossover from in-plane to perpendicular anisotropy in Pt/CoFe/AlO_x sandwiches as a function of Al oxidation: A very accurate control of the oxidation of tunnel barriers’, *Applied Physics Letters*, 80(22), pp. 4157–4159. doi: 10.1063/1.1483122.
- Moore, T. A. *et al.* (2008) ‘High domain wall velocities induced by current in ultrathin Pt/Co/AlO_x wires with perpendicular magnetic anisotropy’, *Applied Physics Letters*, 93(26), p. 262504. doi: 10.1063/1.3062855.
- Moreau-Luchaire, C. *et al.* (2016) ‘Additive interfacial chiral interaction in multilayers for stabilization of small individual skyrmions at room temperature’, *Nature Nanotechnology*, (January). doi: 10.1038/nnano.2015.313.
- Moriya, T. (1960) ‘Anisotropic superexchange interaction and weak ferromagnetism’, *Physical Review*, 120(1), pp. 91–98. doi: 10.1103/PhysRev.120.91.
- Mougin, A. *et al.* (2007) ‘Domain wall mobility, stability and Walker breakdown in magnetic nanowires’, *Europhysics Letters (EPL)*, 78(5), p. 57007. doi: 10.1209/0295-5075/78/57007.
- Mühlbauer, S. (2009) ‘Skyrmion Lattice in a Chiral Magnet’, *Science*, 323, pp. 915–919. doi: 10.1126/science.333.6048.1381-b.

- Nagaosa, N. and Tokura, Y. (2013) 'Topological properties and dynamics of magnetic skyrmions.', *Nature nanotechnology*. Nature Publishing Group, 8(12), pp. 899–911. doi: 10.1038/nnano.2013.243.
- Nakatani, Y., Thiaville, A. and Miltat, J. (2005) 'Head-to-head domain walls in soft nano-strips: a refined phase diagram', *Journal of Magnetism and Magnetic Materials*, 290–291, pp. 750–753. doi: 10.1016/j.jmmm.2004.11.355.
- Nembach, H. T. *et al.* (2015) 'Linear relation between Heisenberg exchange and interfacial Dzyaloshinskii–Moriya interaction in metal films', *Nature Physics*, 11(10), pp. 825–829. doi: 10.1038/nphys3418.
- Ng, K.-O. and Vanderbilt, D. (1995) 'Stability of periodic domain structures in a two-dimensional dipolar model', *Physical Review B*, 52(3), pp. 2177–2183. doi: 10.1103/PhysRevB.52.2177.
- O'Handley, R. C. (2000) *Modern Magnetic Materials principles and applications*, *Materials Science Forum*. doi: 10.4028/www.scientific.net/MSF.414-415.139.
- Ou, Y. *et al.* (2016) 'Origin of fieldlike spin-orbit torques in heavy metal/ferromagnet/oxide thin film heterostructures', *Physical Review B*, 94(14), p. 140414. doi: 10.1103/PhysRevB.94.140414.
- Pai, C.-F. *et al.* (2012) 'Spin transfer torque devices utilizing the giant spin Hall effect of tungsten', *Applied Physics Letters*, 101(12), p. 122404. doi: 10.1063/1.4753947.
- Pai, C.-F. *et al.* (2014) 'Enhancement of perpendicular magnetic anisotropy and transmission of spin-Hall-effect-induced spin currents by a Hf spacer layer in W/Hf/CoFeB/MgO layer structures', *Applied Physics Letters*, 104(8), p. 082407. doi: 10.1063/1.4866965.
- Pai, C.-F. *et al.* (2015) 'Dependence of the efficiency of spin Hall torque on the transparency of Pt/ferromagnetic layer interfaces', *Physical Review B*, 92(6), p. 064426. doi: 10.1103/PhysRevB.92.064426.
- Parkin, S. S. P., Hayashi, M. and Thomas, L. (2008) 'Magnetic Domain-Wall Racetrack Memory', *Science*, 320(5873), pp. 190–194. doi: 10.1126/science.1145799.
- Pellegren, J. P., Lau, D. and Sokalski, V. (2017) 'Dispersive Stiffness of Dzyaloshinskii Domain Walls', *Physical Review Letters*, 119(2), p. 027203. doi: 10.1103/PhysRevLett.119.027203.
- Petit, D. *et al.* (2015) 'Two-dimensional control of field-driven magnetic bubble movement using Dzyaloshinskii–Moriya interactions', *Applied Physics Letters*, 106(2), p. 022402. doi: 10.1063/1.4905600.
- Pham, T. H. *et al.* (2016) 'Very large domain wall velocities in Pt/Co/Gd trilayers with Dzyaloshinskii–Moriya interaction', 67001, pp. 1–7. doi: 10.1209/0295-5075/113/67001.
- Pi, U. H. *et al.* (2010) 'Tilting of the spin orientation induced by Rashba effect in ferromagnetic metal layer', *Applied Physics Letters*, 97(16), p. 162507. doi: 10.1063/1.3502596.
- Quessab, Y. *et al.* (2018) 'Helicity-dependent all-optical domain wall motion in ferromagnetic thin films', *Physical Review B*, 97(5), p. 054419. doi: 10.1103/PhysRevB.97.054419.
- Quinsat, M. *et al.* (2017) 'Dzyaloshinskii–Moriya interaction in Pt/Co/Pt films prepared by chemical vapor deposition with various substrate temperatures', *AIP Advances*, 7(5), p. 056318. doi: 10.1063/1.4977547.
- Ramaswamy, R. *et al.* (2016) 'Hf thickness dependence of spin-orbit torques in Hf/CoFeB/MgO heterostructures', *Applied Physics Letters*, 108(20), p. 202406. doi: 10.1063/1.4951674.
- Rodmacq, B. *et al.* (2003) 'Crossovers from in-plane to perpendicular anisotropy in magnetic tunnel junctions as a function of the barrier degree of oxidation', *Journal of Applied Physics*, 93(10), pp.

7513–7515. doi: 10.1063/1.1555292.

Rodmacq, B. *et al.* (2009) ‘Influence of thermal annealing on the perpendicular magnetic anisotropy of Pt/Co/AlO_x trilayers’, *Physical Review B*, 79(2), p. 024423. doi: 10.1103/PhysRevB.79.024423.

Rohart, S. and Thiaville, A. (2013) ‘Skyrmion confinement in ultrathin film nanostructures in the presence of Dzyaloshinskii-Moriya interaction’, *Physical Review B*, 88(18), p. 184422. doi: 10.1103/PhysRevB.88.184422.

Roy, P. E., Otxoa, R. M. and Moutafis, C. (2019) ‘Controlled anisotropic dynamics of tightly bound skyrmions in a synthetic ferrimagnet due to skyrmion deformation mediated by induced uniaxial in-plane anisotropy’, *Physical Review B*. American Physical Society, 99(9), p. 094405. doi: 10.1103/PhysRevB.99.094405.

Ryu, K.-S. *et al.* (2012) ‘Current Induced Tilting of Domain Walls in High Velocity Motion along Perpendicularly Magnetized Micron-Sized Co/Ni/Co Racetracks’, *Applied Physics Express*, 5(9), p. 093006. doi: 10.1143/APEX.5.093006.

Ryu, K.-S. *et al.* (2014) ‘Chiral spin torque arising from proximity-induced magnetization.’, *Nature communications*. Nature Publishing Group, 5(May), p. 3910. doi: 10.1038/ncomms4910.

Ryu, K.-S. *et al.* (2016) ‘Current-driven domain wall motion due to volume spin transfer torque in Co/Ni multilayer systems on Au underlayer’, *Japanese Journal of Applied Physics*, 55(9), p. 093002. doi: 10.7567/JJAP.55.093002.

Ryu, K. S. *et al.* (2013) ‘Chiral spin torque at magnetic domain walls.’, *Nature nanotechnology*. Nature Publishing Group, 8(7), pp. 527–33. doi: 10.1038/nnano.2013.102.

Safeer, C. K. *et al.* (2015) ‘Spin-orbit torque magnetization switching controlled by geometry.’, *Nature nanotechnology*. Nature Publishing Group, 11(2), pp. 143–146. doi: 10.1038/nnano.2015.252.

Sampaio, J. *et al.* (2013) ‘Nucleation, stability and current-induced motion of isolated magnetic skyrmions in nanostructures’, *Nature Nanotechnology*. Nature Publishing Group, 8(11), pp. 839–844. doi: 10.1038/nnano.2013.210.

Schäfer, R. (2007) ‘Investigation of Domains and Dynamics of Domain Walls by the Magneto-optical Kerr-effect’, in *Handbook of Magnetism and Advanced Magnetic Materials*. Chichester, UK: John Wiley & Sons, Ltd. doi: 10.1002/9780470022184.hmm310.

Schryer, N. L. and Walker, L. R. (1974) ‘The motion of 180° domain walls in uniform dc magnetic fields’, *Journal of Applied Physics*, 45(12), pp. 5406–5421. doi: 10.1063/1.1663252.

Schulz, T. *et al.* (2012) ‘Emergent electrodynamics of skyrmions in a chiral magnet’, *Nature Physics*. doi: 10.1038/nphys2231.

Schulz, T. *et al.* (2015) ‘Spin-orbit torques for current parallel and perpendicular to a domain wall’, *Applied Physics Letters*, 107(12), p. 122405. doi: 10.1063/1.4931429.

Shahbazi, K. *et al.* (2019) ‘Domain-wall motion and interfacial Dzyaloshinskii-Moriya interactions in Pt/Co/Ir/Ta multilayers’, *Physical Review B*, 99(9), p. 094409. doi: 10.1103/PhysRevB.99.094409.

Shepley, P. M. *et al.* (2018) ‘Magnetic properties, domain-wall creep motion, and the Dzyaloshinskii-Moriya interaction in Pt/Co/Ir thin films’, *Physical Review B*. American Physical Society, 97(13), p. 134417. doi: 10.1103/PhysRevB.97.134417.

Šipr, O. *et al.* (2008) ‘Influence of composition, many-body effects, spin-orbit coupling, and disorder on magnetism of Co-Pt solid-state systems’, *Physical Review B*, 78(14), p. 144403. doi: 10.1103/PhysRevB.78.144403.

- Skyrme, T. H. R. (1962) 'A unified field theory of mesons and baryons', *Nuclear Physics*, 31(C), pp. 556–569. doi: 10.1016/0029-5582(62)90775-7.
- Slonczewski, J. C. (1996) 'Current-driven excitation of magnetic multilayers', *Journal of Magnetism and Magnetic Materials*, 159(1–2), pp. L1–L7. doi: 10.1016/0304-8853(96)00062-5.
- Slonczewski, J. C., Graham, C. D. and Rhyne, J. J. (1972) 'DYNAMICS OF MAGNETIC DOMAIN WALLS', in, pp. 170–174. doi: 10.1063/1.3699416.
- Sokalski, V. *et al.* (2012) 'Optimization of Ta thickness for perpendicular magnetic tunnel junction applications in the MgO-FeCoB-Ta system', *Applied Physics Letters*, 101(7), p. 072411. doi: 10.1063/1.4746426.
- Soucaille, R. *et al.* (2016) 'Probing the Dzyaloshinskii-Moriya interaction in CoFeB ultrathin films using domain wall creep and Brillouin light spectroscopy', *Physical Review B*, 94(10), p. 104431. doi: 10.1103/PhysRevB.94.104431.
- Soumyanarayanan, A. *et al.* (2017) 'Tunable room-temperature magnetic skyrmions in Ir/Fe/Co/Pt multilayers', *Nature Materials*, 16(9), pp. 898–904. doi: 10.1038/nmat4934.
- Suzuki, T. *et al.* (2011) 'Current-induced effective field in perpendicularly magnetized Ta/CoFeB/MgO wire', *Applied Physics Letters*, 98(14), p. 142505. doi: 10.1063/1.3579155.
- Tanaka, M. *et al.* (2015) 'Current-induced dynamics of bubble domains in perpendicularly magnetized TbFeCo wires', *Applied Physics Express*, 8(7), p. 073002. doi: 10.7567/APEX.8.073002.
- Tanaka, M. *et al.* (2017) 'Electric-current-induced dynamics of bubble domains in a ferrimagnetic Tb/Co multilayer wire below and above the magnetic compensation point', *AIP Advances*, 7(5). doi: 10.1063/1.4974067.
- Tanigawa, H. *et al.* (2013) 'Thickness dependence of current-induced domain wall motion in a Co/Ni multi-layer with out-of-plane anisotropy', *Applied Physics Letters*, 102(15), p. 152410. doi: 10.1063/1.4802266.
- Tarasenko, S. V. *et al.* (1998) 'Bloch wall dynamics in ultrathin ferromagnetic films', *Journal of Magnetism and Magnetic Materials*, 189(1), pp. 19–24. doi: 10.1016/S0304-8853(98)00230-3.
- Tatara, G. and Kohno, H. (2004) 'Theory of Current-Driven Domain Wall Motion: Spin Transfer versus Momentum Transfer', *Physical Review Letters*, 92(8), p. 086601. doi: 10.1103/PhysRevLett.92.086601.
- Tetienne, J.-P. *et al.* (2014) 'Nitrogen-vacancy-center imaging of bubble domains in a 6-Å film of cobalt with perpendicular magnetization', *Journal of Applied Physics*, 115(17), p. 17D501. doi: 10.1063/1.4861557.
- Tetienne, J.-P. *et al.* (2015) 'The nature of domain walls in ultrathin ferromagnets revealed by scanning nanomagnetometry', *Nature Communications*, 6, p. 6733. doi: 10.1038/ncomms7733.
- Thiaville, a. *et al.* (2005) 'Micromagnetic understanding of current-driven domain wall motion in patterned nanowires', *Europhysics Letters (EPL)*, 69(6), pp. 990–996. doi: 10.1209/epl/i2004-10452-6.
- Thiaville, A. *et al.* (2004) 'Domain wall motion by spin-polarized current: A micromagnetic study', *Journal of Applied Physics*, 95(11 II), pp. 7049–7051. doi: 10.1063/1.1667804.
- Thiaville, A. *et al.* (2012) 'Dynamics of Dzyaloshinskii domain walls in ultrathin magnetic films', *EPL (Europhysics Letters)*, 100(5), p. 57002. doi: 10.1209/0295-5075/100/57002.
- Thiele, A. A. (1973) 'Steady-State Motion of Magnetic Domains', *Physical Review Letters*.

- American Physical Society, 30(6), pp. 230–233. doi: 10.1103/PhysRevLett.30.230.
- Tomasello, R. *et al.* (2015) ‘A strategy for the design of skyrmion racetrack memories’, *Scientific Reports*, 4(1), p. 6784. doi: 10.1038/srep06784.
- Tomasello, R. *et al.* (2018) ‘Micromagnetic understanding of the skyrmion Hall angle current dependence in perpendicularly magnetized ferromagnets’, *Physical Review B*. American Physical Society, 98(22), p. 224418. doi: 10.1103/PhysRevB.98.224418.
- Tretiakov, O. A. *et al.* (2008) ‘Dynamics of Domain Walls in Magnetic Nanostrips’, *Physical Review Letters*, 100(12), p. 127204. doi: 10.1103/PhysRevLett.100.127204.
- Trifu, A. V. (2017) *Spin-orbit torque measurements in Pt-based heavy metal/ferromagnetic heterostructures with in-plane magnetic anisotropy*.
- Tserkovnyak, Y., Brataas, A. and Bauer, G. E. W. (2002) ‘Enhanced Gilbert Damping in Thin Ferromagnetic Films’, *Physical Review Letters*, 88(11), p. 117601. doi: 10.1103/PhysRevLett.88.117601.
- Tveten, E. G. *et al.* (2013) ‘Staggered Dynamics in Antiferromagnets by Collective Coordinates’, *Physical Review Letters*, 110(12), p. 127208. doi: 10.1103/PhysRevLett.110.127208.
- Ueda, K. *et al.* (2014) ‘Transition in mechanism for current-driven magnetic domain wall dynamics’, *Applied Physics Express*, 7(5). doi: 10.7567/APEX.7.053006.
- Ueda, K. *et al.* (2015) ‘In-plane field-driven crossover in the spin-torque mechanism acting on magnetic domain walls in Co/Ni’, *Physical Review B*, 91(6), p. 060405. doi: 10.1103/PhysRevB.91.060405.
- Vaňatka, M. *et al.* (2015) ‘Velocity asymmetry of Dzyaloshinskii domain walls in the creep and flow regimes.’, *Journal of Physics C*, 27(32), p. 326002. doi: 10.1088/0953-8984/27/32/326002.
- Wang, X. and Manchon, A. (2012) ‘Diffusive Spin Dynamics in Ferromagnetic Thin Films with a Rashba Interaction’, *Physical Review Letters*, 108(11), p. 117201. doi: 10.1103/PhysRevLett.108.117201.
- Wang, X., Pauyac, C. O. and Manchon, A. (2014) ‘Spin-orbit-coupled transport and spin torque in a ferromagnetic heterostructure’, *Physical Review B*, 89(5), p. 054405. doi: 10.1103/PhysRevB.89.054405.
- Wang, Z. *et al.* (2019) ‘Generation and Hall effect of skyrmions enabled via using nonmagnetic point contacts’. doi: arXiv:1902.06954v1.
- Weindler, T. *et al.* (2014) ‘Magnetic damping: Domain wall dynamics versus local ferromagnetic resonance’, *Physical Review Letters*. doi: 10.1103/PhysRevLett.113.237204.
- Wells, A. W. J. *et al.* (2017) ‘Effect of interfacial intermixing on the Dzyaloshinskii-Moriya interaction in Pt/Co/Pt’, *Physical Review B*, 95(5), p. 054428. doi: 10.1103/PhysRevB.95.054428.
- Woo, S. *et al.* (2014) ‘Enhanced spin-orbit torques in Pt/Co/Ta heterostructures’, *Applied Physics Letters*, 105(21), pp. 2012–2017. doi: 10.1063/1.4902529.
- Woo, S. *et al.* (2016) ‘Observation of room-temperature magnetic skyrmions and their current-driven dynamics in ultrathin metallic ferromagnets’, *Nature Materials*, 15(5), pp. 501–506. doi: 10.1038/nmat4593.
- Woo, S. *et al.* (2017) ‘Spin-orbit torque-driven skyrmion dynamics revealed by time-resolved X-ray microscopy’, *Nature Communications*, 8, p. 15573. doi: 10.1038/ncomms15573.
- Woo, S. *et al.* (2018) ‘Current-driven dynamics and inhibition of the skyrmion Hall effect of ferrimagnetic skyrmions in GdFeCo films’, *Nature Communications*. Springer US, 9(1), p. 959. doi:

10.1038/s41467-018-03378-7.

Woodhouse, N. M. J. (2003) ‘Einstein’s Special Theory of Relativity’, in, pp. 57–73. doi: 10.1007/978-1-4471-0083-6_4.

Xiao, J., Zangwill, A. and Stiles, M. D. (2006) ‘Spin-transfer torque for continuously variable magnetization’, *Physical Review B*, 73(5), p. 054428. doi: 10.1103/PhysRevB.73.054428.

Yamada, K. *et al.* (2011) ‘Influence of Instabilities on High-Field Magnetic Domain Wall Velocity in (Co/Ni) Nanostrips’, *Applied Physics Express*, 4(11), p. 113001. doi: 10.1143/APEX.4.113001.

Yamada, K. and Nakatani, Y. (2015) ‘Excitation of magnetic domain wall velocity in (Co/Ni) nanowires induced by blocking the motion of vertical Bloch lines’, *Applied Physics Express*, 8(9), p. 093004. doi: 10.7567/APEX.8.093004.

Yamaguchi, A. *et al.* (2004) ‘Real-Space Observation of Current-Driven Domain Wall Motion in Submicron Magnetic Wires’, *Physical Review Letters*, 92(7), p. 077205. doi: 10.1103/PhysRevLett.92.077205.

Yamanouchi, M. *et al.* (2006) ‘Velocity of Domain-Wall Motion Induced by Electrical Current in the Ferromagnetic Semiconductor (Ga,Mn)As’, *Physical Review Letters*, 96(9), p. 096601. doi: 10.1103/PhysRevLett.96.096601.

Yang, H. *et al.* (2015) ‘Anatomy of Dzyaloshinskii-Moriya Interaction at Co / Pt Interfaces’, *Physical Review Letters*, 115(26), p. 267210. doi: 10.1103/PhysRevLett.115.267210.

Yang, H. X. *et al.* (2011) ‘First-principles investigation of the very large perpendicular magnetic anisotropy at Fe | MgO and Co | MgO interfaces’, *Physical Review B*, 84(5), p. 054401. doi: 10.1103/PhysRevB.84.054401.

Yoo, S. C., Moon, K. W. and Choe, S. B. (2013) ‘Analytic description of domain-wall deformation caused by the Oersted field in current-driven domain-wall motion’, *Journal of Magnetism and Magnetic Materials*. Elsevier, 343, pp. 234–238. doi: 10.1016/j.jmmm.2013.05.015.

Yoshimura, Y. *et al.* (2016) ‘Soliton-like magnetic domain wall motion induced by the interfacial Dzyaloshinskii–Moriya interaction’, *Nature Physics*, 12(2), pp. 157–161. doi: 10.1038/nphys3535.

Yu, G. *et al.* (2016) ‘Room-Temperature Creation and Spin–Orbit Torque Manipulation of Skyrmions in Thin Films with Engineered Asymmetry’, *Nano Letters*, 16(3), pp. 1981–1988. doi: 10.1021/acs.nanolett.5b05257.

Yu, G. *et al.* (2017) ‘Room-Temperature Skyrmion Shift Device for Memory Application’, *Nano Letters*, 17(1), pp. 261–268. doi: 10.1021/acs.nanolett.6b04010.

Yu, J. *et al.* (2016) ‘Large spin-orbit torques in Pt/Co-Ni/W heterostructures’, *Applied Physics Letters*, 109(4), p. 042403. doi: 10.1063/1.4959958.

Yu, X. Z. *et al.* (2010) ‘Real-space observation of a two-dimensional skyrmion crystal’, *Nature*, 465(7300), pp. 901–904. doi: 10.1038/nature09124.

Zakeri, K. *et al.* (2012) ‘Magnon Lifetimes on the Fe(110) Surface: The Role of Spin-Orbit Coupling’, *Physical Review Letters*, 108(19), p. 197205. doi: 10.1103/PhysRevLett.108.197205.

Zang, J. *et al.* (2011) ‘Dynamics of Skyrmion Crystals in Metallic Thin Films’, *Physical Review Letters*, 107(13), p. 136804. doi: 10.1103/PhysRevLett.107.136804.

Zeissler, K. *et al.* (2018) ‘Discrete Hall resistivity contribution from Néel skyrmions in multilayer nanodiscs’, *Nature Nanotechnology*, 13(12), pp. 1161–1166. doi: 10.1038/s41565-018-0268-y.

Zhang, S. and Li, Z. (2004) ‘Roles of Nonequilibrium Conduction Electrons on the Magnetization Dynamics of Ferromagnets’, *Physical Review Letters*, 93(12), p. 127204. doi:

10.1103/PhysRevLett.93.127204.

Zhang, X., Zhou, Y. and Ezawa, M. (2016) 'Magnetic bilayer-skyrmions without skyrmion Hall effect', *Nature Communications*. Nature Publishing Group, 7(1), p. 10293. doi: 10.1038/ncomms10293.

Résumé

L'étude du déplacement par le courant électrique des parois de domaine magnétique a généré beaucoup d'intérêt depuis l'observation de leurs importantes vitesses de déplacement dans des multicouches ayant une asymétrie d'inversion verticale (SIA).

Cet intérêt se justifie par leur fort potentiel pour de nouvelles applications à basse consommation d'énergie en mémoire cache ou mémoires centrale. L'inversion de symétrie (SIA) induit deux mécanismes dont l'action conjointe permet de déplacer efficacement les parois de domaines. Il s'agit d'une contribution énergétique chirale, appelée l'interaction Dzyaloshinskii-Moriya (DMI), et des couples de spin-orbite (SOT).

Ce modèle reste incomplet vu qu'il n'explique pas plusieurs résultats expérimentaux. De plus, une contribution dissipative chirale appelée l'amortissement anisotrope, également induite par la SIA, a été proposée récemment et dont le rôle, sous courant, n'as pas encore été étudié.

Le but de ce travail a été d'amener une connaissance détaillée des différentes interactions en jeu dans la dynamique des parois de domaine. Pour cela, j'ai étudié la propagation de parois sous courant dans une géométrie non colinéaire. Cette étude a été réalisée dans des systèmes ayant des SIA différentes (Pt/Co/Pt et Pt/Co/AlOx). Dans cette géométrie, j'ai observé l'asymétrie du déplacement qui illustre la compétition entre les contributions chirales d'énergie et d'amortissement dans des multicouches à faible SIA. Quant aux multicouches à forte SIA, l'asymétrie ne peut être expliquée par l'action conjointe de DMI et SOT même dans le régime à forte mobilité. Une des conséquences de ce type de déplacement est de contribuer à la déviation des bulles de skyrmion en mouvement. Nous avons appelé cet effet l'effet Hall extrinsèque des skyrmions.

En mettant en évidence de nouveaux effets induits par SIA, les résultats de cette thèse contribuent à une meilleur compréhension des mécanismes intervenant dans les déplacements des parois et des skyrmions sous courant dans les multicouches magnétiques.

Mots clés : parois de domaines magnétiques, couples de spin-orbite, interaction Dzyaloshinskii-Moriya, amortissement magnétique anisotrope, skyrmions, déplacement des parois de domaines magnétiques, microscopie à effet Kerr, mémoires magnétiques, électronique de spin.

Abstract

The study of the current-induced magnetic domain walls motion has attracted a lot of interest since the report of their large velocities of motion in thin layers with structural inversion asymmetry (SIA).

This interest comes from their high potential for low power consumption functionalities in cache and main memories applications. The SIA induces two mechanisms whose combined action allows to drive efficiently the domain walls. The two mechanisms are the chiral energy term, called the Dzyaloshinskii-Moriya interaction (DMI), and the spin-orbit torques (SOT). This model is still incomplete since it does not explain several experimental results. In addition, a chiral dissipation term called the chiral damping, also induced by SIA, has recently been proposed. However, its effect on current-induced domain wall motion has not been studied.

The objective of this work was to bring a more detailed understanding of the interactions involved in the domain wall motion. To that end, I have studied the domain wall motion in a non-collinear geometry with respect to the current, in materials with different SIA (Pt/Co/Pt and Pt/Co/AlOx). This motion has been found to be asymmetric. It illustrates the interplay between chiral energy and chiral dissipation in current-induced domain wall motion in weak SIA materials. In large SIA materials, the DMI and SOT model, even in the flow regime of motion, cannot explain this asymmetry.

I have also evidenced that the asymmetric non-collinear domain wall motion induces a well-defined deflection of the skyrmion bubbles. This is the first observation of the extrinsic skyrmion Hall effect.

The results of this thesis contribute to the understanding of the physical mechanisms behind domain wall and skyrmion motion in ultrathin layers by evidencing supplementary effects from SIA.

Key words: magnetic domain wall, spin-orbit torques, Dzyaloshinskii-Moriya interaction, Chiral Damping, magnetic skyrmion bubbles, domain wall motion, Kerr microscopy, the skyrmion Hall effect, magnetic memory devices, spintronics

